27 June 2008 : 319

Science

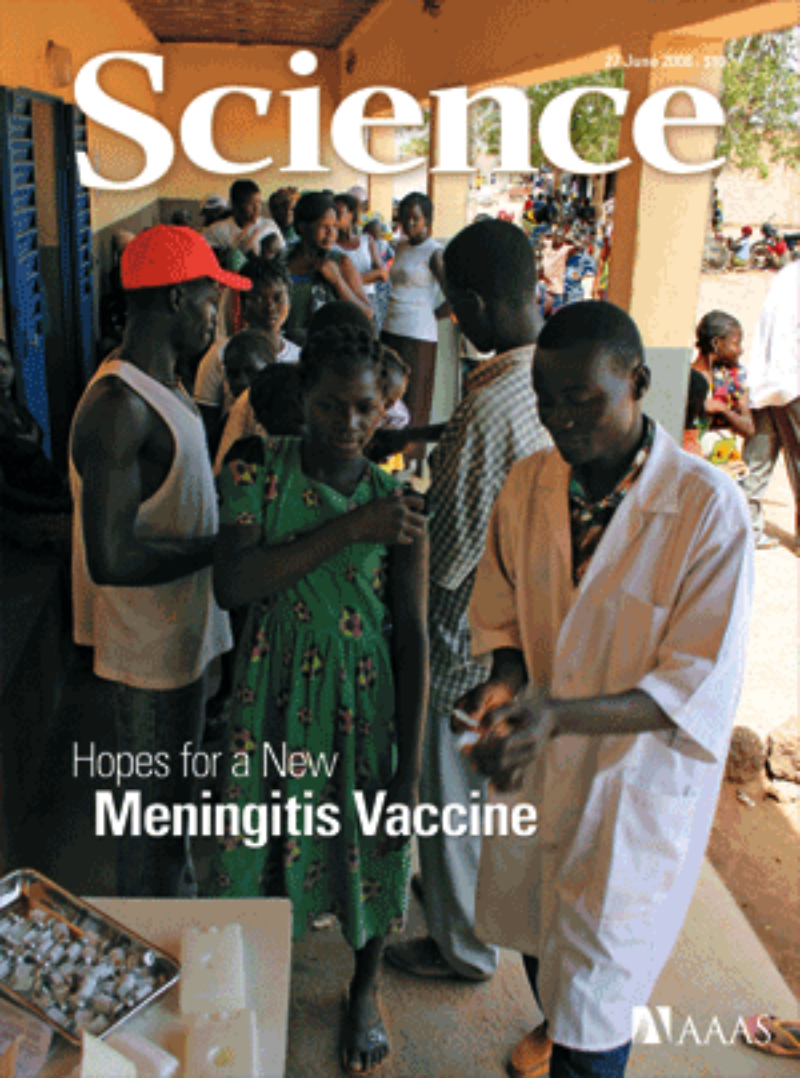

Hopes for a New Meningitis Vaccine

AAAS

Volume 320, Issue 5884

COVER

Waiting for a vaccination to curb a meningitis epidemic under way in Koudougou district, Burkina Faso, in March. An affordable new meningitis vaccine in the works promises to prevent, not just control, these frequent epidemics. See page 1710.

Image: Monique Berlier/MVP-PATH

DEPARTMENTS

EDITORIAL

NEWS OF THE WEEK

NEWS FOCUS

1710

LETTERS

BOOKS *ET AL.*

EDUCATION FORUM

PERSPECTIVES

1721

CONTENTS continued >>

Published by AAAS

Science

CONTENTS

SCIENCE EXPRESS

www.sciencexpress.org

BIOCHEMISTRY

Crystal Structure of the Termination Module of a Nonribosomal Peptide Synthetase

A. Tanovic, S. A. Samel, L.-O. Essen, M. A. Marahiel

A large enzyme complex assembles peptide natural products without ribosomal participation by successive catalytic steps at the end of a flexible, substrate-loaded arm.

10.1126/science.1159850

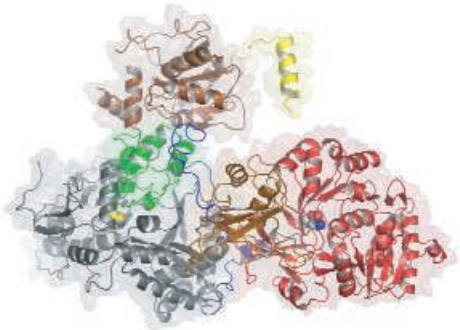

CHEMISTRY

Measurement of the Distribution of Site Enhancements in Surface-Enhanced Raman Scattering

Y. Fang, N.-H. Seong, D. D. Dlott

The distribution of electric field–enhancing sites on a nanostructured substrate is measured by using the enhanced field to damage those sites.

10.1126/science.1159499

ASTRONOMY

Properties of Gamma-Ray Burst Progenitor Stars

P. Kumar, R. Narayan, J. L. Johnson

Analysis of the x-ray afterglow of intense gamma-ray bursts shows that the bursts result from consumption of the outer part of a dense star and define the star's rotation rate.

10.1126/science.1159003

REVIEW

BREVIA

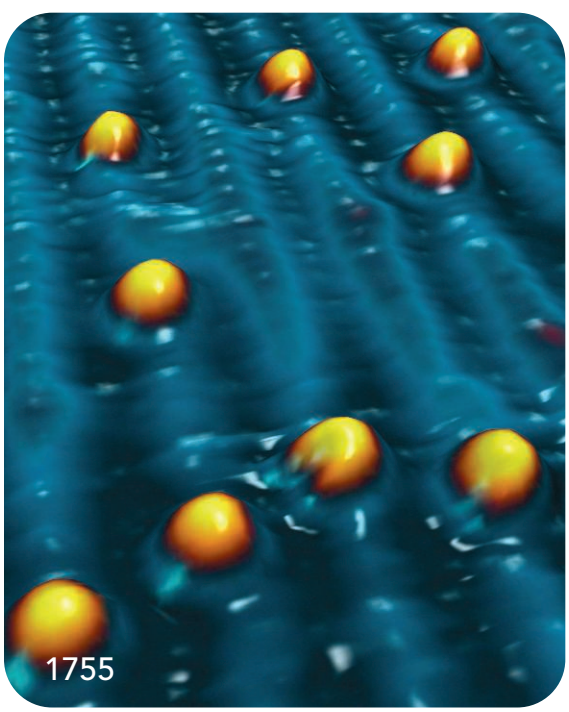

RESEARCH ARTICLE

REPORTS

CONTENTS continued **>>**

REPORTS *CONTINUED...*

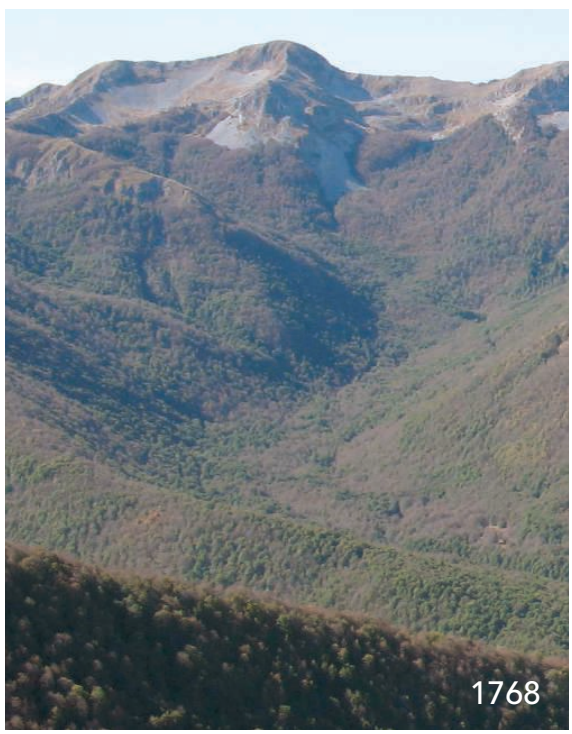

AAAS
ADVANCING SCIENCE, SERVING SOCIETY

SCIENCE (ISSN 0036-8075) is published weekly on Friday, except the last week in December, by the American Association for the Advancement of Science, 1200 New York Avenue, NW, Washington, DC 20005. Periodicals Mail postage (publication No. 484460) paid at Washington, DC, and additional mailing offices. Domestic individual membership and subscription (51 issues): $144 ($74 allocated to subscription). Domestic institutional subscription (51 issues): $770; Foreign postage extra: Mexico, Caribbean (surface mail) $55; other countries (air assist delivery) $85. First class, airmail, student, and emeritus rates on request. Canadian rates with GST available upon request, GST #1254 88122. Publications Mail Agreement Number 1069624. **Printed in the U.S.A.**

Change of address: Allow 4 weeks, giving old and new addresses and 8-digit account number. **Postmaster:** Send change of address to AAAS, P.O. Box 96178, Washington, DC 20090–6178. **Single-copy sales:** $10.00 current issue, $15.00 back issue prepaid includes surface postage; bulk rates on request. The identification code for *Science* is 0036-8075. *Science* is indexed in the *Reader's Guide to Periodical Literature* and in several specialized indexes.

CONTENTS continued **>>**

Good eatin'.

SCIENCE**NOW**

www.sciencenow.org

HIGHLIGHTS FROM OUR DAILY NEWS COVERAGE

Smart Girls Eat Fish
Choice of dietary fat affects intelligence.

It's a Dog's (Genetic) Life
Pointing, herding, and life span of dogs linked to specific stretches of DNA.

Down Under, Fish Numbers Climb Up
Rapid recovery of a key species in Australia points to efficacy of fishing bans.

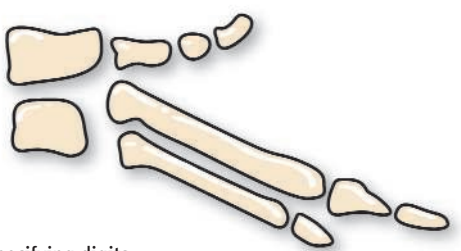

Specifying digits.

SCIENCE **SIGNALING**

www.sciencesignaling.org

THE SIGNAL TRANSDUCTION KNOWLEDGE ENVIRONMENT

PERSPECTIVE: Uncoupling the Role of Sonic Hedgehog in Limb Development—Growth and Specification
P. Francis-West and R. Hill
Sonic hedgehog (Shh) is required for both proliferation and specification of cells in the developing limb bud.

PERSPECTIVE: p53 Brings a New Twist to the Smad Signaling Network
A. Atfi and R. Baron
Interactions between p53 and Smad proteins influence the responses to the TGF-β pathway, which may be important for progression of some types of cancer.

Balancing teaching and research.

SCIENCE **CAREERS**

www.sciencecareers.org/career_development

FREE CAREER RESOURCES FOR SCIENTISTS

Mastering Your Ph.D.: Better Communication With Your Supervisor
P. Gosling and B. Noordam
When was the last structured conversation you had with your supervisor?

Liberal Arts College Faculty: Finding the Sweet Spot
S. Webb
You need to find the elusive balance between teaching and research.

Creativity and Persistence Overcome Failure
L. Laursen
A senior scientist shares how he got past some early challenges.

***Science* Careers Blog**
Science *Careers Staff*
Find interesting information related to scientific careers, updated often.

SCIENCE**PODCAST**

www.sciencemag.org/multimedia/podcast

FREE WEEKLY SHOW

Download the 27 June *Science* Podcast to hear about an upward shift in plant species' optimum elevation, the evolutionary history of birds, recent letters to *Science*, and more.

Separate individual or institutional subscriptions to these products may be required for full-text access.

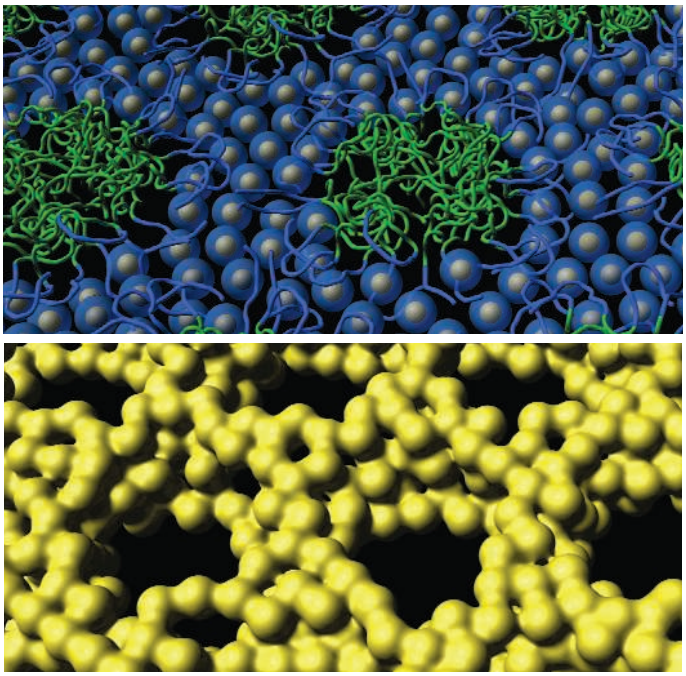

<< Mesoporous Metal Composites from Nanoparticles

Metallic materials with internal pores on the scale of 10 nanometers could be useful as high-surface-area electrodes or catalysts, but many metals have high surface energies that tend to encourage the closure of such pores and decrease surface area. In principle, it should be possible to assemble metal nanoparticles into composites, but the surface coatings on nanoparticles can lead to low overall metal content in the final composite. **Warren *et al.*** (p. 1748) chose a block polymer that could bind ligand-stabilized platinum nanoparticles and form lamellar or inverse hexagonal phases with high nanoparticle loadings. Pyrolysis created an ordered, highly conductive platinum-carbon composite with open pores ≥10 nanometers in size; almost all of the carbon could be removed from thin section samples with a plasma treatment to yield porous platinum mesostructures.

After the Asteroid

About 35 million years ago, a large asteroid hit the continental shelf of North America in what is now the southeastern tip of the Delmarva Peninsula, just east of the Chesapeake Bay, forming a crater nearly 90 kilometers across. **Gohn *et al.*** (p. 1740) describe results from two cores drilled from the crater. Within a few minutes of the impact, huge granite blocks were rapidly transported several kilometers inward. The top of the crater was filled with a large debris flow and seawater from the time of the impact remains trapped in the pores of the crater. Although the high heat of impact probably sterilized the local rocks and sediments, the seawater has never been flushed since soon after the impact, and in the deepest part of the crater the water contains abundant microbes.

Let There Be Light

Very high energy gamma rays are thought to be produced as matter falls into supermassive black holes in distant galaxies. Using a large gamma-ray telescope, the **MAGIC Collaboration** (p. 1752) detected an extremely energetic source of gamma rays more than 5 billion light-years from Earth. En route, the gamma rays will have interacted with relic light from older stars and galaxies that formed during the evolution and expansion of the universe, which allows an independent measurement of this extragalactic background light. The results are consistent the amount of light expected from galaxy counts.

Birds, Birds, Birds

The relationships among bird families and orders have been difficult to establish due to the existence of conflicting phylogenies from morphology and to the availability of a relatively limited number of samples of avian DNA sequences. **Hackett *et al.*** (p. 1763; see the news story by Pennisi) have performed a phylogenetic analysis of 25 kilobases of nuclear DNA sequence per species representing multiple chromosomes, genes, and noncoding regions of genomes across the Aves. While many established relationships were upheld in this phylogeny, several surprising results were noted, which suggests that bird evolutionary relationships are complex and that previously grouped species may not be closely related but instead show convergence of particular life history traits.

Electron Relay Station

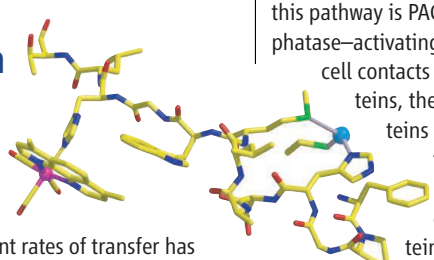

Many proteins promote rapid electron transfer over surprisingly long distances. One proposed mechanism to account for such efficient rates of transfer has been the transient oxidation and/or reduction of intermediate residues along the path from donor to acceptor. **Shih *et al.*** (p. 1760; see the Perspective by **Bollinger**) present quantitative evidence for this type of relay mechanism in a series of engineered azurin mutants bearing a tryptophan, tyrosine, or phenylalanine residue between coordinated copper donor and rhenium acceptor complexes. Transient absorption spectroscopy in the visible and infrared revealed that the intervening tryptophan accelerated the electron transfer more than a hundredfold. In comparison, neither tyrosine nor phenylalanine had the same effect, highlighting the narrow range of intermediary redox potentials necessary for the acceleration.

Linking Cell Contact and Polarity

Polarization of the early embryo enables essential patterning events such as gastrulation and cell specification. In certain animals, including worms and mammals, cell-cell contact polarizes early embryos by inducing asymmetries in cortical PAR proteins. **Anderson *et al.*** (p. 1771) identify a pathway linking cell-cell contact to the PAR asymmetries that polarize early embryos of the nematode, *Caenorhabditis elegans*. A key member in this pathway is PAC-1, a Rho guanosine triphosphatase–activating protein. PAC-1 is recruited to cell contacts and locally excludes PAR proteins, thereby restricting the PAR proteins to contact-free surfaces. In turn, PAR proteins induce radial polarity that asymmetrically positions cytoskeletal proteins needed for gastrulation.

Developing the Lateral Line

Fish use the lateral line to sense changes in pressure and water movements that may signal the arrival of food or predators. **Nechiporuk and Raible** (p. 1774) now use genetics, cell transplantation, and live imaging to study lateral line development in zebrafish. In zebrafish, the lat-

Continued on page 1693

CREDITS (TOP TO BOTTOM): COURTESY OF SCOTT WARREN AND ULI WIESNER, CORNELL UNIVERSITY; SHIH *ET AL.*

Continued from page 1691

eral line develops from front to back, with a migrating zone of progenitor cells laying down repeated clusters of hair cells in its wake. Fibroblast growth factor signaling is involved in several aspects of the process: migration, deposition of a primordium, and differentiation.

Expanding β-Arrestin's Remit

The β-arrestin proteins help restore G protein–coupled receptors to an inactive state after stimulation. Recently, positive signaling roles for the arrestins have been revealed, as well as roles in signaling by other types of receptors, including the receptor Smoothened (Smo), which has structural similarity to G protein–coupled receptors, but signals in a distinct manner. **Kovacs *et al.*** (p. 1777, published online 22 May; see the Perspective by **Rohatgi and Scott**) report that β-arrestins 1 and 2 in cultured cells were detected in a complex with a tagged version of the Smo protein and with Kif3A, a kinesin motor protein. Depletion of β-arrestin 1 or β-arrestin 2 inhibited localization of Smo to primary cilia, which function as "antenna"-like structures rich in receptor proteins. Smo-dependent transcriptional activation was also inhibited if the arrestins were depleted. This Smo-dependent interaction of β-arrestins with Kif3A may link Smo to the transport apparatus that brings it to the primary cilium.

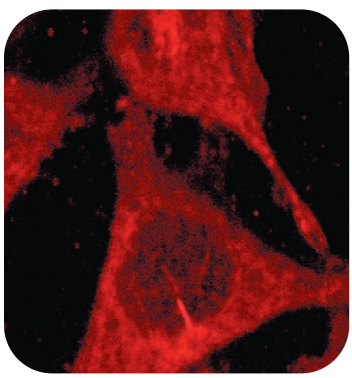

CREDIT: JEFFREY J. KOVACS

Dissecting Spliceosome Functions

Many eukaryotic genes are split into several pieces by the presence of noncoding introns. Introns are spliced out of transcribed RNA by a large RNA protein complex, the spliceosome. Very similar transesterification reactions are carried out by self-splicing Group II intron RNAs. Self-splicing reactions are fully reversible. The potentially much more complex spliceosome reactions should, in principle, also be reversible, but this has not been demonstrated. Now **Tseng and Cheng** (p. 1782) use a spliceosome variant unable to release the spliced RNA products of the splicing reaction to show that in the absence of monovalent ions, the second transesterification step of splicing can run backwards at high efficiency. Spliceosomes arrested after the first transesterification reaction can also carry out the reverse reaction, this time in the presence of KCl, raising questions about the function of various components of the spliceosome.

Same But Different

The genetic code is inherently redundant, with synonymous codons encoding the same amino acid. A level of bias has evolved in terms of how often particular codons are actually used to encode a given amino acid because, in the context of the whole sequence, particular codon usage affects secondary structure and/or translation of the transcribed RNA. Similarly, the many ways in which synonymous codons are paired with one another can show particular leanings (probably for similar reasons), which is known as codon-pair bias. **Coleman *et al.*** (p. 1784; see the news story by Enserink) explore how bias of synonymous codon pairs at a genome level might influence the biology of a system. An algorithm was designed to recode the DNA sequence for the poliovirus capsid protein, while maintaining the original amino acid sequence, to generate two recoded chimeric strains of the virus carrying either under- or overrepresented codon pairs. Although marginal effects were seen with the latter, chimeric viruses carrying underrepresented codon pairs had reduced translation, were less able to infect cells, and showed reduced pathogenicity in mice.

Human Migration Unraveled

The ability to follow the migration and demography of the earliest human settlers helps us understand the significance of cultural remains. **Gilbert *et al.*** (p. 1787, published online 29 May) have sequenced a human hair sample from approximately 3000 years ago and assembled a complete mitochondrial genome from one of the oldest human inhabitants of Greenland. Comparisons with existing human mitochondrial genomes suggest that this individual, unlike the current population, was related to eastern Asian populations. Thus the first human occupation of the far north may have been by migrants from East Asia, and these early inhabitants were subsequently replaced by a later migration within America giving rise to the existing Eskimo populations.

Published by AAAS

Edouard Brézin, a former president of the French Academy of Sciences, is a professor of physics.

Antoine Triller is a senior researcher at INSERM, Ecole Normale Supérieure, Paris.

Long Road to Reform in France

OVER THE PAST 2 YEARS, SEVERAL CHANGES HAVE OCCURRED IN THE FRENCH SYSTEM OF scientific research and higher education, and more are on the way. As the country struggles to find ways of modernizing a structure that has been forged over two centuries, the intention to improve things is a good sign.

Change is needed because the French system is mired in numerous idiosyncrasies, including a dichotomy between public universities and specialized public institutions of higher education—the *grandes écoles*. The latter are selective but mainly emphasize undergraduate education. The other major problem is a research workforce fragmented between universities and government agencies such as the Centre National de la Recherche Scientifique (CNRS) for basic sciences and the French National Institute for Health and Medical Research (INSERM). This structure inhibits the flow of professional talent between these institutions.

In August 2007, the French government proposed giving universities more autonomy and a stronger role in driving research. It is too early to judge whether universities will use their increased, but still limited, freedom effectively. However, several drawbacks remain. Students, technicians, and professors will continue to elect university presidents. Their representatives, often chosen by politicized unions, will retain significant influence in a matter for which competence should be the only criterion. The procedure for hiring professors has also resulted in severe local "inbreeding." Will the imminent new powers given to university presidents for appointing ad hoc recruitment committees with 50% external members improve the situation? Furthermore, universities will still not be allowed to select students on the basis of their abilities but remain obligated to accept all applicants. In fields such as mathematics, physics, and chemistry, universities suffer from competition with the *grandes écoles* for attracting the best students, and this will not change. Yet, despite the selectivity of the *grandes écoles*, their students are rarely exposed to research and have little incentive to complete graduate education. In 2007, only 6% of the 42,000 students of the science and engineering *grandes écoles* advanced into Ph.D. programs.

Although the successes of French research have largely relied on partnerships between the universities and government agencies, some political forces want to abolish permanent nonteaching research positions. But the decline of these positions within the agencies would be the demise of French research if it happens before the new organization of universities has demonstrated its ability to conduct research.

The Agence Nationale de la Recherche (ANR), established in 2005, provides research grants on a competitive basis (awarding €825 million in 2007) and provides career-development opportunities to young researchers. However, more than 70% goes to programs with targeted objectives defined a priori by the government. The 30% devoted to broader, excellence-based programs is too small. In addition, the ANR grants support very limited overhead costs. It is shortsighted not to acknowledge the important role of the infrastructure in which individual researchers operate.

The teaching load of newly recruited professors has increased by 50% since 1983, severely impairing their research capacities. The CNRS has proposed creating 5-year chair positions that have no teaching duties for assistant professors, giving them a chance to remain active in research. This is potentially a good idea whose generalization would be welcome, but only if the hiring procedures at universities improve. The meaning of the transformation of the CNRS into a federation of institutes, announced last month by Science Minister Valerie Pécresse, is still obscure. However, most scientists believe that the badly needed reinvigoration of the universities cannot be achieved simply by jeopardizing comparatively more efficient organizations such as the CNRS.

The future of France's research and education system ultimately depends on its ability to attract the best young minds to science and give them the appropriate means to develop their ideas. Their opportunities have improved slightly, but the end of the road is not yet in sight.

– Edouard Brézin and Antoine Triller

10.1126/science.1161025

Published by AAAS

EDITED BY GILBERT CHIN AND JAKE YESTON

IMMUNOLOGY

AID-ing Up MicroRNA Functions

MicroRNAs are key regulators of gene function, yet the full scope of their influence is not known. In the immune system, miR-155 has multiple roles, although B cells show a particular dependence on its effects. Two studies now provide evidence that this is largely due to its targeting of the enzyme activation-induced cytidine deaminase (AID), which regulates somatic hypermutation and class-switch recombination of antibody genes.

After identifying miR-155 response elements in the 3′ region of AID mRNA, Teng *et al.* designed constructs containing a reporter linked either to a functional AID locus or to one in which the miR-155 elements had been mutated. In the latter case, loss of the ability to respond to miR-155 led to increases in AID expression and class-switch recombination in stimulated B cells. In contrast, somatic hypermutation was unaffected, although affinity maturation was unexpectedly impaired. Dorsett *et al.* noted similar effects of mutations in the AID mRNA miR-155 binding site, which again corresponded with increased AID levels. A higher rate of AID-associated chromosomal translocations was also detected, suggesting that beyond its influence on normal B cell functions, this microRNA helps minimize potential oncogenic events. — SJS

Immunity **28**, 621; 630 (2008).

BIOMEDICINE

A Brush with Infection

The human mouth harbors a surprisingly diverse complement of bacteria. Although most are harmless, a subset—if they enter the bloodstream—are believed to cause a potentially life-threatening heart condition called infective endocarditis, especially in individuals with preexisting heart valve damage. For this reason, at-risk patients are often prescribed prophylactic antibiotics before invasive dental procedures such as tooth extraction. This practice has become increasingly controversial, however, both because of general concerns about the overuse of antibiotics and because the extent of bacteremia caused by tooth extraction has never been compared to that caused by other seemingly less traumatic activities, such as tooth brushing or mastication. Using 16*S* ribosomal RNA sequencing and quantitative polymerase chain reaction assays, Lockhart *et al*. profiled the bacteria in sequential blood samples drawn from patients who had undergone a tooth extraction with or without antibiotic treatment and from untreated patients who simply brushed their teeth. Thirty-two bacterial species that can cause infective endocarditis were identified in blood samples from patients after a tooth extraction and, as expected, antibiotic treatment significantly reduced their numbers. Surprisingly, brushing alone also caused a substantial increase in infective endocarditis–causing bacteria. Given that tooth brushing is a daily activity, the authors conclude that it could pose a risk for bacteremia comparable to that of a tooth extraction, thus underscoring the need for controlled clinical trials to evaluate current practices. — PAK

Circulation **117**, 3118 (2008).

CLIMATE SCIENCE

Charting Global Runoff

One widely expected potential consequence of climate warming is an intensification of the hydrological cycle, including more precipitation and more extreme precipitation events. Evidence that such intensification already has begun is available for some regions, but the question of whether or not the phenomenon is global remains unanswered. Milliman *et al.* have analyzed the runoff records of 137 rivers located on six continents, covering the last 50 years of the 20th century, in order to provide that answer. They find that global discharge has not changed significantly over that time, although regional changes were clearly apparent: Discharge decreases occurred disproportionately in Africa, Asia, and Australia, while Europe, North America, and South America experienced increases more often. Thus, the evidence seems not to show an intensification of the global hydrological cycle over the last half of the 20th century. That time period is too short, however, to draw firm conclusions about longer-term trends. — HJS

Global Planet. Change **62**, 187 (2008).

CHEMISTRY

Sensors with Sparkle

For sensing applications, diamond nanowires offer advantages in terms of stability, as well as the capacity for facile tailoring of electronic properties, both of the bulk material itself (through doping) and of the surface (through termination either with hydrogen or oxygen). Yang *et al*. have

CREDITS (TOP TO BOTTOM): JUPITER IMAGES

Published by AAAS

grown vertically aligned, boron-doped diamond nanowires at high density (3- to 10-nm-long wires spaced 11 nm apart) and anchored single-stranded DNA molecules to the ends via phenyl groups that were attached electrochemically. They found that the redox potentials and peak currents of the $[Fe(CN)_6]^{3-}/[Fe(CN)_6]^{4-}$ couple, as measured by cyclic voltammetry, are highly sensitive to DNA hybridization in this environment and can reveal single-base mismatches in the incoming strands being detected, with a 2-pM sensitivity limit. — PDS

Angew. Chem. Int. Ed. **47**, 10.1002/anie.200801706 (2008).

CELL BIOLOGY

Not So Identical Twins

During mitosis, somatic cells divide into two apparently identical daughter cells—but are they really the same? The production of nonidentical daughters occurs during differentiation when one daughter enters one developmental lineage while its sister remains a stem cell.

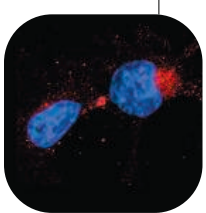

Catenin (red) in the nuclear bay of one daughter cell.

Fuentealba *et al*. see unequal inheritance even in divisions that had been thought to generate identical daughters; proteins destined for degradation, such as ubiquitinylated Smad1 transcription factor and phospho-β-catenin, were asymmetrically partitioned into one daughter. The process by which these proteins are preferentially inherited involves their microtubule-dependent association with peripheral centrosomal proteins, which is maintained through several rounds of division and in a variety of cell types. The unequal partitioning of misfolded and aggregated proteins in so-called aggresomes has already been observed, and this capacity for keeping one daughter free of defunct proteins may help to avoid a wholesale loss of cell populations if the load of such potentially damaging proteins becomes too great. — SMH

Proc. Natl. Acad. Sci. U.S.A. **105**, 7732 (2008).

GEOLOGY

Crust on the Move

Earth's plates move at speeds on the order of about 10 cm/year, so that over 100 million years, about 1000 km of ocean crust are consumed back into the mantle along every subduction zone. The mantle is about 2500 km thick, so some swirling, mixing, bending, and storage of these relic slabs are required over several billion years of plate tectonics. Some mantle volcanic rocks carry signatures of melting of old consumed ocean crust. Two seismic studies help clarify the fate of recently subducted crust through the upper half of the mantle. Li *et al.* provide an updated *P*-wave tomographic model of Earth's mantle, which reveals large-scale (>100 km) density variations. The geometry of subducted crust, which tends to be colder and denser than ambient mantle, varies: Slabs subducted eastward beneath North and South America appear to be visible to a depth of about 1200 km. The results confirm that some crust that subducted south of Japan is ponded at about 650 km in the mantle, a region of a major phase transition, but that subducted crust to the north and south has proceeded deeper. Separately, Courtier and Revenaugh show *S*-wave reflections from depths of >1000 km beneath North America and the South Pacific that probably map relic slabs there. — BH

Geochem. Geophys. Geosyst. **9**, 10.1029/2007GC001806 (2008); *J. Geophys. Res.* **113**, 10.1029/2007JB005261 (2008).

Science Signaling
AAAS

<< Receptor Rendezvous

B cell systems that protect organisms from viral infection walk a fine line because the molecules they detect—such as unmethylated DNA—can be derived from the host, and an overzealous defense results in autoimmune disease. Chaturvedi *et al*. describe how components of the adaptive and innate immune systems—B cell receptors (BCRs) and Toll-like receptor 9 (TLR9), respectively—act together to sense DNA-containing antigens. The answer was not obvious because BCRs are thought to act primarily on the cell surface, whereas TLR9 is normally present on endocytic vesicles. In mouse B cells in which the BCR was activated, TLR9 was relocated into autophagosomes. When cells were stimulated only through TLR9 with unmethylated DNA, p38 mitogen-activated protein kinase was detected only in endosomes. However, if the BCR was activated with an antibody to immunoglobulin M (alone or with DNA to activate TLR9), p38 was detected in large autophagosome-like structures. The recruitment of TLR9 to this compartment depended on physical internalization of the BCR, and activation of phospholipase D was also necessary. — LBR

Immunity **28**, 799 (2008).

CREDIT: FUENTEALBA *ET AL., PROC. NATL. ACAD. SCI. U.S.A.* **105**, 7732 (2008)

Published by AAAS

www.sciencemag.org

Science

1200 New York Avenue, NW
Washington, DC 20005
Editorial: 202-326-6550, FAX 202-289-7562
News: 202-326-6581, FAX 202-371-9227
Bateman House, 82-88 Hills Road
Cambridge, UK CB2 1LQ
+44 (0) 1223 326500, FAX +44 (0) 1223 326501

Subscription Services For change of address, missing issues, new orders and renewals, and payment questions: 866-434-AAAS (2227) or 202-326-6417, FAX 202-842-1065. Mailing addresses: AAAS, P.O. Box 96178, Washington, DC 20090-6178 or AAAS Member Services, 1200 New York Avenue, NW, Washington, DC 20005

Institutional Site Licenses please call 202-326-6755 for any questions or information

Reprints: Author Inquiries 800-635-7181
Commercial Inquiries 803-359-4578

Permissions 202-326-7074, FAX 202-682-0816

Member Benefits AAAS/Barnes&Noble.com bookstore www.aaas.org/bn; AAAS Online Store http://www.apisource.com/aaas/ code MKB6; AAAS Travels: Betchart Expeditions 800-252-4910; Apple Store www.apple/eppstore/aaas; Bank of America MasterCard 1-800-833-6262 priority code FAA3YU; Cold Spring Harbor Laboratory Press Publications www.cshlpress.com/affiliates/aaas.htm; GEICO Auto Insurance www.geico.com/landingpage/go51.htm?logo=17624; Hertz 800-654-2200 CDP#343457; Office Depot https://bsd.officedepot.com/portalLogin.do; Seabury & Smith Life Insurance 800-424-9883; Subaru VIP Program 202-326-6417; VIP Moving Services http://www.vipmayflower.com/domestic/index.html; Other Benefits: AAAS Member Services 202-326-6417 or www.aaasmember.org.

science_editors@aaas.org	(for general editorial queries)
science_letters@aaas.org	(for queries about letters)
science_reviews@aaas.org	(for returning manuscript reviews)
science_bookrevs@aaas.org	(for book review queries)

Published by the American Association for the Advancement of Science (AAAS), *Science* serves its readers as a forum for the presentation and discussion of important issues related to the advancement of science, including the presentation of minority or conflicting points of view, rather than by publishing only material on which a consensus has been reached. Accordingly, all articles published in *Science*—including editorials, news and comment, and book reviews—are signed and reflect the individual views of the authors and not official points of view adopted by AAAS or the institutions with which the authors are affiliated.

AAAS was founded in 1848 and incorporated in 1874. Its mission is to advance science, engineering, and innovation throughout the world for the benefit of all people. The goals of the association are to: enhance communication among scientists, engineers, and the public; promote and defend the integrity of science and its use; strengthen support for the science and technology enterprise; provide a voice for science on societal issues; promote the responsible use of science in public policy; strengthen and diversify the science and technology workforce; foster education in science and technology for everyone; increase public engagement with science and technology; and advance international cooperation in science.

Information for Authors
See pages 634 and 635 of the 1 February 2008 issue or access www.sciencemag.org/about/authors

EDITOR-IN-CHIEF **Bruce Alberts**
EXECUTIVE EDITOR **Monica M. Bradford**
DEPUTY EDITORS **R. Brooks Hanson, Barbara R. Jasny, Katrina L. Kelner**
NEWS EDITOR **Colin Norman**

Editorial supervisory senior editor Phillip D. Szuromi; **senior editor/perspectives** Lisa D. Chong; **senior editors** Gilbert J. Chin, Pamela J. Hines, Paula A. Kiberstis (Boston), Marc S. Lavine (Toronto), Beverly A. Purnell, L. Bryan Ray, Guy Riddihough, H. Jesse Smith, Valda Vinson; **associate editors** Jake S. Yeston, Laura M. Zahn; **online editor** Stewart Wills; **associate online editors** Robert Frederick, Tara S. Marathe; **web content developer** Martyn Green; **book review editor** Sherman J. Suter; **associate letters editor** Jennifer Sills; **editorial manager** Cara Tate; **senior copy editors** Jeffrey E. Cook, Cynthia Howe, Harry Jach, Barbara P. Ordway, Trista Wagoner; **copy editors** Chris Filiatreau, Lauren Kmec, Peter Mooreside; **editorial coordinators** Carolyn Kyle, Beverly Shields; **publications assistants** Ramatoulaye Diop, Joi S. Granger, Jeffrey Hearn, Lisa Johnson, Scott Miller, Jerry Richardson, Jennifer A. Seibert, Brian White, Anita Wynn; **editorial assistants** Carlos L. Durham, Emily Guise, Patricia M. Moore; **executive assistant** Sylvia S. Kihara; **administrative support** Maryrose Madrid

News deputy news editors Robert Coontz, Eliot Marshall, Jeffrey Mervis, Leslie Roberts; **contributing editors** Elizabeth Culotta, Polly Shulman; **news writers** Yudhijit Bhattacharjee, Adrian Cho, Jennifer Couzin, David Grimm, Constance Holden, Jocelyn Kaiser, Richard A. Kerr, Eli Kintisch, Andrew Lawler (New England), Greg Miller, Elizabeth Pennisi, Robert F. Service (Pacific NW), Erik Stokstad; **intern** Elsa Youngsteadt; **contributing correspondents** Jon Cohen (San Diego, CA), Daniel Ferber, Ann Gibbons, Mitch Leslie, Charles C. Mann, Virginia Morell, Evelyn Strauss, Gary Taubes; **copy editors** Linda B. Felaco, Melvin Gatling; **administrative support** Scherraine Mack, Fannie Groom; **bureaus** New England: 207-549-7755, San Diego, CA: 760-942-3252, FAX 760-942-4979, Pacific Northwest: 503-963-1940

Production director James Landry; **senior manager** Wendy K. Shank; **assistant manager** Rebecca Doshi; **senior specialist** Chris Redwood; **specialist** Steve Forrester; **Preflight director** David M. Tompkins; **manager** Marcus Spiegler; **specialist** Jessie Mudjitaba

Art director Kelly Buckheit Krause; **associate art director** Aaron Morales; **illustrators** Chris Bickel, Katharine Sutliff; **senior art associates** Holly Bishop, Laura Creveling, Preston Huey, Nayomi Kevitiyagala; **associate** Jessica Newfield; **photo editor** Leslie Blizard

***Science* International**

Europe (science@science-int.co.uk) **editorial: international managing editor** Andrew M. Sugden; **senior editor/perspectives** Julia Fahrenkamp-Uppenbrink; **senior editors** Caroline Ash, Stella M. Hurtley, Ian S. Osborne, Stephen J. Simpson, Peter Stern; **editorial support** Deborah Dennison, Rachel Roberts, Alice Whaley; **administrative support** John Cannell, Janet Clements, Louise Smith; **news: europe news editor** John Travis; **deputy news editor** Daniel Clery; **contributing correspondents** Michael Balter (Paris), John Bohannon (Vienna), Martin Enserink (Amsterdam and Paris), Gretchen Vogel (Berlin); **intern** Lauren Cahoon

Asia Japan Office: Asca Corporation, Eiko Ishioka, Fusako Tamura, 1-8-13, Hirano-cho, Chuo-ku, Osaka-shi, Osaka, 541-0046 Japan; +81 (0) 6 6202 6272, FAX +81 (0) 6 6202 6271; asca@os.gulf.or.jp; **asia news editor** Richard Stone (Beijing: rstone@aaas.org); **contributing correspondents** Dennis Normile (Japan: +81 (0) 3 3391 0630, FAX 81 (0) 3 5936 3531; dnormile@gol.com); Hao Xin (China: + 86 (0) 10 6307 4439 or 6307 3676, FAX +86 (0) 10 6307 4358; cindyhao@gmail.com); Pallava Bagla (South Asia: +91 (0) 11 2271 2896; pbagla@vsnl.com)

Africa Robert Koenig (contributing correspondent, rob.koenig@gmail.com)

EXECUTIVE PUBLISHER **Alan I. Leshner**
PUBLISHER **Beth Rosner**

Fulfillment Systems and Operations (membership@aaas.org); **director** Waylon Butler; **customer service supervisor** Pat Butler; **specialists** Laurie Baker, Latoya Casteel, LaVonda Crawford, Vicki Linton; **data entry supervisor** Cynthia Johnson; **specialist** Tarrika Hill

Business Operations and Administration director Deborah Rivera-Wienhold; **assistant director, business operations** Randy Yi; **senior financial analysts** Michael LoBue, Jessica Tierney; **financial analysts** Benjamin Aronin, Priti Pamnani; **rights and permissions: administrator** Emilie David; **associate** Elizabeth Sandler; **marketing director** John Meyers; **marketing managers** Allison Pritchard, Darryl Walter; **marketing associates** Aimee Aponte, Alison Chandler, Mary Ellen Crowley, Marcia Leach, Julianne Wielga, Wendy Wise; **international marketing manager** Wendy Sturley; **marketing executive** Jennifer Reeves; **marketing/member services executive** Linda Rusk; **site license sales director** Tom Ryan; **sales manager** Russ Edra; **sales and customer service** Mehan Dossani, Iquo Edim, Kiki Forsythe, Catherine Holland, Phillip Smith, Philip Tsolakidis; **electronic media: manager** Lizabeth Harman; **project manager** Trista Snyder; **assistant manager** Lisa Stanford; **senior production specialists** Christopher Coleman, Walter Jones; **production specialists** Nichele Johnston, Kimberly Oster

Advertising director worldwide ad sales Bill Moran

Product (science_advertising@aaas.org); **midwest** Rick Bongiovanni: 330-405-7080, FAX 330-405-7081; **west coast/w. canada** Teola Young: 650-964-2266; **east coast/e. canada** Christopher Breslin: 443-512-0330, FAX 443-512-0331; **uk/europe/asia** Michelle Field: +44 (0) 1223 326524, FAX +44 (0) 1223 326532; **japan** Mashy Yoshikawa: +81 (0) 33235 5961, FAX +81 (0) 33235 5852; **senior traffic associate** Deiandra Simms

Commercial Editor Sean Sanders: 202-326-6430

Classified (advertise@sciencecareers.org); **us: recruitment sales manager** Ian King: 202-326-6528, FAX 202-289-6742; **inside sales manager: midwest/canada** Daryl Anderson: 202-326-6543; **inside sales representative** Karen Foote: 202-326-6740; **key account manager** Joribah Able; **northeast** Alexis Fleming: 202-326-6578; **southeast** Tina Burks: 202-326-6577; **west** Nicholas Hintibidze: 202-326-6533; **sales coordinators** Erika Foard, Rohan Edmonson, Shirley Young; **international: sales manager** Tracy Holmes: +44 (0) 1223 326525, FAX +44 (0) 1223 326532; **sales** Marium Hudda, Alex Palmer, Alessandra Sorgente; **sales assistant** Louise Moore; **japan** Mashy Yoshikawa: +81 (0)3 3235 5961, FAX +81 (0)3 3235 5852; **advertising production operations manager** Deborah Tompkins; **senior production specialists** Robert Buck, Amy Hardcastle; **senior traffic associate** Christine Hall; **publications assistant** Mary Lagnaoui

AAAS Board of Directors retiring president, chair David Baltimore; **president** James J. McCarthy; **president-elect** Peter C. Agre; **treasurer** David E. Shaw; **chief executive officer** Alan I. Leshner; **board** Lynn W. Enquist, Susan M. Fitzpatrick, Alice Gast, Linda P. B. Katehi, Nancy Knowlton, Cherry A. Murray, Thomas D. Pollard, Thomas A. Woolsey

AAAS
ADVANCING SCIENCE, SERVING SOCIETY

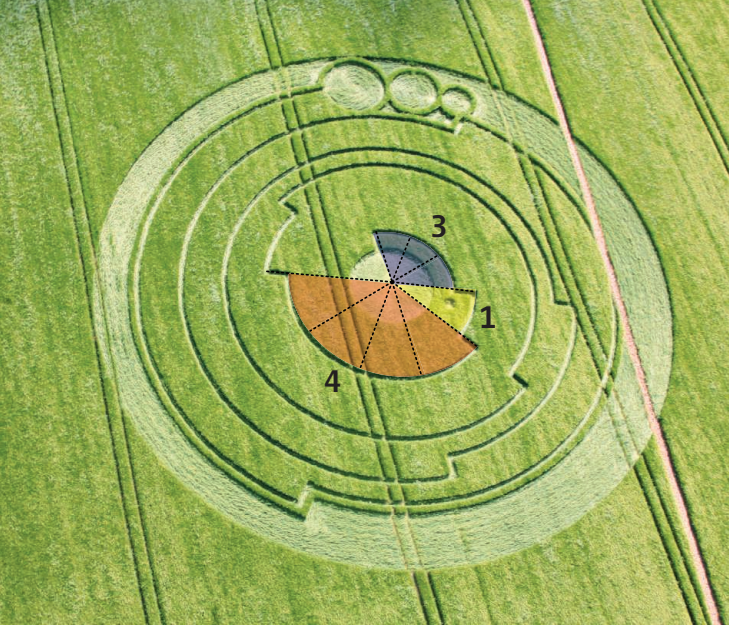

Pi From the Sky?

A math lesson from outer space, or a hoax delivered by cheeky mathematicians with too much time on their hands? It turns out a crop circle that first appeared 12 years ago in Wiltshire, England, actually codes for pi, the fundamental mathematical constant associated with circles. While perusing photos on a Web site devoted to crop circles, retired astrophysicist Michael Reed in South Carolina noticed that the curves in the 76-meter-wide pattern correspond to a 10-digit approximation of pi, 3.141592654. When the circle is sliced into 10 equal parts, each concentric arc, reading from the middle of the figure outward, represents a digit by the number of wedges it crosses. The decimal point even appears as a dot near the center after the first arc. Mathematician Colin Adams of Williams College in Williamstown, Massachusetts, observes that it would make sense for a jokester to use this constant: "If aliens are out there, then pi would be important to them. If I were someone set on making something look alien, this is the number I would pick."

Paracelsus, Eat Your Heart Out

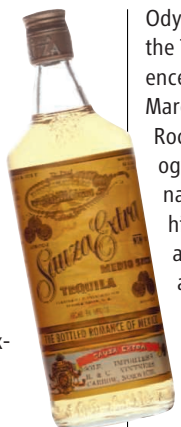

Alchemists never turned lead into gold, but a team of Mexican physicists has transformed tequila into diamond. For decades, researchers have made diamond films by exposing a surface to a hot vapor containing carbon, hydrogen, and oxygen. Usually they begin by vaporizing mixtures such as ethanol and water. But Victor Castaño, Javier Morales, and Miguel Apátiga of the National Autonomous University of Mexico in Querétaro have found that tequila straight out of the bottle does the trick. White tequila, produced by fermenting the flesh of the blue agave plant, has the right concentrations of hydrogen and oxygen to guide the carbon in it to form diamond instead of graphite or carbon black, Castaño says. And impurities in the liquor help nucleate the crystallites. The team reports its work on the arXiv preprint server (www.arxiv.org).

Using booze to make diamond isn't new. In the 1980s, Japanese scientists reportedly used sake, Russians used vodka, and Americans used whiskey. Paul May, a physical chemist at the University of Bristol, U.K., says his group even moved from the bar to the grill: "We once grew diamond using as a source of carbon the grease from a leftover lamb kebab" that was exposed to a hydrogen plasma, he says. After all, there are better uses for the liquor.

Homer and the Eclipse

Hints of a solar eclipse at the climax of Homer's epic the *Odyssey* may be based on fact, a biophysicist and an amateur astronomer say.

The poem describes the adventures of Odysseus on his journey home to Ithaca from the Trojan War. Intrigued by astronomical references in the text, Constantino Baikouzis and Marcelo Magnasco of New York City's Rockefeller University constructed a chronology of the final 40-day voyage that culminates when Odysseus returns home and slays his wife Penelope's suitors. Before the fight, a seer mentions the obliteration of the sun and sudden darkness—a line some scholars believe describes an eclipse.

The researchers analyzed four astronomical references to Mercury, Venus, the new moon, and the appearance of two constellations—the Pleiades and Boötes—that are rarely seen together, they report online this week in the *Proceedings of the National Academy of Sciences*. Using powerful new astronomy software, Magnasco says, "we matched the pattern in which they happen in the *Odyssey*" and found that it occurs only once every 2000 years. The computations placed Odysseus's return on 16 April 1178 B.C.E. That's the exact date astronomers have identified for a total solar eclipse that would have been visible from the Ionian islands.

Magnasco says the analysis suggests that there may be more factual truth in the *Odyssey* than some scholars have believed and that Homeric Greeks may have known about movements of the planets some 400 years before Plato wrote about them.

GET ONLINE, LITTLE DOGIES

When roboticist Daniela Rus visited an Australian cattle ranch a few years ago, she saw an opportunity to innovate. The company used helicopters to herd 24,000 cows across rangeland the size of Vermont, but the biggest headache was maintaining the fences. Rus, now at the Massachusetts Institute of Technology in Cambridge, has created a "smart collar" to keep cows from straying. "It's a next step in cow manipulation," she says.

The bovines wear GPS-equipped headsets that make noises to scare them when they try to leave a designated area. After trying sounds such as roaring lions and crashing cars, the researchers found that barking dogs usually do the trick. If a cow ignores the yapping, its solar-powered unit delivers a mild electric shock. Rus has since teamed up with Dean Anderson, an animal scientist with the U.S. Department of Agriculture in Las Cruces, New Mexico, who had been working on the same idea. (His warning noises included cowboy songs and pickup truck engines.) This August, the pair will outfit 10 cows with headsets programmed to herd them from pasture back to their barns.

The collars can also be used to collect data on animal movements and other behaviors. "You can log in to specific cows," Rus says. The pair plan to add webcams, allowing e-cowboys to watch for trouble, and possibly heart-rate monitors to monitor animal stress levels.

EDITED BY KELLI WHITLOCK BURTON

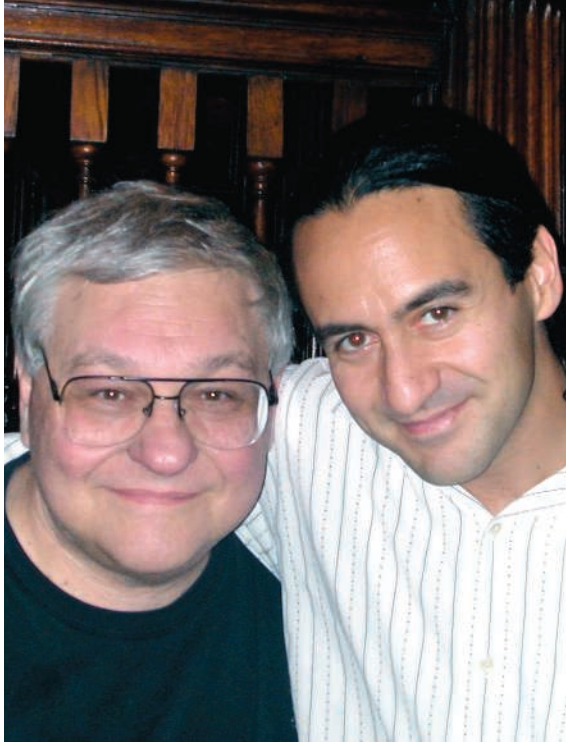

In the News

THE SON ALSO RISES. A new father-and-son team wants to tap the sun's rays—from on high. Martin "Marty" Hoffert, an energy expert at New York University, and his son Eric, a New Jersey entrepreneur, are trying to get U.S. science agencies or venture capitalists to fund their $50 million experiment to beam the intense solar energy collected in orbit down to Earth.

Space solar power isn't a new concept. But high launch costs have relegated the idea to "science fiction" for decades. The Hofferts' experiment would deliver up to 150 kilowatts—enough to power roughly 40 homes—by laser to a collector on the ground at initial prices more than 10 times the average cost of power. It would serve customers in remote locations. Bigger systems would mean cheaper power, they say. "Hope springs eternal," says Washington, D.C., space consultant John Pike, who remains skeptical that the cost of getting equipment into orbit will drop anytime soon.

While they look for backers, the father-son pair is relishing the collaboration. "We both felt it was important to work to do something about the energy problem," says Marty, who adds his science to his son's business acumen. "We definitely lock horns; we're both strong personalities," says Eric, who has worked at Apple and AT&T's Bell Laboratories. Marty sees another advantage to the two-generation approach: "No matter how brilliant I think I am, I know it's not going to happen in my lifetime."

MOVERS

COMING FULL CIRCLE. Paleoclimate modeler Eric Barron began his career at the National Center for Atmospheric Research (NCAR) in Boulder, Colorado. Now he's returning to be its director.

Barron, 56, came to NCAR as a graduate student to model the ice ages. After serving as a staff scientist, he held positions at Pennsylvania State University and the University of Texas and recently stepped down as board chair of the organization managing NCAR for the National Science Foundation.

"I think he's a fantastic choice," says climate modeler Michael MacCracken of the Climate Institute in Washington, D.C. "He's very good in areas where people have differing views."

"The climate change issue is turning a corner in this nation," Barron says, but "there is still a disconnect between the science and how it can be utilized for society." He's hoping his $150-million-a-year budget and 950-person staff, which studies everything atmospheric from yesterday's thunderstorms to ancient ice ages, will help close that gap.

SUPERMAN? As an astrophysicist, Edward Seidel uses high-performance computers to simulate the relativistic world of Einstein's equations. This fall, he'll take leave from Louisiana State University in Baton Rouge to direct the U.S. National Science Foundation's (NSF's) Office of Cyberinfrastructure (OCI), which aims to provide all scientists with the computing tools they need. "Since I accepted the job, I've gotten comments from a lot of colleagues about how now I will be able to solve all their problems," he laughs.

OCI was moved from the computing science and engineering directorate into the NSF director's office in 2005 to separate the development of better computing facilities from the discipline itself. Seidel, 50, knows his $185 million budget will limit just how many problems he can fix. One pressing challenge is to transform NSF's $100-million-a-year TeraGrid computing program, which ends in 2010, into the next-generation "Extreme Digital" initiative. Another is to increase the number of computational scientists.

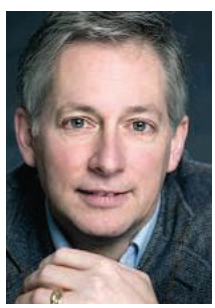

John Towns of the National Center for Supercomputing Applications in Urbana, Illinois, one of the original NSF supercomputing centers, calls Seidel "the type of visionary leader OCI needs. The office is standing up, and now it needs to start running."

<< AWARDS

KYOTO PRIZE. Two Canadians and one American are being honored with the Kyoto Prize for lifelong contributions to basic sciences, advanced technology, and arts and philosophy in a way that benefits humanity.

Anthony Pawson (far left), a molecular biologist at Mount Sinai Hospital's Samuel Lunenfeld Research Institute in Toronto, Canada, receives the basic sciences prize in life sciences for work on signal transduction involved in regulating cell growth and differentiation. His studies have led to the development of new cancer drugs. The advanced technology prize goes to Richard Karp (above, right), an electrical engineer and computer scientist at the University of California, Berkeley. He's being honored for developing computer algorithms and advancing computer science theory. And Charles Taylor, professor emeritus of philosophy at McGill University in Montreal, Canada, wins this year's arts and philosophy prize.

The Kyoto Prize is awarded by the Inamori Foundation, established by Kazuo Inamori, who made a fortune as the founder of Kyocera Corp., a high-tech ceramics company. Each laureate will receive approximately $460,000.

Got a tip for this page? E-mail people@aaas.org

CREDITS (TOP TO BOTTOM): SOURCE: ERIC HOFFERT; LSU; UCAR; INAMORI FOUNDATION

Published by AAAS

Salvaging U.S. fisheries 1706

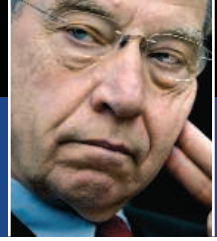

Research conflicts probed 1708

ARCHAEOLOGY

Early Stonehenge Pilgrims Came From Afar, With Cattle in Tow

Each year, nearly a million tourists are drawn to Stonehenge's massive stone pillars. Now evidence fresh from the lab suggests that the iconic monument in southern England was a place of pilgrimage even in prehistoric times. But why they came remains a mystery.

Isotopic studies of teeth from six cattle found at a nearby earthen henge show that the animals were herded to the site from distant parts of Britain. Some of the animals apparently came from as far away as Wales—also the origin of Stonehenge's smaller "bluestones." The unpublished results, coming on the heels of new dates for human remains at Stonehenge, are fueling ongoing debates about whether the 5000-year-old monument served chiefly as a "place of the dead" or whether its stones were valued for their healing properties.

The cattle findings "are potentially exciting," says Mike Pitts, editor of *British Archaeology*, because they "imply an unusually large social and political network behind [Stonehenge's] creation." Archaeologist Alasdair Whittle of Cardiff University in the U.K. says the new data support evidence that Stonehenge was preceded by "centuries of movement and connections" among prehistoric peoples in Britain. But both researchers note that the results are still preliminary. "Six [animals] is a small sample, so caution is appropriate," says Whittle.

The cattle teeth come from ancient rubbish deposits at a site 3 kilometers away called Durrington Walls. This massive circular earthwork, about 500 meters in diameter, has long been thought to be related to Stonehenge, which itself was first built as an earthwork.

The teeth were analyzed by Sarah Viner, a graduate student with University of Sheffield zooarchaeologist Umberto Albarella. Viner, in collaboration with Jane Evans of the Natural Environment Research Council's Isotope Geosciences Laboratory in Nottingham, U.K., looked at the ratio of two strontium isotopes, ^{87}Sr and ^{86}Sr, in the teeth of adult animals. This ratio varies depending on what type of soil the animals have grazed on: Higher ratios stem from Britain's older geological formations, and lower ratios arise in the younger chalklands of southern England where Stonehenge is located (see map). The strontium "signature" is laid down when the teeth are formed in growing animals and does not change later.

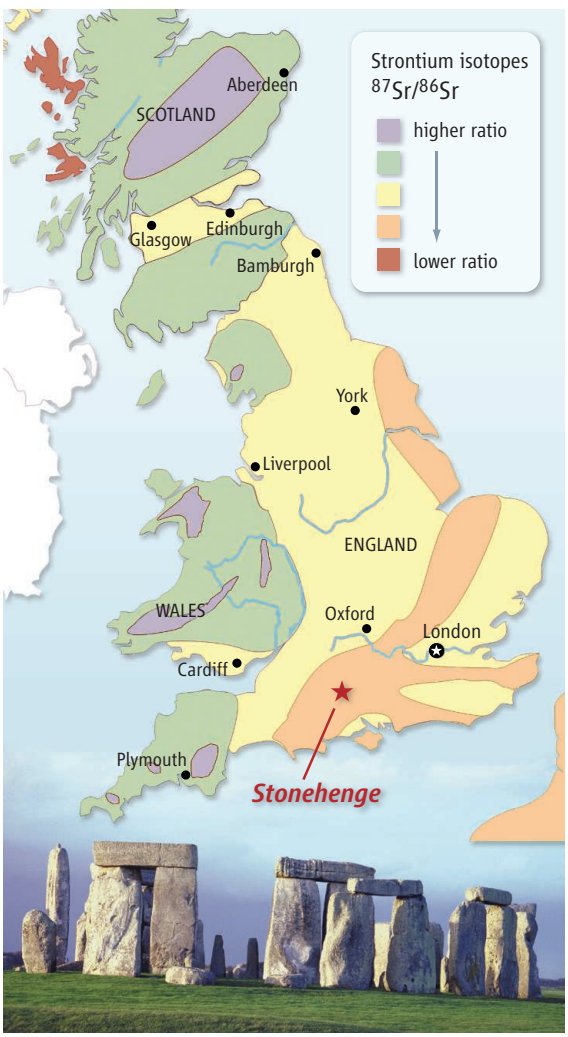

Well-traveled. The strontium ratios of cattle teeth found near Stonehenge (orange-colored area) show that they were raised far from the monument (yellow-, green-, and violet-colored areas).

Viner and Evans found that none of the six animals was raised in the chalklands. Two appeared to come from Wales or Scotland, the others from locations in England that could not be determined.

Sheffield archaeologist Michael Parker Pearson, who led excavations at Durrington Walls, says these results fit other signs that people came to the site only periodically. "There is no evidence of cereals or grinding stones," he says, as would be expected at a site permanently occupied by the early farmers who then inhabited Britain. Moreover, Albarella says, none of the cattle or pig bones were from very young animals, making it unlikely that animals were raised at the site. Instead, he believes they must have been brought there from afar, perhaps during episodes of feasting at the summer and winter solstices.

Parker Pearson says the findings support his hypothesis that Stonehenge and its surrounding landscape were places where the living came to venerate the dead. "I think the people who built Stonehenge brought their ancestors from Wales in stone form," he says. Last month, his team reported new radiocarbon dates from human cremation burials indicating that Stonehenge had been a "cemetery" back to about 3000 B.C.E., the time of its first construction and before the stones were erected.

Yet the discoveries at Durrington Walls are only relevant to Stonehenge if the two monuments are related. That has been unclear because of uncertainties in dating at both sites. Parker Pearson's team now appears to have closed this dating gap considerably: A reanalysis of earlier Stonehenge radiocarbon dates, published last year in *Antiquity*, puts the erection of the large stones—which weigh as much as 45 tons and were brought from about 30 kilometers away—at 2600 to 2400 B.C.E. An antler pick apparently used in the construction of the earthwork at Durrington Walls clocked in at 2570 to 2350 B.C.E., and a pig bone there was dated to between 2830 and 2470 ▶

MAP SOURCE: ADAPTED FROM JANE EVANS/NERC; PHOTO CREDIT: PHOTOS.COM

Published by AAAS

Hope for Africa's meningitis belt
1710

Tree of life reconstructed
1716

B.C.E. "Mike needed to get those two monuments closer together in time, and he's done it," says Richard Bradley, an archaeologist at the University of Reading in the U.K., though he notes that some wiggle room remains.

Even if Durrington Walls and Stonehenge were part of a single "ritual landscape," as Parker Pearson has argued, their symbolic meaning is still open to debate. For example, archaeologist Timothy Darvill of Bournemouth University in Dorset, U.K., has coproposed the idea that the bluestones were transported from Wales because of their healing properties and that Stonehenge was a center of healing (*Science*, 11 April, p. 159). "To have animals coming in from Wales fits our idea quite nicely," says Darvill.

This summer, Parker Pearson's team plans to find out more about the founders of Stonehenge by excavating possible seasonal houses just west of the monument. The new site is roughly dated to about 3000 B.C.E., when Stonehenge was still just an earthwork circle and the monument we see today was just a gleam in a prehistoric eye.

–MICHAEL BALTER

FRANCE

Despite Protest, CNRS Moves Toward Major Shakeup

PARIS—Researchers and science labor unions last week stopped a proposed reform of one of Europe's biggest research agencies with their bodies. But their victory may be short-lived, as France's science ministry says the makeover of the National Center for Scientific Research (CNRS) will proceed.

On 19 June, the leaders of more than 1000 protesting researchers and workers occupied an ornate meeting room inside the Parisian headquarters of CNRS, where the agency's board of trustees was to vote on the controversial reform plan. Worried that angry protesters might take over the entire building, CNRS President Catherine Bréchignac canceled the meeting.

Under protest. Researchers and union members gathered outside and inside the headquarters of France's National Center for Scientific Research, delaying a key vote on reforms.

The proposed shakeup would create eight new institutes within CNRS. The protesters say that amounts to "dismantling" the science flagship. But other researchers contend that the reforms will improve CNRS and could plant the seeds for a new national institute that would unify the life sciences in France.

With a €3.3 billion budget and a staff of 32,000, CNRS spans the disciplines from anthropology to astrophysics. Its researchers—civil servants with jobs for life—are spread out across the country, often working in close collaboration with university scientists. "Horizon 2020," a strategic plan drawn up by the center's leadership and France's ministry of higher education and research, proposes to replace CNRS's department-based structure with institutes based on scientific fields such as chemistry, mathematics, and physics. Some of these could become "national institutes" and take a leading role. The structure would be clearer and more efficient, according to the plan.

But the unions and Sauvons la Recherche (SLR), a movement founded in 2003 to protest budget cuts by the previous government, says the plan would be the "death" of CNRS and another step toward a U.S.-style system in which researchers face cutthroat competition and permanent job insecurity. The groups have fought previous reforms such as the creation of a national research agency for project-based funding and a law that gives universities more autonomy (see Editorial, p. 1695).

CNRS's own scientific council isn't happy, either. On 16 June, its members voted 10 to 7 against the plan. The breakup into distinct institutes would hamper interdisciplinary work, a key CNRS strength, says anthropobiologist Gilles Boëtsch, who chairs the council.

Under CNRS rules, the board must hold another meeting within 20 days with the same agenda. Union and SLR leaders want Bréchignac and French science minister Valérie Pécresse to hold a new round of consultations and delay implementation of any reform. A ministry spokesperson says that Pécresse will reassure scientists that CNRS will continue to exist and preserve the rights of staff but that she will stick with the plan.

Complicating the debate are several long-running divisions. Some SLR members accuse President Nicolas Sarkozy's conservative government of settling political scores with the left-leaning CNRS. There have also been tensions within CNRS between physicists, who have dominated its leadership, and biologists, who say they have been given short shrift. (Bréchignac, an atomic physicist, fanned those flames when she said recently that CNRS biologists could perform better.)

Biologist Jules Hoffmann, president of the French Academy of Sciences, says the time is ripe for coordinating programs at CNRS, the National Institute for Health and Medical Research (INSERM), and perhaps other government players. The creation of a strong life sciences institute within CNRS, he adds, could even be the first step toward a full-fledged merger, which could correct a fragmented structure that weakens French science.

–MARTIN ENSERINK

CREDIT: HALEY/SIPA/AP PHOTO

Published by AAAS

U.S. OCEAN POLICY

Proposed Rule Would Limit Fish Catch but Faces Data Gaps

The U.S. government has proposed first-ever annual catch limits in an attempt to stop overfishing.

Environmentalists are welcoming the draft rule, published in the *Federal Register* on 9 June by the National Oceanic and Atmospheric Administration (NOAA). But experts caution that it will be difficult—and hugely expensive—for the agency to regulate the many marine species about which little is known. Some scientists also worry about economic repercussions if the rule ends up curtailing fishing in healthy populations. "It could have staggering consequences," says fisheries biologist Ray Hilborn of the University of Washington, Seattle.

In December 2006, Congress made extensive changes to the federal law that governs fishery management policy (*Science*, 22 December 2006, p. 1857). The job of implementing those changes falls to NOAA's National Marine Fisheries Service (NMFS), which manages more than 1000 marine species, not all of which are economically important. Some 41 of the 528 stocks that NMFS monitors are being overfished, mostly off the East Coast.

The rule spells out how NMFS intends to end the overfishing, rebuild depleted stocks, and ensure "optimum yield." All eight regional fishery management councils would be required to set annual catch limits, which must be approved by a council's scientific advisory committee. The limits must incorporate a safety margin to account for scientific uncertainty surrounding the stock assessment, as well as uncertainty about technical aspects of implementation.

Mysterious catch. A proposed regulation could lead to tighter catch limits for the red grouper and other species about which little is known.

There's tough enforcement language in the new rules. If the councils don't meet their deadline for rebuilding overfished stocks, they will have to cut the annual catch limits. Lee Crockett of the Pew Environment Group in Washington, D.C., calls the language "a pleasant surprise."

One unanswered question is how to deal with so-called data-poor species. "It's a big black box," says Andrew Cooper of Simon Fraser University in Burnaby, Canada. He predicts that catch limits will be set low and that the fishing industry will agree to contribute more data and analysis to the agency.

Hilborn worries about the negative impact on trawl fisheries, which scoop up large numbers of a few abundant commercial species but also many low-value species about which little is known. Trawlers could be prohibited from catching anything at all in order to protect data-poor species that may not be in danger. "You're going to give up a lot of fish," he says. NMFS scientists are working on technical guidance about how to deal with data-poor species.

It won't be cheap to fill in the data with ▶

2008 U.S. BUDGET

House Gives $400 Million to Four Science Agencies

Science agencies are barely a footnote in the $186 billion supplemental spending bill to continue funding the U.S. war effort in Iraq and Afghanistan approved by the House of Representatives last week. But the footnote includes a welcome bump-up of $400 million for four agencies whose research budgets were flattened late last year by legislators.

"It's not that much money. But as a statement of priorities, we're very gratified," says Howard Garrison of the Federation of American Societies for Experimental Biology in Bethesda, Maryland, referring to the $150 million that the House approved for the National Institutes of Health for the 2008 fiscal year that runs until 30 September. That could fund 260 additional grants across most of the 27 institutes and centers. Lawmakers also doled out $62.5 million each for the National Science Foundation (NSF), the Department of Energy's Office of Science, and NASA (sciencenow.sciencemag.org/cgi/content/full/2008/620/1), plus $62.5 million for DOE's environmental cleanup efforts at Hanford, Washington.

Science advocates have been lobbying for much more—$900 million—for NSF, DOE science, and the National Institute of Standards and Technology to restore those agencies to levels requested by President George W. Bush in his 2008 budget and initially backed by Congress before a last-minute reversal (*Science*, 4 January, p. 18). Although the White House loudly opposed adding domestic spending to the war supplemental, last week it bent to pressure from House Democrats and agreed to accept expanded unemployment and veterans education benefits as well as $8.5 billion in emergency spending for disaster relief. The Senate, which last month had approved $1.2 billion more for research in its version of the war supplemental, was expected this week to accede to the terms of the House bill (H.R. 2642).

The DOE science funding is intended to stave off layoffs at two high-energy physics laboratories, Fermi National Accelerator Laboratory and the Stanford Linear Accelerator Center (*Science*, 11 January, p. 142). Most of the additional NSF funding will go to improving precollege math and science instruction through its existing Noyce Scholarship program for undergraduates and a new master's level program modeled on a 4-year-old initiative in New York City called Math for America. The NASA funding will bolster science and aeronautics programs cut to fix the shuttle system in the wake of the 2003 Columbia disaster.

The $400 million in the supplemental represents what House and Senate Democratic leaders decided they could afford after agreeing to extend a helping hand to the scientific community. "Any split was as rational as any other," explains a congressional aide about the allocation between NSF and NASA. "I'm not sure the [2008] requests had anything to do with it."

–JEFFREY MERVIS

CREDIT: JIM STEM/BLOOMBERG NEWS/LANDOV

Published by AAAS

rigorous stocks assessments and marine surveys. Accordingly, President George W. Bush has requested an increase of $8.9 million to NOAA's $31.6 million budget next year for fishery assessments, and Congress seems amenable to the hike. But Hilborn doubts that amount would be nearly enough. "To do it right would take a staggering increase in resources," he says.

Another regulation will give NMFS more data on recreational fishing, which can rival the impact of commercial fishing in some parts of the country, by creating a registry of saltwater anglers. The agency will accept public comments through 11 August, and the catch-limit rule remains open for public comment until 8 September. The agency hopes to finalize both rules by the end of the year.

–ERIK STOKSTAD

FUSION REACTOR

ITER Costs Give Partners Pause

Last week, ITER scientists revealed a new cost estimate for the multibillion-dollar fusion reactor that was 30% higher than earlier calculations. Now the project's seven international partners must decide whether they can afford it.

ITER, or the International Thermonuclear Experimental Reactor, is designed to show conclusively that fusing together hydrogen isotopes at extreme temperatures—the process that powers the sun—can be harnessed on Earth as a practical energy source. Fifteen years of discussion and experiment led in 2001 to a "final" design for the 20,000-ton ITER reactor, twice the size in linear dimensions of the world's current largest. Since then, the partners—China, the European Union, India, Japan, Russia, South Korea, and the United States—have chosen Cadarache in southern France as a site and set up the organization that will build the reactor (*Science*, 13 October 2006, p. 238).

The current price tag is €10 billion, half of which will pay for construction. Last week, the project's governing council met in Aomori, Japan, to hear about a new review of that 2001 design that includes numerous refinements and upgrades to components, including magnets and heating systems, plus additional magnets to help control explosive discharges at the plasma edge (*Science*, 13 June, p. 1405). Those design changes will cost an extra €1.2 billion to €1.6 billion, ITER managers estimate, and the council immediately ordered an independent assessment of the costs in time for its next meeting in November. In the meantime, the council did approve a 2-year delay, to 2018, in the expected start-up of the reactor.

Fusion experts say that it's notoriously hard to keep such large projects within budget. "When they actually go out and build things, they always cost more," says Stephen Dean, president of Fusion Power Associates, a lobby group in Gaithersburg, Maryland. But ITER scientists believe that the design changes are crucial to the project's chance of success and that the partners should approve the new cost estimate. "It will define what we can do and when we can do it," says David Campbell, assistant head of ITER's department of fusion science and technology. It won't be an easy sell, however: Some ITER partner governments won't be happy at being asked to fork out more.

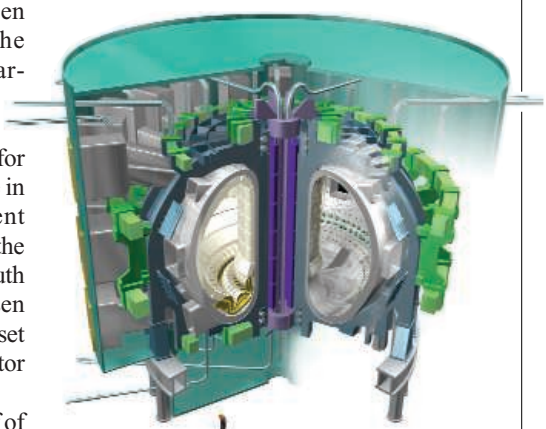

Going up. As ITER's partners prepare to start construction, design changes are bumping up the cost.

The panel tasked with assessing the new cost estimate will be led by Frank Briscoe, former operations director of the JET fusion reactor near Oxford, U.K. The European Union, which as host must bear nearly 50% of the cost, declined comment on the new estimate beyond saying, in the words of research spokesperson Catherine Ray, that "we're happy [Briscoe's] group has been set up." Meanwhile, the partners in the world's most expensive experiment will be debating its future. "There will be some very, very hard diplomatic negotiations over what the partners are prepared to pay," says a senior European researcher who asked not to be named.

–DANIEL CLERY

ILLUSTRATION: ERIC VERDULT, COPYRIGHT 2008 WWW.KENNISINBEELD.NL

Hungary: Where Europe Will Be EITing

Budapest will host the headquarters of the new European Institute of Innovation and Technology (EIT). Conceived as a way to boost innovation à la the Massachusetts Institute of Technology, EIT has been roundly criticized by European scientists as misconceived and politically motivated (*Science*, 21 September 2007, p. 1676). But József Pálinkás, president of the Hungarian Academy of Sciences, says he hopes EIT will attract new investors to the region and inspire Hungary's students and young scientists. "It shows that Hungary is a player" in the European science scene, he says.

Hungary beat out Wroclaw, Poland; Jena, Germany; the Spanish city of Sant Cugat des Vallés; and a twin bid by Vienna, Austria, and Bratislava, Slovakia, for the right to host the administrative headquarters of the virtual institute, which is slated to receive €300 million through 2013. **–GRETCHEN VOGEL**

Council: Machine Won't Destroy Earth

With only weeks to go before particles begin whizzing around in the Large Hadron Collider (LHC), the world's most powerful particle accelerator, at CERN near Geneva, Switzerland, the lab's governing council sought last week to get one thing straight: Yes, it's safe. Honest.

Citing some of the more exotic theories of fundamental physics, online commentators have suggested that the LHC's particle collisions could create a microscopic black hole that, if stable, could swallow up Earth. Other potential threats include vacuum bubbles, magnetic monopoles, and strangelets. Two people even filed a lawsuit in U.S. federal court in Hawaii in March to try to halt LHC operations until a safety and environmental audit is carried out.

Although the lab looked into the issue in 2002, media interest in the perceived risks and new results and theories in physics drove the lab to reexamine it. CERN's 15-page report, released last week, concluded that "there is no basis for any concerns," principally because thousands of cosmic rays with energies much higher than LHC can achieve bombard Earth every day, yet no black hole or exotic particle has yet devoured the planet. "The Web has become a place where people can steer the scientific process in unpredictable ways," says CERN theorist Michelangelo Mangano, a co-author of the new report.

–DANIEL CLERY

Published by AAAS

ETHICS

Senate Inquiry on Research Conflicts Shifts to Grantees

Senate investigators began poking around academic medical centers last summer, looking for information on who was receiving corporate money and who was reporting it in compliance with conflict-of-interest rules. At the same time, they asked drug companies to name whom they were paying, and how much. This month, the two halves of the bomb came together, revealing discrepancies with a bang. The fallout struck Harvard Medical School and the affiliated Massachusetts General Hospital (MGH) in Boston. Congressional sleuths allege that three faculty psychiatrists failed to properly report hundreds of thousands of dollars of outside income.

Casting a net. Senator Charles Grassley wants to know how institutions monitor faculty conflicts.

As investigators under Senator Charles Grassley (R–IA) sift through the cases, the biomedical community is facing a couple of angst-inducing questions: Will there be more bombshells? And how will grant overseers at the National Institutes of Health (NIH) and academic deans respond? The short answer is, yes, Grassley plans more detonations. The senator has said he is investigating about 30 individuals at 20 universities who may have broken federal conflict-of-interest reporting rules. This week, he asked Stanford University why it did not require that a faculty psychiatrist report the full value of his $6 million in stock in a company that makes a drug being studied in an NIH-funded trial that the psychiatrist oversees. Stanford was preparing a statement as *Science* went to press (sciencenow.sciencemag.org/cgi/content/full/2008/624/1).

Universities, meanwhile, say they're scrambling to tighten procedures to track conflicts, hoping to reassure the public and stave off more stringent measures that they say could stifle cooperation with industry. "I think the community's been awakened," says David Korn, former dean of Stanford University School of Medicine and now a senior vice president of the Association of American Medical Colleges (AAMC) in Washington, D.C. Health policy researcher Eric Campbell of MGH, who has documented the prevalence of industry ties in academia, says an overhaul is long overdue: "Consulting has been one of the great wink-winks of all time."

Biomedical researchers in government came under pressure 4 years ago, when the House Energy and Commerce Committee investigated media reports that several top-level NIH intramural researchers had failed to report consulting income. That led NIH Director Elias Zerhouni to ban all company consulting by in-house researchers.

Now NIH-funded extramural researchers are feeling the heat, thanks to Grassley, ranking minority member of the Senate Finance Committee. A 1995 Public Health Service (PHS) regulation requires that investigators seeking NIH funding tell their institutions about income of $10,000 or more a year, or 5% equity in a company, "that would reasonably appear to be affected by the research." Last year, Grassley found that child psychiatrist Melissa DelBello of the University of Cincinnati in Ohio had apparently underreported $138,000 in drug company income.

Earlier this month, Grassley netted the Boston fish: Joseph Biederman, Timothy Wilens, and Thomas Spencer, all highly respected child psychiatrists at Harvard and MGH. Grassley says reports filed by the three initially suggested that they had earned about $200,000 each in consulting income since 2000. But they later said the total was actually $3.6 million. When Grassley compared data from drug companies with their conflict-of-interest reports, he found the amounts didn't always match up, according to tables he released. Harvard and MGH have said they are investigating.

Grassley's tables suggest a precision that may not exist in academic forms. For example, Harvard and MGH required only ranges of income to be reported, not specific amounts. In some cases, the Harvard or MGH investigators overreported income from a company one year, suggesting a mismatch in dates. Other discrepancies make them look more culpable, however. Two of the investigators led NIH-funded clinical trials for psychiatric drugs but may have failed to report income from the drugs' makers that exceeded the $10,000 PHS threshold—if so, a clear conflict.

If any of the three have indeed broken the PHS reporting rules, Harvard and MGH could be subject to fines or suspension of grants, say NIH officials. NIH says it is undertaking a systemwide review of its conflict-of-interest policies, after the Department of Health and Human Services inspector general hammered the agency for lax oversight in January (sciencenow.sciencemag.org/cgi/content/full/2008/118/1). However, NIH has rejected a recommendation that it routinely collect details from institutions on their management of conflicts. That responsibility should remain with institutions, says NIH extramural research chief Norka Ruiz Bravo.

Institutions acknowledge that they have a long way to go. AAMC and the Association of American Universities (AAU) have issued conflict-of-interest guidelines, most recently in February. They recommended that all payments, not just those above the $10,000 limit, be reported, and in specific amounts. But only some institutions follow these policies now. And many are still migrating from paper forms to electronic databases that can be easily accessed, say, by ethics review boards. "It has to be electronic to be effective," says Robert Rich, dean of the School of Medicine at the University of Alabama, Birmingham, and co-chair of the recent AAMC/AAU report.

Even then, the best system won't keep some researchers from failing to report. Another idea is for universities to crosscheck faculty reports with a public database. Grassley has proposed a law that would require drug companies to report all payments of more than $500 made to doctors.

The academic community is concerned: "The risk is that we'll have a set of rules imposed on us just at a time when universities should be making sure discoveries are turned into useful products. That would be a catastrophe for America," says Harvard University Provost Steven Hyman. "By the same token," he adds, "it is very important that the physician's only interest aligns with the [patient's] interest and not with a company's." But convincing Congress that universities can "thread the needle" on their own, as Hyman says, will be a challenge. **–JOCELYN KAISER**

CREDIT: J. SCOTT APPLEWHITE/AP PHOTO

Published by AAAS

VIROLOGY

'Biased' Viruses Suggest New Vaccine Strategy for Polio and Other Diseases

They're called silent mutations, but they could make a big noise in the vaccine field. Introducing hundreds of these seemingly inconsequential changes into a poliovirus can cripple the virus enough to make it work as a live vaccine in mice, scientists report on page 1784. The technology might lead to safer polio vaccines and perhaps to so-called live attenuated vaccines against other diseases. "It's a nice study and a very promising technology," says Rino Rappuoli, global head of vaccine research at Novartis.

The new vaccine strategy exploits the fact that almost all amino acids can be encoded by multiple codons, triplets of the DNA bases guanine (G), adenine (A), cytosine (C), and thymine (T). GAA and GAG, for instance, both represent the amino acid glutamic acid. But many organisms, including viruses, have a bias toward certain codons in their genes. This may be because those codons are easier to translate at ribosomes, the cell's protein factories, thus speeding up protein production. Researchers have learned to take advantage of codon bias: For example, they insert a microbe's favorite codons when engineering it to make a desired protein.

The vaccine approach does the opposite: It creates underperforming viruses by giving them unfavored codons. The hope is that these strains will be too weak to cause disease yet produce the same proteins and elicit the same immune response as wild-type virus. Two teams have been exploring that idea independently, by synthesizing a new version of the poliovirus's capsid gene with hundreds of small changes and stitching it into the RNA genome of either a wild poliovirus or a vaccine strain. In 2006, a group led by Olen Kew of the U.S. Centers for Disease Control and Prevention (CDC) in Atlanta, Georgia, first showed that such a strain could barely grow in human cells. Shortly after, a team led by Eckard Wimmer at Stony Brook University in New York state presented a similar study.

Wimmer's group now shows that codon-crippled viruses can work as a vaccine. Rather than directly using codon bias, the team took advantage of a related phenomenon called codon pair bias: that is, codons tend to be followed much more often by certain codons than others. (For instance, the amino acid pair alanine-glutamic acid is much more often encoded by the codons GCA-GAG than by GCC-GAA.) With the help of computer scientists, the team assembled two polioviruses, each of whose capsid protein genes had hundreds of underrepresented codon pairs. Mice injected with either strain didn't get sick but developed immunity against a challenge with a lethal dose of the real poliovirus.

Although a massive worldwide campaign with a live virus vaccine has all but eradicated polio, there's room for a new vaccine. After eradication is complete, plans call for the use of killed vaccines. Production of killed vaccines is risky, because viruses can escape from vaccine factories before they're inactivated. The weakened viruses made by the Stony Brook team could provide a safer starting material for a killed vaccine, says Roland Sutter of the World Health Organization in Geneva, Switzerland—although other potential routes are under study as well. Steffen Mueller, the paper's lead author, says his team hasn't yet killed its polio strain to see if it also works as a vaccine, but there's no reason to believe it wouldn't.

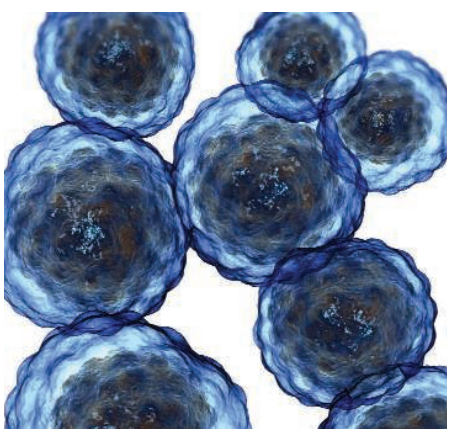

New shot. Weakening polioviruses (*above*) by subtly altering a gene could provide a vaccine strain.

The "big payback" from the new method may be that it can weaken almost any other virus as well, Sutter says. "The nice thing is that we don't really have to understand the virus and the way it functions," Mueller says. Getting approval for vaccines created this way will be a "huge job," Rappuoli predicts, because researchers will have to show that the wimpy strains can't mutate and cause disease—the big worry with any live-attenuated vaccine. But the fact that so many mutations are involved should minimize chances of this happening, says Mueller.

–MARTIN ENSERINK

CREDIT: 3D4MEDICAL.COM/GETTY IMAGES

New Woes for NPOESS

The effort to launch the five-satellite National Polar-orbiting Operational Environmental Satellite System (NPOESS) got a bit tougher last week.

According to a new report by the U.S. Government Accountability Office, the price tag for the multisatellite program, designed to take crucial weather and climate measurements, has risen from $12.5 billion to roughly $14 billion for security, technical, and operating reasons. The higher costs could make it harder to restore planned climate sensors that were removed from the satellites. The overruns may also make it less likely that two satellites will be able to calibrate certain delicate measurements by taking two readings simultaneously. Representative Nick Lampson (D–TX), who chaired the hearing, worries that "the risk of [a] data gap is growing along with the cost of this program." National Oceanic and Atmospheric Administration (NOAA) Administrator Conrad Lautenbacher, however, says that the "White House is committed" to maintaining climate measurements over the long haul.

Pentagon officials are also threatening to cut funding for the project in October unless work is completed on key documents that should have been signed 2 years ago. The Pentagon, NASA, and NOAA are pointing fingers at one another. **–ELI KINTISCH**

Canada-CIRM Cancer Deal

Research on cancer stem cells—one of the hottest topics in stem cell research—is being revved up with a 3-year agreement between the California Institute for Regenerative Medicine (CIRM) and Canada's newly formed Cancer Stem Cell Consortium, a group of public and private research agencies. California and Canada, which together do 70% of all research on cancer stem cells, want to generate some synergy by teaming up. So the consortium is putting up $100 million for Canadian researchers who collaborate with researchers in California. CIRM, meanwhile, which has been gearing up to support applied stem cell research, will devote a portion of the $122 million in disease-related grants to be awarded to California scientists next year to collaborative cancer stem cell research with Canadian scientists. Mick Bhatia, director of McMaster University's Stem Cell and Cancer Research Institute in Hamilton, Canada, says Canadian and California researchers will meet in workshops soon to discuss how to "leverage and complement each other's work."

–CONSTANCE HOLDEN

Published by AAAS

CREDIT: MONIQUE BERLIER/MVP-PATH

An Ill Wind, Bringing Meningitis

Crippling epidemics of meningococcal meningitis sweep across Africa with the onset of the dry season and harsh harmattan winds. An affordable, effective vaccine in the works could change that

OUAGADOUGOU, BURKINA FASO; BAMAKO, MALI; GENEVA, SWITZERLAND—The dust is inescapable, burning your eyes, clogging your nose, penetrating into your lungs, and making breathing ragged. In March, on the road to Koudougou, some 100 km west of Ouagadougou, the landscape is moonlike. In the cratered bottom of a lakebed, dust-caked men, barely distinguishable from their surroundings, fashion bricks from the mud. The bricks will dry quickly in the baking heat, which tops 45°C each day.

It is the dry season in Burkina Faso. And with the dust and the hot, dry wind, known as the harmattan, that blasts across the Sahel come meningococcal meningitis epidemics, caused by the bacterium *Neisseria meningitidis*. What, exactly, about these conditions triggers the epidemics remains mysterious, but they come like clockwork, hitting Burkina Faso every year and engulfing the entire "meningitis belt," which runs from Ethiopia in the east to Senegal and The Gambia in the west, every 6 to 12 years.

The last big one, in 1996–97, sickened hundreds of thousands and killed more than 25,000 in 10 countries. In 2007, the death toll climbed alarmingly high again, prompting the World Health Organization (WHO) to warn that another huge epidemic was likely in 2008. But this season turned out to be relatively quiet, with some 9400 cases in Burkina Faso and 27,000 across the entire belt. As always, the epidemics in Burkina Faso stopped suddenly with the first rains in May, as the population in this country, one of the poorest in the world, braced for the inevitable onslaught next year.

Koudougou district officially passed the epidemic threshold in mid-March, and scarce supplies of the meningitis vaccine were made available to try to curb the epidemic's spread. At a rudimentary health center there, hundreds of people—mostly women and children—queue up for vaccinations, seeking shade by the buildings or under a scrawny tree. Most have been waiting patiently for hours, but some occasionally surge to the front of the line only to be pushed back by the men in charge of crowd control.

At best, this reactive vaccination strategy, as it is called, is a "Band-Aid," says Rosamund Lewis, a physician and meningitis expert at the GAVI Alliance (formerly the Global Alliance for Vaccines and Immunization). The reason is that the vaccine being used, a 1960s design using a polysaccharide from the bacterium's coat and still the only affordable one in Africa, doesn't work very well. Although this vaccine prevents those carrying the bacterium from getting sick, it doesn't stop them from passing it on to others; immunity lasts only a few years; and the vaccine has minimal effect on children under age 2. Because of these limitations, WHO has long recommended that it be used only to control epidemics, not to prevent them—a strategy that has its critics. "The epidemic is sometimes over by the time vaccine arrives," concedes William Perea, a Colombian-born epidemiologist who leads Epidemic Readiness and Interventions at WHO and who nonetheless supports the strategy for lack of a cost-effective alternative.

F. Marc LaForce wants to change all that. He is heading an innovative public-private partnership known as the Meningitis Vaccine

Published by AAAS

Too little, too late. A meningitis vaccine exists, but it can only stop an epidemic, not prevent one. Here at a rural health center near Fottigué, Burkina Faso, people wait for their shots during the 2007 epidemic.

Project (MVP) to develop an affordable, effective, long-lasting vaccine for African meningitis—a conjugate vaccine that includes a protein to boost the immune reaction. The conjugate will cost roughly 50 cents a dose—a price many African governments say they can afford—and is already being tested in clinical trials at several African sites. Barring any further delays, it will be introduced in a massive trial of some 9 million people in Burkina Faso in late 2009. LaForce hopes the new vaccine will eventually be used in preventive campaigns across the entire meningitis belt and spell the end of these devastating epidemics.

"It will change completely the approach to meningitis, and that will be great," says Myriam Henkens, a physician at Médecins Sans Frontières (MSF) in Brussels, Belgium. "We are counting on the conjugate," she says. "It will be so much cheaper and so much better."

And all indications are that countries will be clamoring for it. Although other diseases exact a bigger toll, they are not as feared as meningitis, which can kill within 24 hours and often leaves survivors deaf or otherwise disabled. "Boy, do they want this vaccine," agrees Emil Gotschlich of Rockefeller University in New York City, who developed the existing polysaccharide vaccine.

But the road between here and there is littered with potholes. MVP, a joint project of WHO and the Seattle, Washington–based health nonprofit PATH, has already encountered unexpected obstacles. Originally promised for 2007, the vaccine may not be ready for the 2009 rollout in Burkina Faso, LaForce admits. And questions remain about just how long immunity will last, whether a booster will be needed—which would affect the overall cost of a vaccination strategy—and perhaps more worrisome, whether once *N. meningitidis* group A—which causes the majority of epidemic disease in Africa and is the target of this vaccine—has been beaten down, other strains will arise to replace it.

"Vaccine-making is not for the faint of heart," concedes LaForce.

Mysterious cycles

Meningitis is an infection of the meninges, the thin membrane that surrounds the brain and spinal column. Several different bacteria can cause meningitis, including *Haemophilus influenzae* type B (*Hib*) and *Streptococcus pneumoniae*—and also a few viruses—but only *N. meningitidis*, or meningococcus, spawns the huge epidemics that sweep across the belt. Of the dozen or so meningococcal groups, A is by far the worst, causing roughly 80% to 90% of epidemic disease most years. (Groups C and B, by contrast, fell adolescents and college students in Europe and the United States.)

Roughly 1 in 20 people "carry" the bacterium asymptomatically in the back of their throats and can transmit it to others; what triggers invasive disease remains mysterious. Once the disease begins, with its characteristic sudden fever, headache, and stiff neck, it progresses rapidly. Even with prompt treatment with antibiotics, which is often impossible in remote villages, about 10% die, and up to 25% of survivors are left with permanent disabilities such as deafness or mental retardation.

For about 100 years now, experts have puzzled over the remarkable seasonality of the epidemics, which begin with the dry season in December, peak after a few months, and disappear with the first rains in May or June. One hypothesis is that dust and wind increase transmission of the disease, which is spread person to person through respiratory droplets. The other, which seems more likely, is that the harsh environmental conditions irritate the mucus membranes, enabling the bacterium to more easily penetrate and enter the spinal fluid, where it causes invasive disease.

Similarly, although epidemics are inevitable, almost all efforts to predict exactly when and where they will strike have failed miserably. It has defied the best scientific minds, says Perea, who also works with MVP.

Failed policy?

MVP was born of what everyone refers to as the "terrible epidemic" in 1996–97. African leaders and global health officials watched in horror as the largest meningococcal meningitis epidemic ever recorded swept across the belt. More than 250,000 people fell ill, and the death toll soared beyond 25,000. Clearly, the epidemic response system wasn't working.

Shortly thereafter, WHO, UNICEF, MSF, and the International Federation of Red Cross and Red Crescent Societies banded together to create the International Coordinating Group (ICG) on Vaccine Provision for Epidemic Meningitis Control. Headquartered at WHO in Geneva, Switzerland, ICG tries to ensure that limited supplies of the polysaccharide vaccine are rapidly sent to where they can do the most good. Following the recommendations of a pivotal 2000 *Lancet* paper by Lewis—then at MSF's research institute, Epicentre—and colleagues, WHO lowered the epidemic threshold to 10 cases among 100,000 people in 1 week, shaving more than a week off the usual response time. Perea says that if a country can launch a reactive vaccination campaign within 3 to 4 weeks of an epidemic's onset, it can prevent 70% of the cases. Response times have improved substan-

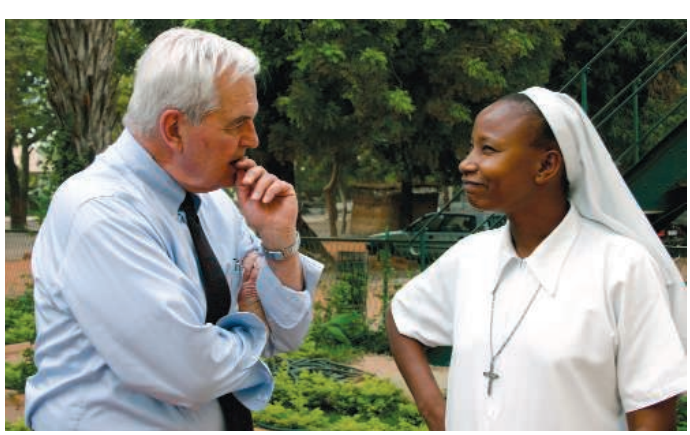

On a mission. Marc LaForce, shown here with community worker Sister Christine in Bamako, Mali, wants to get an affordable and effective meningitis vaccine to Africa.

CREDIT: MONIQUE BERLIER/MVP-PATH

Published by AAAS

tially, but campaigns start within 3 weeks only about 60% of the time, he says.

These improvements were just a stopgap, all conceded. What was needed, recommended a WHO advisory group in 2000, was an entirely new type of meningitis vaccine, a conjugate vaccine that would confer lasting immunity and could be used preventively, modeled on the Men C vaccine that had all but eliminated the disease in the United Kingdom.

A conjugate vaccine uses the same polysaccharide but links, or conjugates, it to a protein to increase its immunogenicity. Conjugate vaccines developed to date, including those for *Hib* and *S. pneumoniae*, confer longer lasting immunity than polysaccharide vaccines, work in infants, and, perhaps more important, reduce transmission of the bacteria, thereby providing herd immunity and protecting even those who are not immunized.

The newly established Bill and Melinda Gates Foundation didn't need much convincing; in May 2001, it sprang for $70 million over 10 years to establish MVP to develop, test, license, and introduce an affordable conjugate vaccine for Africa.

From the outset, some questioned the approach, worrying that it would take too long and arguing that alternatives already existed. Gotschlich and vaccinologist John B. Robbins of the U.S. National Institute of Child Health and Human Development, who both won Lasker Awards for their pioneering work, had long railed against what they considered WHO's failed policy of waiting for an epidemic before starting mass vaccination. In a series of papers, including a roundtable in the *WHO Bulletin* in 2003, they argued that WHO should urge countries to use the polysaccharide vaccine preventively.

True, the polysaccharide vaccine is by no means perfect, says Gotschlich—although he says it is more effective than others now acknowledge. And without question, he says, the conjugate vaccine will be far superior: "I am all for it," says Gotschlich, who serves on MVP's advisory committee. But the polysaccharide vaccine was available and could save lives right away for just pennies a dose, says Gotschlich, who kicks himself for not urging WHO to be proactive back in the 1970s.

"In theory, he is right," says Perea, but he doubts the strategy would work. And it would be hugely expensive. Because epidemics are so unpredictable, he says, this approach would require vaccinating the entire population of the meningitis belt—roughly 400 million people—every 3 years for an estimated $400 million a campaign. "To arrange a countrywide vaccination every 3 years is nuts. The number of resources, from my point of view, is totally unjustified to introduce the polysaccharide as a preventive vaccine," says Perea. With limited resources, he asks, why not focus instead on a "real solution": a conjugate vaccine.

Trials and tribulations

Two months after the Gates money came through, LaForce was on the job, setting up shop in July with a small, energetic staff in Ferney-Voltaire, across the French border from WHO headquarters in Geneva. An infectious disease expert and former meningitis officer for the U.S. Centers for Disease Control and Prevention (CDC), LaForce had recently quit academic medicine, fed up with the paperwork

Family burden. During the 2007 epidemic, families cared for their kin outside the overflowing health center in Fottigué, Burkina Faso.

CREDIT: MONIQUE BERLIER/MVP-PATH

Costs of Meningitis Outbreaks Are Crippling, Too

OUAGADOUGOU, BURKINA FASO—The government of Burkina Faso prides itself on providing free health care to anyone affected by meningitis. Try telling that to the family from Koudougou gathered at Yalgado Hospital here in the capital city.

Last year, during a "reactive" vaccination campaign, their daughter hid from the vaccinators, afraid of the needle, her mother explains. That may be why she got sick this March when another epidemic hit the same district. Now the 14-year-old is lying on a bare cot in a sparse, concrete-floored room, naked in the heat except for her underpants and an IV dripping into her thin arm. She has been here 2 weeks and still has a stiff neck and seems listless. Rigobert Thiombiano, the head of the infectious disease ward, suspects she may have septicemia.

Both her parents are with her in the hospital room, as is the custom in Burkina Faso. Hospitals here do not provide the services Western patients take for granted. The family must buy the medicine, provide and cook the food, wash the laundry, and otherwise care for their kin.

One illness in a family can exact a huge toll on household income, says Anaïs Colombini, a health economist at the French aid group Agence de Médicine Préventive (AMP) in Ouagadougou, who, with her colleagues, recently completed a detailed socioeconomic study, supported by the Meningitis Vaccine Project (MVP) and the World Health Organization, of the burden of meningitis in Burkina Faso.

Government claims aside, AMP found that most families pay on average $25 in direct medical costs, which includes medicine, testing, and lab analysis. Other nonmedical direct costs, say, for food, soap, transportation, and telephone, run another $15.

The indirect costs, from loss of income and property such as cattle and crops, are even higher, running $50 per episode. That adds up to almost half of a family's average annual income of roughly $220. Worse still, says Colombini, just one episode can throw a family into "a downward spiral of poverty" from which it can be impossible to recover.

"Most people don't realize that meningitis is such an important contributor to poverty," she says, with both short- and long-term costs. "For instance, if you can't be home to tend to the crops, they die, and future income is lost." Colombini is eager for MVP's new meningitis vaccine, which she hopes will help eliminate poverty along with this feared disease in Africa. **–L.R.**

Published by AAAS

and the ever-increasing administrative demands. "I wanted to make an impact on global public health before I retired," he says.

In August, LaForce and WHO's Luis Jodar, an early member of MVP, were on a plane to Africa where they began informal consultations with African leaders and health officials about what they wanted in a vaccine. He distinctly remembers a discussion with Hassane Adamou, the secretary general for Niger's Ministry of Health, who said: "Please don't give us a vaccine we can't afford. That is worse than no vaccine." When he asked leaders what was affordable, the answer was 50 cents a dose or less, significantly lower than the $2 to $3 a dose the collaborators had originally envisioned. Won over, LaForce immediately began pushing for the best and least expensive vaccine possible: a First World vaccine at a Third World price.

Vaccine expert Rino Rappuoli, now head of global vaccine research at Novartis, argued vociferously that waiting for the cheapest vaccine was actually more expensive, in terms of lives lost in the interim. While at Chiron in the 1990s, Rappuoli had developed the first conjugate vaccine against meningitis, targeted against groups A and C. It was a "beautiful vaccine," he laments, that performed well in field tests in Niger and The Gambia. But as the group C component was developed for the lucrative market in the United Kingdom, "we were asked to remove A," which was needed only for Africa, he recalls. "The market was only for C." Instead of reinventing the wheel, urged Rappuoli, MVP should dust off his vaccine and make it quickly available.

MVP stuck to its plan for an affordable vaccine. But LaForce says he could find no major vaccine manufacturer willing to produce a Men A conjugate for $2 a dose, much less the price he thought was needed. So in an unusual strategy, LaForce insisted on a guaranteed selling price—50 cents or less—and then found a developing country manufacturer, Serum Institute of India Limited (SIIL) in Pune, willing to take it on. (Although the company has agreed to a fixed price for Africa, it is free to sell the vaccine elsewhere at higher prices.)

Next, MVP lined up suppliers for the raw ingredients: the group A polysaccharide and the protein it would be conjugated with, a tetanus toxoid. And they contracted with a European research group to develop a new conjugation technology and then transfer it to SIIL.

From the outset, MVP decided to concentrate on a monovalent vaccine against group A. Creating a multivalent vaccine that could protect against the other groups in Africa would jack up the cost, not to mention the risk of failure, and stretch out the time frame of development. "If we could [address] 85% of the burden with the simplest approach, … to me, that was a completely acceptable wager with public money," says LaForce. The unexpected emergence of a new epidemic strain, W135, in 2000 caused considerable soul-searching. Even though W135 appeared to be a significant new threat, in the interest of speed, MVP decided against a midcourse change. "History will tell if that was the right decision," says Lewis.

Manufacturing didn't go smoothly. The conjugation technology proved finicky, causing some delays. But still, the partners thought they were roughly on track until, in spring 2003, the European research group MVP was collaborating with announced it was unwilling to transfer the technology to SIIL. That was the absolute low point, says LaForce. Even friends of the project said it was doomed, he recalls, and several called for his ouster. But others lobbied to give him more time.

MVP found a solution at the U.S. Food and Drug Administration, where longtime vaccine experts Robert Lee and Carl Frasch at the Center for Biologics Evaluation and Research had already developed an alternative conjugation technology and quickly transferred it to SIIL with no strings attached. "These guys are heroes," says LaForce. Preclinical animal studies began

Deadly Cycles

For at least 100 years, when the hot, dry harmattan wind blows, meningitis outbreaks have swept across the meningitis belt (see map). Experts suspect that the unforgiving environmental conditions make the body more susceptible to the bacterium. When meningitis cases soared in 2007, WHO warned that 2008 might be an especially bad year, but it was relatively mild. No one knows what 2009 will bring.

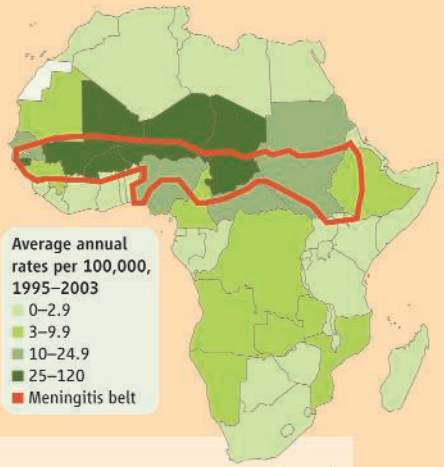

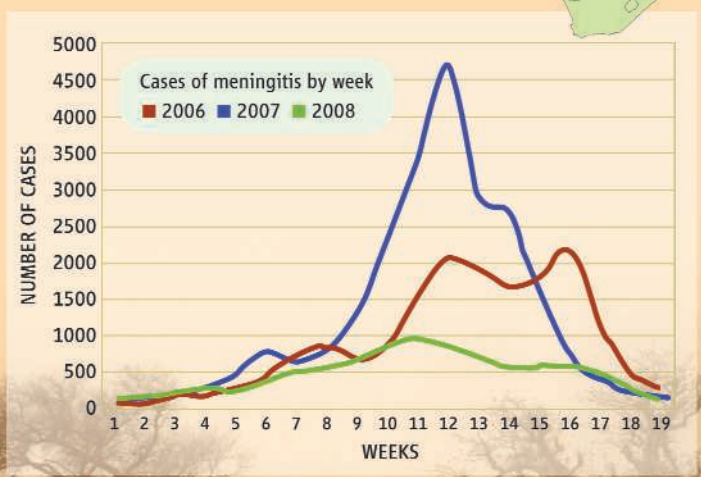

CREDIT: JOSE AZEL/AURORA/GETTY IMAGES; SOURCE: © WHO 2004; MDSC/WHO

Published by AAAS

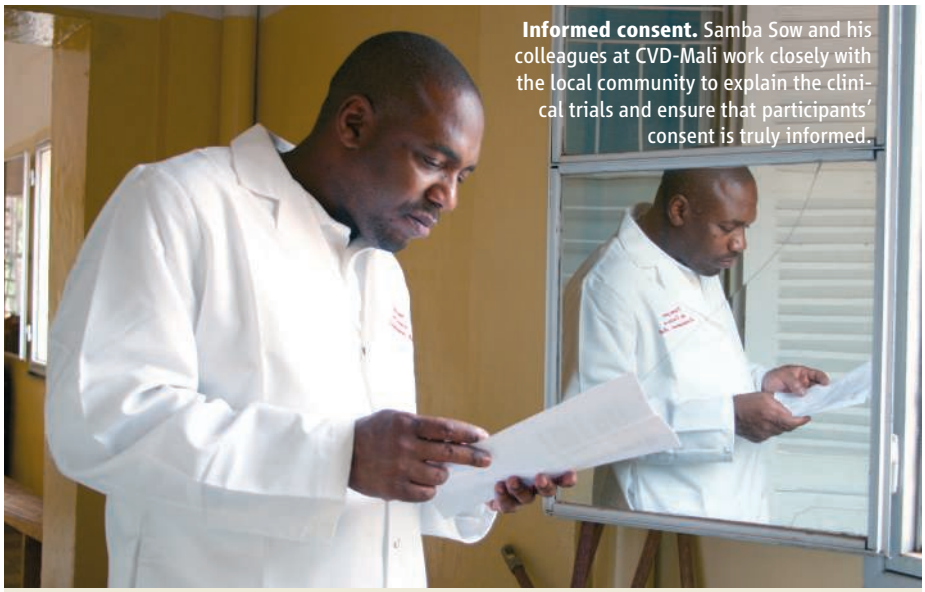

Informed consent. Samba Sow and his colleagues at CVD-Mali work closely with the local community to explain the clinical trials and ensure that participants' consent is truly informed.

Clinical Trials: Dispelling Suspicions, Building Trust in Mali

BAMAKO, MALI—Across West Africa, suspicions of Western medicine—and in particular the fear of being used as a guinea pig in clinical trials—run high. That is true here in Bamako, where Samba Sow of the Center for Vaccine Development (CVD) is doing clinical testing of a new conjugate vaccine developed by the Meningitis Vaccine Project (MVP) (see main text).

Before trials can begin, Sow, like his counterparts leading trials in The Gambia and Senegal, has to win the trust of the local community so he can enlist participants and ensure that consent is truly informed—a task that can't be undertaken lightly, Sow says. He does it by convincing the poor, largely Muslim and illiterate or semiliterate population that the vaccine being tested is designed to help break the cycle of deadly meningitis epidemics rather than make them sterile or infect them with the AIDS virus, as is widely believed.

At the same time, he and MVP have to design a study protocol and consent process that will pass muster with the four institutional review boards (IRBs) that oversee the studies: one at each of MVP's partners, PATH in Seattle, Washington, and the World Health Organization; one at the University of Bamako; and another at the University of Maryland (UMD), with which CVD-Mali is affiliated. A Malian and Muslim physician who went to medical school in Mali and then was trained in epidemiology at the London School of Hygiene and Tropical Medicine—and who now also serves on the faculty of UMD—Sow manages to bridge both worlds.

Sow starts with the all-important "chef de village"—Bamako, with a population of 1.5 million to 2 million, has six districts, which in turn contain five to 12 "souscartiers," or local jurisdictions, each with its own leader. Sow explains the trial to the village head and his advisers, showing them the regulatory approvals from the Minister of Health and the Bamako regional health director, and ethical approvals from all four IRBs, and asks him to convene a community meeting.

"If the leader is not convinced, they will say no, and no one is allowed to sign up. That is the way it works in Mali," Sow says. On the flip side, he says, once one leader says yes, others are also likely to. Sow chairs every single community meeting, during which he describes the study and how the vaccine "acts like a soldier in the body" to protect against meningitis; then the community can ask questions.

The information sheet and consent forms are available in print and on audiotape in English, French, and the most common spoken language here, Bambara. Some questions concern the motives of his group and the Western collaborators. He answers: "Why would I hurt the people where I grew up and who paid for my education? I am here to make my country proud." Other questions are specific, such as "Why do you have to take blood, and why twice?"

The process is repeated again when individuals sign up. Each participant—or the mother if the participant is a child—meets privately with a physician at CVD's clinical center, where they again review the forms and listen to the audiotape. Sometimes the mothers go home to confer with family and community before deciding, says Sow. But so far, the refusal rate is "very, very low."

–L.R.

soon after. Since then, LaForce has been traveling around the world selling his vision—a continent free of deadly meningitis outbreaks—while generally greasing the wheels for the vaccine's introduction.

LaForce, a 69-year-old American, is a big man with a big voice. "*Mon ami, mon ami, comment ça va*?" he boomed on a recent trip to Ouagadougou, as he clasped hands and patted shoulders of collaborators and hotel clerks alike. "*Le vieux blanc*," or old white man, as he sometimes refers to himself, is invariably upbeat, even as he delivers the bad news that, because of a regulatory snafu in India, the vaccine's introduction in Burkina Faso will be delayed from 2008 until 2009. But the vaccine will come, he assures, and it will be great.

Thinking locally

Phase II and II/III clinical trials of MVP's Men A vaccine candidate are under way in Mali, The Gambia, Senegal, and India, where SIIL plans to license the vaccine to protect against that country's occasional outbreaks.

Samba Sow, a Malian physician and epidemiologist, is running the trials in Bamako, Mali, at the Center for Vaccine Development, a partner lab of the University of Maryland's CVD. With MVP support, a former leprosarium—a small group of former patients still lives on the grounds—has been converted into a cheery clinical center for testing the new conjugate and other vaccine candidates.

The challenge in setting up the trials in some of the poorest countries in the world, says Simonetta Viviani, an Italian physician who heads MVP's vaccine development from Ferney-Voltaire, was to create a "functional but minimalist" system that would meet all international standards for ethics and good clinical practices but could also be continued with local experts once MVP is gone. That means hiring and training local staff, working closely with the community, and respecting local traditions, she says (see sidebar at left).

In Mali, explains Sow, the initial contacts with the community—and also the first person parents see when bringing their children to the clinic—should be older and preferably religious, which implies a certain wisdom and trustworthiness. Even in this predominantly Muslim nation, says Sow, a Catholic nun still carries significant clout, whereas bright, young doctors, no matter how prestigious their degrees, or white people will not pass muster, he says.

Results from the "pivotal" phase II trial of the Men A conjugate vaccine, conducted here and in Basse, The Gambia, and announced in

CREDIT: MONIQUE BERLIER/MVP-PATH

Published by AAAS

June 2007, "put us on the map in Africa," says LaForce. The trial of 600 healthy toddlers age 12 to 23 months, half at each site, showed that the conjugate vaccine produced antibody titers almost 20-fold higher than the current polysaccharide vaccine.

MVP's clinical team recently unblinded the results from the second arm of the study, in which the same cohort of 12- to 23-month-olds were randomized to receive a booster dose of the conjugate or the polysaccharide or the control vaccines 8 to 12 months later. The as-yet-unpublished data are "fantastic," raves Viviani. She and LaForce suspect that the vaccine will protect for at least 10 years, although Gotschlich and others caution that the duration of protection won't be known until the vaccine is used in real-world conditions.

A phase II/III trial of 900 participants and controls, under way in Bamako, Basse, and Dakar, Senegal, is testing the safety and immunogenicity of a single dose in 2- to 29-year-olds and will also look at its effect on "carriage"—that is, whether it actually does reduce the load of bacteria carried in the back of the throat. Next up is a study of safety and immunogenicity of different dose schedules in infants, expected to start later this year in Ghana.

Optimism, tempered

If the remaining trials go as expected, if the lot-consistency studies under way in Pune, India, go without a hitch, if production can be scaled up, if India licenses the vaccine and WHO "prequalifies" it, if funding comes through, and tens of other details go right, MVP will introduce the vaccine in Burkina Faso in 2009 or perhaps 2010. And that, LaForce hopes, will be the beginning of the end of meningitis epidemics in Africa.

The vaccine will be given to Burkina Faso's entire population of 1- to 29-year-olds, roughly 9 million people. Kader Konde, director of WHO's Multi-Disease Surveillance Centre (MDSC) in Ouagadougou, who is also MVP's general troubleshooter for Africa, says the president and senior health officials are on board and are pushing MVP to move faster. LaForce says he wishes they could but adds that "it's important that all the regulatory steps are taken so no one feels they have a substandard product."

MVP has already lined up partners to conduct follow-on studies to measure the vaccine's impact. Surveillance will be critical. CDC will help MDSC look for changes in circulating strains. "We must be able to document any case to see if it is a failure of the vaccine or another strain," like W135, rearing its head, says MDSC epidemiologist Mamoudou Harouna Djingarey. That requires strengthening surveillance across the entire belt.

The hub of these efforts is MDSC in Ouagadougou. Housed in a building that still bears the name Onchocerciasis, the revamped facility boasts state-of-the-art equipment, including a real-time polymerase chain reaction machine, a recent gift from CDC, for analyzing cerebrospinal fluid samples to determine the bug and the group. Meanwhile, a half-dozen epidemiologists, microbiologists, and data experts track the bug's every move in 14 countries.

Before MDSC, there was "not much," recalls Perea, who notes that surveillance is now "pretty good" but is still spotty in some countries, such as Chad and Nigeria. Even in Burkina Faso, adds Djingarey, cases are still missed, cerebrospinal samples are degraded in transport, and data dribble in late from some districts. All that must be fixed, he says.

Long lasting. If the MVP meningitis vaccine candidate confers long-lasting immunity, it could end the need for almost yearly vaccinations.

Following the planned 2009 introduction, MVP, MDSC, the Burkina Faso Ministry of Health, and CDC, in collaboration with the Norwegian Institute of Public Health and the Centre for Prevention of Global Infections at the University of Oslo, will conduct carriage studies. Other academic, governmental, and nongovernmental partners, coordinated by Brian Greenwood at the London School of Hygiene and Tropical Medicine, will monitor how long immunity lasts and whether a booster shot is needed, as turned out to be the case with the Men C conjugate in the United Kingdom.

Provided no major problems surface, WHO and its AFRO bureau and UNICEF will introduce the vaccine, first in the three hyperendemic countries: Burkina Faso, Mali, and Niger. Because production will be limited to about 45 million doses for the first few years, the partners are trying to allocate it to the populations at highest risk. By 2016, there should be enough vaccine for the most vulnerable population of the meningitis belt, roughly 250 million people, says LaForce. He envisions that countries will do "catch-up" vaccination campaigns every 5 years or so until the vaccine is approved for infants and can be integrated into routine childhood immunizations. As *Science* went to press, the GAVI secretariat recommended that its board approve $370 million to cover the vaccine introduction in Burkina Faso and subsidize the vaccine's rollout across the belt. Eventually, GAVI's support would wane and countries would pick up the tab themselves.

In the interim, stresses Perea, it will be essential to keep up supplies of the polysaccharide vaccine, which plummeted because of a production decline after MVP was announced, leaving a global shortfall that still persists. It was an unpredictable market to begin with, and manufacturers thought the conjugate would "put them out of business," says LaForce, so "most moved on."

"They stopped 10 years too soon," says Lewis. Since then, two manufacturers have agreed to produce the vaccine if WHO guarantees to purchase it.

The next priority, all agree, is an affordable multivalent conjugate vaccine that would offer even wider protection from all meningococcal groups in Africa. (The Menactra quadrivalent conjugate vaccine licensed in the United States sells for about $100 a dose.) Right now, it's not clear who will take the lead on the multivalent. MVP won't, says LaForce—although he hopes it has shown what is possible—as the project will shut its doors and he will retire in 2011.

The rains started in late May in Burkina Faso, and the epidemic, which had affected more than 9000 and killed 900 there, waned. Although that's a much lower toll than everyone had feared for this year, "it's still 9000 cases too many," says LaForce. He won't hazard a guess about how bad next year's epidemic will be, but he is hoping for a quiet season. "We need another year's breathing room," he says, before the next big one hits.

–LESLIE ROBERTS

CREDIT: MONIQUE BERLIER/MVP-PATH

EVOLUTION

Building the Tree of Life, Genome by Genome

Cheaper sequencing has put many more genes into the hands of researchers trying to sort out the degree of relatedness of a menagerie of organisms

Phylogenetic studies have gone 'omic. Whereas researchers used to be satisfied comparing one gene, or a few, to sort out the branching of the tree of life, the push now among those building phylogenies is to consider whole genomes—at the very least, dozens of genes and thousands of DNA bases—in establishing kinships among flora and fauna. In this way, evolutionary biology is joining the bandwagon of data-intensive studies pioneered by genomics.

Thanks to one such phylogenomic analysis reported on page 1763, bird guides may never be the same. According to this new avian family tree, grebes will share a section with flamingos, not loons. Dull brown night jars and iridescent hummingbirds would now go together. Even parrots and songbirds share a closer kinship than has been appreciated, says Shannon Hackett, an ornithologist at The Field Museum of Natural History in Chicago, Illinois.

She and more than a dozen colleagues constructed the new genealogy after analyzing 32,000 bases from 19 genes in 169 species. More than just rearranging which birds perch on what branches of the tree, the results raise questions about the evolution of flight; some birds that don't fly are unexpectedly grouped with those that do. "It's the most impressive paper in the higher level phylogeny of birds to come along in a long time," says Joel Cracraft, an evolutionary biologist at the American Museum of Natural History in New York City. "It will be used by avian systematists and non-avian systematists for a very long time."

The bird work follows two phylogenomic studies published over the past 3 months that have shaken up perceived evolutionary relationships among animals and more broadly among eukaryotes. In the former effort, a team led by Casey Dunn, now at Brown University, has rearranged the animal kingdom such that comb jellies, not sponges, are among the earliest fauna. In the latter, a European team now divides eukaryotes into two megagroups, not a half-dozen. Together, the three trees speak to the potential of phylogenomics. "We are just beginning to understand what large sequence data sets have to say about the evolution of life on Earth," says Hackett.

Entering the genome age

The term "phylogenomics" was coined by Jonathan Eisen a decade ago to describe incipient efforts to integrate evolutionary thinking into genomic analyses and vice versa. What this evolutionary biologist at the University of California, Davis, had in mind was using information about the relatedness of newly sequenced organisms to help sort out gene function and identify comparable stretches of DNA in genomes that have been deciphered. But the term has been "kidnapped," says Eisen jokingly, by the likes of Hackett and others to describe large-scale efforts to build family trees based on lots of molecular data.

Systematists may like the label, but there's no agreement about how many genes it takes to make an evolutionary tree phylogenomic. "We would say our study is phylogenomic because we have sampled many different genes from many different chromosomes across a subset of avian species, but others would say we still sampled a small portion of the genome," Hackett points out. And ornithologist Michael Sorenson of Boston University applies an even tougher standard: "I would reserve the term for what lies ahead, i.e., comparisons of whole genomes."

In traditional molecular phylogeny, researchers pick out a short stretch of one gene, often a mitochondrial gene, count up the sequence differences between species in that stretch, and use sophisticated computer programs to come up with the hierarchy of evolutionary relationships between the species. Most simply, the fewer the differences, the more closely related two species were considered to be.

Gradually, however, researchers realized "that single-gene trees are prone to errors and that many genes are necessary," explains Jose Castresana of the CSIC Institute of Molecular Biology of Barcelona in Spain. Because genes can evolve at different rates, it's not always possible to pinpoint the true time a species under consideration diverged from a common ancestor by looking just at the changes in one gene from that species. In some cases, there are too few changes to provide statistically reliable results. Other times, the transfer of a gene from one species to another causes phylogenetic chaos.

When Hackett, her postdoc Sushma Reddy, Rebecca Kimball of the University of Florida, Gainesville, and colleagues started their avian project in 2003, collaborators first

CREDITS (LEFT TO RIGHT): GARY KRAMER/U.S. FISH AND WILDLIFE SERVICE; FRANK KRAHMER/ZEFA/CORBIS; WIKIPEDIA

Published by AAAS

Treed. An in-depth comparison of DNA showed that Western tanagers, parrots, and falcons (*left to right*) are closer kin than expected.

did a computer simulation to determine how much and what kind of DNA sequence would enable them to figure out the early history of birds. The simulation directed the team to collect at least 20,000 bases from introns and intergenic regions, where mutations occur frequently enough for there to be significant differences in the various lineages. At first, the researchers sampled only about 75 species, but after realizing how much more robust results would be with a larger number, they doubled it.

"The ultimate goal is to provide the rest of the ornithological community with the roots and base of the tree that they can leaf out more effectively," Hackett says. Traditionally, avian systematists have had trouble sorting out those early days of bird evolution, notes Harvard University ornithologist Scott Edwards. The new results are "bold in setting an agenda for future research," he says.

In agreement with previous avian phylogenies, Hackett, Kimball, and Reddy found that the South American bird family tinamous, along with ratites—kiwis, ostriches, and the like—split off close to the base of the bird tree. Slightly later, chickens, ducks, and their kin branched away from the main group of birds. The subsequent history of birds has been enigmatic, but the new work offers some clarity. Songbirds, for example, are a sister group to parrots, and the two groups encompass all the descendents from their most recent common ancestor. Hummingbirds descended from night jars, evolving bright colors and a diurnal lifestyle along the way.

One of the more controversial results is that tinamous, all capable of flight, belong in the same group as the flightless ratites. This "can change the way people look at the evolution of flight," Hackett says. Grouping the birds together suggests either that flightlessness evolved multiple times, not once in the ancestor to this group, or that flight evolved more than once in birds, showing up independently in the tinamous and in other flying birds. "This result flies in the face of many other kinds of data," says Edwards.

Shaky branches

The phylogenomics study of eukaryotes, conducted by Fabien Burki and Jan Pawlowski, both at the University of Geneva, Switzerland, and Kamran Shalchian-Tabrizi of the University of Oslo, Norway, also upsets old assumptions. Interested in deciphering the deep roots of eukaryotes, which include protists, plants, animals, and fungi, they combed the public databases, coming up with 135 genes from 65 species to compare. Based on the pattern of differences in the sequences, they and their colleagues came up with three early branches, two containing almost all eukaryotes and one tentatively placed branch representing excavates, protists that include *Euglena* and *Giardia*.

Unlike past analyses based on just a few eukaryotic genes, or just one, this phylogenomic effort, published online 3 June in *Biology Letters*, brought all photosynthetic organisms—save *Euglena* and its relatives—into one group. The researchers suggest that the cyanobacterium that gave rise to the modern chloroplasts seen in plants and in green and red algae was acquired much earlier in eukaryotic evolution than had been thought, though more data is needed to confirm this idea, says Burki.

That plants now group with dinoflagellates, diatoms, or freshwater flagellates—all previously considered independent "supergroups"—has raised some eyebrows. "I think this is untenable," says Patrick Keeling at the University of British Columbia in Vancouver, Canada. Nonetheless, he adds, "this paper represents one of the right ways we should be going to resolve the tree of eukaryotes." The challenge is to include more organisms in future studies. In doing so, "it's entirely possible that strong support for many relationships will evaporate," he notes.

When Dunn and his colleagues wanted to tackle the animal kingdom, they couldn't find enough publicly available DNA sequence for the many species they needed to examine. So they sequenced 39.9 million bases from 29 of nature's more peculiar and little-studied creatures, including water bears, comb jellies, sea spiders, and a variety of worms. These data, combined with existing information, enabled them to evaluate 150 genes from 71 animals.

In some cases, the major branches of the new animal family tree confirmed researchers' suspicions. For example, based on a suite of similar traits seen in the animals, morphologists have long thought that mollusks all stem from a common ancestor. Yet there is no single unifying trait among the phylum, which includes scallops, squid, chitons, and snails. Many, but not all, have a toothlike structure called a radula, and a subset have no shell, even though mollusk means "thin-shelled." Moreover, the molecular data did not back up the premise that all traditional mollusks belong together. Dunn's new tree shows that the mollusks are one big family, however. "It's nice to have tied [this relatedness] down," says Dunn.

But the conclusion that comb jellies are the oldest animals is a surprise, says Dunn, who adds that the reaction has ranged from " 'That is so cool' to 'There is no way.' " Dunn himself calls that result provisional and sees his 10 April *Nature* paper as just the beginning. Thanks to new sequencing technologies, "within a year or two, we'll be seeing studies that have 10 times as many genes from 10 times as many taxa," he predicts.

And he's not the only one to soon be awash in data. Burki is generating more sequences for his work with eukaryotes, and Hackett and colleagues are expanding their data set as well. "Phylogenomics is becoming the rule," says Hervé Philippe, who develops new phylogenetic techniques at the University of Montreal, Canada. Philippe looks forward to more phylogenomics studies that use gene order, even gene content or intron positions, to infer relationships—approaches that will become "more natural when complete genomes are available," he says.

Philippe and others caution, however, that more data don't always guarantee better family trees. "It will be important to reanalyze [data sets] with many different and emerging methods to see if the results change at all," says Edwards. And a few scientists question whether, even then, the full tree of life can really be resolved. But, Edwards argues, "phylogenomics is our best shot."

–ELIZABETH PENNISI

Rooting animals. After sequencing DNA from 29 animals, researchers concluded that comb jellies (*above*) are likely the most primitive known animals and that nudibranchs (*left*) and other mollusks are really true kin.

CREDITS: CASEY BROWN

LETTERS

edited by Jennifer Sills

The Verbosity Epidemic

MANY PUBLIC HEALTH INITIATIVES CITE THE NEED FOR TRANSPARENCY IN RESEARCH. CLARITY AND honesty are integral to the value of study results, funding sources, and institutional, political, and individual involvement. However, transparency becomes more challenging as the language of international health becomes increasingly convoluted. The terminology used in the field of public health has developed into a code that is nearly incomprehensible. Commonplace vocabulary includes "capacity-strengthening," "harmonization and alignment," developing the "fiscal space" for countries "under stress" or with "special needs," using "cluster strategies," and "partnerships" between "NGOs, FBOs, CBOs." But what do these terms actually mean?

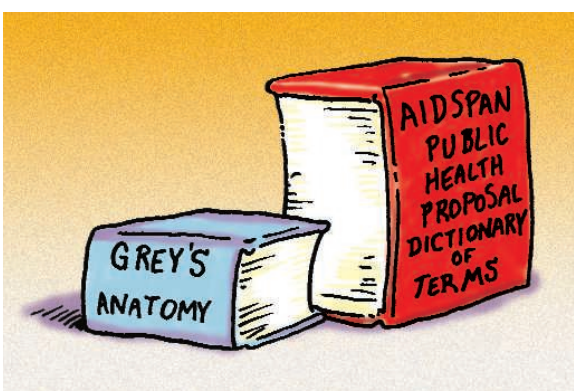

The Global Fund to Fight AIDS, Tuberculosis and Malaria's Guidelines for Proposals (Round 7) is riddled with confusing language that puzzles even proficient English speakers and encourages misinterpretation. The response to frequently asked question number 76 (What is meant by "technical and management assistance"?) is "This phrase is intended to capture relevant forward-looking activities and costs identified as being appropriate to support and manage efficient, effective, equitable, and transparent implementation arrangements" (*1*). The language problem of this application process is so serious that the independent nongovernmental organization Aidspan has emerged with the goal of demystifying the application process (*2*).

Unfortunately, this new language is contagious. Applicants who use these terms are often successful. Large amounts of money have become available for research that involves important, expensive, but often ill-defined areas such as "minimizing the knowledge gap" (*3*). As a result, complexity and imprecision usually prevail. After all, who among us is going to risk losing millions of dollars in potential funding for programs or research by using plain English?

REBECCA F. GRAIS,[1,2]* E. A. ASHLEY,[1] N. J. WHITE[3,4]

[1]Epicentre, 8 rue Saint Sabin, 75011 Paris, France. [2]Harvard Humanitarian Initiative, Harvard University, Cambridge, MA 02138, USA. [3]Faculty of Tropical Medicine, Mahidol University, Bangkok, Thailand. [4]Centre for Clinical Vaccinology and Tropical Medicine, Churchill Hospital, University of Oxford, UK.

*To whom correspondence should be addressed. E-mail: rebecca.grais@epicentre.msf.org

References and Notes

1. The Global Fund to fight AIDS, Tuberculosis and Malaria, *Round 7 Call for Proposals Documentation* (www.theglobalfund.org/en/apply/call7/documents/).
2. D. Garmaise, *The Aidspan Guide to Round 7 Applications to the Global Fund* (Aidspan, New York, 2007); www.aidspan.org/index.php.
3. J. H. Remme *et al.*, *Trends Parasitol.* **18**, 421 (2002).
4. The views of the authors do not reflect the views of their respective institutions. We acknowledge the many organizations that have funded our capability-strengthening, cross-cutting research in resource-challenged settings, thereby providing an overarching enabling empowerment. In other words, we thank our funders.

The Future of the *CMJ*

WE THANK *SCIENCE* FOR A BALANCED PRESentation of the current problems in the *Croatian Medical Journal* (*CMJ*) ("Croatian editors fight with medical school over journal's fate," G. Vogel, News of the Week, 18 April, p. 304). We have opened the pages of the *CMJ* to provide a forum for evidence-based discussion to all of its stakeholders and the scientific community in general, and we have specifically invited Dean Professor Nada Čikeš to present the opinion of the Zagreb Medical School (*1*, *2*). The Dean did not answer the journal's invitation, but we are glad she voiced her concerns to *Science* about the position of the editors and the governing structure of the *CMJ*. In answer to her statement that the editors "have never been formally evaluated or elected to their positions," we must respectfully point out that M. Marušić was appointed co–editor-in-chief of the *CMJ* in 1991 and that A. Marušić was elected co–editor-in-chief by the Editorial Board in 1994. The current Agreement on the Governance of the *CMJ*, signed by four deans in 2004 (*3*), states in clause 12.1. that the present structure of the journal, including its editors, is officially recognized. Under the current Agreement (clause 5.2.), the work of the editors-in-chief is formally evaluated by the Editorial Board every 2 years.

Dean Čikeš also told *Science* that the changes to the Governance Agreement proposed by her school "would bring the journal in line with governance standards recommended by the World Association of Medical Editors." The proposed changes to the Agreement are published in the latest issue of the *CMJ* (*4*), together with the opinion from John Hoey, former editor of the *Canadian Medical Association Journal* (*5*). The *CMJ* receives public funds from the Croatian Ministry of Science, and its owners are public institutions, so the public is an important stakeholder in all matters related to the journal. We invite the scientific community to evaluate the Agreement and the proposed changes, and help the *CMJ* and its

CREDIT: JOE SUTLIFF

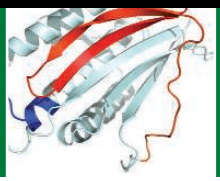

Conformation flexibility

1725

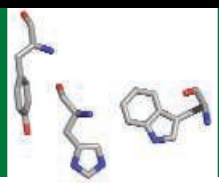

Accelerating electron transfer

1730

owners reach the best solution for the future of the journal.

MATKO MARUŠIĆ AND ANA MARUŠIĆ

Co–Editors-in-Chief, *Croatian Medical Journal,* University of Zagreb Medical School, 10000 Zagreb, Croatia.

References

1. M. Marušić, A. Marušić, *Croat. Med. J.* **48**, 779 (2007).
2. M. Marušić, A. Marušić, *Croat. Med. J.* **49**, 8 (2008).
3. M. Marušić, D. Bosnjak, S. Rulic-Hren, A. Marušić, *Croat. Med. J.* **44**, 663 (2003).
4. M. Marušić, A. Marušić, *Croat. Med. J.* **49**, 158 (2008).
5. J. Hoey, *Croat. Med. J.* **49**, 161 (2008).

The Case Against the *CMJ*'s Editors

IN THE NEWS OF THE WEEK STORY, "CROATIAN editors fight with medical school over journal's fate" (18 April, p. 304), G. Vogel's intention to remain neutral and objective was compromised, as she did not accept the invitation from the Rector of the University of Zagreb to visit and gain insight into the relevant documents. Hence, the story regarding the *Croatian Medical Journal* (*CMJ*) was predominantly based on opinions of the *CMJ* editors. The concluding message is that, given the relative success of the journal, its editors should be left alone to do their work. While we do agree that the *CMJ* has been a relatively successful journal, we believe that the ethical and legal responsibilities of its editors are not beyond the scope of evaluation and discussion.

The problems of the editors were caused by their own actions, and not by the reputation of the *CMJ*. We do not agree with the statement by the Marušić's that "their troubles started in 2001 when the journal rejected a paper by a Zagreb colleague, based on unfavorable reviews." According to our School's rules, even Ph.D. students cannot defend their doctoral thesis before publishing at least one research article in an international peer-reviewed journal with an impact factor above 1.0. However, the *CMJ*'s impact factor is around 0.8, and it has been declining. Thus, failure to publish in the *CMJ* could not "thwart careers" at the University of Zagreb, as suggested by Vogel.

We also disagree with the suggestion that the Marušić's have played a pioneering role in bringing to light corruption and plagiarism in the Croatian academic community. They first raised accusations against colleagues only after Ana Marušić was charged with plagiarism and other forms of unethical conduct of research. Since then, Ana Marušić has received a public reprimand (according to our bylaws the mildest among ethical measures) from the School's Court of Honor, for plagiarism of Moore's Clinically Oriented Anatomy textbook for medical students (1992), after three independent, expert committees ascertained that she had deliberately

translated substantial parts of the foreign textbook under her name (*1*–*4*). This was confirmed in a vote of the School's Council: 41 voted affirmative and 4 abstained. It was not a question of one (Croatian) publisher failing to obtain permission from another publisher (Williams & Wilkins), but the simple case of misappropriating 22 out of 26 tables and 30% of the text with Moore's specific clinical examples without quoting the author. In addition, the Court of Honor considered Ana Marušić's actions to be even more reprehensible in light of the fact that she not only teaches anatomy but also presides over the Council of Science Editors and serves as co-editor of the *CMJ* (*4*). The fact that she is currently teaching academic integrity to our medical students is especially disturbing. Concurrently, Matko Marušić offended the entire academic and scientific community by accusing them of being corrupt without providing any evidence. This is the real background of the controversy between the *CMJ*'s editors (not the journal as such) and the Medical School of Zagreb, which has recently introduced rules for professional and ethical conduct of research and teaching quite similar to those practiced at the Yale University.

We remain confident that the relative success of the *CMJ* as a journal cannot and should not be used as an excuse for nontransparent, questionable, and unethical actions by its editors. The main issue is not the editors' fight over the journal's fate, which has never been in question. Rather it is the editors' inappropriate and unacceptable behavior, which is continuously harming the academic community.

NADA ČIKEŠ

Dean, University of Zagreb Medical School, 10000 Zagreb, Croatia.

References

1. Report No. 450/2006 of Expert Committee for evaluation of authorship of textbook Human Anatomy (24 October 2006).
2. Report of Committee for Scientific Research of the Medical School (29 May 2007).
3. Report of official court interpreter for English language, L. N. Zanella (12 October 2007).
4. Decision of the Court of Honor at Medical School, University of Zagreb (12 December 2007).

Making Memories, Again

IN THEIR REPORT, "THE CRITICAL IMPORTANCE of retrieval for learning" (15 February, p. 966), J. D. Karpicke and H. L. Roediger III show that delayed recall is optimized, not with repeated studying sessions, but with repeated testing sessions. The authors conclude that "retrieval during tests produces more learning than additional encoding."

We suggest a complementary interpretation. Classically, encoded information becomes consolidated and can later be retrieved. The tacit assumption is that retrieval of a consolidated memory is a read-only mechanism, which does not affect the memory. Recent studies have shown that elicited memories are in fact labile and become reconsolidated following each retrieval (*1*–*5*). Labile elicited memories require de novo protein synthesis to be maintained, similar to that of newly acquired memories (*3*). Neurobiological differences between consolidation and reconsolidation processes were recently described in *Science* (*6*). On the psychological level, reconsolidation is useful for explaining false and biased memories (*7*). Reconsolidation also leads to a memory model called multiple-trace theory (*8*): Every time a memory is reactivated, a new version of it is reconsolidated, leaving multiple traces of the same memory.

With respect to Karpicke and Roediger's study, we hypothesize that repeated testing (retrieval) should lead to multiple traces (due to repeated reconsolidation), which facilitate recall. Reinterpreting Karpicke and Roediger's results from a multiple-trace reconsolidation perspective supports this hypothesis and provides a new framework for explaining the effectiveness of frequent in-class assessments in pedagogies such as Peer Instruction (*9*).

NATHANIEL LASRY,[1] EMMANUELLE LEVY,[2] JACQUES TREMBLAY[2]

[1]School of Engineering and Applied Sciences, Harvard University, Cambridge, MA 02138, USA. [2]Department of Psychiatry, Douglas Mental Health University Institute, McGill University, Montreal, QC H4H 1R3, Canada.

References

1. K. Nader, *Nature*, **425**, 571 (2003).
2. K. Nader, *Trends Neurosci*. **26**, 65 (2003).
3. K. Nader, G. E. Schafe, J. E. LeDoux, *Nat. Rev. Neurosci*. **1**, 216 (2000).
4. J. Przybyslawski, S. J. Sara, *Behav. Brain Res*. **84**, 241 (1997).
5. S. J. Sara, *Learn. Memory* **7**, 73 (2000).
6. J. L. C. Lee, B. J. Everitt, K. L. Thomas, *Science* **304**, 839 (2004).
7. E. F. Loftus, *Learn. Memory* **12**, 361 (2005).
8. M. Moscovitch, L. Nadel, *Curr. Opin. Neurobiol*. **8**, 297 (1998).
9. C. H. Crouch, E. Mazur, *Am. J. Phys*. **69**, 970 (2001).

Letters to the Editor

Letters (~300 words) discuss material published in *Science* in the previous 3 months or issues of general interest. They can be submitted through the Web (www.submit2science.org) or by regular mail (1200 New York Ave., NW, Washington, DC 20005, USA). Letters are not acknowledged upon receipt, nor are authors generally consulted before publication. Whether published in full or in part, letters are subject to editing for clarity and space.

Don't Forget the Fungi

IN E. PENNISI'S NEWS FOCUS STORY ON developing crops that are more resistant to drought ("The blue revolution, drop by drop, gene by gene," 11 April, p. 171), I was surprised that there was no reference to mycorrhizal or endosymbiont fungi, which are well documented to increase plant resistance to drought and to increase plant water uptake (*1*–*4*). Much of the work cited referred to *Arabidopsis* genes, but (illustrating the danger of working with a single model organism) *Arabidopsis* is one of the minority of land plants that lack the receptors for arbuscular mycorrhizal symbiosis (*5*). Still, even *Arabidopsis* has been shown to respond with increased heat tolerance to the presence of a particular desert fungus in its surrounding soil (*6*).

Plants are not isolated, individual organisms; they and their rhizospheres form ecosystems. In the interests of producing more food in the face of the increased heat and drought of climate change, researchers cannot afford to ignore plants' helper organisms and the complex systems that exist, in the soil that surrounds plants and in the roots and leaves of the plants themselves. While much valuable information has come from isolated organisms in the laboratory, applied research often requires looking at real-life systems in all their gloriously messy complexity.

SUSAN GOLDHOR

Center for Applied Regional Studies, Cambridge, MA 02138, USA.

References

1. R. M. Auge, *Mycorrhiza* **11**, 3 (2001).
2. R. S. Redman *et al*., *Science* **298**, 1581 (2002).
3. R. J. Rodriguez *et al*., *Mitig. Adapt. Strategies Global Change* **9**, 261 (2004).
4. L. M. Márquez *et al*., *Science* **315**, 513 (2007).
5. J. Marx, *Science* **304**, 234 (2004).
6. C. A. McClellan *et al*., *Plant Physiol*. **145**, 174 (2007).

CORRECTIONS AND CLARIFICATIONS

Random Samples: "High science" (6 June, p. 1267). The altitude of the Pyramid station on Mount Everest is incorrect. The correct altitude is 5050 meters.

Newsmakers: "Shepherding cats" (16 May, p. 857). Panthera's budget should have been listed as $6.7 million, not $6.4 million. Also, the organization spends a total of $5.5 million on cat conservation, not just the $400,000 for research grants mentioned in the article.

News Focus: "Science by the masses" (28 March, p. 1750). Prize4Life would like to clarify that unlike most clients of Innocentive, Prize4Life does not require those submitting solutions to its prize challenges to relinquish their intellectual property in order to receive the advertised award. All IP rights remain with the solver unless the solver specifically chooses to waive them.

Published by AAAS

ERRATUM

Post date 31 October 2008

Letters: "The case against the *CMJ*'s editors" by N. Čikeš (27 June, p. 1719). Čikeš stated that "the *CMJ*'s impact factor is around 0.8, and it has been declining." In fact, *CMJ*'s impact factor has had an increasing trend and reached 1.174 in 2007, thus becoming the first Croatian scientific journal ever to achieve an impact factor greater than 1. Čikeš also failed to state that the decision of the School's Court of Honor against A. Marušić was officially abolished by the Ministry of Science, Education, and Sports (ruling UP/I-040-01/08-01/00001, no. 533-01-08-0001 from 28 January 2008).

COMMUNICATING SCIENCE

Peaks of 20th-Century Presentation

Hanne Andersen

> For years as a college tutor at Oxford, I would try the intelligence and reasoning powers of entrance candidates by asking them at interview to muse aloud on the conundrum of why mirror images appear left-right reversed but not upside down. It is a provocative puzzle, which is hard to situate among academic disciplines. Is it a question in psychology, in physics, in philosophy, in geometry, or just commonsense? I wasn't necessarily expecting my candidates to "know the right answer." I wanted to hear them think aloud, wanted to see if the question piqued their interest and their curiosity. If it did, they would probably be fun to teach. (*1*)

Piquing interest and curiosity lies at the heart of *The Oxford Book of Modern Science Writing*, a collection of modern science writing, selected and commentated upon by Richard Dawkins. Dawkins (who holds a chair in the public understanding of science at Oxford University) is well known as a brilliant writer whose work inspires experts and laymen alike. In this volume, he has selected writings from other gifted writers in an effort to show how good science writing brings science and literature together.

Dawkins's selections are all from the last 100 years, and primarily they are works that were originally composed in English. Within these restrictions, the collection covers a wide variety of fields, from theoretical physics to paleontology, and includes researchers such as Rachel Carson, Francis Crick, Theodosius Dobzhansky, Albert Einstein, Richard Feynman, Stephen Jay Gould, Douglas Hofstadter, Primo Levi, Ernst Mayr, Roger Penrose, Carl Sagan, C. P. Snow, and Alan Turing.

Focusing on "good writing by professional scientists," the volume constitutes a literary kaleidoscope that highlights the many ways in which the scientific mind can work and the allure of science's particular way of understanding the world around us. Thus, one theme that the collection effectively conveys is science as a process of wondering—wondering about deeply fundamental issues such as how, in Per Bak's words, "the universe [can] start with a few types of elementary particles at the big bang, and end up with life, history, economics, and literature" (*2*), or, as in the earlier quote from one of Dawkins's brief introductions to the selections, wondering about familiar phenomena like the left-right reversal of mirror images.

The Oxford Book of Modern Science Writing

Richard Dawkins, Ed.

Oxford University Press, Oxford, 2008. 437 pp. $34.95, £20. ISBN 9780199216802.

Although the collection contains many details and interesting facts, in most of the sampled texts the emphasis is not on particular pieces of scientific knowledge but rather on the scientific reasoning. Some pieces demonstrate how to cut through the contingent particulars to recognize general principles, such as the thermodynamical structure of change, whether this is, Peter Atkins notes, "simple change, as when a bouncing ball comes to rest, or when ice melts" or "more complex change, as in digestion, growth, reproduction, and death" (*3*). Other pieces spotlight a unique detail in need of explanation, such as the calcareous eyes of the trilobites discussed by Richard Fortey (*4*). Still others illustrate the insights gained from the crossing of disciplinary boundaries, as when astrophysicist Fred Hoyle looks at evolution and is "overwhelmingly impressed by the way in which chemistry has gradually given way to electronics" (*5*). The character of the scientists themselves has also been included in the collection and is displayed with loving respect and honesty, from the moral integrity in J. Robert Oppenheimer's reflections on the creation of the atomic bombs (*6*) to the more nerdy impression left by J. B. S. Haldane's rhyming poem to his fatal rectal carcinoma (*7*).

Dawkins has excluded his own writings from the collection. Instead, his voice is distributed throughout the book as short, personal introductory remarks on each extract. These are appetizers rather than analyses, and the book therefore conveys its messages on the nature of science by way of the many examples, not by explicit analysis or explanations. The selections are grouped into four sections—"What Scientists Study," "Who Scientists Are," "What Scientists Think," and "What Scientists Delight In"—although, as Dawkins notes in his two-page introduction to the volume, this arrangement is not unequivocal. From the contents of the first section, the life sciences, the mind, and the universe seem to dominate Dawkins's view of science's subject matter. However, it is not clear whether their preponderance simply reflects his personal taste and interests, or whether they are the subjects he believes are most likely to

An earlier approach, meant only for a few. In contrast to most alchemy texts, the writings that Dawkins has selected were generally intended to be understood by a wide range of readers. [This page is from Alexander von Suchten's *Chymische Schrifften* (*9*).]

CREDIT: ROY G. NEVILLE HISTORICAL CHEMICAL LIBRARY, CHEMICAL HERITAGE FOUNDATION

The reviewer is at the Department of Science Studies, Ny Munkegade Building 1521, University of Aarhus, DK-8000 Aarhus C, Denmark. E-mail: hanne.andersen@si.au.dk

Published by AAAS

pique the reader's interest and curiosity. In contrast, mathematicians and theoretical physicists get their share of the third section, but again it remains unspoken how to understand this difference between studying and thinking.

With its focus on sparkling examples rather than analyses of the qualities that make them sparkle, Dawkins's collection will probably appeal more to scientists and laymen than to researchers in science writing or science communication. However, it is a volume intended to celebrate rather than analyze modern science writing, and it fulfills this aim well: it is a book from which the love of science and the love of language shine.

References and Notes

1. This comment forms most of Dawkins's introduction to a six-page selection from Richard Gregory's *Mirrors in Mind* (*8*).
2. P. Bak, *How Nature Works: The Science of Self-Organized Criticality* (Oxford Univ. Press, Oxford, 1997).
3. P. W. Atkins, *Creation Revisited* (Freeman, New York, 1992).
4. R. A. Fortey, *Trilobite! Eyewitness to Evolution* (HarperCollins, London, 2000); reviewed by A. R. Palmer, *Science* **290**, 59 (2000).
5. F. Hoyle, *Man in the Universe* (Columbia Univ. Press, New York, 1966).
6. J. R. Oppenheimer, "War and the nations," a 1962 lecture published in *The Flying Trapeze: Three Crises for Physicists* (Oxford Univ. Press, London, 1964).
7. J. B. S. Haldane, "Cancer's a funny thing," *New Statesman*, 21 February 1964.
8. R. L. Gregory, *Mirrors in Mind* (Freeman, New York, 1997).
9. A. von Suchten, *Chymische Schrifften alle, so viel deren vorhanden, zum ersten Mahl zusammen gedruckt, mit sonderbahren Fleiss von vielen Druckfehlern gesäubert, vermehret, und in zwey Theile, als die Teutschen und Lateinischen verfasset* (Frankfort, 1680).

10.1126/science.1159114

SCIENCE AND THE LAW

Compelling Cases for Change

C. Michael Bowers

Forensics Under Fire
Are Bad Science and Dueling Experts Corrupting Criminal Justice?

by Jim Fisher

Rutgers University Press, Piscataway, NJ, 2008. 339 pp. $24.95. ISBN 9780813542713.

Readers will find *Forensics Under Fire* a compelling exploration of the dark side of forensic science. This shadowy place in forensics does exist and has seldom been so clearly and openly penetrated and discussed. Jim Fisher delves into the arenas where conflicting and scientifically shaky forensic research, methods, and opinions are used to the disadvantage of justice in the United States and abroad.

Fisher's career in law enforcement (as a Federal Bureau of Investigations agent) and forensic education (as a professor at Edinboro University of Pennsylvania) has led to a book that is extremely topical, sharply written, and well researched. The use of forensic science opinions in criminal proceedings rests on a broad base of epidemiology, pathology, neurology, pediatrics, dentistry, fingerprints, shoe prints, hair, fibers, DNA profiling, and bullet identification. The author's critique draws on sources from the milieu of media investigatory journalism, court transcripts, legal commentaries, professionally reviewed articles, and research focused on deconstructing the assumption that forensic science is always unbiased and thus a reliable determiner of the truth. Fisher uses over 30 case studies as vehicles to discuss his points regarding bad science, misadventures of forensic experts, human error, and the inability of our 21st-century judicial system to properly differentiate between valid research and junk science. He also provides his views of what it will take to cure these systemic deficiencies in courtroom science.

We all know "hired guns" as stock characters of cowboy fiction, but many members of the general public may not recognize how frequently they appear in the halls of justice. Fisher presents examples of prosecutorial cherry-picking of experts who, although discredited in other jurisdictions, are still employed because of their persuasiveness with juries. These prosecution's "guns" include a police fingerprint expert who testified to a "match" later disproved by his peers, a bitemark expert who claimed to be reliable because he truly believes in his unscientific assumptions (although his conclusions have been refuted by DNA analyses), and a self-promoting physician who is the "go to" expert on equivocal cases of child death or sexual assault.

The author also gives considerable attention to the actions of law enforcement agencies. He discusses poorly conducted criminal investigations in which the outcomes were generated by tunnel vision and premature assumptions of guilt. As an example of overselling the science, he offers the FBI's comparative bullet lead analysis—a process developed in the early 1980s and discontinued in 2005 after a critical report from the National Research Council.

In general, Fisher characterizes the defense bar as unflinchingly loyal to its unjustly convicted clients. Some may consider this grandstanding on his part, but wrongful conviction cases are real and are being seen in greater frequency on the evening news. Often the exonerated are indigent and underserved minority defendants. They provide the faces to the invariably decades-long postconviction battles Fisher writes about. These cases also provide a framework for the back story on how the original forensic science participants aided the miscarriage of justice. In one study, 63% of 86 wrongful convictions (in which the defendant was later exonerated by DNA evidence) contained forensic science testing errors at trial (*1*).

I highly recommend *Forensics Under Fire* to anyone interested or involved in criminal justice, constitutional law, civil rights, forensic science, or law enforcement. With their compelling details, the cases discussed provide excellent material for problem-based training. Fisher offers readers the chance to see behind the news headlines and the portrayal of forensic science by the entertainment industry.

A critical examination of the evidence. Although media exposure, including television series such as *CSI*, has increased public expectations of forensic science, persistent problems in its actual practice suggest the need for substantial reform.

CREDIT: CBS-TV/THE KOBAL COLLECTION

The reviewer is at 2284 South Victoria Avenue, Suite 1-G, Ventura, CA 93003, USA. E-mail: cmbowers@aol.com

References

1. M. J. Saks, J. J. Koehler, *Science* **309**, 892 (2005).

10.1126/science.1159103

THE EARLY YEARS

Preschool Programs Can Boost School Readiness

Preschool programs in Oklahoma help children to succeed in school.

William T. Gormley Jr.,* Deborah Phillips, Ted Gayer

Early childhood programs have been heralded by both scholars and decision-makers as a promising avenue for fostering school readiness (*1*–*4*). In the United States, these sentiments have fueled ambitious preschool initiatives from both state and federal resources.

Oklahoma's prekindergarten (pre-K) program has generated attention because it is universal, is based in the school system, and reaches a higher percentage of 4-year-olds than any other state pre-K program. Oklahoma's state-funded pre-K program channels aid to local school districts, which are free to run full-day programs, half-day programs, or both. Federally funded Head Start programs, which are targeted to poor or otherwise at-risk children, and private day care centers are also eligible for state funding if they establish "collaborative" relations with their local school district. The Oklahoma pre-K program has relatively high standards compared with those of other states and offers relatively high pay and benefits to well-qualified teachers. Every lead teacher must have a B.A. degree and must be certified in early-childhood education. Student teacher ratios of 10-to-1 and class sizes of 20 must be maintained. The Community Action Project (CAP) of Tulsa County, whose Head Start program serves the largest number of children in Tulsa, is eligible for state funding. Its teachers meet the same standards as their Tulsa Public Schools (TPS) counterparts and receive similar pay (*5*).

Preschool programs strengthen reading, writing, and math skills

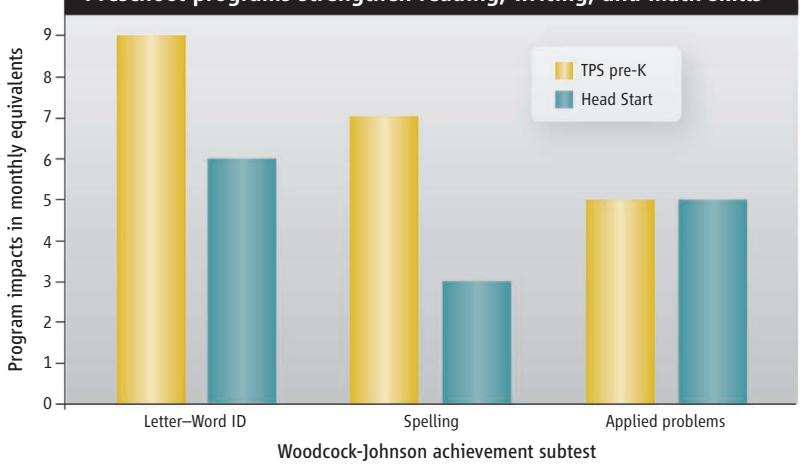

Here, we estimate the short-term test score gains for children in Tulsa's pre-K and Head Start programs. In August 2006, we administered three subtests of the Woodcock-Johnson Achievement Test to incoming Tulsa students entering pre-K and Head Start programs and kindergarten. The tests were administered just before the commencement of classes by the individual who would be teaching the child that year. About 78% of all pre-K entrants, 69% of all Head Start entrants, and 73% of all kindergarten entrants were tested. The tested students closely mirrored the universe of students, except for the kindergarten cohort, where some differences between the two groups were found (*6*). While the child was being tested, the parent completed a survey to provide demographic information. Program participation and school lunch eligibility were determined separately (*7*).

The three subtests we used were the letter-word identification test (a measure of prereading skills); the spelling test (a measure of prewriting skills); and the applied problems test (a measure of premath skills). These subtests have been shown to be especially appropriate for children aged 4 to 5 and have been used by other researchers studying both at-risk and more diverse groups of children. Woodcock-Johnson test scores at or before school entry help to predict later scholastic achievement (*8*).

A difficult methodological challenge that confronts education researchers is selection bias. Here, the concern is that children whose parents choose for them to participate in the voluntary pre-K or Head Start programs will differ from nonparticipants and that these differences will affect test scores. To overcome such selection bias, we have used two separate regression-discontinuity estimations. First, the treatment group consisted of 1264 kindergarten students who attended Tulsa's pre-K program and the comparison group was 1492 children who were about to begin that program. For the second estimation, the treatment group consisted of 327 kindergarten students who attended Tulsa's Head Start program, and the comparison group was 483 children about to enter that program.

This research design is possible because the TPS and the Tulsa Head Start program strictly enforce a 1 September birthday requirement for enrollment in the 4-year-olds' program.

Our analysis estimates the continuous relation between age and test score separately on both sides of the age cut-off. This is achieved by regressing test scores against the child's precise date of birth (the number of days born before or after the cut-off qualification date), an age cut-off indicator variable, and an interaction variable that allows for different slopes on both

Georgetown Public Policy Institute and Center for Research on Children in the United States (CROCUS), Georgetown University, Washington, DC 20007, USA.

*To whom correspondence should be addressed. E-mail: gormleyw@georgetown.edu

Published by AAAS

sides of the cut-off point. The coefficient for the cut-off indicator is the estimated treatment effect. This estimated treatment effect is unbiased if there are no discontinuous differences at the cut-off in characteristics that contribute to test scores.

We tested this condition by comparing the regression-adjusted observed characteristics for children in the treatment and comparison groups at the age cut-off limit. For our TPS comparisons, the characteristics were not statistically different at the cut-off. For our Head Start comparisons, the characteristics matched very well, except that children in the comparison group were somewhat more likely to be female, somewhat more likely to be eligible for a reduced price lunch, and somewhat more likely to have a mother with no high-school degree. Consequently, one should be more cautious about interpreting the Head Start results.

In all of our regressions, we also included a wide range of demographic variables, including gender, race and/or ethnicity, school lunch eligibility, mother's education, whether the child lives with his or her biological father, and whether the child has Internet access at home (*9*). We handle missing data for three variables obtained through the parent survey by using multiple imputation. All of our numbers estimate the effects of treatment on the treated.

The TPS pre-K program has sharply improved students' cognitive development. One way to capture this is to look at the effect sizes: 0.985 for letter-word identification, 0.743 for spelling, and 0.355 for applied problems (*10*). These effect sizes substantially exceed those reported for pre-K programs generally and are somewhat greater than those reported for five states with relatively high quality pre-K programs (*11, 12*). The effects of the Tulsa Head Start program, though less spectacular, are also impressive: 0.514 for letter-word identification, 0.334 for spelling, and 0.369 for applied problems. These effect sizes exceed those reported for a national study of Head Start with random assignment of children (*13*).

Another way to express program effects is to convert test score impacts into monthly equivalents (see chart, page 1723). These gains are above and beyond those that otherwise occur through aging and maturation.

The different estimated test effects across Tulsa pre-K and Tulsa Head Start could be due to differences in the types of children enrolled or to differences in how the programs function. In order to focus on the latter, we trim the Head Start sample to include only children who were eligible for free lunches (typically children whose family income is less than 130% of the federal poverty level). We then trim the pre-K sample to include only children who were eligible for free lunches and who participated in a full-day program (all Head Start children participated in a full-day program) (*14*). Even with these modifications, the two samples differ in the race and/or ethnicity of the students, although not in other observable characteristics. We therefore estimate separate program effect sizes for blacks and Hispanics, for both pre-K and Head Start. We do not report results for whites or Native Americans because of small Head Start sample sizes for these two subgroups.

Focusing on the pre-K population that most resembles the population of Head Start students allows us to better compare the two programs. There are larger test impacts for children who are eligible for free lunch in the TPS pre-K full-day program compared with those similarly qualified in the Tulsa Head Start program (a full-day program), for both blacks and Hispanics (fig. S2). The differences are larger for prereading and prewriting skills than for premath skills, where the TPS and Head Start programs are equally effective.

What explains these differences? One possibility is that the programs attract students of different abilities and family circumstances, even though we condition on free-lunch eligibility, full-day program, and race. Another possible explanation may lie in the differing classroom priorities: TPS emphasizes letters and sounds more, whereas Head Start emphasizes fantasy play more (fig. S3). Our analysis of kindergarten students who attended the two types of programs the previous year suggests that these two variables do help to explain part of the difference in verbal test score gains between TPS and Head Start (*15*). Specifically, the Head Start variable explains less of the variance in letter-word identification and spelling test scores in a model that includes these two classroom variables than in a model that excludes them. This suggests that the two classroom variables account for some of the performance gap between TPS and Head Start. However, we also find that TPS places more emphasis on math, which does not translate into higher pre-math test scores compared to Head Start.

Early childhood education programs in the United States face enormous challenges. The overwhelming majority of Head Start program participants are poor, and many Head Start children face additional risk factors, such as a single-parent home or a home where English is not the primary language spoken. Pre-K programs targeted to poor or otherwise at-risk children face similar challenges. Even universally available programs, such as Oklahoma's, must cope with the realities of poor families, fragmented families, and immigrant families.

Against this backdrop, it is instructive to compare the potency of program participation variables with that of other variables in our statistical models. For the TPS model, program participation is a more powerful predictor of prereading and prewriting test score outcomes than gender, race and/or ethnicity, free lunch eligibility, mother's education, or whether the biological father lives at home (fig. S4). For the Head Start model, program participation is a more powerful predictor of premath outcomes than gender, free lunch eligibility, mother's education, or whether the biological father lives at home (fig. S5). Early childhood education can therefore make a big difference for short-term test scores, substantially muting the negative effects of family and environmental risk factors.

References and Notes

1. W. S. Barnett, *Am. J. Orthopsychiatry* **63**, 500 (1993).
2. A. J. Reynolds, J. A. Temple, D. L. Robertson, E. A. Mann, *JAMA* **285**, 2339 (2001).
3. J. J. Heckman, *Science* **312**, 1900 (2006).
4. E. Zigler, W. S. Gilliam, S. M. Jones, *A Vision for Universal Preschool Education* (Cambridge Univ. Press, New York, 2006).
5. The starting salary for a TPS teacher was $29,000 for the 2005–06 school year; the starting salary for a CAP Head Start teacher was $29,500.
6. Tested kindergarten students were somewhat less likely to be poor and black and somewhat more likely to be middle-class and white than the universe of kindergarten students.
7. Pre-K participation was determined from TPS administrative data; Head Start participation was determined from CAP Head Start of Tulsa County administrative data.
8. G. J. Duncan *et al.*, *Dev. Psychol.* **43**, 1428 (2007).
9. If the covariates balance on each side of the cut-off point, then including them in the regression does not reduce bias of the treatment effect.
10. Experts disagree on the best way to measure effect sizes. We prefer to divide the regression coefficient by the standard deviation of the control group, because the latter is the counterfactual of interest.
11. K. A. Magnuson, C. Ruhm, J. Waldfogel, *Econ. Educ. Rev.* **26**, 33 (2007).
12. V. C. Wong, T. D. Cook, W. S. Barnett, K. Jung, *J. Policy Anal. Manag.* **27**, 122 (2008).
13. M. Puma *et al.*, *Head Start Impact Study: First Year Findings* (Department of Health and Human Services, Washington, DC, 2005).
14. About two-thirds of all TPS program participants enroll in a full-day program.
15. We used hierarchical linear modeling (HLM) to distinguish between organizational-level and individual-level effects on cognitive development. See our SOM for details.

16. This research was supported by generous grants from the Foundation for Child Development, the Spencer Foundation, the David and Lucile Packard Foundation, and the A.L. Mailman Family Foundation. The authors alone are responsible for the contents. For additional information on the Oklahoma project, see www.crocus.georgetown.edu.

10.1126/science.1156019

Supporting Online Material
www.sciencemag.org/cgi/content/full/320/5884/1723/DC1

BIOCHEMISTRY

Metamorphic Proteins

Proteins that can adopt more than one native folded conformation may be more common than previously thought.

Alexey G. Murzin

It is generally accepted that natural proteins possess unique, evolutionarily conserved three-dimensional structures. Yet, this empirical rule may be in need of revision. A small but growing number of "metamorphic" proteins adopt different folded conformations for the same amino acid sequence in native conditions. Unlike prions, they undergo reversible conformational changes. Most of these proteins have been treated as special cases, because the transitions between their alternative conformations are triggered by environmental factors. The discoveries of a new metamorphic protein capable of independent interconversion (*1*) and of an abrupt fold change in a protein lineage (*2*) point to a more general nature of this phenomenon.

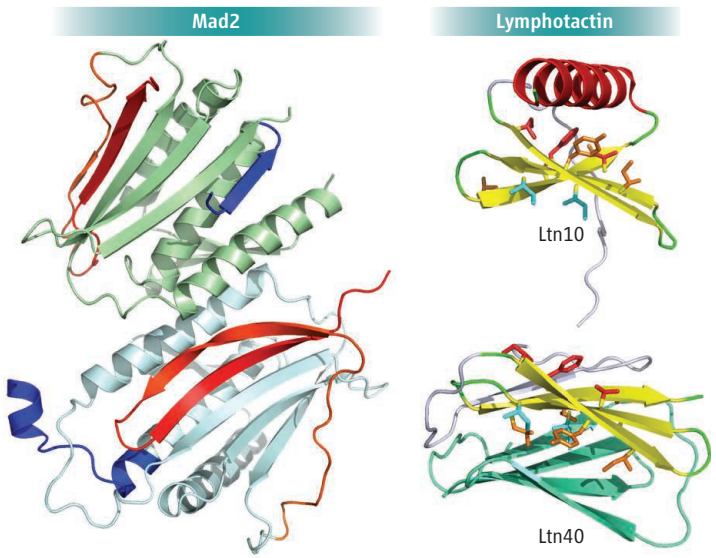

Protein metamorphoses facilitated by dimerization. (**Left**) The structure of alternatively folded parts (blue and red) of one Mad2 conformer (gray) is additionally stabilized by the interactions with the other conformer (light green) in a transient asymmetric dimer. (**Right**) The interconversion between monomeric Ltn10 (top) and dimeric Ltn40 (bottom) involves an isomerization of the β sheet. Structurally equivalent residues are few and contribute either to the Ltn10 core (red) or to the dimeric interface of Ltn40 (cyan). Other nonpolar residues (orange) change sides, such that the formation of the dimeric interface on one side of the β sheet destabilizes the hydrophobic core on the other side and vice versa.

Examples of dramatic conformational changes include the transition between the initiation and elongation states of an RNA polymerase (*3*, *4*), a pH-induced structural rearrangement in a viral glycoprotein (*5*), a redox-controlled structural transition in a chloride ion channel protein (*6*), and the activation of a lysozyme protein by disulfide isomerization (*7*). So far, only the spindle assembly checkpoint protein Mad2 has been shown to adopt two distinct conformations at equilibrium in a ligand-free state (*8*). In all these cases, the different conformers share a large common substructure that may be retained during interconversion.

In contrast, the chemokine lymphotactin (Ltn) studied by Tuinstra *et al.* adopts two distinct folds at equilibrium in physiological conditions, and interconversion between the conformers involves almost complete restructuring of its hydrogen bond network and other stabilizing interactions (*1*). One conformer, Ltn10, adopts the canonical chemokine fold and binds natural and decoy Ltn receptors (*9*). The other, Ltn40, forms a dimeric β-sheet sandwich and binds to heparin, a polysaccharide component of the extracellular matrix. These mutually exclusive activities of the two conformers are both essential for full Ltn function in vivo.

Tuinstra *et al.* suggest that this unusual folding behavior has evolved for a biological purpose (*1*). Similarly, the two-state behavior of Mad2 is essential for Mad2's biological function and may have evolved for this purpose. But there is a more general explanation for the existence of metamorphic proteins: The above empirical rule is merely a product of natural selection and can be broken in certain conditions (*10*). The existence of multiple folded conformations is not prohibited by principles of physics and chemistry. However, in vivo, a protein must quickly form its biologically active conformation, and stable alternative folds would act as kinetic traps that slow the rate of protein folding (*11*). To avoid this complication, different folded states should be able to interconvert without going through a fully unfolded state. This is probably the case for both Mad2 and Ltn, whose metamorphoses in the absence of external factors are facilitated by self-dimerization (see the figure) (*1*, *8*).

An engineered Ltn variant with a destabilizing point mutation in the Ltn10 core adopts only the Ltn40 structure (*1*). Such a mutation in vivo could originate a new lineage of the chemokine family with an unrelated fold. Recent discoveries of protein families containing members of distinct folds suggest that there could have been metamorphic ancestors in their evolutionary histories (*10*, *12*). In all these families, the structurally different proteins have only moderate sequence similarity, but their homology can be traced through one or more proteins with intermediate, more similar sequences.

If the different folds in such a family have evolved abruptly rather than gradually, as follows from the hypothesis of a metamorphic ancestor, the intermediate sequences are expected to adopt one or the other of the observed folds rather than some intermediate structures. Roessler *et al.* (*2*) show that this is the case for the Cro family of bacteriophage transcription factors. The authors first identified new members with sequences intermediate between those of the structurally distinct P22 Cro and λ Cro. They then determined the structures of two of these intermediates, which have a high (40%) sequence identity to each other. One structure was found to be similar to λ Cro, and the other to P22 Cro, confirming an abrupt fold change in the λ Cro lineage.

Concurrently with Roessler *et al.*'s research, another example of abrupt change was discovered accidentally by a structural genomics project targeting new protein families. Two orthologous proteins from different *Shewanella* species show a very high (54%) sequence identity to each other, yet their crystal structures, determined in similar conditions, revealed large-scale differences in the subunit conformations and distinct dimerization modes (*13*). It remains

MRC Centre for Protein Engineering, Hills Road, Cambridge CB2 0QH, UK. E-mail: agm@mrc-lmb.cam.ac.uk

Published by AAAS

unclear whether these proteins are truly metamorphic and can interconvert between the different conformations.

Metamorphic proteins may not be as rare as it currently seems. It may even be, as argued by Tuinstra *et al.* (*1*), that most structural biology efforts have inadvertently selected against their detection. If so, then we may find more manifestations of this phenomenon as new proteins are studied and old proteins reexamined. Such discoveries will enhance our understanding of protein folding, function, and evolution.

References and Notes

1. R. L. Tuinstra *et al.*, *Proc. Natl. Acad. Sci. U.S.A.* **105**, 5057 (2008).
2. C. G. Roessler *et al.*, *Proc. Natl. Acad. Sci. U.S.A.* **105**, 2343 (2008).
3. Y. Whitney Yin, T. A. Steitz, *Science* **298**, 1387 (2002).
4. T. H. Tahirov *et al.*, *Nature* **420**, 43 (2002).
5. S. Roche, F. A. Rey, Y. Gaudin, S. Bressanelli, *Science* **315**, 843 (2007).
6. D. R. Littler *et al.*, *J. Biol. Chem.* **279**, 9298 (2004).
7. M. Xu *et al.*, *Science* **307**, 113 (2005).
8. M. Mapelli *et al.*, *Cell* **131**, 730 (2007).
9. J. M. Alexander-Brett, D. H. Fremont, *J. Exp. Med.* **204**, 3157 (2007).
10. A. Andreeva, A. G. Murzin, *Curr. Opin. Struct. Biol.* **16**, 399 (2006).
11. J. N. Onuchic, P. G. Wolynes, *Curr. Opin. Struct. Biol.* **14**, 70 (2004).
12. G. A. Belogurov *et al.*, *Mol. Cell* **26**, 117 (2007).
13. The structures have been determined by the Joint Center for Structural Genomics (www.jcsg.org) with Protein Data Bank entries 2OOK and 2Q3L.

10.1126/science.1158868

CELL BIOLOGY

Arrestin' Movement in Cilia

A signaling protein localizes to primary cilia through its interaction with a complex that contains a motor protein.

Rajat Rohatgi[1,2] and Matthew P. Scott[1]

Most cells in our bodies bear immotile hairlike protrusions called primary cilia (*1*). Only a few micrometers long, they are marvelously complex sensors, detecting and interpreting signals from the environment, such as light, odorants, fluid flow, and proteins that signal between cells. In each case, the receptor for the signal, along with some of the proteins that transmit the message into the cell, are localized in cilia. Their movement into and out of cilia controls signaling pathways that ultimately trigger responses such as cell division and differentiation. Thus, a central challenge is to understand how transmembrane proteins, especially receptors, are targeted to primary cilia. In humans, defective trafficking to cilia can cause pathological conditions ranging from cystic kidney disease to brain malformations and obesity (*2*). On page 1777 of this issue, Kovacs *et al.* (*3*) describe a new mechanism for the movement of the transmembrane protein Smoothened (Smo) into primary cilia. Smo is a component of the signaling pathway that responds to secreted proteins in the Hedgehog (Hh) family. The Hh pathway has been previously linked to cilia (*4*–*6*) and plays fundamental roles in development, stem cell function, and carcinogenesis (*7*).

Sonic Hedgehog (Shh) is a secreted ligand that initiates signaling by binding to its receptor Patched 1 (Ptc1). In the absence of Shh, Ptc1 is concentrated in cilia and inhibits Smo activity (*8*). Shh binding to Ptc1 inactivates the receptor and causes Ptc1 to move out of cilia. This allows the activation of Smo, which accumulates within the ciliary membrane (*4*). The movement of Smo to cilia brings it near other components of the signaling pathway, resulting in activation of transcription factors in the Gli family that regulate gene expression (*9*).

Smo is a seven-pass transmembrane protein that resembles heterotrimeric GTP-binding protein (G protein)–coupled receptors. Such receptors transmit signals either through trimeric G proteins or through β-arrestin proteins and G protein–coupled receptor kinases (Grks) (*10*). The roles of β-arrestins are quite broad. Recruited to receptors by ligand binding and Grk phosphorylation, they can desensitize receptors to further stimulation and assemble protein complexes that have trafficking and signaling functions (*10*). The

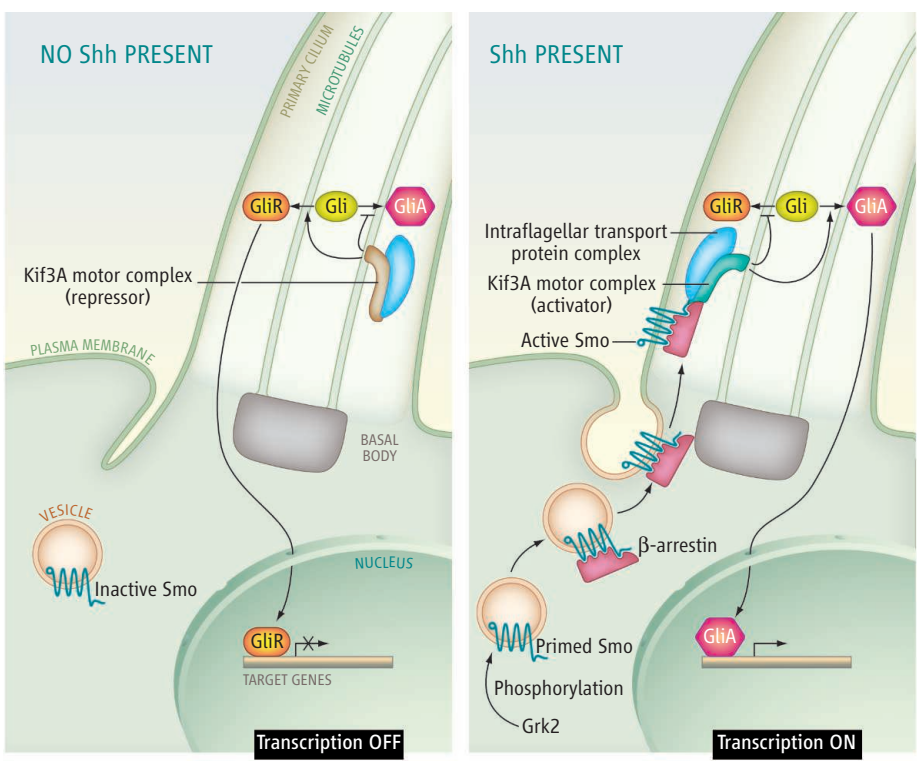

Opposing control of signaling by a motor complex. The primary cilium is depicted as a compartment where activator (GliA) and repressor (GliR) forms of the Gli transcription factor are produced. (**Left**) In the absence of Shh, Kif3A forms a repressive complex that promotes production of GliR. (**Right**) In the presence of Shh, Grk2 induces the association of Smo and β-arrestin, which together move into primary cilia. Smo–β-arrestin recruits the motor protein Kif3A to an activator complex that promotes GliA formation. In this model, the distribution of Kif3A between these two complexes determines the ratio of GliA to GliR.

CREDIT: P. HUEY/*SCIENCE*

[1]Departments of Developmental Biology, Genetics, and Bioengineering, and [2] Department of Oncology, Howard Hughes Medical Institute, Stanford University School of Medicine, Stanford, CA 94305–5439, USA. E-mail: mscott@stanford.edu

depletion of Grk2 and β-arrestin 2 in cultured mammalian cells and zebrafish embryos blocks Hh signaling (*11*–*13*). Smo activation leads to the Grk2-mediated association of β-arrestin 2 with Smo, which then triggers the internalization (endocytosis) of Smo (*12*).

Kovacs *et al.* investigate the next important question: How does recruitment of β-arrestin 2 to Smo activate signaling? Using RNA interference in cultured mouse fibroblasts, the authors show that depletion of β-arrestin 1 or 2 prevents the movement of Smo to cilia as well as subsequent target gene transcription. The authors propose that Smo trafficking to cilia is mediated by Shh-enhanced association of the Smo–β-arrestin complex with the type II kinesin motor Kif3A. The finding that β-arrestin is required for both endocytosis and ciliary targeting of Smo seems contradictory; however, vesicles that carry Smo to the cilia may originate from the plasma membrane as recycling endosomes rather than directly from an intracellular source (the Golgi).

Kif3A, a component of the kinesin II motor complex, transports protein cargos within cilia. Materials are conveyed along microtubules at the core of the cilium by an elaborate intraflagellar transport system (*1*). This system is composed of a Kif3A-driven motor complex that moves toward the tip of the cilium and a second complex driven by the motor protein dynein that moves back toward the base. The link between cilia and Hh signaling emerged from the observation that mouse embryos lacking intraflagellar transport components, including Kif3A, have damaged Hh signaling (*5*).

Mice carrying mutations in the genes encoding Kif3A and other intraflagellar transport proteins suffer from developmental abnormalities caused by a lack of both Gli activator function (such as neural tube defects) and Gli repressor function (such as limb defects) (*6*). Does the discovery of a Smo–β-arrestin–Kif3A complex shed light on these complex phenotypes? The role of Kif3A in activating Gli proteins is consistent with its role in promoting Smo movement to cilia. However, Kif3A has a second role in Hh signaling that is probably independent of Smo. In the absence of Shh, Kif3A promotes conversion of Gli3 into a truncated repressor form, Gli3R (*6*). Thus, Kif3A represses target genes by promoting Gli3R formation in the absence of Shh, but promotes Gli activator formation by transporting Smo into cilia in the presence of Shh (see the figure). The switch between these two states may be triggered by the formation of the Smo–β-arrestin–Kif3A complex. This is reminiscent of the dual role played by the motor protein Costal2 in Hh signaling in the fly *Drosophila melanogaster* (*7*).

Several seven-transmembrane receptors, such as those for somatostatin and serotonin, are located in primary cilia, so an important question is whether these receptors also rely on a β-arrestin–Kif3A complex for their localization. In mammalian photoreceptor cells, Kif3A transports arrestin and the seven-transmembrane receptor opsin through a specialized variant of primary cilia (*14*). Because many seven-transmembrane receptors associate with β-arrestin, but only a small number localize in cilia, additional factors must control ciliary localization. The Bardet-Biedl syndrome protein complex controls trafficking of seven-transmembrane receptors to cilia (*15*, *16*). Unraveling how these and other mechanisms together regulate movement of transmembrane proteins to cilia will continue to shed light on Hh and other signaling pathways in primary cilia, illuminating new aspects of cell biology and potentially new paths to disease therapies.

References and Notes

1. J. L. Rosenbaum, G. B. Witman, *Nat. Rev. Mol. Cell Biol.* **3**, 813 (2002).
2. J. L. Badano *et al.*, *Annu. Rev. Genomics Hum. Genet.* **7**, 125 (2006).
3. J. J. Kovacs *et al.*, *Science* **320**, 1777 (2008); published online 22 May 2008 (10.1126/science.1157983).
4. K. C. Corbit *et al.*, *Nature* **437**, 1018 (2005).
5. D. Huangfu *et al.*, *Nature* **426**, 83 (2003).
6. D. Huangfu, K. V. Anderson, *Proc. Natl. Acad. Sci. U.S.A.* **102**, 11325 (2005).
7. L. Lum, P. A. Beachy, *Science* **304**, 1755 (2004).
8. R. Rohatgi *et al.*, *Science* **317**, 372 (2007).
9. C. J. Haycraft *et al.*, *PLoS Genet.* **1**, e53 (2005).
10. R. J. Lefkowitz, K. Rajagopal, E. J. Whalen, *Mol. Cell* **24**, 643 (2006).
11. A. M. Wilbanks *et al.*, *Science* **306**, 2264 (2004).
12. W. Chen *et al.*, *Science* **306**, 2257 (2004).
13. A. R. Meloni *et al.*, *Mol. Cell. Biol.* **26**, 7550 (2006)
14. J. R. Marszalek *et al.*, *Cell* **102**, 175 (2000).
15. N. F. Berbari, J. S. Lewis, G. A. Bishop, C. C. Askwith, K. Mykytyn, *Proc. Natl. Acad. Sci. U.S.A.* **105**, 4242 (2008).
16. M. V. Nachury *et al.*, *Cell* **129**, 1201 (2007).
17. M.P.S is an investigator of the Howard Hughes Medical Institute and R.R. is supported by the National Cancer Institute (grant 1K99CA129174).

10.1126/science.1160448

ATMOSPHERIC SCIENCE

Himalaya—Carbon Sink or Source?

Jerome Gaillardet[1] and Albert Galy[2]

Chemical analysis of hot springs in the Himalaya suggest that the carbon released from mountain forming regions may warm Earth.

In 1845, the French mining engineer Joseph Ebelmen described how atmospheric CO_2 reacts with rock minerals to form dissolved salts and bicarbonate. He envisioned the possibility of a global carbon cycle, in which the CO_2 injected into the atmosphere by volcanoes is first transformed into soluble bicarbonate and then participates in the precipitation of carbonates in the ocean.

Today, the global carbon cycle and its influence on the long-term (million to billion years) evolution of climate are still a matter of research. The theory of plate tectonics gave a better framework for the concept of sediment recycling (*1*). The role of silicate weathering as a climate regulator has been strengthened by modeling of the carbon cycle (*2, 3*), a better understanding of the interrelationships with other biogeochemical cycles, and the accumulated data from the geological archive. In addition to this, previously unconsidered CO_2 inputs to the atmosphere by the Himalayan range have been recently discovered (*4, 5*).

The key idea of today's carbon cycle models is that Earth sequestrates CO_2 degassed from Earth's interior in limestone, thus preventing it from being released into the atmosphere and causing warming. The only valid sequestration mechanism at geological time scales is the weathering of Ca-Mg silicates and subsequent precipitation of carbonate in the ocean. Photosynthesis, weathering of carbonate rocks, and the burial of organic carbon into sediments are all sequestrating processes that are balanced by return fluxes (respiration, precipitation of carbonates in the ocean, and oxidation of inland organic matter). But these processes occur on a time scale shorter than millions of years. The most recent estimate of pre-anthropogenic CO_2 consumption flux by silicate weathering reaction is 0.07 PgC/year (*6*) (see the figure).

Numerous uncertainties in this geological carbon cycle still remain, the principal of those being the amount of carbon entering the atmosphere now and in the past. The degassing flux was estimated based on the flux emitted by volcanoes in different geodynamic contexts and

[1]Institut de Physique du Globe de Paris, University Paris-Diderot, CNRS, France. [2]University of Cambridge, UK and Institut de Physique du Globe de Paris, University Paris-Diderot, France. E-mail: gaillardet@ipgp.jussieu.fr

include carbon from the mantle (magmatic) and carbon degassed from rocks in subduction zones (metamorphic) (*7*). This flux does not take into account CO_2 derived from orogenic zones (regions of mountain building), where, because of continental collision, organic-rich sediment and limestone may be buried at depths at which CO_2 is formed by metamorphic reactions.

Release of metamorphic CO_2 in collision zones has already been suggested (*8*). Evans *et al*. (*4*) have recently attempted to estimate the flux of metamorphic CO_2 based on the chemistry of Himalayan hot springs. They exploit the fact that carbon isotopes are fractionated when dissolved carbon species are transformed into gaseous CO_2. A fluid containing dissolved carbon will preferentially lose the light isotope of carbon (^{12}C). The isotopic composition of the remaining carbon in the fluid can then be used to estimate the intensity of degassing.

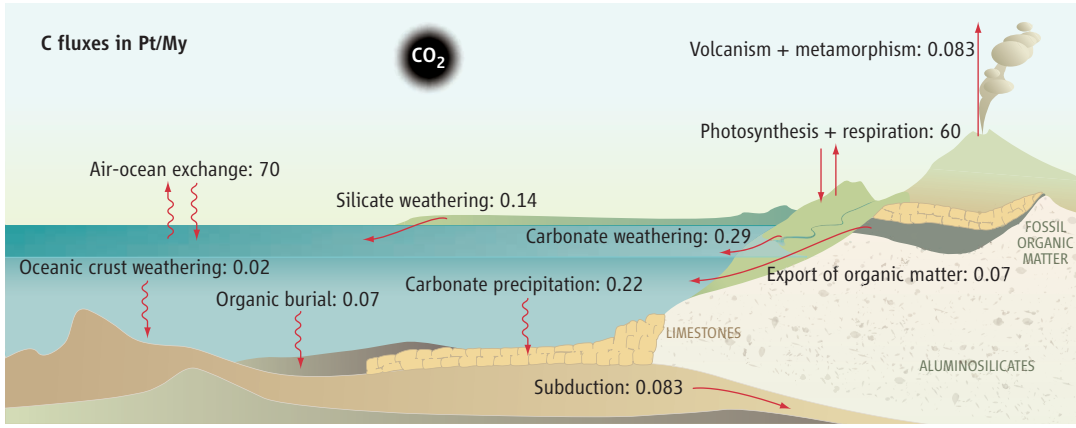

The geological carbon cycle. The natural regulation of atmospheric CO_2 implies different carbon reservoirs playing roles on different time scales. Ocean and biomass reservoirs play a role at time scales lower than a couple of thousand years. At longer (geological) time scales, carbonate weathering is balanced by carbonate precipitation in the ocean, but the volcanic input of CO_2 to the atmosphere is only compensated by the weathering of Ca-Mg silicate minerals in soils ($CaSiO_3 + CO_2 = CaCO_3 + SiO_2$). For each mol of C precipitated into carbonate, a mol of C is released to the atmosphere, and the net sequestration of atmospheric carbon is 0.07 PgC/year. The organic sequestration in the form of fossil organic matter buried in sediments is thought to be compensated by the oxidation of ancient organic matter on land (not shown). New findings (*4, 5*) in the Himalaya lead to a new flux of CO_2 degassing in mountain ranges and make mountains a locus of CO_2 production instead of CO_2 consumption. Fluxes in PgC/year or PtC/My.

The carbon isotopic composition measured in hot springs located near the main central deformation zone of the Himalayan range indicates that the flux of degassed CO_2 is considerable (up to 97% of the total initially dissolved carbon) (*4*). The authors concluded that the flux of metamorphic CO_2 injected into the atmosphere is four times the uptake by silicate weathering reactions in the Narayani Basin, a 32,000-km^2 catchment in Nepal. Extrapolated to the whole Himalayan Arc, the authors propose that metamorphic processes in the Himalaya add 0.02 PgC/year, a quarter of the global flux of CO_2 consumed by silicate weathering. Given the uncertainties in the silicate weathering flux, this result does not necessarily introduce a major imbalance in the global carbon cycle but shows that mountain belts may not be net sinks for atmospheric CO_2. The results corroborate the conclusion reached by another study based on the composition of carbon isotopes and also on the thermodynamic modeling of the dissolved elements in these hot springs (*5*). If these studies are correct, then mountain building would inject CO_2 into the atmosphere and would warm Earth.

These conclusions contradict the famous "Raymo" hypothesis (*9*) that mountains are regions of active physical erosion that sustain high chemical weathering rates because these conditions favor the contact of water and mineral surfaces, an idea that is confirmed by the analysis of river data (*6*). In that case, how could the observed temporal relationship between mountain building and global glaciation periods in the geological record (*10*) be explained?

There are, however, three assumptions to this scenario. First, Evans *et al.* extrapolate from a measurement of the short-term flux to the geological long-term flux for the whole mountain range. Due to changes over the thermal history, an orogenic zone could well be a source or a sink of CO_2. Second is that the organic subcycle of carbon in the Himalaya does not differ from the whole organic subcycle of carbon and is not a major flux of CO_2 consumption. This has been recently challenged by Galy *et al.* (*11*), who showed that the Himalaya scavenges a factor of 10 more CO_2 by organic burial than by chemical weathering. The third assumption questions the time scale at which a mountain range becomes carbon neutral. The CO_2 degassed by the Himalaya will ultimately react with silicate minerals and lead to the formation of carbonate. If these carbonates are incorporated into subduction or collision zones, heated and degassed, they will then liberate the sequestered carbon. On the time scale of this geological loop [typically 20 to 50 million years (My)], the net effect of metamorphic CO_2 on the global carbon cycle, at steady state, is null. If steady state is not achieved and a fraction of sedimentary carbon is re-injected into the mantle and degassed at mid-oceanic ridge or hot spots, mountain ranges only become carbon neutral on greater time scales of billions of years.

Mountain ranges have several impacts on the global carbon cycle and hence global climate. Whether they are net sources or sinks of atmospheric CO_2 can only be resolved by considering the importance of different processes at their relevant time scales: the consumption of CO_2 by rock weathering (silicate and carbonate), the balance between organic matter burial and oxidation of sedimentary organic matter, and the fluxes of CO_2 degassing. Reconstructing the evolution of Earth's atmospheric CO_2 over geological time will depend on how these mechanisms and their respective time scales interact. Clearly, scanning mountain ground for CO_2 degassing is rich in promise.

References

1. R. M. Garrels, F. T. Mackenzie, *Evolution of Sedimentary Rocks* (Norton, New York, 1971).
2. J. C. G. Walker, P. B. Hays, J. F. Kasting, *J. Geophys. Res.* **86**, 9776 (1981).
3. R. A. Berner, A. C. Lasaga, R. M. Garrels, *Am. J. Sci.* **283**, 641 (1983).
4. M. J. Evans, L. A. Derry, C. France-Lanord, *Geochem. Geophys. Geosystem.* **9**, Q04021 (2008); 10.1029/2007GC001796
5. J. A. Becker, M. J. Bickle, A. Galy, T. Holland, *Earth Planet. Sci. Lett.* **265**, 616 (2008).
6. J. Gaillardet, B. Dupré, P. Louvat, C. J. Allègre, *Chem. Geol.* **159**, 3 (1999).
7. R. A. Berner, *Am. J. Sci.* **291**, 339 (1991).
8. D. M. Kerrick, K. Caldeira, *Chem. Geol.* **108**, 201 (1993).
9. M. E. Raymo, W. F. Ruddiman, P. N. Froelich, *Geology* **16**, 649 (1988).
10. M. E. Raymo, *Geology* **19**, 344 (1991).
11. V. Galy *et al.*, *Nature* **450**, 407 (2007).

10.1126/science.1159279

MATERIALS SCIENCE

The Statistical Mechanics of Strain-Hardened Metals

The average distance that dislocations in crystals travel before freezing into place is a key quantity in describing how metals harden when strained.

Anter El-Azab

When metals are worked by stamping or forging, they become harder. This change in mechanical properties is caused by dislocations—linear defects in the otherwise ordered lattice of atoms in a crystal. A dislocation can be created by forcing two adjacent planes of atoms in a crystal to slip relative to each other over a finite area; the line that demarcates the slipped and unslipped regions is the dislocation line (see the figure, left panel). Dislocations move under the influence of mechanical stress, which causes permanent plastic deformation through a shearing process (see the figure, right panel). As the deformation proceeds, more and more dislocations accumulate, interact with each other, and impede each other's motion, causing the crystal to be less deformable. The crystal is then said to be strain- or work-hardened. On page 1745 of this issue, Devincre *et al.* (*1*) report on theoretical work that can help to better understand this hardening phenomenon.

Early attempts to explain strain hardening in metals in terms of dislocations and their interactions was mostly carried out by metallurgists. They framed the hardening phenomenon into a relation between the flow stress—the stress required to continue the deformation process—and the density of dislocations, which evolves due to deformation. A famous result in this regard is Taylor's hardening law, which states that the flow stress is proportional to the square root of the dislocation density (*2*). This law was successfully incorporated into the continuum theory of crystal plasticity, together with an evolution law of the dislocation density (*3*).

A commonly accepted evolution law for the dislocation density includes two density evolution mechanisms: dislocation storage and recovery (*4, 5*). Dislocation storage involves the immobilization of moving dislocations as a result of forming strong junctions with "forest dislocations" (which thread the slip planes of the mobile dislocations). Recovery occurs as a result of cross slip, a process that involves change of the slip plane of a moving dislocation.

The mechanism of dislocation storage depends on the dislocation mean free path (the distance a dislocation travels before being frozen by the microstructure). This quantity, which is statistical in nature, is central in the work of Devincre *et al.* (*1*). These authors modeled the dislocation mean free path, among other important parameters, using the method of dislocation dynamics simulation (*6*), and used this quantity to fix the dislocation density evolution law. They then used this law in conjunction with Taylor's law to predict strain hardening using the continuum theory of crystal plasticity.

The dislocation dynamics simulation method treats dislocations as a dynamical system and tracks their trajectory in the crystal by computer simulation. In this simulation, the evolution of the dislocation system is described by an equation of motion that connects the stress acting on dislocations to their velocity. Mutual dislocation interactions at long range, junction formation and destruction, and cross slip processes are also considered.

The approach used by Devincre *et al.* yields surprisingly accurate results for the hardening behavior of crystals, despite the phenomenological nature of two of the building blocks of the approach—Taylor's hardening law and the evolution law for the dislocation density. Indeed, in describing hardening, Taylor (*2*) dealt with a highly idealized dislocation configuration. The evolution law for the dislocation density, involving storage and recovery, was also derived based on an oversimplification of the underlying kinetic processes. Given that the work of Devincre *et al.* yields accurate results, one is tempted to believe that both Taylor's law and the evolution law for the dislocation density represent fundamentally correct laws of deformation, although they were not derived from first principles.

Another striking aspect of the authors' approach is that they use dislocation dynamics simulations (which treat dislocations as dynamical systems) to complement a purely static theory of strain hardening based on Taylor's law (which is derived for an array of dislocations in static equilibrium with the applied stress). At first glance, combining these two approaches might seem contradictory. However, the detailed microscale dynamics of dislocation slip, which are revealed by the simulation method, clearly show that, in practice, the dislocation mean free path sums up most of the dynamical aspects of the dislocation system and that the hardening process is dominated by the static

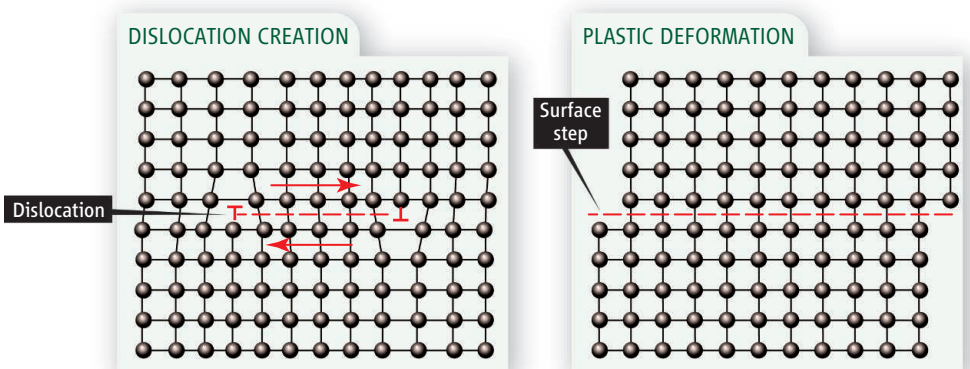

Illustration of dislocation creation and slip in crystals. (Left) The horizontal dashed line indicates an area over which the adjacent upper and lower atomic planes have been shifted relative to each other to create a dislocation at the periphery of this area. **(Right)** The dislocation motion to the surface results in the formation of surface steps and plastic deformation (shape change) of the crystal.

CREDIT: ADAPTED BY P. HUEY/*SCIENCE*

School of Computational Science and Materials Science and Engineering Program, College of Arts and Sciences, Florida State University, Tallahassee, FL 32306, USA. E-mail: anter@scs.fsu.edu

Published by AAAS

equilibrium of stored dislocations with the applied stress.

Devincre *et al*. thus show that strain hardening of crystals can be predicted without having to predict the evolution of the dislocation system. This is a remarkable result. Critical issues remain, but some of these might be resolved with extensions of their approach. For example, rate sensitivity—the fact that crystals harden faster at faster deformation rates—is better represented by Orowan's law, which connects the shear rate with the dislocation density and velocity (*6*), as opposed to using a phenomenological law for the shear rate in terms of the shear stress. Analysis of the dislocation dynamics simulation results should help in this regard. However, in this case, the statistics of the dislocation velocity—in addition to the dislocation storage statistics—will become important.

Rate sensitivity is also related to the temporal characteristics of crystal slip. At the microscale, crystal slip involves successive strain bursts, known as slip avalanches, which occur due to the sudden mobilization of stored dislocations as the stress increases. In addition to revealing the spatial scale of avalanches through the dislocation mean free path, the temporal properties of avalanches can also yield characteristic time scales. Two such scales would be the mean avalanche duration time and the mean time between avalanches, which, respectively, may be considered as counterparts of the collision times and mean time between collisions in the classical kinetic theory of particle systems (*7*).

Substantial differences exist between dislocations and particles. Nevertheless, modern attempts to model the dynamics and statistics of dislocation systems along the lines of the kinetic theory of particle systems are already in progress (*8*). In these attempts, the spatial, temporal, line-orientation, and velocity statistics of dislocations are key concepts, yielding much information about the characteristic spatial and temporal scales of crystal slip. It remains open whether these attempts will produce a hardening theory, but the work by Devincre *et al.* clearly shows that the dislocation dynamics simulation method will be important in making progress toward understanding strain hardening using these statistical mechanics approaches.

References and Notes

1. B. Devincre, T. Hoc, L. Kubin, *Science* **320**, 1745 (2008).
2. G. I. Taylor, *Proc. R. Soc. London A* **145**, 362 (1934).
3. P. Franciosi, M. Berveiller, A. Zaoui, *Acta Metall.* **28**, 273 (1980).
4. U. F. Kocks, H. Mecking, *Prog. Mater. Sci.* **48**, 171 (2003).
5. D. Kuhlmann-Wilsdorf, *Metall. Mater. Trans. A* **16**, 2091 (1985).
6. V. V. Bulatov, W. Cai, *Computer Simulations of Dislocations* (Oxford Univ. Press, Oxford, 2006).
7. L. Boltzmann, *Lectures on Gas Theory* (Univ. of California Press, Berkeley, 1964).
8. A. El-Azab, *Scripta Mater*. **54**, 723 (2006).
9. I acknowledge support from the Office of Basic Energy Sciences of the U.S. Department of Energy, through contract DE-FG02-08ER46494 at Florida State University.

10.1126/science.1160003

BIOCHEMISTRY

Electron Relay in Proteins

Electron transfer in proteins can be accelerated by electron relay along a chain of residues.

J. Martin Bollinger Jr.

The movement of electrons between cofactors in proteins is fundamental to photosynthesis, nitrogen fixation, aerobic respiration, and many other life processes. Researchers have long asked how the protein architecture separating two cofactors influences the rate of electron transfer between them (*1*). Most studies have addressed reactions that occur in a single tunneling step, with the protein matrix between electron donor and electron acceptor acting (almost) passively as a "tunneling bridge." On page 1760 of this issue, Shih *et al.* (*2*) report a model system for a different type of protein electron transfer reaction, in which amino acids of the protein act as semiconductor relay elements to facilitate the transfer. This electron relay occurs in several important proteins, and scientists hope to exploit it in the design of new energy-yielding devices.

Measured rates of single-step electron transfer reactions in natural and engineered proteins conform to the central prediction of Marcus theory that the rate is greatest when the driving force for the reaction ($-\Delta G°$) matches the reorganization energy (λ) associated with rearranging the protein and solvent atoms between their most stable configurations in the reactant and product states (*1*). For a given $-\Delta G°$ and λ, the rate falls off approximately exponentially with increasing distance between donor and acceptor (*1*, *3*), but a consensus on how the intervening protein structure between the donor and acceptor affects the electron transfer rate was at first elusive (*3*).

The use of semisynthetic model proteins was instrumental in eventually forging a consensus on this issue (*1*). In this approach, a redox-active metal complex is chemically tethered at a strategic location on the protein's surface, where it is poised to undergo photochemically initiated electron transfer with a redox partner (such as copper in azurin). Such studies revealed rate variations as large as a factor of 1000 for driving force–optimized reactions at fixed donor-acceptor distances and, in other cases, identical rates at donor-acceptor distances differing by up to 5 Å, proving that the structure of the tunneling bridge does matter. The matrix-rate effects were attributed to differences in the donor-acceptor electronic superexchange coupling mediated by a given bridge (*4*). Still, the effects are subtle enough to lead some to doubt whether optimization of the bridges for maximum efficiency could have been an important consideration in the evolution of electron transfer proteins (*3*).

At the high reduction potentials of the electron acceptors in some electron transfer proteins, at least two amino acids—tyrosine and tryptophan—can potentially participate more actively in electron transfer, becoming alternately oxidized and reduced as semiconductor relay elements. Matrix-rate effects can be even more pronounced in these reactions. The ultimate example is class I ribonucleotide reductase (RNR) (*5*), in which a cysteine residue in the α_2 subunit donates an electron to a tyrosyl radical in the β_2 subunit to initiate turnover (see the figure). Donor and acceptor are thought to be separated by a cavernous ~3.5 nm (*6*), which—according to distance-rate relations for single-step tunneling (*1*)—should limit the electron transfer step to time scales of hours to years (*5*). Yet a single turnover happens in ~200 ms (*7*). Electron transfer must be at least this fast.

An electron relay mechanism has been proposed to explain this unexpectedly fast electron transfer step (*8*–*11*). In this mechanism, a chain of one tryptophan and three tyrosine residues shuttles the electron across

Department of Chemistry and Department of Biochemistry and Molecular Biology, Pennsylvania State University, University Park, PA 16802, USA. E-mail: jmb21@psu.edu

the 3.5-nm cavern by forming amino acid radical intermediates (see the figure). Stubbe and co-workers recently detected such radicals in α_2 and β_2 subunits in which any one of the three tyrosine residues was substituted by a more easily oxidized analog (such as aminotyrosine) (*12*, *13*). These and earlier results provide strong support for the proposed mechanism, and the distance-rate analysis implies that the relay mechanism is faster than the corresponding single-step tunneling reaction would be by at least a factor of 10^4 (and perhaps more than 10^9) (*5*). The entire relay chain is conserved across species, and, if just one element is replaced by a relay-incompetent surrogate, the enzyme becomes inactive (*8*–*11*).

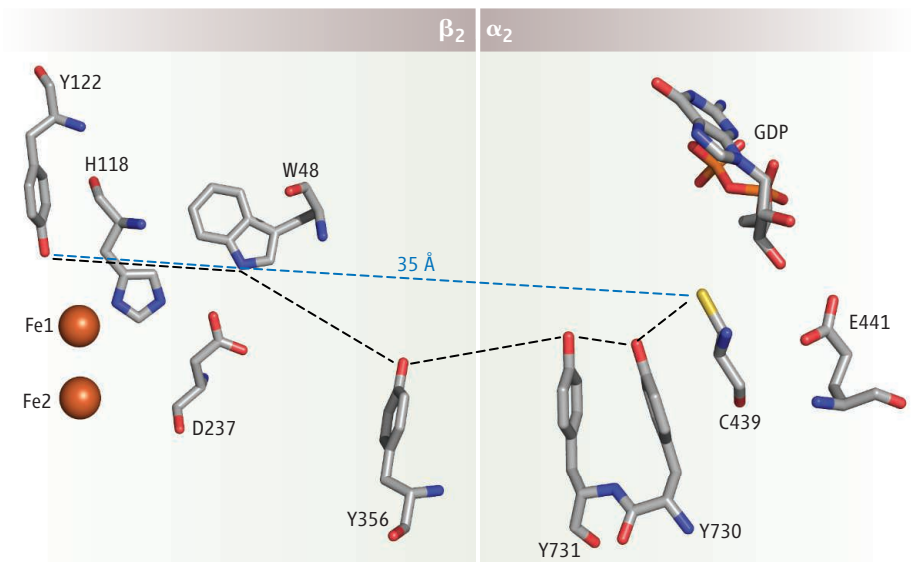

Long-distance transfer. The postulated electron relay chain in *Escherichia coli* RNR enables electron transfer over ~3.5 nm from Cys^{439} in α_2 to $Tyr^{122\bullet}$ in β_2 in less than 200 ms (*15*). Shih *et al.* have analyzed a similar relay process in a semisynthetic system that allows detailed analysis of the relay mechanism. GDP, guanosine diphosphate; amino acid abbreviations: C, Cys; D, Asp; E, Glu; H, His; W, Trp; Y, Tyr. [Figure adapted from (*15*)].

The ability of an electron relay chain to outperform a tunneling bridge has ample support from kinetic modeling and theoretical calculations (*1*, *14*). Yet rigorous experimental validation and a versatile model system have lagged behind. Shih *et al.* now report the development of just such a model system for electron relay.

The authors generated a potently oxidizing Re^{II}/ligand-radical charge-transfer state by irradiating a Re^{I} complex tethered to the surface of the copper protein azurin. They then examined the effect of introducing a relay residue (Trp^{122}) into the 1.9-nm space between the Re^{II} acceptor and the Cu^{I} donor. Without the relay residue, radiative decay of the excited state is much faster than electron transfer from Cu^{I} to Re^{II}, and the latter is not observed. With the relay residue, electron transfer is the faster process, presumably because of electron relay via a tryptophan cation radical. The tryptophan relay accelerates the electron transfer by a factor of ~300.

The results imply that electron relay can accelerate charge separation at minimal cost to the free energy of the migrating electron or hole. The system should allow for light-driven, 1.4-μs, 1.9-nm charge separation, even if the reduction potential of the donor site were raised high enough (for example, by adjusting the ligand sphere or replacing the metal ion) to support water oxidation. Charge recombination by single-step electron transfer is sufficiently slow at this distance to inspire hope that the donor site might be engineered to catalyze a redox reaction fast enough to compete with recombination. The resulting light-driven redox catalyst might serve as the basis for a practical, energy-yielding photochemical cell.

Shih *et al.*'s model system conforms to the rules given above for single-step tunneling reactions. The distance and driving force dependencies of the individual steps and the kinetic behavior of sequential reactions can fully explain the kinetic advantage of the two-step reaction. Is the factor of ~300 rate enhancement from the single relay element in the model system sufficient to explain the factor of 10^4 to 10^9 enhancement from the multiple elements in RNR? The answer is probably yes, but questions remain.

The most intriguing question is how proteins regulate electron relay. RNR must switch electron relay on and off for the tyrosyl radical in β_2 to remain stable in the resting enzyme but then be used to generate the cysteine radical in α_2 during catalysis. Is switching a function of the relay residues, the donor, the acceptor, or a combination of all three? How does the switch work?

At least part of the answer must lie in the linkage between protonation and oxidation states in the tryptophan and tyrosine residues. The ring oxygen of tyrosine and the nitrogen of tryptophan tend to lose their protons when the residues are oxidized to their radical forms. As a result, proton-coupled electron transfer reactions can be more favorable than pure electron-transfer reactions when these residues are involved. For tyrosine, the tendency to lose its proton is almost absolute. This characteristic may allow a tyrosine relay or acceptor to be switched on and off by protein environments or conformation changes that favor or disfavor proton transfer. This is precisely the explanation given by Shih *et al.* for the relay incompetence of tyrosine in their model system (*2*) and (in part) by Stubbe *et al.* for gating of electron relay in RNR (*5*).

In contrast to tyrosine, tryptophan can function as a relay at biologically relevant potentials even in protein environments that disfavor proton transfer. The two residues in combination thus provide a versatile toolkit for construction of gated electron relay systems, such as that in class I RNR. As the earlier work on single-step electron tunneling reactions so clearly showed, model systems like the one reported by Shih *et al.* should be invaluable in understanding these more complex electron relay proteins and reactions.

References

1. H. B. Gray, J. R. Winkler, *Q. Rev. Biophys.* **36**, 341 (2003).
2. C. Shih *et al.*, *Science* **320**, 1760 (2008).
3. C. C. Page, C. C. Moser, X. Chen, P. L. Dutton, *Nature* **402**, 47 (1999).
4. D. N. Beratan, J. N. Betts, J. N. Onuchic, *Science* **252**, 1285 (1991).
5. J. Stubbe, D. G. Nocera, C. S. Lee, M. C. Chang, *Chem. Rev.* **103**, 2167 (2003).
6. U. Uhlin, H. Eklund, *Nature* **370**, 533 (1994).
7. J. Ge, G. X. Yu, M. A. Ator, J. Stubbe, *Biochemistry* **42**, 10071 (2003).
8. M. Ekberg, M. Sahlin, M. Eriksson, B. M. Sjöberg, *J. Biol. Chem.* **271**, 20655 (1996).
9. S. S. Mao, G. X. Yu, D. Chalfoun, J. Stubbe, *Biochemistry* **31**, 9752 (1992).
10. U. Rova, A. Adrait, S. Pötsch, A. Gräslund, L. Thelander, *J. Biol. Chem.* **274**, 23746 (1999).
11. U. Rova *et al.*, *Biochemistry* **34**, 4267 (1995).
12. M. R. Seyedsayamdost, J. Stubbe, *J. Am. Chem. Soc.* **129**, 2226 (2007).
13. M. R. Seyedsayamdost, J. Xie, C. T. Chan, P. G. Schultz, J. Stubbe, *J. Am. Chem. Soc.* **129**, 15060 (2007).
14. H. B. Gray, J. R. Winkler, *Proc. Natl. Acad. Sci. U.S.A.* **102**, 3534 (2005).
15. M. R. Seyedsayamdost *et al.*, *J. Am. Chem. Soc.* **128**, 1562 (2006).

10.1126/science.1160001

SCIENCE & HUMAN RIGHTS

Summit Promotes Wireless Technology as Human Rights Tool

For citizens of the developed world, wireless communications are a way to log on to the Internet from a favorite coffee shop, schedule a meeting via Blackberry, or check sports scores on a cell phone. But for the developing world, experts said at a recent AAAS forum, wireless technology offers a chance to address more weighty concerns, such as the promotion of free expression and democracy.



Amir Dossal, Agnès Callamard

More than just a luxury, access to digital technology is an important tool for helping those in the developing world to "live better, learn better," said Amir Dossal, executive director of the United Nations Office for Partnerships.

Dossal was among 175 experts from 20 nations who gathered at the International Summit for Community Wireless Networks, hosted by AAAS from 28 to 30 May. As the community activists, academic specialists, and technology innovators discussed the challenges of building a wireless world, a theme emerged: The universal human right to free expression can be enhanced and protected through broader use of wireless technology both in the United States and abroad.

Dossal noted that access to cell phones is becoming widespread and has been a factor in helping to locate people in the aftermath of the devastating earthquake in China. Wireless technology also has helped refugees connect and find lost family members in other areas of crisis. But Dossal said there is much more to be done.

"At the United Nations, we've realized that if we are to make any difference to the people of the developing world, we must take a quantum leap," he said. One leap, he said, is to broaden the use of wireless technology as a means to provide unfettered communication in societies. Dossal cited efforts by groups such as the U.N. Global Alliance for Information and Communications Technology and Development and the nonprofit One Laptop Per Child initiative.

Providing wireless access can be a formidable task in states where repressive regimes restrict access to technology and distrust open communication, Dossal said. But Agnès Callamard, executive director of Article XIX, a London-based international human rights organization specializing in freedom of expression, said there are clear international obligations for states to respect the rights of their citizens to communicate freely via any medium.

Callamard said her group has been working on issues surrounding the allocation of the electromagnetic spectrum, which includes the frequencies for wireless communication. "We are quite worried about the very strong free-market approach" to allocation in many countries, she said, noting that the approach may limit access to a spectrum that she says should be viewed as a public good.

AAAS's Science and Human Rights Program (SHRP) has undertaken a Wireless Communication Technologies and Human Rights Project to promote the reach and impact of human rights groups working in poor, remote, or high-risk regions where access to the Internet by conventional means is too costly, too difficult, or too dangerous. "We want to support efforts to generate new and innovative ideas for connecting people to the Internet, as well as enhance the work of human rights organizations through wireless technologies," said Josh Robbins, the SHRP project manager who heads the initiative.

Jonathan Adelstein, a member of the U.S. Federal Communications Commission, said community wireless networks can spur economic development as well as provide digital inclusion. The free flow of information is the lifeblood of open societies, Adelstein said. "Availability of broadband really furthers human rights," he added. "This could become one of the greatest tools the world has ever seen in promoting democracy."

The summit was cosponsored by SHRP, the New America Foundation, the CUWiN Foundation, and the Acorn Active Media Foundation.

— Earl Lane

COMMUNICATION

Screeners Needed for AAAS Science Journalism Awards

Scientist volunteers are needed to review entries in the prestigious AAAS Science Journalism Awards program. Scientists residing in the Washington, D.C., area, or who will be in the area in mid-August to mid-September, are invited to help screen print, online, radio, and television reports for scientific accuracy. If interested, please contact Molly McElroy (202-326-6434; mmcelroy@aaas.org) in the AAAS Office of Public Programs.

Winners of the awards, which are sponsored by Johnson & Johnson Pharmaceutical Research & Development, L.L.C., will be honored at a ceremony in February 2009 at the AAAS Annual Meeting in Chicago. Members of the screening committees will be recognized in the awards booklet distributed during the ceremony.

EDUCATION

AAAS Trains Leaders in Local Science Education

After 3 years of intensive evening classes, weekend meetings, and never giving up a day job in the classroom, 48 Washington, D.C., teachers graduated this spring from a AAAS cosponsored program that provided new depth to their knowledge of science and math and prepared them to be educational leaders at their middle schools.

"I'm amazed by how much you can learn after you think you've already learned something," said Ronald Tate, a D.C. teacher at Lemon G. Hine Junior High School. Last month, Tate and his colleagues received master's degrees from the College of Professional Studies at George Washington University for their participation in the program.

"You're ready to go forward and accomplish something that is truly remarkable," Shirley Malcom, head of Education and Human Resources at AAAS, told the graduates, their families, and other supporters during a 17 May ceremony at AAAS. "With this, there truly is no child left behind."

The programs, DC ACTS (DC Advancing Competencies in Technology and Science) and DC FAME (DC Fellows for the Advancement of Mathematics Education) are filling a critical need, said Ali Eskandarian, senior associate dean at George Washington University's College of Professional Studies. "Science and math educa-

Published by AAAS

tion at the K–12 level is deficient nationwide, but the situation is particularly dire in D.C."

For DC ACTS graduate Gloria Allen, the program offered a way to obtain a solid science knowledge base. "Science is constantly changing and updating itself," said Allen, who teaches 5th-grade science at Plummer Elementary School in southeast D.C. "As science teachers, we need to be as timely as possible."

Today's science teachers, trained as generalists, have to rely on textbooks that aren't always accurate to get their science background, according to Allen. With the training provided by DC ACTS, Allen and her peers are better able to evaluate the material they see in books, she said.

DC ACTS focused on a different science subject—physical science, earth science, and life science—each year of the program. Middle-school science teachers are held accountable for teaching each of those subjects, yet many teachers don't have a formal education background in some of the topics.

By strengthening their understanding of the material, "they can move more easily between subjects that they're required to teach each year," said Joan Abdallah, AAAS director of DC ACTS.

With greater skills and confidence provided by the program, teachers are better equipped to review curricula, provide leadership throughout their school districts, and discuss the best ways to increase student achievement.

Like DC ACTS, the mathematics program DC FAME aims to deepen the knowledge of middle-school math teachers. But the DC FAME program was—and is—more about developing leadership skills in teachers. "It's a genuine leadership program," said Florence Fasanelli, director of DC FAME with AAAS Education and Human Resources. "And you can't be a leader unless you understand what you're teaching," she said.

The program required teachers to do extensive writing in term papers and personal journals, chronicling their attitudes about mathematics. In his final paper, DC FAME Fellow Sam Reheard described how learning a topic deeply leads to new discoveries. "There are limits to what my mind can discover and process in a day," wrote Reheard, a mathematics teacher for special education classes at the KIPP (Knowledge is Power Program) in D.C. "Reflection is an essential part of the learning process."

Before DC FAME, Reheard had taken formal math courses but had no classes on how to be a math teacher. "I felt something was missing," he said, voicing a common reason that participants enrolled in the program. "The more I know, the more confident I am."

A new cohort of DC FAME Fellows, funded by the State Education Agency for D.C. Public Schools, will begin a 3-year program on 30 June. DC ACTS, supported by the U.S. Department of Education, is pursuing new funds to welcome a second cohort in fall 2008.

— *Molly McElroy*

SCIENCE & SCHOOLS

Illinois Teacher Wins AAAS Education Prize

Diane Riendeau

School crafts carried home to proud parents might have been a distant memory to students at Deerfield High School—until they stepped into Diane Riendeau's classes. Now, the students are schooling their parents in the physics of stadium horns, marshmallow guns, and homemade hovercraft as part of the innovative teaching that made Riendeau the 2008 winner of AAAS's Leadership in Science Education Prize for High School Teachers.

Riendeau's "Make It, Take It, Teach It" program at the Deerfield, Illinois, school gives students a chance to observe basic physics concepts as they build a simple object like a kaleidoscope and use their creation to teach their parents about reflection, for example. The combination of hands-on learning and teaching by the students—along with positive feedback from their families—has raised physics comprehension and interest, according to data collected on the program.

Deerfield science department head Judi Luepke said the number of physics survey classes at the high school has doubled since Riendeau began teaching them, "as it has a reputation for being a fun and engaging class with reasonable expectations."

The annual prize of $1000, supported by AAAS member Dr. Edith Neimark, recognizes a high school teacher who has contributed significantly to the AAAS goal of advancing science education by developing an innovative and demonstrably effective classroom strategy, activity, or program. In this second year of the competition, the prize also includes a visit to the Shanghai International Forum on Science Literacy of Precollege Students.

"This year we are very pleased that Diane's accomplishments will also be recognized by educators abroad," said Jo Ellen Roseman, director of Project 2061, AAAS's science literacy initiative. "Improving science education is truly a global concern, and the generous invitation from our colleagues in Shanghai is testimony to that."

Riendeau devised her program with an eye to giving "the more creative students a way to excel in a science class" while luring others in with the science's practical side. Projects like the marshmallow guns—which teach students about velocity—can end up as elaborately decorated and "named" creations, she said.

"They also try to adjust the design a bit once they see my gun. I have the longest barrel because I want them to learn that the long barrel will produce a faster marshmallow. It's my secret weapon when we have our battle," Riendeau joked.

Last year, Deerfield launched an ambitious new program to bring more physics classes to freshmen, ensuring that all students will leave the high school with some physics experience. For Riendeau, a 20-year teaching veteran and active member of the American Association of Physics Teachers, it's a welcome change. "Years ago, physics was a course for the cream of the crop," she said. "Only the best of the best got to it. That was a tragedy."

For more information on the AAAS Leadership in Science Education Prize for High School Teachers, see www.aaas.org/go/scied_prize.

— *Becky Ham*

AAAS

New Dues Rates Approved for 2009

The AAAS Board of Directors has approved a dues increase for 2009. The Board authorizes increases to cover two kinds of expenses: unavoidable costs associated with running AAAS and publishing *Science*, and new expenses that add value to membership. Postage and paper increases and improving online resources are examples of the kinds of expenses the Board anticipated in setting the 2009 rates.

The new rates are effective for membership terms beginning after 31 December 2008. As listed below, they do not include postage or taxes for international members, which is additional.

• Regular professional members	$146
• Postdocs and K–12 teachers	$99
• Emeritus members who receive print *Science*	$115
• Students	$75
• Patrons	$310
• Institutional rate for print for high schools and public libraries	$360
• All other institutions receiving print	$835

For further information, including subscription rates for *Science* Online, librarians should contact AAAS or their subscription agents, or go to the *Science* Online Web site.

All members will be advised of the new dues rates on their renewal notices for 2009. Member dues and voluntary contributions form the critical financial base for a wide range of AAAS activities. For more information, contact the AAAS Membership Office at 202-326-6417, or www.aaas.org/membership/.

Quantum State Engineering and Precision Metrology Using State-Insensitive Light Traps

Jun Ye,[1]* H. J. Kimble,[2] Hidetoshi Katori[3]

Precision metrology and quantum measurement often demand that matter be prepared in well-defined quantum states for both internal and external degrees of freedom. Laser-cooled neutral atoms localized in a deeply confining optical potential satisfy this requirement. With an appropriate choice of wavelength and polarization for the optical trap, two electronic states of an atom can experience the same trapping potential, permitting coherent control of electronic transitions independent of the atomic center-of-mass motion. Here, we review a number of recent experiments that use this approach to investigate precision quantum metrology for optical atomic clocks and coherent control of optical interactions of single atoms and photons within the context of cavity quantum electrodynamics. We also provide a brief survey of promising prospects for future work.

Precision measurement and quantum information science (QIS) require coherent manipulations of electronic states for atoms and molecules with long decoherence times. However, photon recoils create an inevitable back-action on the atomic center-of-mass motion, hence limiting precision and control. In a deeply bound trap, atomic localization within a fraction of an optical wavelength (the Lamb-Dicke regime) greatly reduces motional effects. This capability is exemplified in the Lorentz force-based trapped ion systems with minimal perturbations to internal electronic states. The separation of internal and external dynamics is critical for precision measurement, frequency metrology, and coherent manipulations of quantum systems (*1*).

For neutral atoms, external trapping potentials are created from spatially inhomogeneous energy shifts of the electronic states produced by an applied magnetic, electric, or optical field. In general, such energy shifts are electronic-state dependent, and hence, atomic motion leads to dephasing of the two states. A carefully designed optical trap that shifts the energies of the selected states equally provides a solution to this problem.

Light traps employ ac Stark shifts $U_i(\vec{r}) = -1/2\,\alpha_i(\lambda,\varepsilon)|E_L(\vec{r},\lambda,\varepsilon)|^2$ introduced by a spatially inhomogeneous light field $E_L(\vec{r},\lambda,\varepsilon)$, where λ is the wavelength and ε the polarization. Two atomic states generally have different polarizabilities α_i (i = 1, 2), resulting in different trapping potentials. A state-insensitive optical trap works at a specific wavelength λ_L and polarization ε_L, where $\alpha_1(\lambda_L,\varepsilon_L) = \alpha_2(\lambda_L,\varepsilon_L)$ and $U_1(\vec{r}) = U_2(\vec{r})$ (Fig. 1A). Consequently, the transition frequency ω_0 between the two light-shift–modified electronic states is nearly decoupled from the inhomogeneous $E_L(\vec{r},\lambda,\varepsilon)$, so long as higher order contributions $O(|E_L|^{n\geq 4})$ are negligible; that is, $\hbar\omega_0' = \hbar\omega_0 - 1/2\,[\alpha_2(\lambda,\varepsilon) - \alpha_1(\lambda,\varepsilon)]|E_L(\vec{r},\lambda,\varepsilon)|^2 + O(|E_L|^4) \approx \hbar\omega_0$, where $\hbar$ is Planck's constant h divided by 2π.

This scenario is possible as $\alpha_i(\lambda,\varepsilon)$ is set by multiple off-resonant atomic transitions. For alkaline earth atoms, the double valence electrons give rise to two distinct series of singlet and triplet states, and the long-lived triplet metastable states are ideal for precision spectroscopy (*2*). In Sr atoms (Fig. 1B), intercombination optical transitions from the ground state $5s^2\ {}^1S_0$ to the lowest ${}^3P_{0,1,2}$ metastable states offer narrow linewidths for clocks. The task then is to find a trapping wavelength for $U_{1_{S_0}}(\vec{r}) = U_{3_{P_{0,1,2}}}(\vec{r})$, with negligible scattering losses. For $\lambda > 461$ nm, $\alpha_{1_{S_0}}$ is always positive, leading to a trapping potential at intensity maximum. For ${}^3P_0$, the resonances at 2.7 and 0.68 μm make the polarizability vary from negative to largely positive as λ decreases (Fig. 1C), guaranteeing a match of $\alpha_{1_{S_0}}$ and $\alpha_{3_{P_0}}$ at a "magic" wavelength λ_L (solid line curves in Fig. 1D), with its value determined from many relevant electronic states with dipole couplings to ${}^1S_0$ and ${}^3P_0$. The shaded curves in Fig. 1D highlight the complexity due to light polarization and the vector nature of an electronic state with angular momentum $J \neq 0$ (e.g., ${}^3P_1$).

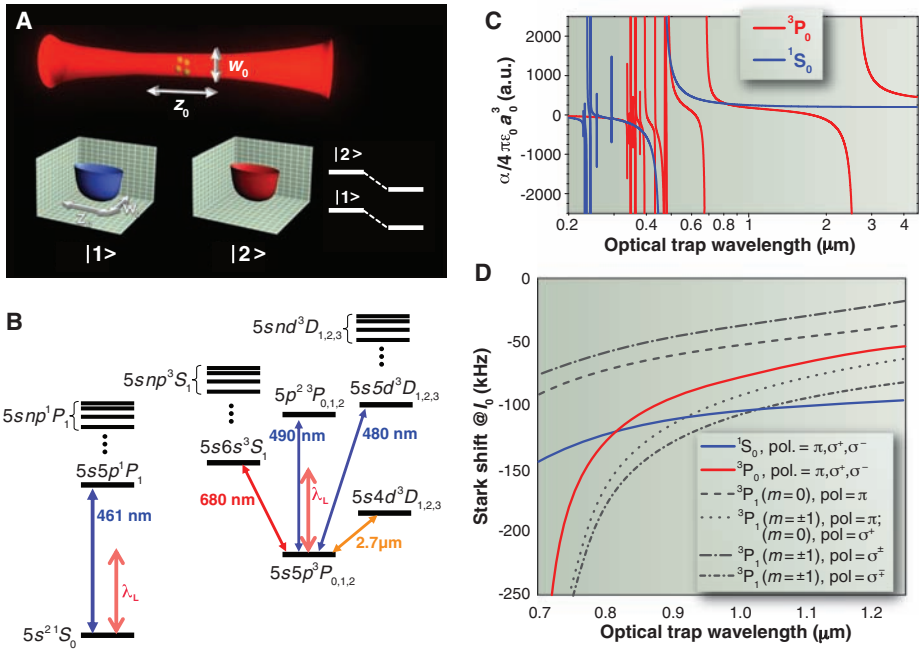

Fig. 1. (**A**) Atoms inside an optical field experience energy level shifts from the ac Stark effect. When the light field is spatially inhomogeneous (a focused beam with Rayleigh range z_0 and diameter w_0), a light trap is formed. When the polarizabilities of states |1> and |2> are matched by appropriate choices of the light wavelength and polarization, the optical trap becomes state-insensitive. (**B**) Level diagram for Sr atoms. The polarizability of the ground state is determined mainly from the strong ${}^1S_0$ to ${}^1P_1$ resonance. The metastable triplet states are coupled to the ${}^3S$, ${}^3D$, and $5p^2\ {}^3P$ states, with the dominant interactions given by the specific levels shown. (**C**) Wavelength dependence of the ${}^1S_0$ and ${}^3P_0$ polarizabilities, given in atomic units (a.u.) via scaling by a factor of $1/4\pi\varepsilon_0 a_0^3$, where a_0 is the Bohr radius. (**D**) Wavelength-dependent ac Stark shifts for the ${}^1S_0$, ${}^3P_0$, ${}^3P_1$ (magnetic sublevel m = 0), and ${}^3P_1$ (m = ±1) states, under various light polarizations (pol) and intensity $I_0 \sim 10$ kW/cm^2.

[1]JILA, National Institute of Standards and Technology (NIST) and University of Colorado, Boulder, CO 80309–0440, USA. [2]Norman Bridge Laboratory of Physics 12-33, California Institute of Technology, Pasadena, CA 91125, USA. [3]Department of Applied Physics, School of Engineering, University of Tokyo, Bunkyo-ku, Tokyo 113-8656, Japan.

*To whom correspondence should be addressed. E-mail: ye@jila.colorado.edu

Equalizing light shifts using two different-colored lasers was proposed (*3*), and laser cooling between states of similar polarizabilities in an optical trap was discussed (*4*). To minimize decoherence for quantum-state manipulations, an experimental scheme emerged for a single-wavelength, far-off-resonance dipole trap (FORT) with state insensitivity (*5*). A magic wavelength trap allows (i) two states with the same ac Stark shifts, (ii) atoms trapped in the Lamb-Dicke regime, and (iii) atomic center-of-mass motion independent of its internal state (*6*). The experimental realization (*7*) of this proposal (*8*) in strong-coupling cavity quantum electrodynamics (cQED) involving the Cs $6S_{1/2}$ to $6P_{3/2}$ optical transition led to an extended atomic trap lifetime and the demonstration of diverse phenomena for the interaction of single atoms and photons (*9*). Unlike alkali atoms, intercombination transitions in Sr have linewidths substantially narrower than typical Stark shifts, which critically modify transition dynamics. Efficient cooling on the narrow $^1S_0$ to $^3P_1$ line (*10*) in a state-insensitive optical trap was demonstrated (*11*). An optical lattice clock was proposed using the ultranarrow $^1S_0$ to $^3P_0$ optical transition in ^{87}Sr (*12*). The use of scalar electronic states ($J = 0$) allows for precise control of the Stark shifts solely by the light wavelength, a much better controlled quantity than light intensity or polarization. This is a clear advantage of a state-insensitive trap.

Thus, with independent control of atomic transition and center-of-mass motion, neutral atoms confined in state-insensitive optical traps emulate many parallel traps of single ions, creating greatly enhanced measurement capabilities and new tools for scientific investigations with quantum arrays of atoms and molecules. Two categories of work are progressing rapidly with exciting prospects: (i) precision spectroscopy and frequency metrology (*13*–*20*) and (ii) quantum-state engineering in the context of cQED (*9*).

Precision Frequency Metrology

Lasers with state-of-the-art frequency control now maintain phase coherence for 1 s (*21*), and the recent development of optical frequency combs has allowed this optical phase coherence to be faithfully transferred to other parts of optical or microwave domains (*5*). A new generation of atomic clocks based on optical frequencies, surpassing the performance of the primary Cs standard, has been developed (*20*, *22*). A key ingredient is the preservation of the coherence of light/matter interactions enabled by a clean separation between the internal and external degrees of freedom for trapped atoms.

For Sr, the presence of a strong spin-singlet ($^1S_0$ to $^1P_1$) transition and a weak spin-forbidden ($^1S_0$ to $^3P_1$) transition (Figs. 1B and 3A) allows efficient laser cooling in two consecutive stages, reaching high atomic densities and low temperatures limited by photon recoils (<1 μK) (*10*, *23*). Transitions between pure scalar states are strictly forbidden. In ^{87}Sr, nuclear spin $I = 9/2$ and the resulting hyperfine interaction weakly allows the spin- and dipole-forbidden $^1S_0(F = I) \rightarrow {}^3P_0(F = I)$ transition (F total angular momentum) with a natural linewidth of ~1 mHz, permitting a high quality factor for the optical resonance (*16*).

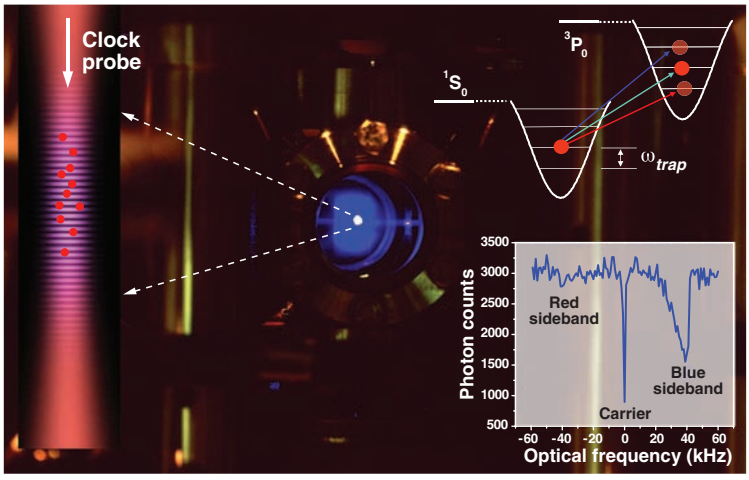

Fig. 2. ^{87}Sr lattice clock. Blue laser light ($^1S_0$ to $^1P_1$) is used to cool and trap Sr atoms at the center of the vacuum chamber. Atoms are further cooled with red light ($^1S_0$ to $^3P_1$) in the second stage. Atoms are then loaded into a state-insensitive, vertical 1D optical lattice made of near-infrared light. (Top Right) Schematic levels for lattice spectroscopy, where the two electronic states are convolved with the quantized motional states. (Bottom Right) Line shape of a saturated $^1S_0$ to $^3P_0$ electronic transition and the motional sidebands.

Precision atomic spectroscopy inside a magic-wavelength trap. With the laser-cooled atoms loaded into a one-dimensional (1D) optical standing wave (optical lattice) oriented vertically (Fig. 2), atomic spectroscopy of the $^1S_0$ to $^3P_0$ superposition probes the light-matter coherence at ~1 s. The probe is aligned precisely parallel to the lattice axis to avoid transverse excitations. The Doppler effect is quantized by the periodic atomic motion and is removed by means of resolved-sideband spectroscopy where the trap frequency far exceeds the narrow transition linewidth. When the probe laser is frequency-scanned, a carrier transition appears without a change of the motional state. Blue and red sidebands result from corresponding changes of the motional states by ±1 (Fig. 2). The absence of photon recoil and Doppler effects from the carrier transition sets the stage for high-precision spectroscopy inside the lattice.

Zooming into the carrier transition, 10 closely spaced resonances are observed with π excitation (Fig. 3B) under a small bias magnetic field, due to the slightly different Landé g-factors between $^1S_0$ and $^3P_0$. This differential g-factor, and consequently the hyperfine interaction-induced state mixing in $^3P_0$ and its lifetime, is directly determined from the frequency gap of the resolved transitions (*24*). This high-resolution optical spectroscopy measures precisely the nuclear spin effects without using large magnetic fields for traditional nuclear magnetic resonance experiments.

Spin polarization is implemented to consolidate the atomic population to $m_F = \pm 9/2$ sublevel. For one particular m_F, resonance profiles as narrow as 1.8 Hz (Fig. 3C) are observed, indicating coherent atom/light interactions approaching 1 s. The corresponding resonance quality factor is 2.4×10^{14}, the highest fractional resolution achieved for a coherent system (*16*). The achieved spectral resolution is limited by the probe laser, with a linewidth below 0.3 Hz at a few seconds and ~2 Hz on 1-min time scales (*21*).

Optical atomic clocks. The concept of a well-engineered trapping potential for accurate cancellation of the differential perturbation to the clock states has led to rapid progress in optical lattice clocks (*13*–*15*), now demonstrating the high resonance quality factor, high stability (*16*, *18*), and low systematic uncertainty (*20*). The high spectral resolution and high signal-to-noise ratio is a powerful combination for precision metrology. Understanding systematic uncertainties of the ^{87}Sr lattice clock sets the stage for the absolute frequency evaluation by the primary Cs standard via an optical frequency comb. At JILA, this measurement is facilitated by a phase-stabilized fiber link that transfers atomic clock signals between JILA and NIST (*25*), where a Cs fountain clock and hydrogen masers are operating (*26*). Data accumulated over a 24-hour run allow the determination of the ^{87}Sr $^1S_0$ to $^3P_0$ transition frequency at an uncertainty of 1×10^{-15}, set by the statistical noise in the frequency comparison (*18*). In Tokyo, the frequency link to Cs reference at the National Metrology Institute of Japan uses a common view Global Positioning System carrier phase technique (*17*). Figure 3D summarizes (*27*) Sr frequency measurements relative to Cs standards in laboratories of Boulder (*14*, *18*), Paris (*15*, *19*), and Tokyo (*17*). The magic wavelength for the ^{87}Sr $^1S_0$ to $^3P_0$ transition has been determined independently to be 813.4280(5) nm (*17*, *18*, *28*) and, as expected (*12*), sharing its value at 7 significant digits is sufficient to provide a 15-digit agreement of the clock frequency among the three continents, demonstrating the reproducibility of optical lattice clocks and the success of a new kind of atomic clocks with engineered perturbation.

Under the current operating conditions, the Sr lattice clock has a quantum-projection–noise-limited instability $<1 \times 10^{-15}$ at 1 s, which is

somewhat degraded by insufficient stability of the optical local oscillator. With this high measurement precision, rigorous evaluations of the overall uncertainty of an optical atomic clock now demand direct comparison against other stable optical clocks. Stable optical frequencies can be transferred over many kilometers by means of a phase-stabilized fiber link with a stability of $1 \times 10^{-17}/\sqrt{\tau}$ (where τ is averaging time) (*25*), permitting evaluation of systematic uncertainties of the JILA Sr clock by remote comparisons against a Ca optical clock at NIST. The overall systematic uncertainty of the Sr lattice clock is currently evaluated near 1×10^{-16} (*20*). The low measurement uncertainty achieved in large ensembles of atoms is a powerful testimony to the importance of state-insensitive traps.

cQED

An important advance in modern optical physics has been the attainment of strong coupling for the interaction of single atoms and photons. The principal setting for this research has been cQED, in which an atom interacts with the electromagnetic field of a high-Q resonator to investigate fundamental radiative processes associated with the strong interaction of one atom and the electromagnetic field (*5*), with applications in quantum optics and QIS (*29*).

Various approaches to trap and localize atoms within high-finesse optical cavities have been developed over the past decade, with the goal of achieving well-defined coupling g_0 between atom and cavity field, where $2g_0$ is the Rabi frequency for a single photon. Beyond atomic confinement per se, it is also important that the mechanism for trapping should not interfere with the desired cQED interactions for the relevant atomic transitions (for instance, $|b\rangle \leftrightarrow |e\rangle$ in Fig. 4A) [see section 3 in (*5*)].

The trapping scheme should also support confinement and long coherence times for auxiliary atomic states (e.g., $|a\rangle \leftrightarrow |b\rangle$ in Fig. 4A). For example, the initial proposal for the implementation of quantum networks (*30*) achieves a quantum interface between light and matter via cQED. "Stationary" qubits are stored in the states $|a\rangle$ and $|b\rangle$ and are locally manipulated at the nodes of the network. Coherent coupling g to the cavity field and thence to "flying" qubits between system A and system B is provided for one leg of the transition ($|e\rangle \leftrightarrow |b\rangle$), with an external control field $\Omega(t)$ exciting the second leg ($|e\rangle \leftrightarrow |a\rangle$) in a "STIRAP" (Stimulated Raman Adiabatic Passage) configuration. Often, $|a\rangle$ and $|b\rangle$ are hyperfine states (e.g., the "clock" transition $F = 3, m_F = 0 \leftrightarrow F = 4, m_F = 0$ in the $6S_{1/2}$ level in Cs), whereas $|e\rangle$ is an excited electronic state (for instance, in the $6P_{3/2}$ manifold in Cs).

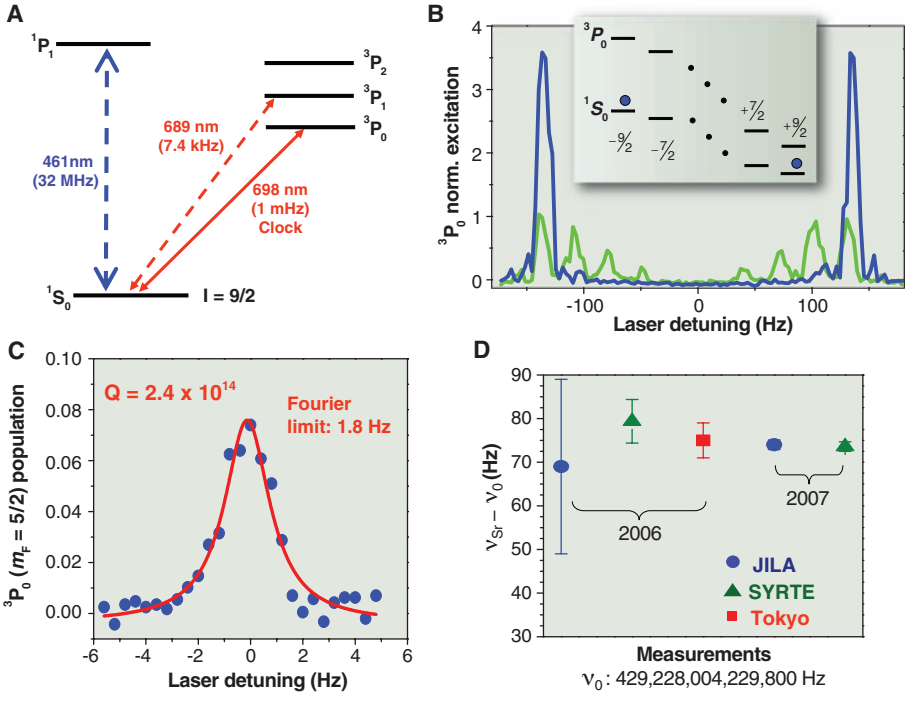

Fig. 3. (**A**) Simplified level diagram for ^{87}Sr lattice clock. Both cooling transitions are shown, along with the clock transition. (**B**) Clock transition under a bias magnetic field. Linear π transitions with and without spin polarization are displayed in blue and green, respectively. (Inset) Individual nuclear spin states. After spin polarization, the population resides in a single spin state. (**C**) High-resolution spectroscopy of the clock π transition for a single m_F state (where m_F indicates magnetic sublevel), showing the ultranarrow (quality factor $Q \sim 2.4 \times 10^{14}$) spectrum achieved with a 500-ms Rabi pulse. (**D**) Recent absolute frequency measurements of the ^{87}Sr clock transition, with respect to Cs standards, in laboratories of JILA (blue circles), Paris (green triangles), and Tokyo (red squares). Error bars indicate ±1 SD in systematic uncertainties. The frequency is reported relative to an offset frequency ν_0 = 429,228,004,229,800 Hz.

cQED and the magic wavelength. In contrast to precision metrology, where the goal is to isolate a particular atomic transition from external perturbations, strong coupling in cQED explicitly introduces large perturbations to the relevant atomic and cavity states. Indeed, for n quanta, the composite eigenstates for a two-state atom coupled to the cavity field experience frequency shifts $\sim \pm\sqrt{n}g(\vec{r})$, as illustrated in Fig. 4B for the n = 1,2 manifolds. Moreover, in addition to strong coupling for the internal degrees of freedom of the atomic dipole and cavity field [i.e., $g(\vec{r}) >> (\gamma, \kappa)$, with (γ, κ) the decay rates for atom and cavity], single quanta can also profoundly influence the external, center-of-mass degree of freedom, $g(\vec{r}) >> E_k/\hbar$, with E_k the atomic kinetic energy. Finally, it is possible to interrogate the atom-cavity system at rates exceeding $\gamma \sim 10^8\ s^{-1}$ for an allowed dipole transition, with potentially large heating. This situation differs markedly from the more leisurely inquires employed for frequency metrology with a forbidden transition, for which $\gamma \sim 1\ s^{-1}$.

In general, the atom-cavity coupling $g(\vec{r})$ and the ac-Stark shifts $U_e(\vec{r})$ and $U_g(\vec{r})$ for excited and ground states (e, g) have quite different form and magnitude, resulting in a complex spatial structure for the transition frequencies of the atom-cavity system, as discussed in more detail in section 2 in (*5*). In contrast, in a FORT at λ_L, $U_e(\vec{r}) \cong U_g(\vec{r}) < 0$, so that the dressed states of the atom-cavity system revert to their basic form $\pm\sqrt{n}g(\vec{r})$ with dependence only on $g(\vec{r})$. From a pragmatic perspective, a great benefit of a FORT operating at λ_L is that the powerful techniques for laser cooling and trapping of neutral atoms in free space can be taken over en masse to the setting of cQED.

Strong coupling for one atom in a state-insensitive trap. The initial realization of trapping of a single atom inside a high-Q cavity in a regime of strong coupling employed a conventional FORT (i.e., $U_g(\vec{r}) \approx -U_e(\vec{r}) < 0$) with a trap lifetime $\tau \approx$ 30 ms (*6*). State-insensitive trapping was achieved later for single Cs atoms stored in a FORT operated at the magic wavelength λ_L = 935.6 nm (*7*). The observed lifetime of $\tau \approx 3$ s represented an advance of 10^2 to 10^4 for trapping in cQED (*6*, *31*). Moreover, Sisyphus cooling (*32*) for a strongly coupled atom was made possible by $U_e(\vec{r}) \approx U_g(\vec{r})$. Independent investigations of trapping Cs in a free-space FORT around the magic wavelength were reported (*33*).

The combination of strong coupling and trapping at the magic wavelength enabled rapid advances in cQED (*9*). Included are the realization of a one-atom laser in the regime of strong coupling, the efficient generation of single photons "on demand," the continuous observation of strongly coupled and trapped atoms (*7*, *34*), and the observation of the vacuum-Rabi splitting $\pm g_0$ (*35*). The experiment in (*35*) (Fig. 4C) is important in that technical capabilities built around a magic wavelength FORT allowed for a rudimentary quantum protocol with "one-and-the-same" atom, as shown in Fig. 4D. In contrast, all earlier experiments

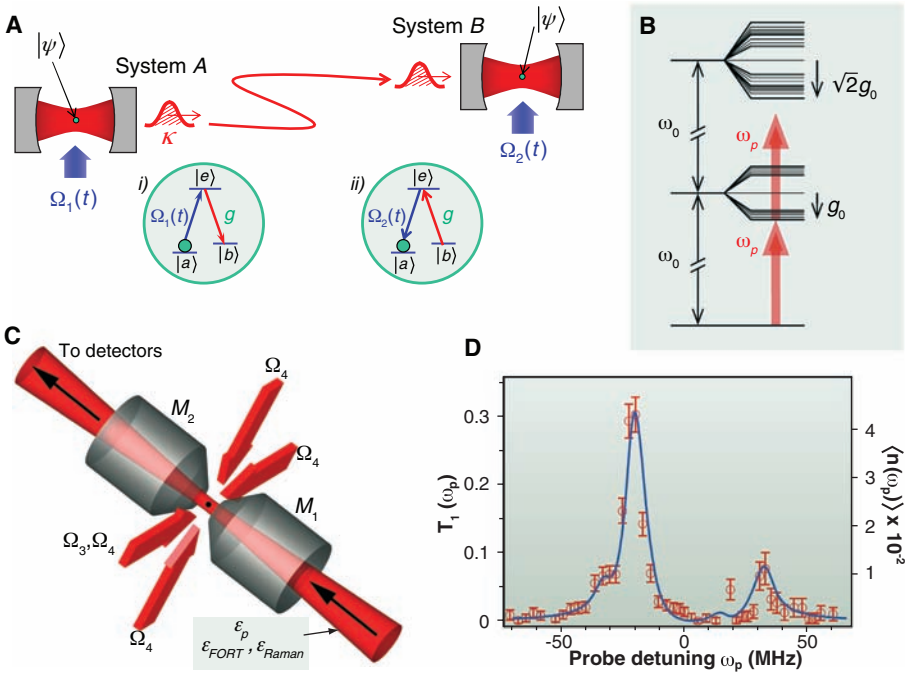

Fig. 4. (**A**) Illustration of the protocol of (*30*) for the distribution of quantum states from system *A* to system *B* by way of atom/photon interactions in cQED. As shown in inset (*i*), at system *A*, the external control field $\Omega_1(t)$ initiates the coherent mapping of the atomic state $|\psi\rangle = c_a|a\rangle + c_b|b\rangle$ to the intracavity field by way of the coupling *g* and thence to a propagating pulse via the cavity output mirror with coupling κ. $|a\rangle$ and $|b\rangle$ indicate two long-lived atomic ground states. At the second cavity *B*, the control field $\Omega_2(t)$ implements the reverse transformation as in inset (*ii*), with the incoming pulse from *A* coherently transformed back to $|\psi\rangle$ for the atom at *B*. By expanding to a larger set of cavities connected by fiber optics, complex quantum networks can be realized. (**B**) Level diagram for the atom-cavity system showing the lowest energy manifolds with $n = 0, 1, 2$ for an atom of transition frequency ω_A coupled to a cavity with resonance frequency ω_C, with $\omega_A = \omega_C \equiv \omega_0$. Displayed is the eigenvalue structure for the $(6S_{1/2}, F = 4, m_F) \leftrightarrow (6P_{3/2}, F' = 5, m_F')$ transition in Cs [corresponding to $|b\rangle \leftrightarrow |e\rangle$ in (A)] for coupling with rate g_0 to two degenerate cavity modes with orthogonal polarizations. The basis for photon blockade for an incident probe field of frequency ω_p is the suppression of two-photon absorption for the particular detuning ω_p shown by the arrows. Single photons are transmitted for the transition from the ground to the lowest excited manifold (i.e., $n = 0$ to $n = 1$), but photon pairs are "blocked" because of the off-resonant character of the second step up the ladder (i.e., $n = 1$ to $n = 2$) (*38*). (**C**) Experimental arrangement for trapping one atom with an intracavity FORT operated at the magic wavelength $\lambda_L = 936$ nm for one mode of the cavity and driven by ε_{FORT} (*32*). Cooling of the radial atomic motion is accomplished with the transverse fields Ω_4, whereas axial cooling results from Raman transitions driven by the fields ε_{FORT}, ε_{Raman}. The cavity length $l = 42$ μm, and the waist $w_0 = 24$ μm. cQED interactions take place near a second cavity mode at $\lambda_0 = 852$ nm. (**D**) Transmission spectrum $T_1(\omega_p)$ and intracavity photon number $\langle n(\omega_p)\rangle$ versus frequency ω_p of the probe beam ε_p for an individual strongly coupled atom, as in (C) (*35*). $T_1(\omega_p)$ is acquired for one-and-the-same atom, with the two peaks of the vacuum-Rabi spectrum at $\omega_p/2\pi = -20, +32$ MHz in correspondence to the splitting for the lower ($n = 1$) manifold of states in (B). The asymmetry of the spectrum arises from tensor shifts of the m_F excited states in the FORT. The small auxiliary peaks are from the distribution of Clebsch-Gordon coefficients for the $(6S_{1/2}, F = 4, m_F) \leftrightarrow (6P_{3/2}, F' = 5, m_F')$ transitions. The full curve is from the steady-state solution to the master equation (*35*). Error bars represent ±1 SD from the finite number of recorded photo-counts.

related to strong coupling in cQED had required averaging over ~10^3 to 10^5 single-atom trials. Essential components of this work were the state-insensitive FORT and a new Raman scheme for cooling to the ground state of axial motion (*36*). The implementation of complex algorithms in QIS requires this capability for repeated manipulation and measurement of an individual quantum system [e.g., for the generation of single photons (*37*)].

The experimental arrangement depicted in Fig. 4C has also enabled strong photon/photon interactions, as manifest in the phenomenon of photon blockade (*38*). The underlying mechanism is the anharmonicity of the energy spectrum for the atom-cavity system illustrated in Fig. 4B, which arises only for strong coupling and closely mirrors the free-space structure in a FORT at the magic wavelength. Reversible mapping of a coherent state of light to and from the hyperfine states $|a\rangle$ and $|b\rangle$ of an atom trapped within the mode of a high-finesse optical cavity (Fig. 4A) has also been achieved (*39*), thereby demonstrating a fundamental primitive for the realization of cQED-based quantum networks (*29*, *30*).

Atomic localization in cQED. Trapping single atoms within high-*Q* cavities has led to diverse advances in optical physics, including new regimes for optical forces not found in free space (*40*–*44*). Initially, the principal mechanism for trapping was a red-detuned FORT operated relatively close to atomic resonance, for which $U_e(\vec{r}) \approx -U_b(\vec{r}) > 0$ [where $U_b(\vec{r})$ is the trapping potential for the atomic ground state *b* in Fig. 4A] with correspondingly limited trapping times ≤0.1 s (*6*, *43*–*45*). More recently, λ_F (the FORT wavelength) has been shifted beyond 1 μm, and much longer trap lifetimes ~10 s have been achieved (*37*, *46*), as well as the deterministic transport of single atoms into and out of the cavity (*47*).

Strong coupling with trapped ions is an exciting prospect as the trapping potential for the atomic motion is independent of internal states and trapping times are "indefinite." Although great strides have been made (*48*, *49*) and the boundary for strong coupling reached (*49*), an inherent conflict is between small mode volume and stable trapping.

Future Prospects

Precision quantum metrology. Alkaline earth atoms confined in state-insensitive lattice traps provide a fertile playground for quantum optics and precision measurement–based quantum metrology. Although challenging, the precision of atomic spectroscopy will probably reach the limit set by quantum projection noise. This is an important milestone for large ensembles of atoms and will enable atomic clocks to operate with unprecedented stability. With continued improvement of stable lasers, tomorrow's optical lattice clocks will exhibit instabilities below 10^{-16} at 1 s. Quantum nondemolition measurement for spin-squeezing in an optical lattice can prepare a collective macroscopic pseudo-spin to further enhance the clock stability and precision. High measurement precision will be critical for the evaluation of systematic uncertainties of these new clocks. For example, systematic uncertainties $<1 \times 10^{-17}$ would require evaluation times of only a few hundred seconds.

The idea of state-insensitive traps extends to zero nuclear-spin bosonic isotopes of Sr, Yb, or others by using external fields to induce forbidden transitions (*50*, *51*). Application of group IIb elements (Zn, Cd, and Hg) for optical lattice clocks will significantly reduce the sensitivity to the blackbody radiation–induced shift. Recently, magneto-optical trapping of Hg was reported (*52*). State-insensitive optical traps also benefit research on cold molecules, with important directions toward novel quantum dynamics, precision measurement, and ultracold chemistry. The scalar nature of molecular vibrational levels in the electronic ground state simplifies the search for a magic wavelength for matching polarizabilities between two specific vibrational levels, creating a high-accuracy optical molecular clock (*53*). This molecular system is attractive for searching possible time variations of fundamental constants, particularly the electron/proton mass ratio. Comparison among these different clocks will diversify and strengthen tests of the laws of nature.

The combination of quantum manipulation and precision metrology in an optical lattice allows for accurate assessment of the system's quantum coherence while maintaining precise control of interparticle interactions. Quantum statistics of nuclear spins can be used to turn electronic interactions on and off. Meanwhile, couplings between nuclear spins in the lattice can be enhanced via electronic dipolar interactions. These electronic interactions are accessed through narrow-linewidth optical Feshbach resonances (*54*) and may allow entangling nuclear spins. These tunable interactions are ideal for QIS, where qubits are strongly coupled to one another on demand but weakly coupled to the error-inducing environment. Furthermore, individual nuclear spins may be addressed and monitored with the use of high–spectral resolution optical probes under an inhomogeneous magnetic field. Non-uniform properties of an optical lattice can thus be probed and compensated with spatial addressing.

Applications of state-insensitive traps in QIS. Recently, quantum degenerate atomic gases have been trapped and strongly coupled to optical cavities (*55*–*57*), with a variety of atomic collective effects explored. Another area of considerable activity has been the interaction of light with atomic ensembles (that is, a large collection of identical atoms), with important achievements reported for both continuous quantum variables and discrete excitations (*58*). In these areas and others, state-insensitive optical traps can enable new scientific capabilities by minimizing the role of decoherence while at the same time allowing coherent optical interactions mediated by electronic excited states. Of particular interest are the implementation of quantum networks and the exploration of the quantum limits to measurement.

Quantum networks. Quantum state transfer (Fig. 4A) provides a basis for implementing complex quantum networks (*30*). However, experiments in cQED have relied on Fabry-Perot cavities formed by two spherical mirrors. There have been intense efforts to develop alternative microcavity systems (*59*–*62*) for scalable quantum networks and quantum information processing on atom chips (*61*). A candidate for trapping individual atoms near a monolithic microcavity is a FORT operated at two magic wavelengths—one red and the other blue, detuned from resonance (*63*).

With respect to atomic ensembles (*58*), there is clearly a need to extend coherence times for stored entanglement, where currently $\tau \sim 10^{-5}$ s for entanglement of single excitations between remotely located ensembles. A promising mechanism is confinement of atoms within a state-insensitive trap to realize a long-lived material system for the nodes of a quantum network (*64*). In this setting, dephasing because of position-dependent shifts in transition frequency within the trap is minimized.

Quantum measurement. We have previously discussed the prospects for surpassing the limit set by quantum projection noise for precision spectroscopy. In addition to this important possibility, there are other applications of state-insensitive traps to quantum measurement, particularly within the setting of cQED. For example, by separating the functions of trapping (via a state-insensitive FORT) and sensing (by way of a probe field in cQED), it should be possible to confront the quantum limits for real-time detection of atomic motion, including localization beyond the standard quantum limit. The broader context of such research is that of the dynamics of continuously monitored quantum systems, whereby the strong coupling of atom and cavity implies a back reaction of one subsystem on the other as a result of a measurement (*65*).

References and Notes

1. D. Leibfried, R. Blatt, C. Monroe, D. Wineland, *Rev. Mod. Phys.* **75**, 281 (2003).
2. J. L. Hall, M. Zhu, P. Buch, *J. Opt. Soc. Am. B* **6**, 2194 (1989).
3. J. P. Gordon, A. Ashkin, *Phys. Rev. A* **21**, 1606 (1980).
4. R. Taieb, R. Dum, J. I. Cirac, P. Marte, P. Zoller, *Phys. Rev. A* **49**, 4876 (1994).
5. Additional details are available as supporting material on *Science* Online.
6. J. Ye, D. W. Vernooy, H. J. Kimble, *Phys. Rev. Lett.* **83**, 4987 (1999).
7. J. McKeever *et al*., *Phys. Rev. Lett.* **90**, 133602 (2003).
8. H. J. Kimble *et al*., in *Proceedings of the XIV International Conference on Laser Spectroscopy*, vol. XIV, R. Blatt, J. Eschner, D. Leibfried, F. Schmidt-Kaler, Eds. (World Scientific, Innsbruck, Austria, 1999), pp. 80–89.
9. R. Miller *et al*., *J. Phys. B. At. Mol. Opt. Phys.* **38**, S551 (2005).
10. H. Katori, T. Ido, Y. Isoya, M. Kuwata-Gonokami, *Phys. Rev. Lett.* **82**, 1116 (1999).
11. H. Katori, T. Ido, M. Kuwata-Gonokami, *J. Phys. Soc. Jpn.* **68**, 2479 (1999).
12. H. Katori, M. Takamoto, V. G. Pal'chikov, V. D. Ovsiannikov, *Phys. Rev. Lett.* **91**, 173005 (2003).
13. M. Takamoto, F. L. Hong, R. Higashi, H. Katori, *Nature* **435**, 321 (2005).
14. A. D. Ludlow *et al*., *Phys. Rev. Lett.* **96**, 033003 (2006).
15. R. Le Targat *et al*., *Phys. Rev. Lett.* **97**, 130801 (2006).
16. M. M. Boyd *et al*., *Science* **314**, 1430 (2006).
17. M. Takamoto *et al*., *J. Phys. Soc. Jpn.* **75**, 104302 (2006).
18. M. M. Boyd *et al*., *Phys. Rev. Lett.* **98**, 083002 (2007).
19. X. Baillard *et al*., *Eur. Phys. J. D* **48**, 11 (2008).
20. A. D. Ludlow *et al*., *Science* **319**, 1805 (2008); published online 14 February 2008; 10.1126/science.1153341.
21. A. D. Ludlow *et al*., *Opt. Lett.* **32**, 641 (2007).
22. T. Rosenband *et al.*, *Science* **319**, 1808 (2008), published online 6 March 2008; 10.1126/science.1154622.
23. T. H. Loftus, T. Ido, A. D. Ludlow, M. M. Boyd, J. Ye, *Phys. Rev. Lett.* **93**, 073003 (2004).
24. M. M. Boyd *et al*., *Phys. Rev. A* **76**, 002510 (2007).
25. S. M. Foreman, K. W. Holman, D. D. Hudson, D. J. Jones, J. Ye, *Rev. Sci. Instrum.* **78**, 021101 (2007).
26. T. P. Heavner, S. R. Jefferts, E. A. Donley, J. H. Shirley, T. E. Parker, *Metrologia* **42**, 411 (2005).
27. S. Blatt *et al*., *Phys. Rev. Lett.* **100**, 140801 (2008).
28. A. Brusch, R. Le Targat, X. Baillard, M. Fouche, P. Lemonde, *Phys. Rev. Lett.* **96**, 103003 (2006).
29. P. Zoller *et al*., *Eur. Phys. J. D* **36**, 203 (2005).
30. J. I. Cirac, P. Zoller, H. J. Kimble, H. Mabuchi, *Phys. Rev. Lett.* **78**, 3221 (1997).
31. J. Ye *et al*., *IEEE Trans. Instrum. Meas.* **48**, 608 (1999).
32. D. Boiron *et al*., *Phys. Rev. A* **53**, R3734 (1996).
33. J. Y. Kim, J. S. Lee, J. H. Han, D. Cho, *J. Korean Phys. Soc.* **42**, 483 (2003).
34. J. McKeever, J. R. Buck, A. D. Boozer, H. J. Kimble, *Phys. Rev. Lett.* **93**, 143601 (2004).
35. A. Boca *et al*., *Phys. Rev. Lett.* **93**, 233603 (2004).
36. A. D. Boozer, A. Boca, R. Miller, T. E. Northup, H. J. Kimble, *Phys. Rev. Lett.* **97**, 083602 (2006).
37. M. Hijlkema *et al*., *Nat. Phys.* **3**, 253 (2007).
38. K. M. Birnbaum *et al*., *Nature* **436**, 87 (2005).
39. A. D. Boozer, A. Boca, R. Miller, T. E. Northup, H. J. Kimble, *Phys. Rev. Lett.* **98**, 193601 (2007).
40. V. Vuletic, S. Chu, *Phys. Rev. Lett.* **84**, 3787 (2000).
41. S. J. van Enk, J. McKeever, H. J. Kimble, J. Ye, *Phys. Rev. A* **64**, 013407 (2001).
42. P. Domokos, H. Ritsch, *J. Opt. Soc. Am. B* **20**, 1098 (2003).
43. P. Maunz *et al*., *Nature* **428**, 50 (2004).
44. S. Nussmann *et al*., *Nat. Phys.* **1**, 122 (2005).
45. J. A. Sauer, K. M. Fortier, M. S. Chang, C. D. Hamley, M. S. Chapman, *Phys. Rev. A* **69**, 051804 (2004).
46. K. M. Fortier, Y. Kim, M. J. Gibbons, P. Ahmadi, M. S. Chapman, *Phys. Rev. Lett.* **98**, 233601 (2007).
47. M. Khudaverdyan *et al.*, preprint available at http://arxiv.org/abs/0805.0765.
48. A. B. Mundt *et al*., *Phys. Rev. Lett.* **89**, 103001 (2002).
49. M. Keller, B. Lange, K. Hayasaka, W. Lange, H. Walther, *Nature* **431**, 1075 (2004).
50. R. Santra, E. Arimondo, T. Ido, C. H. Greene, J. Ye, *Phys. Rev. Lett.* **94**, 173002 (2005).
51. Z. W. Barber *et al*., *Phys. Rev. Lett.* **96**, 083002 (2006).
52. H. Hachisu *et al*., *Phys. Rev. Lett.* **100**, 053001 (2008).
53. T. Zelevinsky, S. Kotochigova, J. Ye, *Phys. Rev. Lett.* **100**, 043201 (2008).
54. T. Zelevinsky *et al*., *Phys. Rev. Lett.* **96**, 203201 (2006).
55. Y. Colombe *et al*., *Nature* **450**, 272 (2007).
56. F. Brennecke *et al*., *Nature* **450**, 268 (2007).
57. S. Gupta, K. L. Moore, K. W. Murch, D. M. Stamper-Kurn, *Phys. Rev. Lett.* **99**, 213601 (2007).
58. N. J. Cerf, G. Leuchs, E. S. Polzik, Eds., *Quantum Information with Continuous Variables* (World Scientific, Hackensack, NJ, 2007).
59. K. J. Vahala, *Nature* **424**, 839 (2003).
60. T. Aoki *et al*., *Nature* **443**, 671 (2006).
61. P. Treutlein *et al*., *Fortschr. Phys.-Prog. Phys.* **54**, 702 (2006).
62. M. Trupke *et al*., *Phys. Rev. Lett.* **99**, 063601 (2007).
63. D. W. Vernooy, H. J. Kimble, *Phys. Rev. A* **55**, 1239 (1997).
64. L. M. Duan, M. D. Lukin, J. I. Cirac, P. Zoller, *Nature* **414**, 413 (2001).
65. C. M. Caves, G. J. Milburn, *Phys. Rev. A* **36**, 5543 (1987).

66. We gratefully acknowledge C. J. Hood, K. Birnbaum, A. Boca, A. D. Boozer, J. Buck, J. McKeever, R. Miller, C. Nägerl, T. Northup, D. Stamper-Kurn, D. Vernooy, and D. Wilson of Caltech; S. Blatt, M. M. Boyd, G. K. Campbell, S. Foreman, C. Greene, J. L. Hall, T. Ido, T. Loftus, A. D. Ludlow, M. Martin, M. Miranda, J. Thomsen, and T. Zelevinsky of JILA; J. Bergquist, S. Diddams, T. Fortier, S. Jefferts, C. Oates, and T. Parker of the NIST Time and Frequency Division; and M. Takamoto of Tokyo and M. Imae and F.-L. Hong of NMIJ/AIST for their collaborations and discussions. The work at JILA is supported by NIST, NSF, Defense Advanced Research Projects Agency, and the Office of Naval Research. Work at Caltech is supported by NSF and Intelligence Advanced Research Projects Activity. Work at Tokyo is supported by Strategic Information and Communications R&D Promotion Programme and Core Research for Evolutional Science and Technology.

Supporting Online Material

www.sciencemag.org/cgi/content/full/320/5884/1734/DC1
SOM Text
References

10.1126/science.1148259

Serotonin Modulates Behavioral Reactions to Unfairness

Molly J. Crockett,[1,2]* Luke Clark,[1,2] Golnaz Tabibnia,[3] Matthew D. Lieberman,[3] Trevor W. Robbins[1,2]

One of the first social rules we learn as children is the golden one: Treat others as you wish to be treated. Unfortunately, our peers do not always deserve gold stars for their behavior, which tempts us to retaliate. Resisting aggressive impulses may be difficult, but successfully navigating social life sometimes requires self-regulation in the face of perceived injustice.

Serotonin (5-HT) has long been implicated in social behavior, including impulsive aggression, but its precise involvement in impulse control is controversial (*1*). Because social interactions can evoke strong emotions, it is plausible that 5-HT modulates impulsivity via emotion regulation mechanisms. Emotion regulation during social interactions has been studied with the ultimatum game (UG), in which one player (the proposer) proposes a way to split a sum of money with another player (the responder). If the responder accepts the offer, both players are paid accordingly. If the responder rejects the offer, neither player is paid. Responders tend to reject offers less than 20 to 30% of the total stake, despite the fact that such retaliation is costly (*2*), and rejection decisions are predicted by the intensity of the aversive response to the unfair offer (*3*, *4*).

We investigated the effects of manipulating 5-HT function on rejection behavior in the UG. We used a double-blind, placebo-controlled acute tryptophan depletion (ATD) procedure to temporarily lower 5-HT levels in 20 healthy volunteers (*5*). Once after ATD and once after placebo, participants played the role of responder during several one-shot UGs (Fig. 1A) (*5*). Offers fell into one of three fairness categories: 45% of stake (fair), 30% of stake (unfair), or 20% of stake (most unfair). We independently manipulated social reward (fairness) and basic monetary reward (offer size) by varying both the offer amount and the stake size across trials (Fig. 1B) (*5*).

Rejection rates (% of offers rejected) were calculated for each subject at each level of fairness during ATD and placebo treatments. Repeated-measures analysis of variance revealed a highly significant interaction between treatment and fairness ($F = 6.891$, $P = 0.003$). Compared with placebo, ATD significantly increased rejection rates, and this effect was restricted to unfair offers (Fig. 1C). In contrast, ATD did not interact significantly with offer size ($F = 1.164$, $P = 0.294$). Controlling for fairness, participants tended to reject low offers more frequently than high offers, regardless of treatment (*5*).

The increased rejection of unfair offers after ATD cannot easily be attributed to changes in mood, fairness judgment, or basic response inhibition. As found previously (*1*), there was no effect of ATD on self-reported mood (*5*). On each session, we asked participants to indicate the size of a fair offer for each stake, and ATD did not affect these judgments ($F = 0.648$, $P = 0.431$). Lastly, consistent with past research (*1*), we found no effect of ATD on go/no-go performance, a standard test of response inhibition (*5*) (SOM text).

These results show that manipulating 5-HT function can selectively alter reactions to unfairness in a laboratory model of self-regulation. Temporarily lowering 5-HT levels increased retaliation to perceived unfairness without affecting mood, fairness judgment, basic reward processing, or response inhibition. Our results illuminate the neural mechanisms underlying emotion regulation in the UG. Neuroimaging studies of the UG have implicated both dorsolateral prefrontal cortex (DLPFC) and ventral PFC (VPFC) in regulating reactions to unfair offers (*3*, *4*). Although disrupting DLPFC function with transcranial magnetic stimulation leads to decreased rejection of unfair offers (*6*), patients with VPFC damage reject a higher proportion of unfair offers than control participants do (*7*). The present effects of ATD mirror those of VPFC lesions and are consistent with other data (*8*) indicating a critical neuromodulatory role for 5-HT in this region.

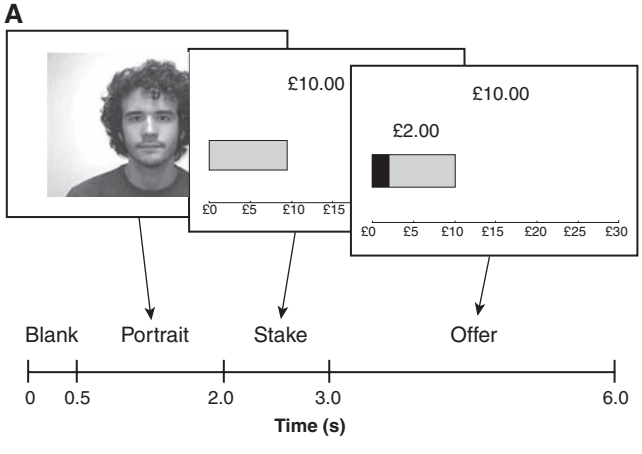

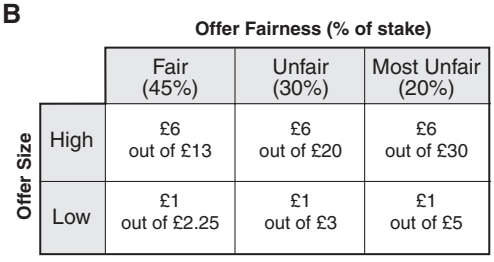

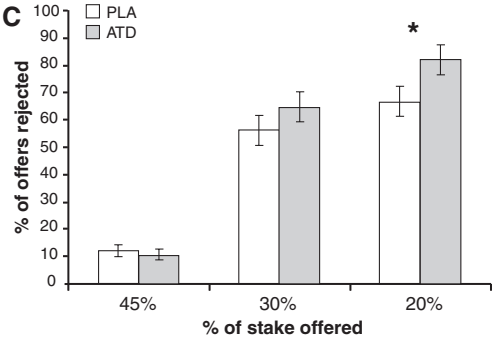

Fig. 1. (**A**) Diagram [adapted from (*4*)] illustrating the structure of each one-shot UG. While each offer was on the screen, participants pressed one button to accept or another button to reject. (**B**) Types of offers. (**C**) Rejection rates for fair, unfair, and most unfair offers after ATD and placebo (PLA) treatments. Error bars represent standard errors of the difference between means. *$P = 0.01$ difference between treatments.

References and Notes

1. E. A. T. Evers *et al.*, *Psychopharmacology (Berlin)* **187**, 200 (2006).
2. W. Guth, R. Schmittberger, B. Schwarze, *J. Econ. Behav. Organ.* **3**, 367 (1982).
3. A. G. Sanfey, J. K. Rilling, J. A. Aronson, L. E. Nystrom, J. D. Cohen, *Science* **300**, 1755 (2003).
4. G. Tabibnia, A. B. Satpute, M. D. Lieberman, *Psychol. Sci.* **19**, 339 (2008).
5. Materials and methods are available on *Science* Online.
6. D. Knoch, A. Pascual-Leone, K. Meyer, V. Treyer, E. Fehr, *Science* **314**, 829 (2006); published online 4 October 2006 (10.1126/science.1129156).
7. M. Koenigs, D. Tranel, *J. Neurosci.* **27**, 951 (2007).
8. H. F. Clarke *et al.*, *J. Neurosci.* **25**, 532 (2005).
9. This work was completed within the University of Cambridge Behavioral and Clinical Neuroscience Institute and funded by a joint award from the Medical Research Council and the Wellcome Trust.

Supporting Online Material

www.sciencemag.org/cgi/content/full/1155577/DC1
Materials and Methods
References

23 January 2008; accepted 25 April 2008
Published online 5 June 2008;
10.1126/science.1155577
Include this information when citing this paper.

[1]Department of Experimental Psychology, University of Cambridge, Cambridge CB2 3EB, UK. [2]Behavioural and Clinical Neuroscience Institute, University of Cambridge, Cambridge CB2 3EB, UK. [3]Department of Psychology, University of California Los Angeles, Los Angeles, CA 90095, USA.

*To whom correspondence should be addressed. E-mail: mc536@cam.ac.uk

Deep Drilling into the Chesapeake Bay Impact Structure

G. S. Gohn,[1]* C. Koeberl,[2] K. G. Miller,[3] W. U. Reimold,[4] J. V. Browning,[3] C. S. Cockell,[5] J. W. Horton Jr.,[1] T. Kenkmann,[4] A. A. Kulpecz,[3] D. S. Powars,[1] W. E. Sanford,[1] M. A. Voytek[1]

Samples from a 1.76-kilometer-deep corehole drilled near the center of the late Eocene Chesapeake Bay impact structure (Virginia, USA) reveal its geologic, hydrologic, and biologic history. We conducted stratigraphic and petrologic analyses of the cores to elucidate the timing and results of impact-melt creation and distribution, transient-cavity collapse, and ocean-water resurge. Comparison of post-impact sedimentary sequences inside and outside the structure indicates that compaction of the crater fill influenced long-term sedimentation patterns in the mid-Atlantic region. Salty connate water of the target remains in the crater fill today, where it poses a potential threat to the regional groundwater resource. Observed depth variations in microbial abundance indicate a complex history of impact-related thermal sterilization and habitat modification, and subsequent post-impact repopulation.

The Chesapeake Bay impact structure (CBIS) is among the largest and best preserved of the known terrestrial impact structures (*1*, *2*) and is the apparent source of the North American tektite strewn field (*3*, *4*). This late Eocene structure [~35.4 million years ago (Ma)] is buried beneath the southern part of Chesapeake Bay, its surrounding landmasses, and the adjacent part of the continental shelf by several hundred meters of post-impact sediments (Fig. 1). The intensely disrupted, 35- to 40-km-wide central crater (collapsed transient cavity) of the structure is surrounded by a less disrupted annular trough of ~25 km radial width, thereby forming a structure with a diameter of 85 to 90 km (*1*, *2*).

The CBIS event is particularly important for understanding wet-target impact processes. The target consisted of three layers of differing strength: (i) a continental-shelf water column, (ii) water-saturated Cretaceous and Tertiary sediments, and (iii) the upper few kilometers of continental crust, composed of pre-Mesozoic igneous and metamorphic silicate rocks. These target characteristics played important roles in producing the ultimate shape, size, and internal stratigraphy of the CBIS (*5*).

Three coreholes were drilled into the CBIS in 2005 and 2006 to a composite depth of 1.76 km at Eyreville Farm, in Northampton County, Virginia, USA (Figs. 1 and 2) (*6*). The drill site is located within the central crater, ~9 km from the structure's center. Here we describe the cores and discuss what they reveal about the geologic, hydrologic, and biologic consequences of a large terrestrial impact.

Crater-fill units. The cored section of crater-fill materials consists of five major units (Fig. 2). The lowest consists of 215 m of fractured mica schist intruded by pegmatite and coarse granite (1766 to 1551 m). These pre-Mesozoic target rocks record impact effects and a pre-impact tectonometamorphic history under retrograde amphibolite-to-greenschist facies conditions.

The schists are well foliated and consist of muscovite, biotite, quartz, and plagioclase with smaller amounts of graphite, fibrolitic sillimanite, pyrite, and (locally) garnet. Interlayers include minor muscovite-biotite-quartz-plagioclase gneiss, mylonitic schist and gneiss with secondary mineralization, sparse amphibolite and epidosite, and rare tourmalinite. The granite pegmatite grades texturally into the coarse-grained granite; both consist of microcline, plagioclase, and quartz, smaller amounts of muscovite, and sporadic occurrences of biotite and garnet. The pegmatite and granite are locally discordant to foliation in the schist, but in other places they are overprinted by mylonitic deformation.

Centimeter- to meter-thick dikes of impact-generated polymict lithic breccias and suevites are locally present. The dike rocks contain sparse shock-deformed clasts and, in the case of the suevites, impact-melt particles. These materials record a wide range of shock pressures, from <10 GPa (planar fractures only) to >45 GPa (impact melt). However, except near one breccia dike, convincing evidence of shock metamorphism is lacking in the schist, pegmatite, and granite.

Brittle cataclastic deformation is unevenly overprinted on these rocks. This cataclasis could be related, at least in part, to the impact event, as indicated by fractures associated with the impact-breccia dikes. Some narrow veins that are now completely altered to secondary mineral assemblages (but may represent original melt veins) also are offset by microfault networks, indicating that fault displacements continued after emplacement of these veins.

Above the lowest unit, 154 m of suevitic (melt-bearing) and lithic impact breccias are present (1551 to 1397 m). The lower half of this section is melt-poor and contains boulders of cataclastic rock. Suevites with an average 20 to 30% by volume of melt particles are present in the upper half. They contain mineral and lithic clasts that exhibit all stages of shock metamorphism. Clast-rich impact-melt rocks (clasts in melt matrix) are locally present. The upper few meters of this unit contain impact-melt fragments with distinct shard shapes.

Numerous mineralogic features record the wide range of shock deformation in this unit. Quartz grains show a variety of shock effects, including one and (rarely) two sets of planar fractures (PFs), planar deformation features (PDFs, one or two sets, some decorated with fluid inclusions), and a common "toasted" (brown-stained) appearance. Ballen quartz (crackled devitrification texture) occurs in some melt-rich samples (*7*). Rare feldspar grains with PDFs and mica with kink banding also are present. On average, ~15% of all quartz grains are shocked (PFs and/or PDFs). The amount of melt clasts in individual suevite samples varies widely, from 1 to 77% by volume.

A 26-m-thick unit of gravelly quartz sand and large rock clasts is present at 1397 to 1371 m, just above the suevitic rocks. The base of this sand marks a transition from nearly in-place materials to overlying transported materials (Fig. 2). The rock clasts include a 13-m amphibolite block near the center of the unit, as well as single cataclasite (3.0 m) and suevite (0.4 m) boulders near the base. Gravel-sized, altered melt clasts are present at the base of the sand. The basal boulders and melt clasts are interpreted to be rip-up material from the underlying unit.

A transported, 275-m-thick granitic megablock at 1371 to 1096 m overlies the sand unit (Fig. 2). Four varieties of granite are distinguished on the basis of composition and texture, including gneissic biotite granite, fine-grained biotite granite, medium- to coarse-grained biotite granite, and red altered granite (*7*). Mica foliation is variably developed, and the granites range from foliated to massive. Xenoliths of well-foliated biotite-amphibole gneiss are present but sparse. Two granite samples have been dated at ~615 Ma (Neoproterozoic) and ~254 Ma (Permian), respectively, by the sensitive high-resolution ion microprobe (SHRIMP) U-Pb zircon method (*7*), and granites of similar ages are present elsewhere in the target region (*8*). Fractures and veins in the granite are not unusually abundant, nor are they coated or filled with impact-generated material. Also, no convincing evidence for shock metamorphism was found in the granite.

The uppermost and thickest crater-filling unit (652 m) consists of brecciated target sediments and polymict, sediment-dominated breccias (Fig. 2). The lowest part of this unit (1096 to 867 m) consists of Cretaceous nonmarine sands and clays from the

[1]U.S. Geological Survey, Reston, VA 20192, USA. [2]Department of Lithospheric Research, Center for Earth Sciences, University of Vienna, Althanstrasse 14, Vienna A-1090, Austria. [3]Department of Geological Sciences, Rutgers University, 610 Taylor Road, Piscataway, NJ 08854, USA. [4]Museum of Natural History (Mineralogy), Humboldt-University Berlin, Invalidenstrasse 43, Berlin 10115, Germany. [5]Centre for Earth, Planetary, Space, and Astronomical Research, Open University, Milton Keynes MK7 6AA, UK.

*To whom correspondence should be addressed. E-mail: ggohn@usgs.gov

lower part of the target sediment layer that are present as clasts (pebbles to ~17 m) and as matrix between those clasts. Many of the clasts display well-preserved Cretaceous stratification. Common structureless sand layers (clasts?) and sparse sand dikes indicate local sand liquefaction and fluidization. The interval above (867 to 618 m) also consists primarily of clasts and matrix derived from the Cretaceous nonmarine target sediments. However, intercalated centimeter- to meter-thick zones of Cretaceous nonmarine-sediment clasts in an unstratified, unsorted, fossiliferous, muddy, quartz-glauconite sand and granule matrix are present at the bottom (867 to 861 m) and near the top of this interval. The highest interval (618 to 444 m) consists primarily of nonmarine-sediment clasts in glauconitic matrix, with the addition of sparse shocked rock and mineral clasts and melt particles. The presence of abundant glauconite grains in these intervals represents mixing of Cretaceous and Tertiary marine sediments from the upper part of the target sediment layer with Cretaceous nonmarine sediments from the lower part.

Impact processes. The crater-fill section recovered in the Eyreville cores provides a substantial basis for interpreting the characteristics and sequence of cratering processes (Fig. 3). The near-absence of shock metamorphism in the basal schist-pegmatite-granite unit is inconsistent with its position 9 km distant from the crater's center (0.4 to 0.5 transient-crater radii). From shock barometry and attenuation studies in other craters with crystalline targets, average shock pressures of ~10 GPa or greater are expected at this location (*9*). This observation suggests that the corehole did not reach the presumably shocked in situ crater floor, but instead sampled basement-rock blocks that slumped from higher on the transient-cavity wall toward the center of the cavity.

Some of the brittle cataclasis observed in these rocks may have occurred when the strongly attenuated shock wave and subsequent release wave passed through them. Growth and coalescence of fractures into larger shear zones likely occurred when these rocks became involved in the target flow field. This initial outward- and upward-directed shearing during growth of the transient cavity (Fig. 3A) was succeeded by centrally inward- and downward-directed motion. At the beginning of inward slumping, ~40 s after impact (*5*), the basement-derived blocks were not loaded by a sedimentary cover. The resulting lack of overburden pressure allowed dilatancy, resulting in the opening of fractures and the emplacement of the lithic and suevitic dike breccias (Fig. 3B).

The suevitic and lithic breccias above the schist-pegmatite-granite unit must have been emplaced before the arrival of the overlying unshocked rock and sediment breccias (Figs. 2 and 3), which occurred on the order of 6 to 8 min after the impact (*5*) (Fig. 3C). The apparently short time available for the transportation and deposition of the suevitic and lithic breccias suggests that most of this material never left the transient cavity but was emplaced by base surging along the surface of the cavity. The breccias at depths of 1551 to 1474 m show no signs of aerodynamic transport; they consist of meter-sized lithic blocks and interlayered melt-poor suevites that support the ground-surge scenario (*10*). However, the uppermost suevite section contains shard-like melt particles, indicating airborne quenching typical of ejecta-plume deposits (*11*).

Airborne materials that were thrown high into the atmosphere and fell back later than ~6 to 8 min after impact were mixed into the stratigraphically higher sediment-dominated breccias (Fig. 2). Shock-deformed lithic clasts and melt fragments occur throughout the upper part of these breccias (618 to 444 m); melt clast–enriched horizons occur as high as 458 m depth, only 14 m below the transition to background sedimentation conditions (Fig. 3D). Thus, late ejecta-plume fallback was coeval with late-stage gravitational collapse of the transient cavity and ocean resurge (water flowing back into the cavity) (Fig. 2).

The late-stage collapse of the transient-cavity wall was achieved by mass wasting that preceded and accompanied resurge of the oceanic water column back into the cavity (Fig. 2), which occurred ~7 to 15 min after impact (*5*) (Fig. 3, C and D). The relatively undeformed and unshocked granite megablock (Fig. 2) must have originated outside the shocked crater-floor zone. Possible locations include the rim of the transient cavity, or adjacent areas outside the cavity, which were strongly affected by gravity-driven collapse and by the erosion and transport of materials by ocean resurge. In this scenario, the 275-m-thick megablock was transported at least 5 km, from ~14 km radial distance to its present position at 9 km radial distance, probably within ~6 to 10 min after impact (Fig. 3, C and D). The thin, presumably water-saturated sand layer below the granite may have facilitated this transport.

The abundant preservation of primary stratification in the weakly indurated and brecciated Cretaceous sediments (1096 to 618 m) above the granite suggests transport in a zone of low and/or spatially localized shear stress. The absence of fallback clasts

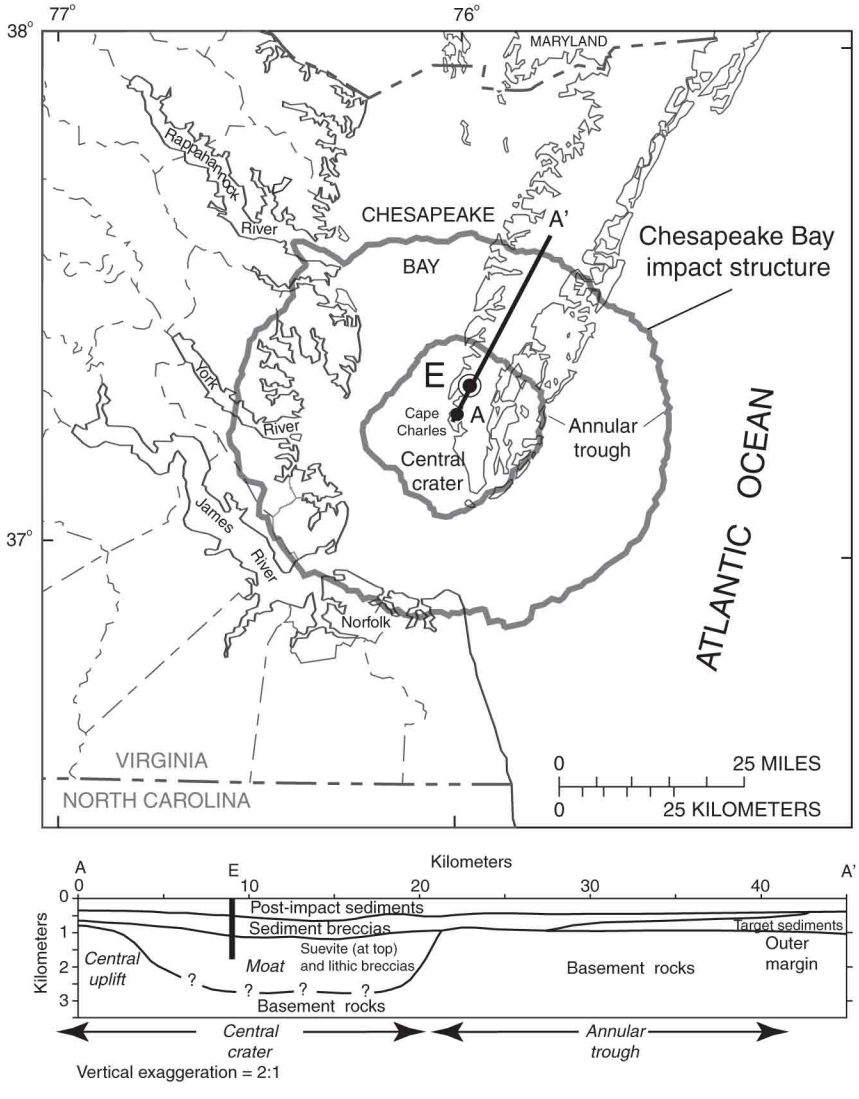

Fig. 1. Location of the Eyreville drill site (E) in the Chesapeake Bay impact structure and generalized radial cross section of the structure. The location of cross section A-A′ is shown on the map.

(shocked-rock and melt particles) in this material suggests rapid movement of a large mass of sediments. Collectively, these characteristics suggest rapid mass transport and deposition as a rock avalanche from the rim of the transient cavity.

The presence of the brecciated Cretaceous sediments directly above the granite megablock mimics the target stratigraphy where Cretaceous nonmarine sediments nonconformably overlie pre-Mesozoic igneous and metamorphic rocks. This "ghost stratigraphy" suggests the possibility that the granite and sediment section from 1397 to 618 m depth in the core moved as a single, huge, rock avalanche. The avalanche base is not at the top of the granite megablock, as shear-induced basal features (e.g., substrate folds, mixed substrate and breccia) are not present there. The avalanche base probably is the base of the thin sand below the granite at 1397 m depth, where clasts are reworked from the underlying suevitic and lithic breccias.

The glauconitic sediment-dominated breccias at 618 to 444 m represent the main pulse of ocean-water resurge into the collapsing transient cavity (Figs. 2 and 3D). The unsorted, unstratified, dominantly matrix-supported character of these deposits suggests transport and deposition by large sediment-gravity (debris) flows. The presence of glauconite represents the scouring and entrainment of Cretaceous and Tertiary marine sediments from outside the transient cavity by the resurge flow. The incorporation and dispersion of shocked-rock clasts and melt particles in the resurge indicates the persistence and collapse of the ejecta plume at this stage. A 6-m-thick zone of Cretaceous clasts in glauconitic matrix within the avalanche deposits at 867 to 861 m indicates that early ocean resurge overlapped, and likely facilitated, the gravitational collapse of the transient-cavity wall (Figs. 2 and 3D).

Vertical variations in clast types, sizes, and abundance (618 to 444 m) may indicate various stages of resurge, including inward resurge, outward anti-resurge, and oscillating "swash." The uppermost ~6 m of crater-fill sediments display stratification and size sorting that marks the transitional return to normal shelf sedimentation.

Post-impact sedimentation and tectonics. The Eyreville cores provide a high-resolution (~1 million years) chronostratigraphic record for the post-impact sediment sequences above the CBIS central crater that allows their placement into a regional depositional framework (Fig. 4). Excess accommodation space in the annular trough resulted from compaction of impact-generated materials during the first 7 million years after impact (35.4 to 27.5 Ma) (*12*). Backstripping (accounting for the effects of compaction and sediment loading) indicates that the trough was then uplifted by 50 to 125 m (27.5 to 18 Ma) (*12*). The Eyreville cores show that compaction of impact-generated materials continued to influence sedimentation above the central crater throughout the past 35.4 million years.

Most of the post-impact sequences are thinner outside the CBIS (at Tasley) than correlative sequences above the annular trough (at Exmore) (Fig. 4); previous work revealed similar lithostratigraphic trends (*13*). Sequences thicken even more above the crater moat (at Eyreville) but thin substantially above the central uplift (at Cape Charles). These changes in accommodation are due to differential compaction of variable thicknesses of impact-generated materials in the crater moat (>1000 m thick at Eyreville) versus the annular trough (~100 to 200 m thick at Exmore) and the central uplift (~300 m thick at Cape Charles). Seismic profiles across the CBIS (*1*) show numerous compaction faults offsetting post-impact sediments that dip into and thicken into the crater (*12*), supporting our interpretation.

Eustasy also influenced sedimentation in the CBIS. Eustatic control on sequence boundaries outside the structure (New Jersey–Delaware) is shown by a nearly one-to-one correspondence with ice volume increases inferred from oxygen isotopic changes from the Oligocene through the late Miocene (*14*–*16*). These sequences can be correlated to Tasley with the use of geophysical logs, and many are identified within the CBIS (Fig. 4), indicating eustatic influence.

However, there are also differences due to regional and impact tectonism. For example, Oligocene (~33 to 24 Ma) sequences are relatively thin to absent inside the central crater, in contrast to sections in the annular trough and outside the crater to the north (Fig. 4). The presence of a thick Oligocene section at Langley (Fig. 4, annular trough) argues for sediment starvation of the central crater, whereas the presence of a thick Oligocene section in New Jersey implicates regional tectonics. Lower Miocene sequences C1 to C5 (~24 to 17 Ma) are thin to absent inside the CBIS, in contrast to sections to the north (Fig. 4). Mid-Miocene sequences C6 to C8 (~16 to 13 Ma) are thick at Eyreville and Exmore but are thin or absent at Langley, most likely reflecting uplift of the Norfolk arch (*17*); mid-upper Miocene sequences C9 and C10 (~12 to 10 Ma) extend across the Delmarva Peninsula and are recovered at Exmore but are absent in the central crater and to the south, indicating regional uplift possibly coupled with low sedimentation rates. The preservation of uppermost Miocene to Pliocene (~7 to 2 Ma) sequences within the crater and regions to the south, versus their absence or nonmarine nature to the north, is attributed to excess regional subsidence of Virginia–North Carolina relative to New Jersey–Delaware.

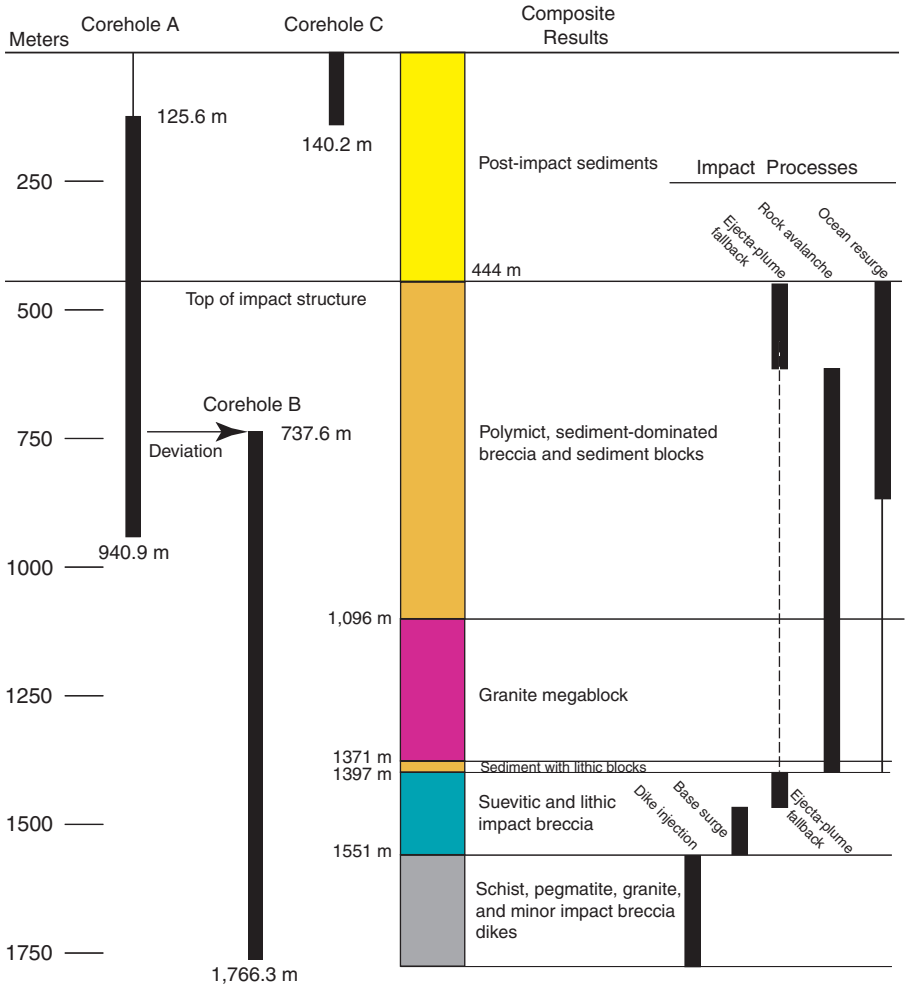

Fig. 2. Corehole depths, cored intervals, geologic column, and inferred impact processes for the A, B, and C coreholes at the Eyreville drill site. Intervals affected by selected impact processes are indicated.

Periods of uplift and excess subsidence at a scale of tens of meters in 1 to 3 million years (*16*) overprint subsidence from simple lithospheric cooling, flexure, and impactite compaction. We suggest that uplift and excess subsidence was caused by regional differential movement of fault-bounded basement blocks in response to variations in intraplate stress.

Hydrologic consequences. The CBIS is colocated with an inland extension of salt water in the coastal aquifers of Virginia (*13*) near population centers that rely heavily on groundwater. In addition, brine (*18*) with salinity exceeding that of seawater was detected at other borehole locations inside the CBIS (*19*, *20*). A recent analysis shows that hydraulic conditions within the CBIS would not have allowed groundwater to be flushed out since the time of impact (*21*). Thus, the brine likely is a residual from early post-impact hydrothermal boiling (*22*) or some other impact process.

In the Eyreville core, pore waters change from fresh to salty between depths of 100 and 440 m within the post-impact section (Fig. 5A). The monotonic trend in salinity suggests that molecular diffusion is a dominant process with little lateral advection of groundwater since the impact. Below 300 m, core samples containing brine with salinities up to twice that of seawater extend down to 1000 m. The brine in the breccias is too voluminous to be from hydrothermal boiling in the suevite layer (*23*), which suggests that it existed within the target sediments before impact; similar deep brine occurs north and south of the CBIS today (*24*, *25*). The local salinity variability and minima between 500 and 800 m could be inherited from the sediment clasts, or it could have been a zone of flushing during recent low sea levels. However, the salinity minima in this zone correlate with clay-rich sediments in the core, suggesting a connate rather than a recent seawater or meteoric origin, because flushing would tend to focus less saline water through the coarse-grained sediments. The evidence indicates that most of the groundwater currently in the CBIS survived the impact and has never been flushed out. Sluggish hydraulic conditions (*21*) would delay the migration of brine toward the population centers.

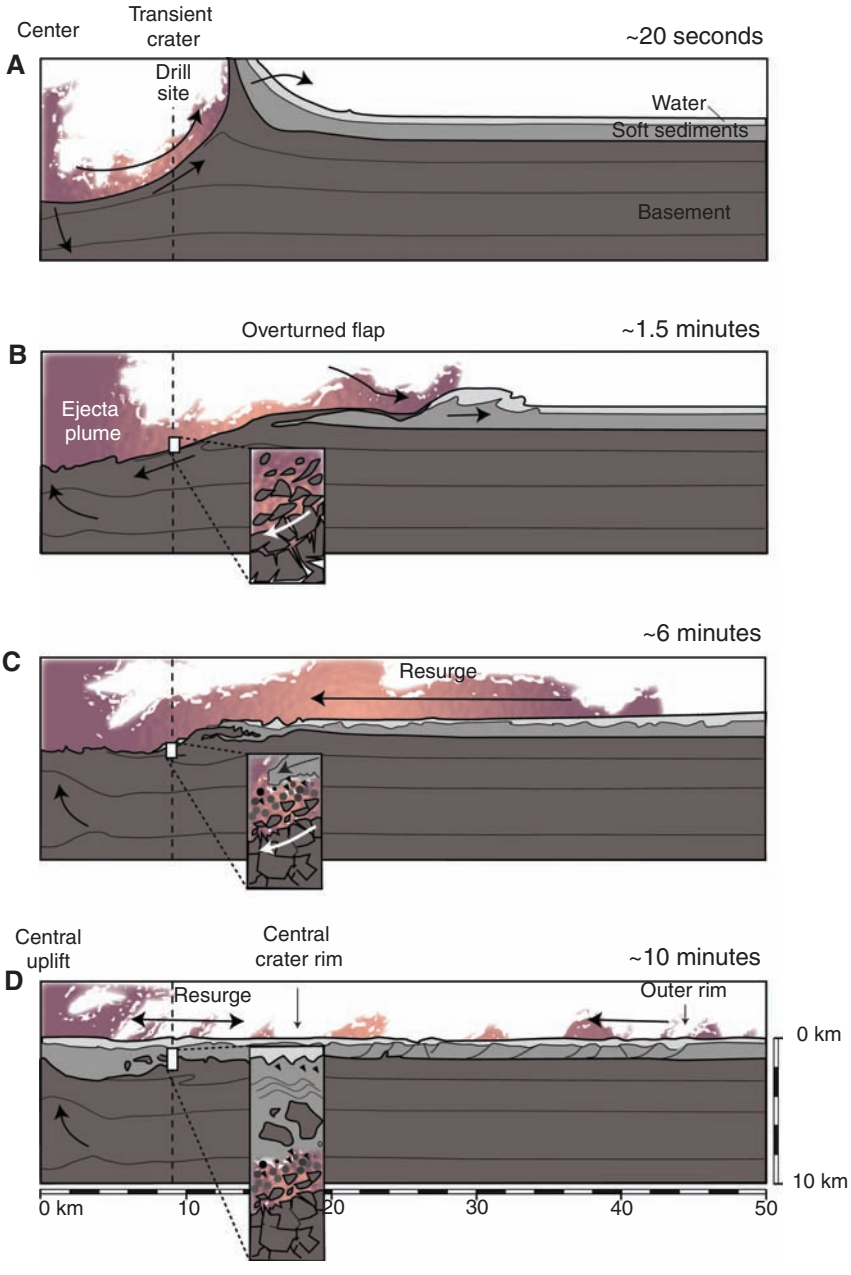

Fig. 3. Diagram illustrating the processes and history of crater collapse in four stages, (**A**) to (**D**). The close-ups illustrate the cratering processes at the corehole location. [Modified from (*5*)]

Effects on deep subsurface biota. The CBIS core provided microbiological samples from the deep terrestrial subsurface. Robust protocols were used to prevent and monitor contamination during recovery of samples (*26*). Samples were obtained at intervals of ~30 m for enumeration (Fig. 5B) and at intervals of ~60 m for culture and molecular biologic investigations.

Microbial abundance declines logarithmically from the surface across the transition from the post-impact sediments to the sediment breccias to near the middle of those breccias at a depth of ~800 m. This decline is steeper than that typical of many deep marine sediments covering a similar distance and geologic time interval (late Eocene to present), although near-surface abundances are similar (*27*–*29*). This observation could be related to more rapidly declining available carbon at depth relative to the deep marine biosphere and/or increasing salt concentration. Salinity concentrations substantially exceeding that of seawater (Fig. 5A) would limit the diversity and abundance of microorganisms capable of growing (*30*).

In the lower part of the sediment breccias (1096 to 867 m), salinity peaks at 65% and no cells were detected with our methodology except in two locations (samples collected from a mixed-clast region just above clay boulders at 1064 to 1025 m). The permeability of this section is generally low, and water within the section is likely a relict of the immediate post-impact environment. Our data are consistent with a scenario that includes sterilization of the section by impact-generated heat (either directly or as a result of vertically advected heat from the suevites and impact-melt rocks) (*22*) and high salinity that has limited microbial recolonization. Thus, most of this interval may have remained biologically impoverished since the impact.

The abundance of cells markedly increases below the granitic megablock, corresponding to the region of suevite and associated lithic breccias and the region of crystalline-rock blocks (1766 to 1397 m). The interval from 1424 to 1397 m consists of 20 to 30% impact-melt clasts with a suggested average temperature at the time of deposition of >350°C on the basis of numerical calculations used for modeling thermal maturity (*31*). This clearly exceeds the upper limit for growth and the accepted sterilization temperature for most microorganisms (>121°C steam or

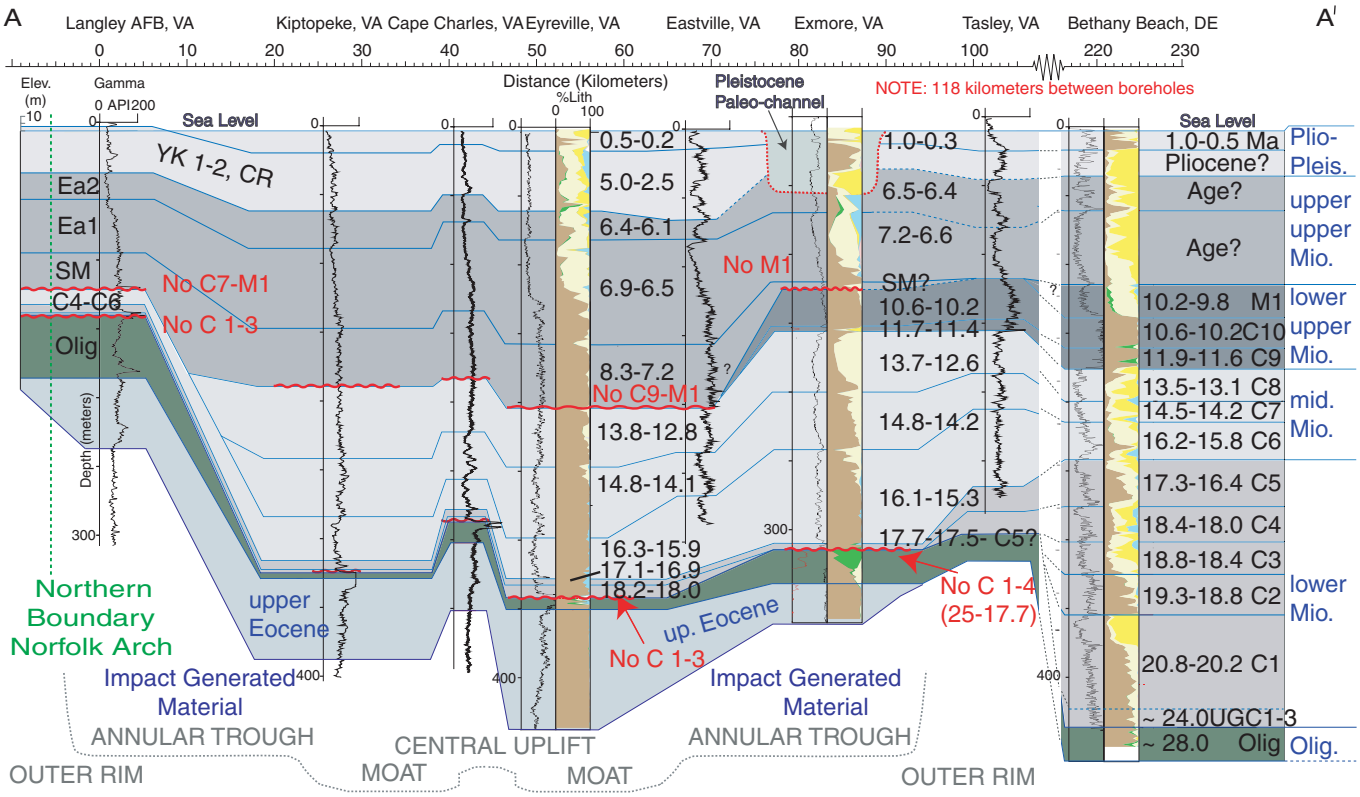

Fig. 4. Corehole and well log cross section, Langley, Virginia, to Bethany Beach, DE. Bethany Beach (*16*), Langley, Kiptopeke, Cape Charles, and Exmore are coreholes; Eastville and Tasley are water wells with gamma-ray logs; sequence ages are based on age-depth plots primarily using Sr isotopes. Sequences C1 to C10 and M1 are defined at Bethany Beach (*16*); YK, Ea1, Ea2, CR, and SM are defined at Eyreville. Blue lines represent sequence boundaries; wavy red lines indicate coalesced sequence boundaries where one or more sequences are absent. Lithologic columns: bright yellow, coarse quartz sand; pale yellow, fine quartz sand; blue, carbonate sand; brown, silt and clay; green, glauconite sand; pink-white, mica or other. See fig. S10 for location of cross section A-A′.

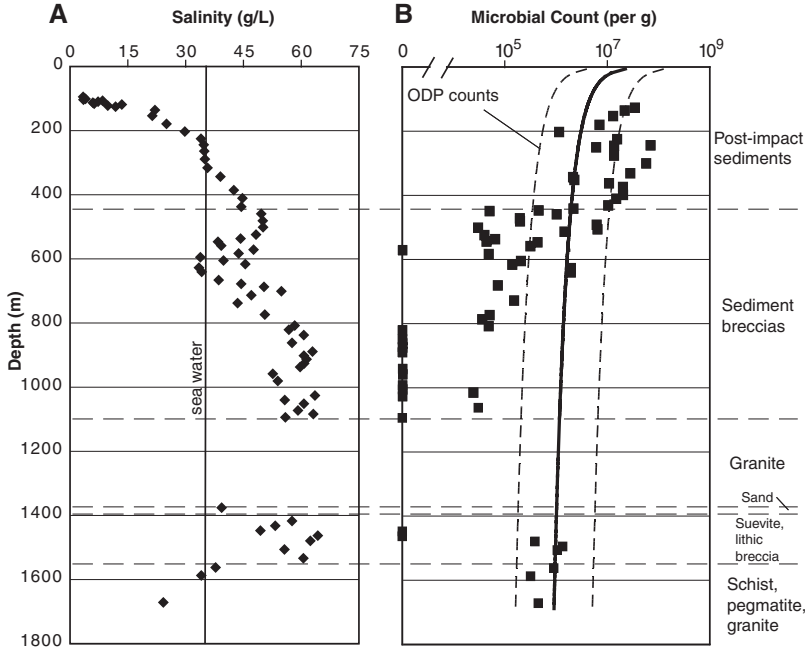

Fig. 5. (**A**) Profile of salinity at the Eyreville drill site, based on pore water extracted from core samples. (**B**) Microorganism count per gram dry weight. Counts are compared to average Ocean Drilling Program (ODP) microorganism data regression (*29*). The ODP regression lines were corrected assuming a conversion factor of 1.3 ml of sediment per gram. The correction factor was calculated by measuring 1 ml of 20 representative samples throughout the core and obtaining the dry weight of sediment. All values were within 10% of the mean.

>160°C dry heat). Microorganisms were reintroduced at some point after ambient temperatures dropped below the upper temperature limit for microbial growth (121°C) (*32*). The widespread presence of fractures in the crystalline rocks suggests that impact and post-impact processes could have contributed to the movement of fluids and perhaps organisms into this deeper region.

Understanding how impacts have influenced the characteristics of the deep subsurface is important for gaining insight into the biological potential of the deep biosphere during the Archean, when the impact flux was higher, as well as the biological potential of the deep biosphere on Mars, where impacts have had a profound influence on surface and subsurface geology. Data from the CBIS suggest that impact events can disrupt the deep subsurface biosphere. Although detrimental effects may be caused by a biologically sterilizing pulse, subsequent recolonization (and even enhanced growth) might occur if reorganization and restructuring of the lithologic units (including fracturing), and/or inundation of the subsurface with seawater and terrestrial materials that potentially introduce fresh electron acceptors and donors, lead to the establishment of a suitable environment.

References and Notes

1. C. W. Poag, C. Koeberl, W. U. Reimold, *The Chesapeake Bay Crater, Geology and Geophysics of a Late Eocene Submarine Impact Structure* (Springer, Berlin, 2004).

2. J. W. Horton Jr., D. S. Powars, G. S. Gohn, Eds., *U.S. Geol. Surv. Prof. Pap. 1688* (2005).
3. C. Koeberl, C. W. Poag, W. U. Reimold, D. Brandt, *Science* **271**, 1263 (1996).
4. A. Deutsch, C. Koeberl, *Meteorit. Planet. Sci.* **41**, 689 (2006).
5. G. S. Collins, K. Wünnemann, *Geology* **33**, 925 (2005).
6. G. S. Gohn *et al*., *Eos* **87**, 349 (2006).
7. J. W. Horton Jr. *et al*., *Geol. Soc. Am. Abstr. Prog.* **39**, 451, abstract 167-5 (2007).
8. J. W. Horton Jr., J. N. Aleinikoff, M. J. Kunk, C. W. Naeser, N. D. Naeser, *U.S. Geol. Surv. Prof. Pap. 1688* (2005).
9. P. B. Robertson, R. A. F. Grieve, in *Impact and Explosion Cratering: Planetary and Terrestrial Implications*, D. J. Roddy, R. O. Pepin, R. B. Merrill, Eds. (Pergamon, New York, 1977), pp. 687–702.
10. A. Wittmann, T. Kenkmann, L. Hecht, D. Stöffler, *Geol. Soc. Am. Bull.* **119**, 1151 (2007).
11. D. Stöffler *et al*., *Meteorit. Planet. Sci.* **39**, 1035 (2004).
12. T. Hayden *et al*., *Geology* **36**, 327 (2008).
13. D. S. Powars, T. S. Bruce, *U.S. Geol. Surv. Prof. Pap. 1612* (1999).
14. K. G. Miller, G. S. Mountain, Leg 150 Shipboard Party, Members of the New Jersey Coastal Plain Drilling Project, *Science* **271**, 1092 (1996).
15. K. G. Miller *et al*., *Science* **310**, 1293 (2005).
16. J. V. Browning *et al*., *Geol. Soc. Am. Bull.* **118**, 657 (2006).
17. D. S. Powars, *U.S. Geol. Surv. Prof. Pap. 1622* (2000).
18. C. W. Poag, *The Chesapeake Invader* (Princeton Univ. Press, Princeton, NJ, 1999).
19. E. R. McFarland, T. S. Bruce, *U.S. Geol. Surv. Prof. Pap. 1688-K* (2005).
20. W. E. Sanford *et al*., *Eos* **85**, 369 (2004).
21. W. E. Sanford, *J. Geochem. Explor.* **78–79**, 243 (2003).
22. W. E. Sanford, *Geofluids* **5**, 185 (2005).
23. See supporting material on *Science* Online.
24. L. Radford, L. B. Cobb, R. L. McCoy, *U.S. DOE Rep. DOE/ET/28373-1* (1980).
25. F. T. Manheim, M. K. Horn, *Southeast. Geol.* **9**, 215 (1968).
26. A. L. Gronstal *et al*., *Geol. Soc. Am. Abstr. Prog.* **39**, 316, abstract 116-22 (2007).
27. R. J. Parkes *et al*., *Nature* **371**, 410 (1994).
28. S. D'Hondt *et al*., *Science* **306**, 2216 (2004).
29. R. J. Parkes, B. A. Cragg, P. Wellsbury, *Hydrogeol. J.* **8**, 11 (2000).
30. W. D. Grant, *Philos. Trans. R. Soc. London Ser. B* **359**, 1249 (2004).
31. M. L. Malinconico, W. E. Sanford, J. W. Horton Jr., abstract for Conference on Large Meteorite Impacts and Planetary Evolution IV, Vredefort Dome, South Africa, abstract 3068 (2008).
32. K. Kashefi, D. R. Lovley, *Science* **301**, 934 (2003).

33. The International Continental Scientific Drilling Program, the U.S. Geological Survey, and the NASA Science Mission Directorate provided funding for the drilling project. NSF and the Austrian Science Foundation provided supplementary funding for the drill-site operations. DOSECC Inc. conducted the administrative and operational management of the deep drilling project. We thank the Buyrn family for use of their land as a drilling site, the scientific and technical staff of the Chesapeake Bay Impact Structure Drilling Project for their many contributions, A. Gronstal (Open University, UK) for the microbe enumeration data, L. Edwards (USGS) for discussions of the post-impact geology, and G. Collins (Imperial College, UK) and K. Wünnemann (Humboldt-University Berlin) for making available the results of their numerical modeling.

Supporting Online Material

www.sciencemag.org/cgi/content/full/320/5884/1740/DC1
Materials and Methods
Figs. S1 to S10
Table S1
References

4 April 2008; accepted 28 May 2008
10.1126/science.1158708

Dislocation Mean Free Paths and Strain Hardening of Crystals

B. Devincre,[1] T. Hoc,[2] L. Kubin[1]*

Predicting the strain hardening properties of crystals constitutes a long-standing challenge for dislocation theory. The main difficulty resides in the integration of dislocation processes through a wide range of time and length scales, up to macroscopic dimensions. In the present multiscale approach, dislocation dynamics simulations are used to establish a dislocation-based continuum model incorporating discrete and intermittent aspects of plastic flow. This is performed through the modeling of a key quantity, the mean free path of dislocations. The model is then integrated at the scale of bulk crystals, which allows for the detailed reproduction of the complex deformation curves of face-centered cubic crystals. Because of its predictive ability, the proposed framework has a large potential for further applications.

Dislocations are complex defects of crystalline materials, which have been investigated for more than 70 years. Their fundamental and economical importance arises from the number of properties they govern, such as the high strength of nanostructured materials, the reliability of semiconductor devices, the processing and service life of structural materials, or the rheological properties of tectonic events in Earth's crust.

The irreversible, or plastic, deformation of crystals results from the motion on crystallographic planes of linear defects, the dislocations (*1*, *2*). These defects carry an elementary amount of shear (the Burgers vector) that is usually the smallest translation of the crystal lattice. During plastic flow, dislocations multiply and their mutual interactions hinder their motion. As a consequence, a shear stress increase $d\tau$ has to be imposed to produce a shear strain increase $d\gamma$. By definition, the ratio $d\tau/d\gamma$ is the strain hardening rate. Although dislocation theory has successfully explained many aspects of the strength of crystalline solids, predicting strain hardening is "the most difficult remaining problem" (*3*). The present dislocation-based models for strain hardening still have difficulties integrating elementary dislocation properties into a continuum description of bulk crystals or polycrystals. As a consequence, current approaches cannot avoid making use of extensive parameter fitting.

The present work takes advantage of three-dimensional dislocation dynamics (DD) simulations (*4*–*8*) for averaging dislocation properties at the intermediate scale of slip systems, which are ensembles of dislocations having the same Burgers vector and slip plane. The use of periodic boundary conditions allows for the tayloring of large dislocation glide paths and the investigation of volumes that are representative of the bulk material (*4*). One can then derive a continuum formulation on the basis of physically justified mechanisms and parameters, and this formulation is further integrated at the scale of a bulk crystal. Face-centered cubic (fcc) crystals are taken as benchmark materials because of their well-documented, but rather complicated, stress/strain response.

We started by considering the critical stress τ_c^i for the activation of slip system i as a function of the dislocation densities ρ^j stored (i.e., temporarily or permanently immobilized) in all slip systems j. This critical stress is given by a generalized Taylor relation (*9*) of the form, $\tau_c^i = \mu b \sqrt{\sum_j a_{ij}\rho^j}$, where μ is the shear modulus and b the modulus of the Burgers vector. In fcc crystals, the symmetric tensor a_{ij} contains six independent dimensionless coefficients, which account for the average strength of pair interactions between slip systems that result from short- and long-range interactions. Their values were recently determined from DD simulations (*5*).

For determining strain hardening, the key quantity is the rate at which the critical stress evolves with strain or, equivalently, the rate at which dislocations accumulate under strain. For this purpose, it is useful to define a dislocation mean free path L, which is the distance traveled by a dislocation segment of length l before it is stored by interaction with the microstructure. When the line moves by a distance dx, it sweeps an area ldx and produces a shear strain $d\gamma = bldx/V$, where V is the volume of the crystal. The stored density has then statistically increased by $d\rho = (dx/L)l/V$, and the incremental storage rate is $d\rho/d\gamma = 1/bL$. This definition is only valid in differential form, as dislocation lines multiply when they move. Following Kocks *et al*. and

[1]Laboratoire d'Etude des Microstructures, Unité Mixte de Recherche (UMR) 104 CNRS, CNRS–Office National d'Etudes et de Recherches Aérospatiales (ONERA), 20 Avenue de la Division Leclerc, BP 72, 92322 Chatillon Cedex, France. [2]Laboratoire MSSMat, UMR 8579 CNRS, Ecole Centrale Paris, Grande Voie des Vignes, 92295 Chatenay-Malabry Cedex, France.

*To whom correspondence should be addressed. E-mail: ladislas.kubin@onera.fr

Teodosiu *et al.* (*10*, *11*), the net storage rate in each slip system i is written as

$$\frac{d\rho^i}{d\gamma^i} = \frac{1}{b}\left(\frac{1}{L^i} - y\rho^i\right) \quad (1)$$

The last term at the right-hand side, where y is proportional to the critical annihilation distance for screw dislocations, describes the effect of a mechanism called dynamic recovery (*4*). The mean free path L^i also appears in Eq. 1. Very little is presently known about the way L^i depends on dislocation interactions, stress, and specimen orientation.

At a small scale, plastic flow is not continuous but exhibits intermittency, as has been shown in several recent studies (*12*, *13*). Figure 1A, which is extracted from a DD simulation, illustrates that the unzipping of a single junction initiates several successive bursts of dislocation motion and expansion. As a consequence, the stored dislocation density increases in a discontinuous but progressive manner during straining (Fig. 1B), thus inducing strain hardening. Figure 1C shows the probability distribution functions of plastic strain-burst amplitudes, $P(\delta\gamma_p)$, as obtained from three DD simulations performed with different loading axes. For each orientation, a power law $P(\delta\gamma_p) \sim \delta\gamma_p^{-\eta}$ is obtained in a bounded domain of amplitudes, with a scaling exponent $\eta \approx 1.6$ in the range of previously measured values (*12*, *13*).

Because the shear strain is the area swept by dislocations divided by the volume of the deforming crystal, these dislocation avalanches cannot be observed on the stress/strain curves of bulk crystals. This suggests that a continuous description of uniform storage events through a coarse-graining procedure that smoothens out intermittency can be established. To ensure compatibility between the discrete and continuum approaches of storage, the parameters involved in the continuum approach discussed below are estimated as averages over the fluctuating output of DD simulations.

The most important contribution to the mean free paths arises from the interactions of moving dislocations with "forest" dislocations (that is, dislocations of other systems that pierce their slip plane) and their subsequent storage. We examined conditions such that n slip systems are active, with $n > 1$, and we considered one active slip system i. We made a simplifying assumption by replacing the interaction coefficients between slip systems

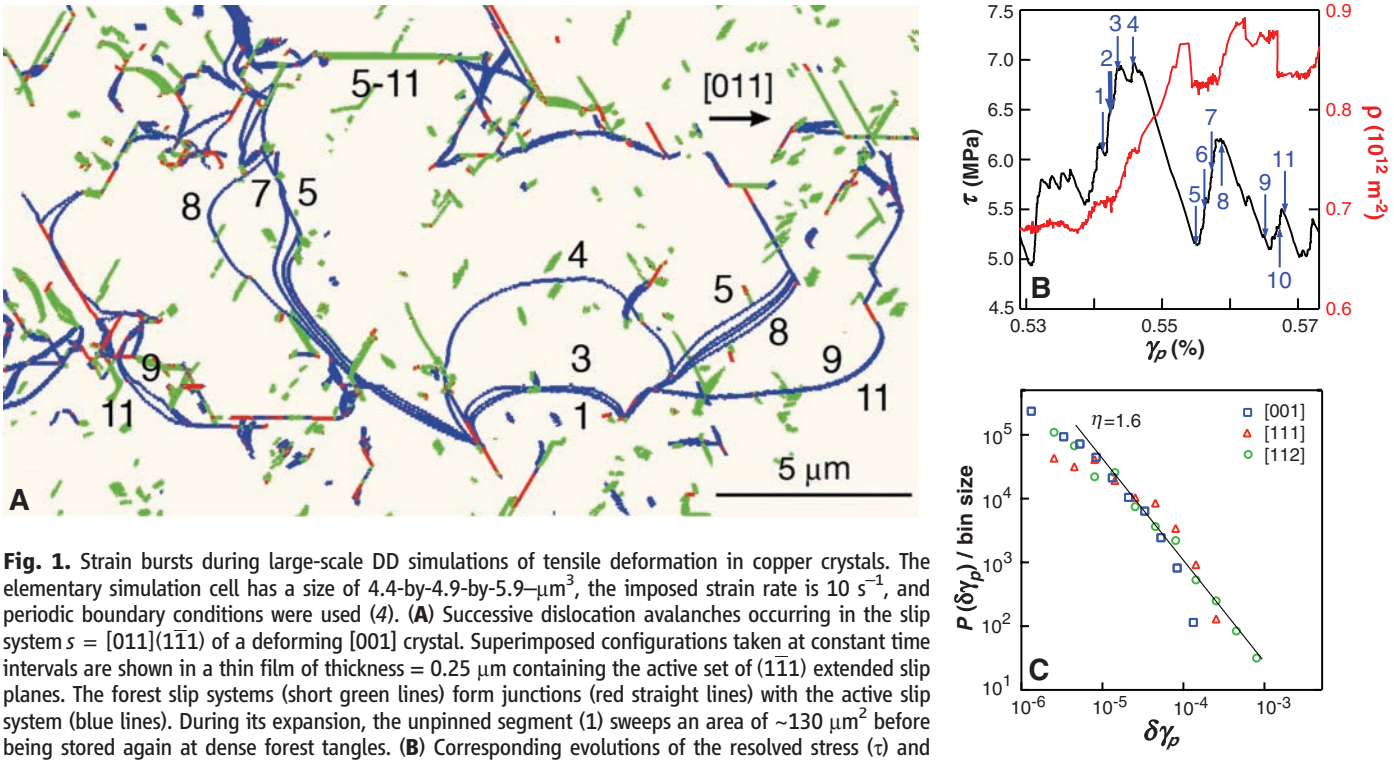

Fig. 1. Strain bursts during large-scale DD simulations of tensile deformation in copper crystals. The elementary simulation cell has a size of 4.4-by-4.9-by-5.9–μm^3, the imposed strain rate is 10 s^{-1}, and periodic boundary conditions were used (*4*). (**A**) Successive dislocation avalanches occurring in the slip system s = [011](1$\bar{1}$1) of a deforming [001] crystal. Superimposed configurations taken at constant time intervals are shown in a thin film of thickness = 0.25 μm containing the active set of (1$\bar{1}$1) extended slip planes. The forest slip systems (short green lines) form junctions (red straight lines) with the active slip system (blue lines). During its expansion, the unpinned segment (1) sweeps an area of ~130 μm^2 before being stored again at dense forest tangles. (**B**) Corresponding evolutions of the resolved stress (τ) and dislocation density (ρ) in s versus the total shear strain (γ_p). Each jerk results from an avalanche, and arrows mark the dislocation configurations shown in (A). (**C**) Probability $P(\delta\gamma_p)$ per bin size of the strain-burst amplitudes $\delta\gamma_p$ for three simulations with high-symmetry orientations.

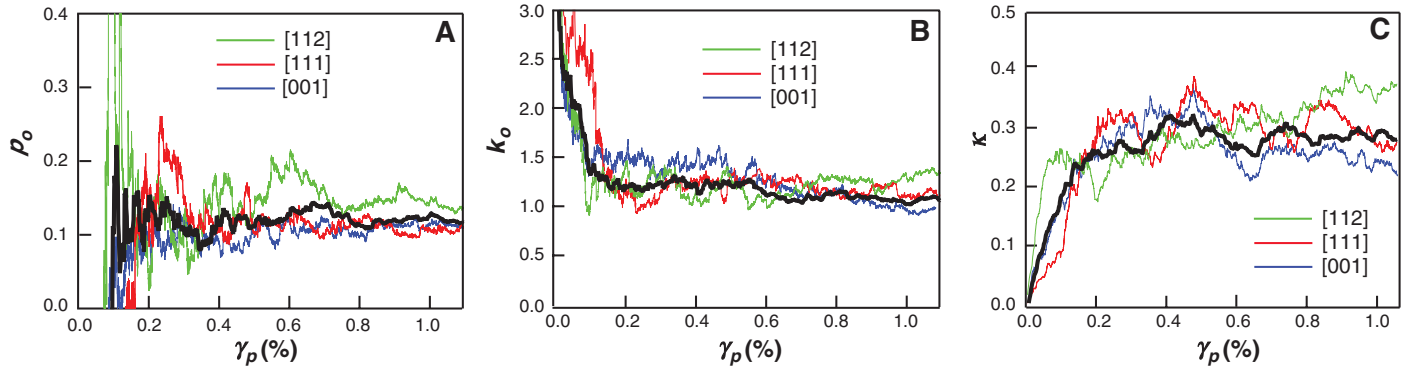

Fig. 2. Measurement of the dimensionless constants p_0 (**A**), k_0 (**B**), and κ (**C**) as a function of plastic shear strain by large-scale DD simulations and for three symmetrical orientations. Black lines represent the mean values. The elementary cell size is about (5 μm)^3, and the imposed strain rate is $\dot{\gamma}$ = 10 s^{-1}.

a_{ij} by their average value $\overline{a}$. During a time interval dt, mobile dislocations in i sweep an area dS^i and produce a strain increment $d\gamma^i = bdS^i$ per unit of volume. The increase in stored density $d\rho^i$ is the product of the number of stable junctions formed during a time increment and the dislocation density stored per junction.

The number of stable junctions formed during dt is the product of two terms. The first one is the number of intersections, dN_{int}, of mobile dislocations with the forest dislocations of i, in density ρ_f^i (where f refers to the forest). This quantity is proportional to ρ_f^i and to the swept area; hence, $dN_{\text{int}} = \rho_f^i d\gamma/b$. The second term incorporates the fact that not all intersections produce stable junctions (Fig. 1A). Because the stability of a junction is proportional to the average strength of the forest interactions (*5*), it is written in the form $p_0\sqrt{\overline{a}}$, where p_0 is a constant.

The density stored by each junction is given by $\overline{\ell}^i/V$, where $\overline{\ell}^i$ is the average length of the stored segments. As usual in dislocation theory, this length is inversely proportional to stress, and one has $\overline{\ell}^i = k_0\mu b/\tau_c^i$, where k_0 is a dimensionless constant. However, one has to account for the contribution of junctions to the average lengths. Although junction lines do not necessarily share the attributes of perfect dislocations, they are redistributed into the densities stored in the active slip systems. This way, they can further react with mobile segments to form second-order junctions (*6*). As a result, one defines a last constant parameter, the ratio of junction density to total density in each slip system, κ.

Collecting all terms, one eventually obtains the storage rate per active slip system or, equivalently, the inverse of the mean free path (Eq. 1). The latter takes a relatively simple form in the case of loading along symmetrical orientations like [001], [111], or [112] when n active slip systems (n = 4, 3, and 2, respectively) equally contribute to the total strain. One then has

$$\frac{1}{L^i} = \frac{\tau_c^i}{\mu b K_{hkl}}, \text{ with}$$

$$K_{hkl} = \left[\frac{n(1+\kappa)^{3/2}}{p_0 k_0 \sqrt{\overline{a}}(n-1-\kappa)}\right] \qquad (2)$$

This mean free path exhibits interesting properties that are also present in more general conditions. From Eq. 2, one can see that it is inversely proportional to the Taylor stress. It is also proportional to an orientation-dependent coefficient K_{hkl}, which depends on the three dimensionless constants (p_0, k_0, and κ) and also on the number n of active slip systems. In short, as n increases, the forest density seen by each active slip system increases too, and the mean free path decreases. Because n depends on the orientation [h,k,l] of the loading axis, an orientation dependence of the mean free path arises, which was not consistently modeled to date.

The constants defining the mean free paths were evaluated from two sets of independent DD simulations carried out with copper as a model material (*4*): (i) model simulations, in which a mobile slip system interacts with an immobile forest slip system, and (ii) large-scale simulations of tensile deformation tests along three symmetrical axes, [112], [111], and [001]. Figure 2 illustrates the determination of the constants p_0, k_0, and κ by large-scale simulations. Table 1 gives average values for the constants in Eq. 2, as obtained from the two sets of DD simulations. The values of the mean free path coefficients, K_{hkl}, can then be compared to the ones predicted by Eq. 2.

From the values of p_0 and κ, one can infer that the fraction of attractive intersections that result in junction formation is ~25%, whereas the average density of junctions is ~30% of the total density in symmetrical conditions. The simulated and calculated values for K_{112} and K_{111} are in good agreement with one another. The difference between the values for K_{001} actually results from a particular dislocation mechanism that is specific to the [001] orientation (*14*). We used the measured value of K_{001} to correct the prediction of the model in that case.

Storage by forest interactions and Taylor hardening constitutes the two major building blocks for modeling strain hardening. Other building blocks are discussed in the supporting online material text. They are essentially concerned with self-interaction mechanisms, which govern strain hardening in single slip conditions (*14*), and dynamic recovery, which is related to the thermally activated annihilation of screw dislocations by cross-slip. Because the annihilation distance y in Eq. 1 incorporates two poorly known factors, a reference value was estimated from an experimental stress/strain curve.

To allow for a comparison between the predicted and experimental mechanical responses of single crystals, a change in scale is performed from mesoscopic to macroscopic dimensions. For this purpose, use is made of a crystal plasticity code (*4*, *15*), which is a specific type of finite element code that takes into account the crystallographic nature of dislocation glide, deformation conditions, and lattice rotations during plastic flow. We then integrated the set of dislocation-based equations on a meshed tensile specimen (fig. S1).

Table 1. Average values of the dimensionless constants for fcc crystals involved in Eq. 2 and their variance. The number of independent measurements is indicated in parentheses in the top row. The values of the mean free path coefficients K_{hkl} can be compared to the ones calculated from Eq. 2 (italic numbers in parentheses). For a resolved shear stress of 10 MPa in copper, these values are almost identical to those of the mean free paths expressed in microns.

p_0 (6)	k_0 (6)	κ (9)	K_{112} (3)	K_{111} (3)	K_{001} (3)
0.117 ± 0.012	1.08 ± 0.005	0.291 ± 0.015	10.42 ± 0.4 (*11.87*)	7.29 ± 1.6 (*7.38*)	4.57 ± 0.3 (*6.21*)

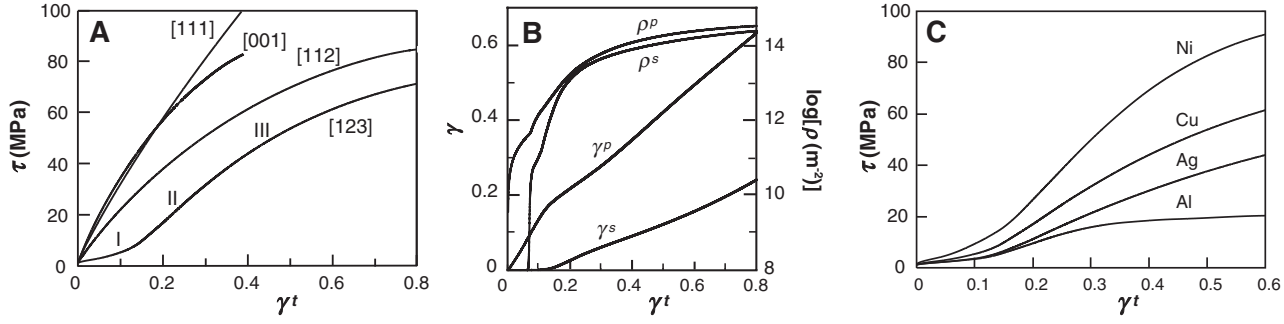

Fig. 3. Simulated mechanical response of fcc single crystals at room temperature. τ and total strains (γ^t) were drawn using traditional conventions for plotting experimental results. (**A**) Copper. Stress/strain curves were resolved on the primary slip system. Notice the strong orientation effect and the occurrence of three stages for the low-symmetry [123] orientation. The strain hardening rate increases from dissymmetrical double slip along [123] to symmetrical slip along [112], [111], and [001]; i.e., it increases with an increasing number of active slip systems. The crossing of the [001] and [111] curves was experimentally observed. This crossing occurs because of a competition between the orientation dependencies of stages II and III. (**B**) Copper, [123] orientation. Densities (ρ) and resolved strains (γ) on the primary (*p*) and secondary (*s*) slip systems as a function of the total resolved strain, showing the transition between easy glide in stage I and forest hardening in stage II. (**C**) Resolved stress versus total shear strain curves for [123] Cu, Al, Ag, and Ni crystals at room temperature.

A selection of results is presented in Fig. 3 for tensile deformation at 300 K, with emphasis on copper crystals. Although the model does not incorporate ad hoc switches, the resolved stress/strain curves (Fig. 3A) exhibit the traditional stages that characterize fcc single crystals (*16*). The low-hardening stage I, during which a single slip system is activated, appears for low-symmetry orientations like [123]. The linear stage II is due to forest hardening, and its slope increases with the number of active slip systems. The subsequent decrease in strain hardening rate is also orientation-dependent and stems from dynamic recovery. All of these features are in excellent agreement with published experimental results (*16*, *17*). Figure 3B shows the evolution of the shear strains and densities on the primary and secondary slip systems during a simulated [123] test. It is representative of the wealth of detailed information that can be obtained at the scale of slip systems. Finally, Fig. 3C illustrates a broader aspect of this type of modeling by presenting [123] stress/strain curves for several fcc crystals at room temperature. In addition to a rescaling of lattice parameters and elastic constants, shifting from one fcc material to the other implies changes in the annihilation properties of screw dislocations during dynamic recovery. To address this, we tentatively used a scaling law derived from Escaig's model for cross-slip (*4*).

The present results indicate that, paradoxically, realistic strain hardening properties in uniaxial deformation are obtained without accounting for dislocation patterning (*18*, *19*); that is, for the emergence of non-uniform microstructures during plastic flow. A possible reason is that the wavelength of dislocation patterns and the mean free path values follow the same scaling relation, in tension or compression.

This study shows that the mean free path of dislocations is the missing link connecting discrete dislocation interactions and avalanche processes to strain hardening properties in the bulk. The present multiscale methodology should apply to several areas of practical importance, such as the mechanical response of polycrystalline materials or size effects in small dimensions.

References and Notes

1. J. Friedel, *Dislocations* (Pergamon, Oxford, 1967).
2. J. Hirth, J. Lothe, *Theory of Dislocations* (Krieger, Malabar, FL, 1992).
3. A. H. Cottrell, in *Dislocations in Solids*, vol. 11, F. R. N. Nabarro, M. S. Duesbery, Eds. (Elsevier, Amsterdam, 2002), p. vii.
4. Simulation methods and additional information are available as supporting material on *Science* Online.
5. B. Devincre, L. Kubin, T. Hoc, *Scr. Mater.* **54**, 741 (2006).
6. V. V. Bulatov *et al*., *Nature* **440**, 1174 (2006).
7. V. Bulatov, F. Abraham, L. Kubin, B. Devincre, S. Yip, *Nature* **391**, 669 (1998).
8. R. Madec, B. Devincre, L. Kubin, T. Hoc, D. Rodney, *Science* **301**, 1879 (2003).
9. P. Franciosi, M. Berveiller, A. Zaoui, *Acta Metall.* **28**, 273 (1980).
10. U. F. Kocks, H. Mecking, *Prog. Mater. Sci.* **48**, 171 (2003).
11. C. Teodosiu, J.-L. Raphanel, L. Tabourot, in *Large Plastic Deformations*, C. Teodosiu, J. L. Raphanel, F. Sidoroff, Eds. (A. A. Balkema, Rotterdam, Netherlands, 1993), p. 153.
12. M.-Carmen Miguel, A. Vespignani, S. Zapperi, J. Weiss, J.-R. Grasso, *Nature* **410**, 667 (2001).
13. F. F. Csikor, C. Motz, D. Weygand, M. Zaiser, S. Zapperi, *Science* **318**, 251 (2007).
14. B. Devincre, L. Kubin, T. Hoc, *Scr. Mater.* **57**, 905 (2007).
15. T. Hoc, C. Rey, J.-L. Raphanel, *Acta Mater.* **49**, 1835 (2001).
16. T. E. Mitchell, *Prog. Appl. Mater. Res.* **6**, 117 (1964).
17. T. Takeuchi, *Trans. JIM* **16**, 629 (1975).
18. L. Kubin, *Science* **312**, 864 (2006).
19. L. Kubin, B. Devincre, T. Hoc, *Mater. Sci. Eng. A* **483–484**, 19 (2008).

20. The authors acknowledge funding by their host institutions: CNRS, ONERA, and Ecole Centrale Paris.

Supporting Online Material

www.sciencemag.org/cgi/content/full/320/5884/1745/DC1
SOM Text
Fig. S1
References

5 February 2008; accepted 2 May 2008
10.1126/science.1156101

Ordered Mesoporous Materials from Metal Nanoparticle–Block Copolymer Self-Assembly

Scott C. Warren,[1,2] Lauren C. Messina,[2] Liane S. Slaughter,[2] Marleen Kamperman,[1] Qin Zhou,[2] Sol M. Gruner,[3] Francis J. DiSalvo,[2] Ulrich Wiesner[1]*

The synthesis of ordered mesoporous metal composites and ordered mesoporous metals is a challenge because metals have high surface energies that favor low surface areas. We present results from the self-assembly of block copolymers with ligand-stabilized platinum nanoparticles, leading to lamellar CCM-Pt-4 and inverse hexagonal (CCM-Pt-6) hybrid mesostructures with high nanoparticle loadings. Pyrolysis of the CCM-Pt-6 hybrid produces an ordered mesoporous platinum-carbon nanocomposite with open and large pores (≥10 nanometers). Removal of the carbon leads to ordered porous platinum mesostructures. The platinum-carbon nanocomposite has very high electrical conductivity (400 siemens per centimeter) for an ordered mesoporous material fabricated from block copolymer self-assembly.

Despite considerable progress in the field of porous solids, major challenges remain in the synthesis of ordered mesoporous materials with high metal content from the coassembly of macromolecular surfactants and inorganic species. Controlling the structure of metals at the mesoscale (2 to 50 nm) is crucial for the development of improved fuel cell electrodes and may also assist in the miniaturization of optical and electronic materials for data transmission, storage, and computation (*1*, *2*).

An early route to preparing mesoporous metals involves the dealloying of a less noble metal from a bimetallic alloy; this has been used for the preparation of Raney nickel and other metals (*3*). Dealloying processes provide limited control over structural parameters such as pore geometry and order. In contrast, block copolymer self-assembly or templating with metal species provides access to highly ordered structures. Synthetic routes to such structures have included adsorbing and then reducing metal ions within a preassembled block copolymer scaffold (*4*) and coassembling ligand-stabilized nanoparticles (NPs) with block copolymers (*5*). More recently, polymer-coated NPs that behave like surfactants have been isolated at the interface of block copolymer domains, which can create a bicontinuous morphology at higher loadings (*6*).

Despite this progress, the conversion of metal-polymer hybrids into mesoporous materials with ordered and large pores (≥10 nm) has not been accomplished, in part because of the low volume fraction of metals in most hybrids and the widespread use of gold, which has a high diffusion coefficient and therefore retains its mesostructure only at low temperatures (*7*–*9*). Although a protective organic layer can be added to metal NPs to prevent uncontrolled aggregation, even a thin organic layer represents a considerable volume of the overall material: For example, a 1-nm-diameter metal NP with a relatively thin 1-nm organic shell is just 4% metal by volume. As a result, the typical metal content in most block copolymer–metal NP hybrids is only a few volume %, and the prospects for converting the hybrid into an ordered mesoporous material, in which the metal would have a volume fraction between 60 and 75% for an inverse hexagonal structure, are poor.

Mesoporous metals have been synthesized at a smaller length scale, with 2- to 4-nm pores, through the coassembly of metal ions with small-molecule surfactants followed by reduction (*10*–*13*). The small pore size, however, limits the flow of liquids through the material, which is essential for many applications (*14*, *15*). Metals have also been deposited onto (*16*) or into (*17*) thin films of block

[1]Department of Materials Science and Engineering, Cornell University, Ithaca, NY 14853, USA. [2]Department of Chemistry and Chemical Biology, Cornell University, Ithaca, NY 14853, USA. [3]Department of Physics, Cornell University, Ithaca, NY 14853, USA.

*To whom correspondence should be addressed. E-mail: ubw1@cornell.edu

copolymers to create metal wires, but the surface-dependent nature of the metal deposition most likely limits these processes to two-dimensional materials.

We report a route to mesostructured Pt NP–block copolymer hybrids with exceptionally high NP loadings and tunable phase-separated morphologies with feature sizes >10 nm. Metal-rich NPs with a thin organic shell made from ionic liquid ligands, combined with NP loadings as high as 79 volume % in the hydrophilic domains of the hybrid, ensure that mesostructure order is retained upon conversion to mesoporous metal-C composites. The C can be removed from the nanocomposites to produce ordered Pt mesostructures with ordered and large (≥10 nm) uniform pores.

We used a strategy in which ligand-stabilized Pt NPs (Fig. 1, A and B) coassemble with block copolymers (Fig. 1C) during the evaporation of organic solvents, forming metal-rich mesostructured NP–block copolymer hybrids (Fig. 1D). Hybrids are pyrolized by heating under an inert atmosphere, leaving behind ordered mesoporous Pt-C composites (Fig. 1E). Finally, the C is removed through use of an Ar-O plasma or acid etch to produce ordered porous Pt mesostructures (Fig. 1F). The success of this strategy depends on the synthesis of mesostructured hybrids with high metal volume fractions in one domain of the block copolymer, which is possible after meeting the following criteria.

First, the NPs should exhibit high solubility in organic solvents. When NPs have low solubility, some fraction of the particles macroscopically precipitates during solvent evaporation and fails to mix with the block copolymer. We recently reported a ligand for metal NPs based on a thiol-containing ionic liquid (*18*) that imparted liquidlike behavior to the NPs, even in the absence of a solvent. This result suggests that the use of certain ionic liquids as NP ligands provides a route to high solubility.

Second, the ligand-stabilized NPs should have at least a modest metal volume fraction. Although metal NPs with high solubility have been reported (*18*, *19*), the metal volume fraction was between 0.6 and 3% (*18*). Higher metal volume fractions are needed to prevent structural collapse upon removal of the organic components. Conventional short ligands can increase the metal volume fraction but usually result in insufficient solubility.

Third, the NPs should be highly dispersible in just one block of the block copolymer (*2*, *20*). Mixing should be driven by favorable enthalpic interactions between that block and the NPs, which can be achieved through ionic interactions, hydrogen bonding, and dipole-dipole interactions, among many possible routes.

Fourth, in order to promote mixing, the diameter of the NPs should be below a critical limit relative to the size of the block with which they mix, approximately the root mean square end-to-end distance (equivalent to $6^{1/2}$ times the radius of gyration for an ideal chain) of the relevant block of the copolymer (*21*). Although the precise cutoff may vary depending on enthalpic considerations and NP concentration, this heuristic provides a guideline for NP size.

We designed ligand-stabilized Pt NPs (Fig. 1, A and B) and a block copolymer (Fig. 1C) that met these four criteria. Two poly(isoprene-*block*-dimethylaminoethyl methacrylate), PI-*b*-PDMAEMA block copolymers (a and b) were synthesized by anionic polymerization (*22*) and had a polydispersity of 1.05 (a) or 1.04 (b) and molecular weights of 31.1 (a) or 27.8 (b) kg/mol, of which 33 (a) or 15 (b) weight % (wt %) was PDMAEMA. After examining a series of possible ligands for the Pt NPs, we selected *N,N*-di-2-propoxyethyl-*N*-3-mercaptopropyl-*N*-methylammonium chloride (Fig. 1A). The synthesis of this ligand as well as the ligand-stabilized Pt NPs are described in the supporting online material (SOM) (*23*).

Transmission electron microscopy (TEM) revealed that the NPs had a metal core diameter of 1.8 ± 0.5 nm (Fig. 2A), and a model of the ligand suggested a maximum radial extension of 1.4 nm (Fig. 1B). Nuclear magnetic resonance (NMR) confirmed the chemical structure of the ligand on the NPs, and thermogravimetric analysis (TGA) revealed a metal content of 56.9% by weight, or 7.5% by volume (SOM) (*23*). The NPs exhibited hydrophilic properties: They were highly soluble in methanol, modestly soluble in water and acetone, poorly soluble in chloroform, and insoluble in tetrahydrofuran and ether. We selected a solvent combination of chloroform and methanol [9:1 weight/weight (w/w)], in which both the block copolymer and NPs exhibited high solubility. The NPs were nearly insoluble in the absence of methanol, and the polymer precipitated in solutions with >20% methanol.

The as-synthesized NPs were too hydrophilic to form macroscopically homogeneous hybrids with PI-*b*-PDMAEMA when films were cast from a chloroform:methanol 9:1 (w/w) solution. The NPs became less hydrophilic upon aging. In particular, boiling the NPs for 5 hours in water decreased their hydrophilicity to the extent that they became more soluble in solvents of moderate or low polarity, such as tetrahydrofuran and chloroform. After aging, the NPs were centrifuged to remove the organic byproducts of the aging process. The metal content in the aged NPs was typically 65.4% by mass or 10.4% by volume. The Pt particle size remained unchanged at 1.8 nm,

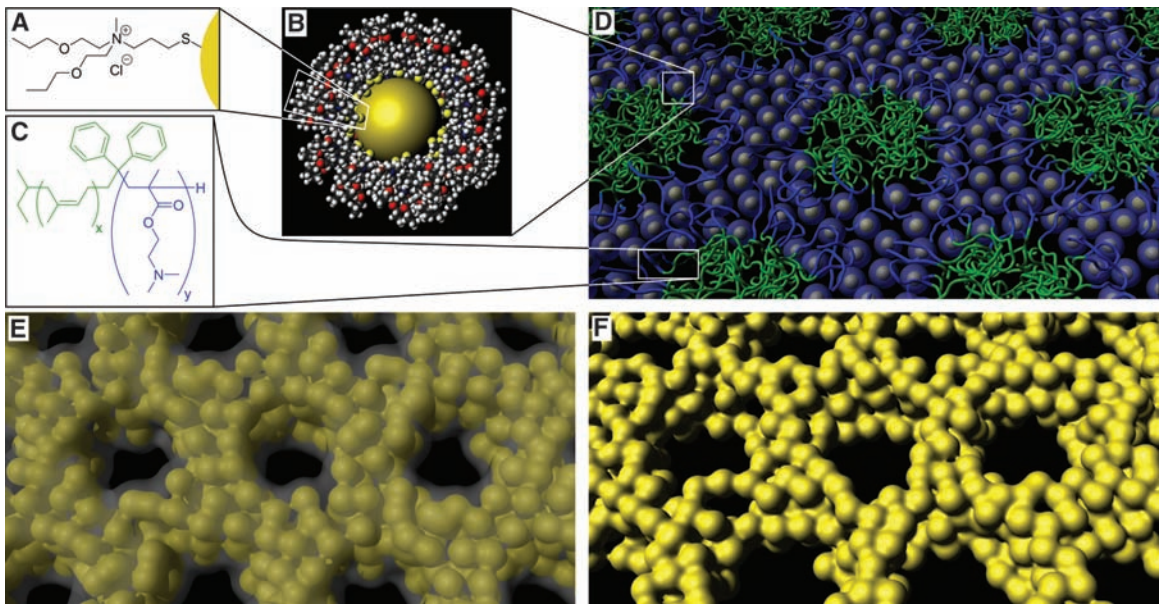

Fig. 1. Illustration of CCM-Pt-6 produced after each stage of the synthesis. (**A**) Chemical structure of *N,N*-di-2-propoxyethyl-*N*-3-mercaptopropyl-*N*-methylammonium chloride, the ligand used to produce moderately hydrophilic Pt NPs with high solubility. (**B**) A true-scale model of a NP with a 1.8-nm-diameter metal core and 1.4-nm ligand shell in which part of the metal surface is artificially exposed for illustrative purposes. The model has the same areal density of ligands as the aged NPs, with about 65 ligands per NP. (**C**) Chemical structure of PI-*b*-PDMAEMA; PI is green and PDMAEMA is blue. [(D) to (F)] Illustrations that attempt to convey the approximate mesostructure geometry and are based on experimental data. (**D**) Self-assembly of Pt NPs with block copolymer followed by annealing affords a hybrid with a regularly ordered structure, such as the inverse hexagonal morphology. (**E**) Pyrolysis of the hybrid under inert atmosphere produces a mesoporous Pt-C composite. (**F**) An Ar-O plasma treatment or acid etch of the Pt-C produces ordered mesoporous Pt.

as measured by TEM, and the Pt domain size increased from 1.2 to 1.4 nm, as determined by peak-width analysis of powder x-ray diffraction (PXRD, Fig. 3B). NMR of the aged NPs showed a spectrum nearly identical to that of the as-synthesized particles (SOM) (*23*). On average, a single aged NP had 65 ligands, a decrease from 93 in the as-synthesized NP (see SOM for calculation) (*23*). The loss of ligands upon heating has been previously documented for planar gold surfaces (*24*) and gold NPs (*25*). Interactions among polymer, ligands, metal surface, and solvents are complex, and the relative contribution of each to NP dispersibility is difficult to determine precisely. We speculate, however, that the substantial decrease in the number of charges per NP (as inferred from the loss of ligands) is responsible for the NPs' diminished hydrophilicity. Furthermore, the loss of ligand may enhance polymer-NP interactions because the PDMAEMA's amine may chemisorb onto the more exposed Pt surface (*26*), thereby preventing the macrophase separation of NPs from block copolymer. Finally, the loss of ligand from the NPs increases the volume fraction of Pt in the NPs by 39%, improving the ability of the mesostructure to survive pyrolysis.

A macroscopically homogeneous solution of aged NPs and block copolymer (a) was prepared by combining 98 mg of NPs, 28 mg of block copolymer, 1040 mg of chloroform, and 110 mg of methanol. The hydrophilic volume fraction [the volume fraction of PDMAEMA and nanoparticles; see SOM for calculations (*23*)] was 65%, which was anticipated to yield a hybrid with an inverse hexagonal mesostructure (CCM-Pt-6). The solution contents were transferred to an aluminum dish 1 cm in diameter and heated at 50°C beneath a hemispherical dish that was designed to slow solvent evaporation. Because chloroform's vapor pressure is greater than that of methanol, and because the solvent composition needed to be maintained near 9:1 chloroform: methanol, a 20-ml vial containing 4 g of chloroform was placed beneath the hemispherical dish, thereby slowing the evaporation of chloroform from the NP–block copolymer solution.

After 1 hour of heating at 50°C, nearly all the solvent had evaporated. The sample was a homogeneous, shiny black solid and was weak and brittle (Fig. 2B). Analysis of the sample by TEM (Fig. 2C) revealed that a mesostructure had formed. The order could be improved, however, by annealing CCM-Pt-6 at 130°C for 2 days under vacuum, as confirmed by small-angle x-ray scattering (SAXS) (Fig. 3A) and TEM (Fig. 2D). Comparison of representative SAXS patterns showed an increased intensity at higher-order reflections for the annealed sample, consistent with a hexagonal lattice (tick marks in Fig. 3A). This structural assignment was corroborated by TEM. The representative TEM image in Fig. 2D revealed an inverse hexagonal mesostructure with grain sizes on the order of a few micrometers. Examination of the mesostructure at higher magnification (Fig. 2E) revealed that individual Pt NPs composed the walls of the CCM-Pt-6 mesostructure, with three to five NPs spanning the thickness of the wall. Comparison of TGA profiles before and after annealing indicated a mass loss of 15% that arose from the loss of ligand (SOM) (*23*). Annealing the sample also caused the diameter of the Pt NPs to increase to 2.3 ± 0.3 nm, as measured by TEM (Fig. 2E). The annealing process thus improves hybrid order and also decomposes the ligands to the extent that the NPs merged and grew. The average grain size of the mesostructure did not increase substantially with longer annealing times, which suggests that ligand decomposition and NP growth were accompanied by a loss in NP mobility.

Besides inverse hexagonal mesostructures (CCM-Pt-6), samples with lamellar morphology (CCM-Pt-4) were produced. We used PI-*b*-PDMAEMA copolymers (a) or (b) to cast hybrids from solution with a hydrophilic volume fraction of 56%. Similarly to the CCM-Pt-6 hybrid, annealing at 130°C led to a well-developed mesostructure as confirmed by SAXS and corroborated by TEM (Figs. 2F and 3A). These results suggest that like oxide structures, metal NP–block co-

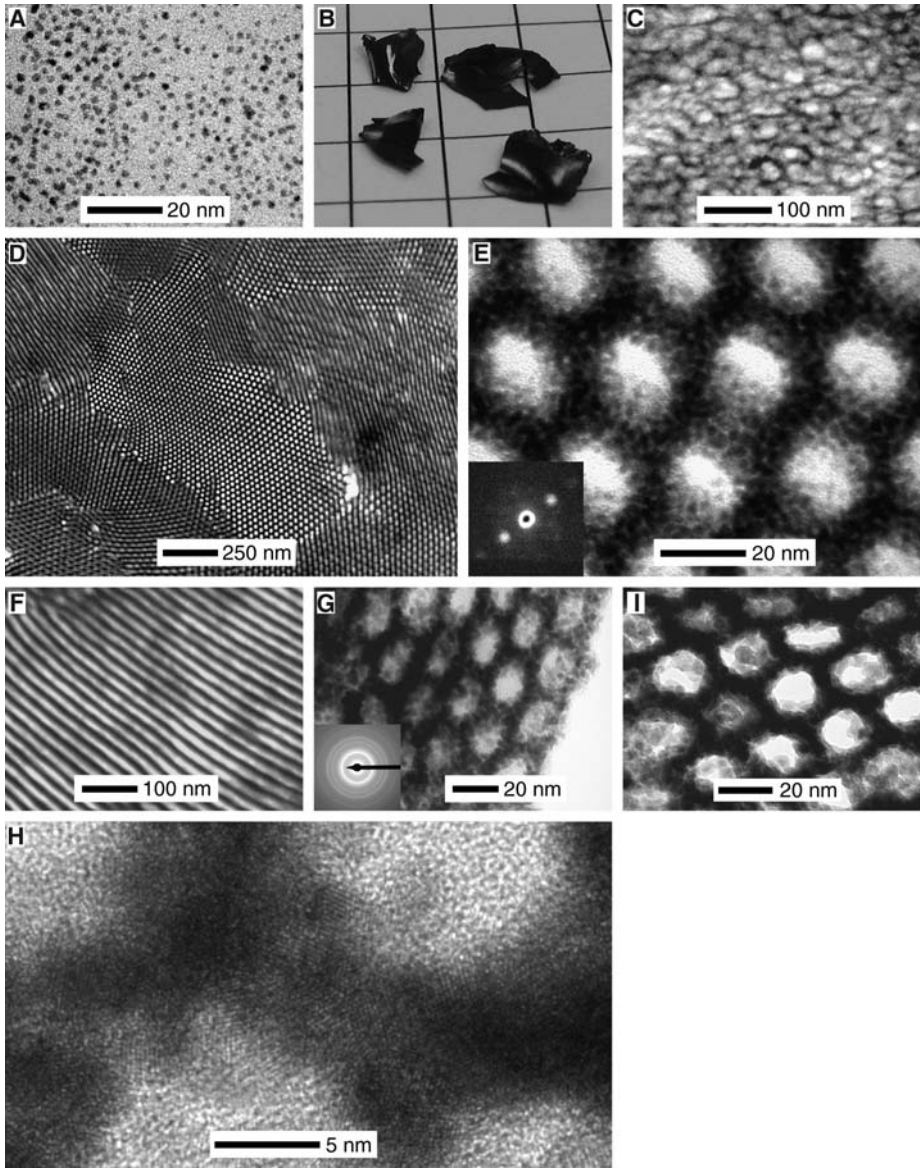

Fig. 2. Bright-field TEM images (A) and (C) to (I) and photograph (B) of materials produced after each stage of the synthesis. (**A**) Ligand-capped Pt NPs. (**B**) Pieces of unannealed CCM-Pt-6 inverse hexagonal hybrid film. The grid paper has 5-mm markings. (**C**) Unannealed inverse hexagonal hybrid. (**D**) An annealed inverse hexagonal hybrid. (**E**) Examination of the hybrid from (D) at higher magnification resolved individual Pt NPs, seen as dark spots in the bright-field image. (Inset) A typical convergent-beam electron diffraction pattern (seen with an ultra–high-vacuum scanning transmission electron microscope) from a single Pt NP, demonstrating its crystallinity. (**F**) An annealed CCM-Pt-4 lamellar hybrid. (**G**) Pyrolysis of an annealed inverse hexagonal hybrid yields a mesoporous Pt-C composite. (Inset) Selected area electron diffraction, showing Pt expected face-centered cubic scattering profile. (**H**) HRTEM of the pyrolized sample resolved the Pt's lattice fringes. (**I**) Removal of carbon with an Ar-O plasma yielded mesoporous inverse hexagonal Pt.

polymer hybrid morphologies can be tailored by simply adjusting the NP volume fraction (*27*).

We used a rapid pyrolysis process (*28*, *29*) to convert the inverse hexagonal hybrid CCM-Pt-6 to an ordered mesoporous Pt-C composite. We heated the sample at 10°C/min under N or Ar to at least 410°C, followed by immediate cooling. Under these conditions, the sp^2-hybridized carbons of the PI block decompose into an amorphous C-rich material with slight graphitic character (Fig. 4A) (*29*). As determined by TGA (SOM) (*23*), the pyrolysis led to a mass loss of 28%. Heating the material to temperatures as high as 550°C did not result in further mass loss. The pyrolysis was accompanied by a decrease in the (1,0) *d*-spacing from 30.0 to 23.7 nm, as revealed by analysis of the SAXS patterns (Fig. 3A). Characterization of the resulting material by TEM (Fig. 2G) indicated that the inverse hexagonal structure was preserved.

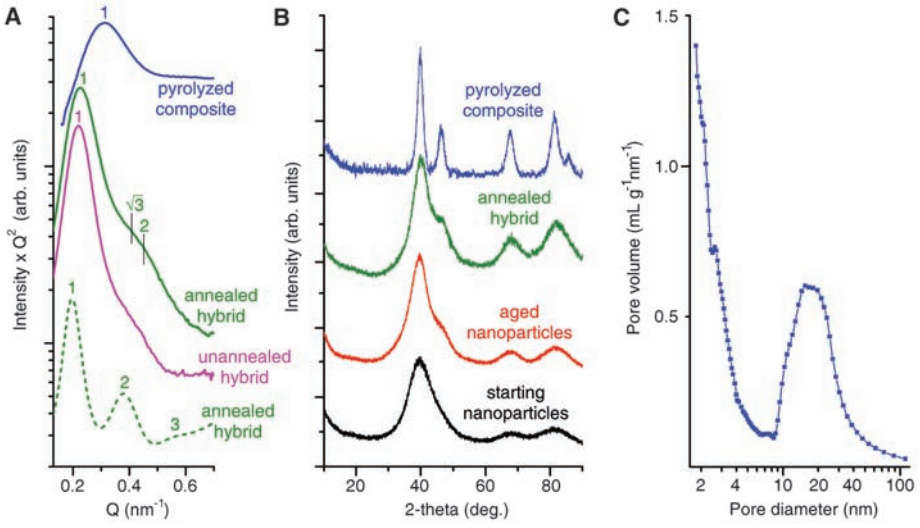

Fig. 3. X-ray and physisorption measurements of materials produced after each stage of the synthesis. (**A**) SAXS profiles of mesostructured materials. *Q*, scattering wavevector. Solid curves correspond to data consistent with an inverse hexagonal mesostructure (CCM-Pt-6), and the dashed curve corresponds to data consistent with a lamellar mesostructure (CCM-Pt-4). For hybrids with the suggested inverse hexagonal hybrid morphology, the (1,0) reflections of the unannealed, annealed, and pyrolized samples correspond to *d*-spacings of 30.3, 30.0, and 23.7 nm, respectively. The first-order reflection of the lamellar sample corresponds to 33.1 nm. Tick marks indicate positions of expected reflections. (**B**) PXRD of samples at various stages of the synthesis. The Pt domain size increases after each stage of processing, from 1.2 nm (starting NPs) to 1.4 nm (aged NPs) to 1.5 nm (annealed hybrid) to 4.1 nm (pyrolized composite), as determined by Scherrer analysis. (**C**) Barrett-Joyner-Halenda pore size distribution as derived from a N physisorption adsorption isotherm reveals a peak mesopore diameter of 17 nm.

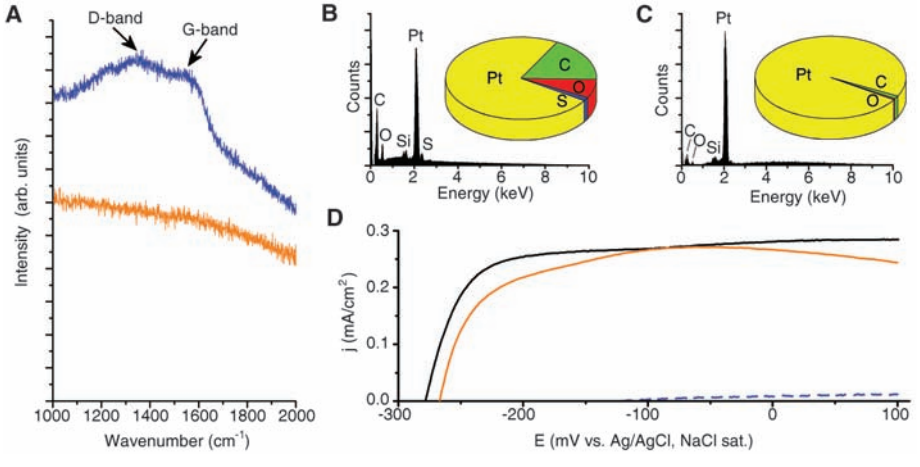

Fig. 4. (**A**) Raman spectra of pyrolized CCM-Pt-6 (top) and Ar-O plasma–treated CCM-Pt-6 (bottom). (**B**) EDS of pyrolized CCM-Pt-6. The pie chart displays elemental weight fractions. The sample was on a Si substrate and the primary energy was 10 keV. Pt = 74 wt %, C = 18 wt %, O = 7 wt %, and S = 1 wt %. (**C**) EDS of acid-treated CCM-Pt-6. Pt = 98 wt %, C = 1 wt %, and O = 0.5 wt %. (**D**) Polarization curves of the H_2 oxidation reaction in H_2-saturated 0.1 M H_2SO_4 solution (at 2000 rpm and 10 mV/s). Blue dashed line, mesoporous Pt-C nanocomposite; orange curve, mesoporous Pt; black curve, planar Pt electrode. *E*, potential; sat., saturated.

At the same time, the Pt interface had roughened, because of the growth of the NPs to 3.3 ± 0.9 nm in diameter. A roughened interface upon pyrolysis is consistent with the loss of higher-order peaks observed in the SAXS profile. Examination of the structure by high-resolution TEM (HRTEM) revealed lattice fringes throughout the Pt walls (Fig. 2H), showing that the walls were composed of crystalline Pt. Analysis by PXRD and application of the Scherrer equation indicated that the Pt nanocrystals' domain size was 4.1 ± 0.4 nm (Fig. 3B), representing a substantial increase from the aged NPs. Together, SAXS, PXRD, and TEM analyses provide a consistent picture of a metal-C composite that is macroscopically homogeneous and uniformly mesostructured.

The C plays an important role in maintaining open, uniform pores of CCM-Pt-6 during pyrolysis (*29*). If the hybrid is heated in air instead of an inert atmosphere, the C is removed (a mass loss of 38% occurs) and the mesostructure is lost. This suggests that the Pt NPs experienced reduced mobility and aggregation within the carbonaceous matrix. In contrast, in the absence of C, the NPs sinter in an uncontrolled fashion. The grainy texture in the TEM images after sintering is indicative of C with a low graphite content (Fig. 2, G and H, for TEM and Fig. 1E for illustration), which is confirmed by Raman spectroscopy (Fig. 4A). Graphitic C has signature D and G bands around 1350 cm^{-1} and 1550 cm^{-1}, respectively (*30*). The weak Raman signature of the C in the hybrid is probably caused by the relatively low temperature (410°C) reached during pyrolysis. Finally, N physisorption indicates that the mesopores are open (Fig. 3C) and that 26% of the sample's volume (micropores and mesopores) is open space, as expected for an inverse hexagonal nanocomposite that has pores lined with C. The Brunauer-Emmett-Teller surface area of CCM-Pt-6 is 18 m^2/g, and the pore diameter is 17 nm.

For many applications, such as fuel cells, it is desirable for the metal surface to be completely exposed. We thus sought a route to remove the C from the CCM-Pt-6 nanocomposite. Heating the pyrolized sample in air to 500°C removed the C but also caused the mesostructure to collapse. Instead, we could remove the C from microtomed thin films (~50 nm thick) of the CCM-Pt-6 nanocomposite using an Ar-O plasma. The mesoporous Pt was structurally similar to the Pt-C nanocomposite, as determined by TEM (Fig. 2I). Close inspection of the pores in TEM images revealed that the grainy texture indicative of the C had disappeared. Furthermore, Raman spectra showed the absence of the D and G bands, suggesting that the C material had been successfully removed (Fig. 4A). Alternatively, for thicker films (10 to 100 μm thick), a sulfuric acid:nitric acid 3:1 (v/v) etch at 70°C (*31*) successfully removed most C. Electrochemical data from acid-etched samples indeed confirmed that the metal surface was exposed, showing current densities nearly identical

to that of bulk Pt (Fig. 4D). Energy-dispersive spectroscopy (EDS) on the CCM-Pt-6 metal-C nanocomposites (Fig. 4B) showed a composition of 74 wt % Pt, 18 wt % C, 7 wt % O, and 1 wt % S. In contrast, after the plasma treatment, EDS revealed that >98 wt % of the sample was Pt, with only trace contributions from C and O (Fig. 4C). C removal was further confirmed by TGA. Pyrolized samples retained 80% of the original mass when heated to 550°C in air, whereas C-etched samples retained 97% of their original mass. TEM confirmed that the samples were still mesostructured and that the grainy texture indicative of C had disappeared.

Because of the easier accessibility of large quantities, we measured the electrical conductivity only of CCM-Pt-6 Pt-C nanocomposites. We chose two-point measurements, which slightly underestimate the true conductivity, because the pyrolized Pt-C composites were too fragile for a four-point measurement, even when pressed as a pellet (*32*). The NP-polymer hybrid had a conductivity of 2.5 mS/cm, which increased to 400 S/cm upon pyrolysis. Despite the presence of C, to the best of our knowledge this value represents the highest electrical conductivity yet measured for ordered mesoporous materials derived from block copolymers.

Because polymer-NP interactions are largely mediated via the nanoparticle ligands, it may be possible to extend the present approach to other metals for which similarly sized ligand-stabilized NPs can be synthesized. Thus, it may be possible to prepare ordered mesoporous metals of other elements, disordered alloys, or even ordered intermetallics. Furthermore, this discovery also creates a potential pathway to a new class of ordered mesoporous metals made from nanoparticles of distinct compositions. Such nanoheterogeneous mesoporous metals may have a range of exceptional electrical, optical, and catalytic properties.

References and Notes

1. A. Haryono, W. H. Binder, *Small* **2**, 600 (2006).
2. A. C. Balazs, T. Emrick, T. P. Russell, *Science* **314**, 1107 (2006).
3. M. Raney, U.S. Patent 1,628,190 (1927).
4. Y. N. C. Chan, R. R. Schrock, R. E. Cohen, *Chem. Mater.* **4**, 24 (1992).
5. D. E. Fogg, L. H. Radzilowski, R. Blanski, R. R. Schrock, E. L. Thomas, *Macromolecules* **30**, 417 (1997).
6. B. J. Kim, G. H. Fredrickson, C. J. Hawker, E. J. Kramer, *Langmuir* **23**, 7804 (2007).
7. P. Buffat, J.-P. Borel, *Phys. Rev. A* **13**, 2287 (1976).
8. R. Li, K. Sieradzki, *Phys. Rev. Lett.* **68**, 1168 (1992).
9. J. Erlebacher, M. J. Aziz, A. Karma, N. Dimitrov, K. Sieradzki, *Nature* **410**, 450 (2001).
10. G. S. Attard *et al.*, *Science* **278**, 838 (1997).
11. G. S. Attard, C. G. Göltner, J. M. Corker, S. Henke, R. H. Templer, *Angew. Chem. Int. Ed. Engl.* **36**, 1315 (1997).
12. Y. Yamauchi, T. Yokoshima, T. Momma, T. Osaka, K. Kuroda, *J. Mater. Chem.* **14**, 2935 (2004).
13. J. Jiang, A. Kucernak, *Chem. Mater.* **16**, 1362 (2004).
14. D. Y. Zhao *et al.*, *Science* **279**, 548 (1998).
15. M. E. Davis, *Nature* **417**, 813 (2002).
16. W. A. Lopes, H. M. Jaeger, *Nature* **414**, 735 (2001).
17. J. Chai, D. Wang, X. Fan, J. M. Buriak, *Nat. Nanotechnol.* **2**, 500 (2007).
18. S. C. Warren *et al.*, *J. Am. Chem. Soc.* **128**, 12074 (2006).
19. S. Sivaramakrishnan, P.-J. Chia, Y.-C. Yeo, L.-L. Chua, P. K. H. Ho, *Nat. Mater.* **6**, 149 (2007).
20. R. B. Thompson, V. V. Ginzburg, M. W. Matsen, A. C. Balazs, *Science* **292**, 2469 (2001).
21. S. C. Warren, F. J. DiSalvo, U. Wiesner, *Nat. Mater.* **6**, 156 (2007).
22. S. Creutz, P. Teyssie, R. Jerome, *Macromolecules* **30**, 6 (1997).
23. See SOM on *Science* Online.
24. E. Delamarche, B. Michel, H. Kang, C. Gerber, *Langmuir* **10**, 4103 (1994).
25. M. J. Hostetler, A. C. Templeton, R. W. Murray, *Langmuir* **15**, 3782 (1999).
26. B. J. Kim, J. Bang, C. J. Hawker, E. J. Kramer, *Macromolecules* **39**, 4108 (2006).
27. M. Templin *et al.*, *Science* **278**, 1795 (1997).
28. C. Liang, K. Hong, G. A. Guiochon, J. W. Mays, S. Dai, *Angew. Chem. Int. Ed.* **43**, 5785 (2004).
29. J. Lee *et al.*, *Nat. Mater.* **7**, 222 (2008).
30. A. C. Ferrari, J. Robertson, *Phys. Rev. B* **61**, 14095 (2000).
31. J. Liu *et al.*, *Science* **280**, 1253 (1998).

32. For future uses in bulk, the material probably will be protected from impact and other damage. Brittleness will not be an issue in static thin-film geometries that are most relevant for applications.

33. The authors acknowledge support of this research by the U.S. Department of Energy (grant DE-FG02-03ER46072) and NSF through a single investigator award (DMR-0605856) as well as through the Cornell Center for Materials Research with funding from the Materials Research Science and Engineering Center program of NSF (cooperative agreement DMR 0520404). X-ray diffraction at the Cornell High Energy Synchrotron Source (CHESS) is supported by NSF under award DMR-0225180. S.C.W. acknowledges support from the Environmental Protection Agency Science to Achieve Results fellowship program. The authors thank H. Abruña for valuable discussions and M. Thomas, A. Burns, J. Lee, and A. Woll for assistance with single-particle electron diffraction, EDS, Raman spectroscopy, and SAXS experimental setup, respectively. A patent application has been submitted based on the findings in this work.

Supporting Online Material

www.sciencemag.org/cgi/content/full/320/5884/1748/DC1
Materials and Methods
SOM Text
Schemes S1 to S3
Figs. S1 to S13
Tables S1 and S2
References

2 May 2008; accepted 29 May 2008
10.1126/science.1159950

Very-High-Energy Gamma Rays from a Distant Quasar: How Transparent Is the Universe?

The MAGIC Collaboration*

The atmospheric Cherenkov gamma-ray telescope MAGIC, designed for a low-energy threshold, has detected very-high-energy gamma rays from a giant flare of the distant Quasi-Stellar Radio Source (in short: radio quasar) 3C 279, at a distance of more than 5 billion light-years (a redshift of 0.536). No quasar has been observed previously in very-high-energy gamma radiation, and this is also the most distant object detected emitting gamma rays above 50 gigaelectron volts. Because high-energy gamma rays may be stopped by interacting with the diffuse background light in the universe, the observations by MAGIC imply a low amount for such light, consistent with that known from galaxy counts.

Ground-based gamma-ray telescopes are sensitive to the Cherenkov light emitted by the electromagnetic showers that are produced by gamma rays interacting in the atmosphere. These telescopes have discovered, since the first detection (in 1989) of gamma rays in this energy range (from 100 GeV to several TeV), more than 20 blazars, which are thought to be powered by accretion of matter onto supermassive black holes residing in the centers of galaxies, and ejecting relativistic jets at small angles to the line of sight (*1*). Most of these objects are of the BL Lac type, with weak or no optical emission lines. Quasar 3C 279 shows optical emission lines that allow a good redshift determination. Satellite observations with the Energetic Gamma Ray Experiment Telescope (EGRET) aboard the Compton Gamma Ray Observatory (CGRO) had measured gamma rays from 3C 279 (*2*) and other quasars, but only up to energies of a few GeV, the limit of the detector's sensitivity. An upper limit for the flux of very-high-energy (VHE) gamma rays was derived in (*3*).

Using MAGIC, the world's largest single-dish gamma-ray telescope (*4*) on the Canary island of La Palma (2200 m above sea level, 28.4°N, 17.54°W), we detected gamma rays at energies from 80 to >300 GeV, emanating from 3C 279 at a redshift of 0.536, which corresponds to a light-travel time of 5.3 billion years. No object has been seen before in this range of VHE gamma-ray energies at such a distance [the highest redshift previously observed was 0.212 (*5*)], and no quasar has been previously identified in this range of gamma-ray energies.

The detection of 3C 279 is important, because gamma rays at very high energies from distant sources are expected to be strongly attenuated in intergalactic space by the possible interaction with low-energy photons ($\gamma + \gamma \rightarrow e^+ + e^-$). These photons [extragalactic back-

*The complete list of authors and their affiliations appears at the end of this paper.

ground light (EBL) (*6*)] have been radiated by stars and galaxies in the course of cosmic history. Their collective spectrum has evolved over time and is a function of distance. For 3C 279, the range of newly probed EBL wavelengths lies between 0.2 and 0.8 μm (ultraviolet/optical). Existing instruments that are sensitive only to higher gamma-ray energies have so far been unable to probe this domain; by contrast, MAGIC is specifically designed to reach the lowest-energy threshold among ground-based detectors.

In observations of 3C 279 over 10 nights between late January and April 2006 (total of 9.7 hours), the gamma-ray source was clearly detected (at >6 SDs) on the night of 23 February, and may also have been detected the night before (Fig. 1). As determined by the χ^2 test, the probability that the gamma-ray flux on all 10 nights was zero is 2.3×10^{-7}, corresponding to 5.04σ in a Gaussian distribution [see (*7*)]. Simultaneous optical R-band observations, by the Tuorla Observatory Blazar Monitoring Program with the 1.03-m telescope at the Tuorla Observatory, Finland, and by the 35-cm Kungliga Vetenskapsakademien (Royal Swedish Academy of Sciences) telescope on La Palma, revealed that during the MAGIC observations, the gamma-ray source was in a generally high optical state, a factor of 2 above the long-term baseline flux, but with no indication of short time-scale variability at visible wavelengths. The observed VHE spectrum (Fig. 2) can be described by a power law with a differential photon spectral index of $\alpha = 4.1 \pm 0.7_{stat} \pm 0.2_{syst}$. The measured integrated flux above 100 GeV on 23 February is $(5.15 \pm 0.82_{stat} \pm 1.5_{syst}) \times 10^{-10}$ photons cm^{-2} s^{-1}.

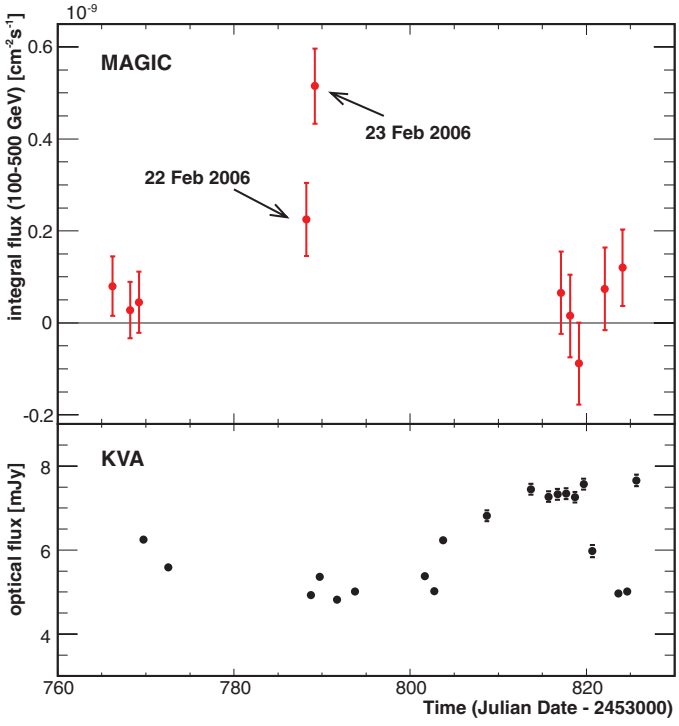

Fig. 1. Light curves. MAGIC (top) and optical R-band data (bottom) obtained for 3C 279 from February to March 2006. The long-term baseline for the optical flux is at 3 mJy.

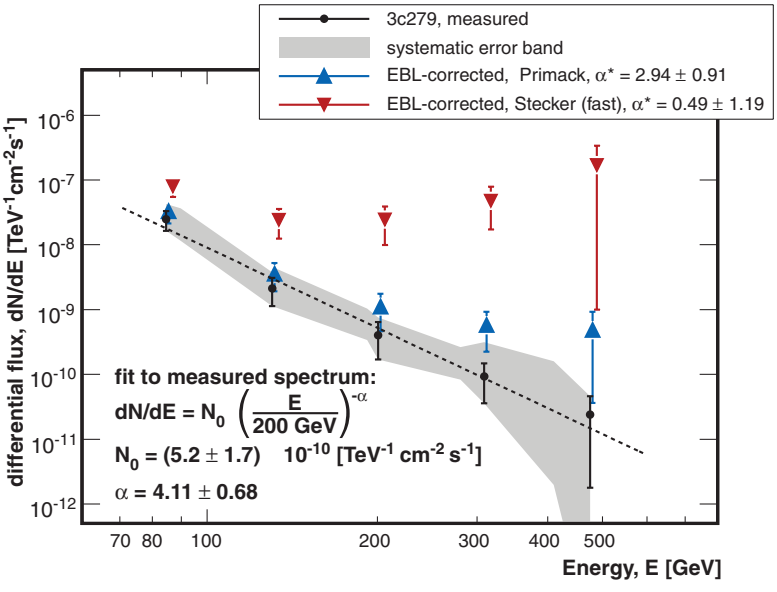

Fig. 2. Spectrum of 3C 279 measured by MAGIC. The gray area includes the combined statistical (1σ) and systematic errors, and underlines the marginal significance of detections at high energy. The dotted line shows compatibility of the measured spectrum with a power law of photon index α = 4.1. The blue and red triangles are measurements corrected on the basis of the two models for EBL density, discussed in the text.

The EBL influences the observed spectrum and flux, resulting in an exponential decrease with energy and a cutoff in the gamma-ray spectrum. Several models have been proposed for the EBL (*6*). All have limited predictive power for the EBL density, particularly as a function of time, because many details of star and galaxy evolution remain uncertain. We illustrate the uncertainty in the EBL by using two extreme models: a model by Primack *et al.* (*8*), close to the lowest possible attenuation consistent with the lower EBL limit from galaxy counts (*9*, *10*); and a "fast-evolution" model by Stecker *et al.* (*11*), corresponding to the highest attenuation of all the models. We refer to these models as "low" and "high," respectively. The measured spectra of 3C 279, corrected for absorption according to these two models, are shown in Fig. 2. They represent the range for the possible intrinsic gamma-ray flux of the source.

A power-law fit to the EBL-corrected points (*12*) results in an intrinsic photon index of $\alpha^* = 2.9 \pm 0.9_{stat} \pm 0.5_{syst}$ (low) and $\alpha^* = 0.5 \pm 1.2_{stat} \pm 0.5_{syst}$ (high). The systematic error is determined by shifting the absolute energy scale by the estimated energy error of 20% and recalculating the intrinsic spectrum. Further discussion of the intrinsic spectrum and the spectral energy density can be found in (*7*).

The measured spectrum of 3C 279 permits a test of the transparency of the universe to gamma rays. The distance at which the flux of photons of a given energy is attenuated by a factor *e* (i.e., the path corresponding to an optical depth τ = 1) is called the gamma-ray horizon and is commonly expressed as a function of the redshift parameter (*13*); we show this energy/redshift relation in Fig. 3. In the context of Fig. 3, we make use of a model based on (*14*) with parameters adapted to the limits given by (*15*) and fine-tuned such that for 3C 279, the intrinsic photon index is $\alpha^* = 1.5$. The tuning allows for the statistical and systematic errors (1 SD, added linearly). Although the intrinsic spectrum emitted by 3C 279 is unknown, $\alpha^* = 1.5$ is the lowest value given for EGRET sources (not

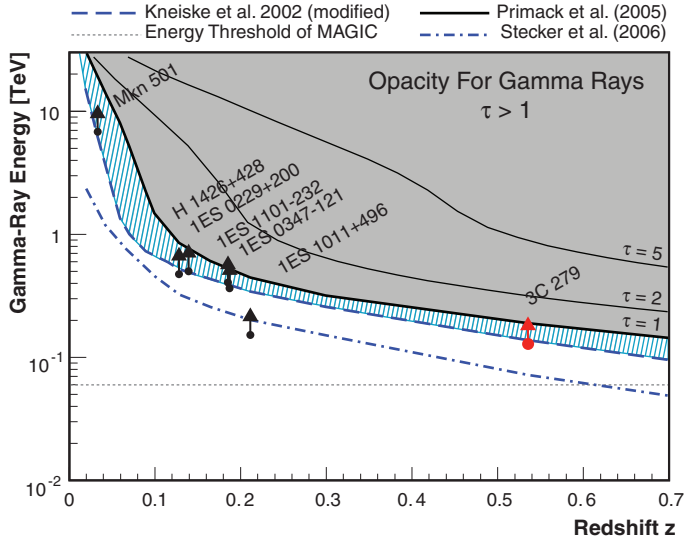

Fig. 3. The gamma-ray horizon. The redshift region over which the gamma-ray horizon can be constrained by observations has been extended up to $z = 0.536$. The prediction range of EBL models is illustrated by (*8*) (thick solid black line) and (*11*) (dashed-dotted blue line). The tuned model of (*14*) (dashed blue line) represents an upper EBL limit based on our 3C 279 data, obtained on the assumption that the intrinsic photon index is ≥1.5 (red arrow). Limits obtained for other sources are shown by black arrows, most of which lie very close to the model (*14*). The narrow blue band is the region allowed between this model and a maximum possible transparency (i.e., minimum EBL level) given by (*8*), which is nearly coincident with galaxy counts. The gray area indicates an optical depth $\tau > 1$, i.e., the flux of gamma rays is strongly suppressed. To illustrate the strength of the attenuation in this area, we also show energies for $\tau = 2$ and $\tau = 5$ (thin black lines), again with (*8*) as model.

affected by the EBL) and all spectra measured by gamma-ray telescopes so far (*16*), so we assume this to be the hardest acceptable spectrum. The region allowed between the maximum EBL determined by the above procedure and that from galaxy counts (*8*) is very small.

The results support, at higher redshift, the conclusion drawn from earlier measurements (*15*) that the observations of the Hubble Space Telescope and Spitzer correctly estimate most of the light sources in the universe. The derived limits are consistent with the EBL evolution corresponding to a maximum star-formation rate at redshift $z \geq 1$, as suggested by (*8*) and similar models.

The emission mechanism responsible for the observed VHE radiation remains uncertain. Leptonic emission models (assuming relativistic electrons in the jet as the source of the gamma rays), generally successful in describing blazar data [e.g., (*17*)], can, with some assumptions, also accommodate the MAGIC spectrum. Hadronic models [involving relativistic protons, e.g. (*18*)] provide a possible alternative. However, a genuine test of the models can be obtained only with simultaneous observations at different wavelengths, which are not available for the observations described here. Future tests of these models should use observations from sources at all wavelengths from radio to VHE gamma rays. In the domain of VHE gamma rays, we can expect important new insights by simultaneous observations with the Large Area Telescope (LAT), the high-energy gamma-ray instrument on the Gamma Ray Large Area Space Telescope [GLAST (*19*)]. Our observations of this distant source in VHE gamma rays demonstrate that a large fraction of the universe is accessible to VHE astronomy.

References and Notes

1. R. D. Blandford, M. J. Rees, *Astrophys. Lett.* **10**, 77 (1972).
2. R. C. Hartman *et al.*, *Astrophys. J.* **385**, L1 (1992).
3. F. Aharonian *et al.*, *Astron. Astrophys.* **478**, 387 (2008).
4. E. Lorenz, *N. Astron. Rev.* **48**, 339 (2004).
5. J. Albert *et al.*, *Astrophys. J.* **667**, L21 (2007).
6. M. G. Hauser, E. Dwek, *Annu. Rev. Astron. Astrophys.* **39**, 249 (2001).
7. Further information on data and methods and additional discussion are available on *Science* Online.
8. J. R. Primack, J. S. Bullock, R. S. Somerville, in *High Energy Gamma-Ray Astronomy*, American Institute of Physics Conference Series, F. Aharonian, H. Voelk, D. Horns, Eds. (American Institute of Physics, Heidelberg, 2005), vol. 745, p. 23.
9. P. Madau, L. Pozzetti, *Mon. Not. R. Astron. Soc.* **312**, L9 (2000).
10. G. Fazio *et al.*, *Astrophys. J. Suppl. Ser.* **154**, 39 (2004).
11. F. W. Stecker, M. A. Malkan, S. T. Scully, *Astrophys. J.* **648**, 774 (2006).
12. We approximate the intrinsic energy spectrum by $dN/dE \propto E^{-\alpha^*}$, where α^* is the intrinsic photon spectral index.
13. G. G. Fazio, F. W. Stecker, *Nature* **226**, 135 (1970).
14. T. M. Kneiske, K. Mannheim, D. H. Hartmann, *Astron. Astrophys.* **386**, 1 (2002).
15. F. Aharonian *et al.*, *Nature* **440**, 1018 (2006).
16. According to recent simulations (*20*), photon indices of <1.5 cannot be entirely excluded.
17. L. Maraschi, G. Ghisellini, A. Celotti, *Astrophys. J.* **397**, L5 (1992).
18. K. Mannheim, P. L. Biermann, *Astron. Astrophys.* **251**, L21 (1992).
19. S. Funk *et al.* (GLAST-LAT Collaboration), *GLAST and Ground-Based γ-Ray Astronomy*, SLAC-PUB-12871; www-glast.stanford.edu/.
20. F. W. Stecker, M. G. Baring, E. J. Summerlin, *Astrophys. J.* **667**, L29 (2007).

21. We thank the Instituto de Astrofisica de Canarias for the excellent working conditions at the Observatorio del Roque de los Muchachos in La Palma, Canary Islands. The support of the German Bundesministerium für Bildung und Forschung and Max-Planck Gesellschaft, the Italian Istituto Nazionale di Fisica Nucleare (INFN), and the Spanish Centro de Investigaciòn Cientifica y Technologica is gratefully acknowledged. This work was also supported by ETH (research grant TH 34/043) and the Polish MNil (grant 1P03D01028).

The MAGIC Collaboration: J. Albert,[1] E. Aliu,[2] H. Anderhub,[3] L. A. Antonelli,[4] P. Antoranz,[5] M. Backes,[6] C. Baixeras,[7] J. A. Barrio,[5] H. Bartko,[8] D. Bastieri,[9] J. K. Becker,[6] W. Bednarek,[10] K. Berger,[1] E. Bernardini,[11] C. Bigongiari,[9] A. Biland,[3] R. K. Bock,[8,9]* G. Bonnoli,[12] P. Bordas,[13] V. Bosch-Ramon,[13] T. Bretz,[1] I. Britvitch,[3] M. Camara,[5] E. Carmona,[8] A. Chilingarian,[14] S. Commichau,[3] J. L. Contreras,[5] J. Cortina,[2] M. T. Costado,[15,16] S. Covino,[4] V. Curtef,[6] F. Dazzi,[9] A. De Angelis,[17] E. De Cea del Pozo,[18] R. de los Reyes,[5] B. De Lotto,[17] M. De Maria,[17] F. De Sabata,[17] C. Delgado Mendez,[15] A. Dominguez,[19] D. Dorner,[1] M. Doro,[9] M. Errando,[2] M. Fagiolini,[12] D. Ferenc,[20] E. Fernández,[2] R. Firpo,[2] M. V. Fonseca,[5] L. Font,[7] N. Galante,[8] R. J. García López,[15,16] M. Garczarczyk,[8] M. Gaug,[15] F. Goebel,[8] M. Hayashida,[8] A. Herrero,[15,16] D. Höhne,[1] J. Hose,[8] C. C. Hsu,[8] S. Huber,[1] T. Jogler,[8] T. M. Kneiske,[6] D. Kranich,[3] A. La Barbera,[4] A. Laille,[20] E. Leonardo,[12] E. Lindfors,[21] S. Lombardi,[9] F. Longo,[17] M. López,[9] E. Lorenz,[3,8] P. Majumdar,[8] G. Maneva,[22] N. Mankuzhiyil,[17] K. Mannheim,[1] L. Maraschi,[4] M. Mariotti,[9] M. Martínez,[2] D. Mazin,[2] M. Meucci,[12] M. Meyer,[1] J. M. Miranda,[5] R. Mirzoyan,[8] S. Mizobuchi,[8] M. Moles,[19] A. Moralejo,[2] D. Nieto,[5] K. Nilsson,[21] J. Ninkovic,[8] N. Otte,[8,23]† I. Oya,[5] M. Panniello,[15]‡ R. Paoletti,[12] J. M. Paredes,[13] M. Pasanen,[21] D. Pascoli,[9] F. Pauss,[3] R. G. Pegna,[12] M. A. Perez-Torres,[19] M. Persic,[17,24] L. Peruzzo,[9] A. Piccioli,[12] F. Prada,[19] E. Prandini,[9] N. Puchades,[2] A. Raymers,[14] W. Rhode,[6] M. Ribó,[13] J. Rico,[25,2] M. Rissi,[3] A. Robert,[7] S. Rügamer,[1] A. Saggion,[9] T. Y. Saito,[8] M. Salvati,[4] M. Sanchez-Conde,[19] P. Sartori,[9] K. Satalecka,[11] V. Scalzotto,[9] V. Scapin,[17] R. Schmitt,[1] T. Schweizer,[8] M. Shayduk,[8,23] K. Shinozaki,[8] S. N. Shore,[26] N. Sidro,[2] A. Sierpowska-Bartosik,[18] A. Sillanpää,[21] D. Sobczynska,[10] F. Spanier,[1] A. Stamerra,[12] L. S. Stark,[3] L. Takalo,[21] F. Tavecchio,[4] P. Temnikov,[22] D. Tescaro,[2] M. Teshima,[8] M. Tluczykont,[11] D. F. Torres,[25,18] N. Turini,[12] H. Vankov,[22] A. Venturini,[9] V. Vitale,[17] R. M. Wagner,[8] W. Wittek,[8] V. Zabalza,[13] F. Zandanel,[19] R. Zanin,[2] J. Zapatero[7]

[1]Universität Würzburg, D-97074 Würzburg, Germany. [2]Institut de Física d'Altes Energies, Edifici Cn., Campus UAB, E-08193 Bellaterra, Spain. [3]ETH Zurich, CH-8093 Zurich, Switzerland. [4]Istituto Nazionale di Astrofisica (INAF) National Institute for Astrophysics, I-00136 Rome, Italy. [5]Universidad Complutense, E-28040 Madrid, Spain. [6]Technische Universität Dortmund, D-44221 Dortmund, Germany. [7]Universitat Autònoma de Barcelona, E-08193 Bellaterra, Spain. [8]Max-Planck-Institut für Physik, D-80805 München, Germany. [9]Università di Padova and INFN, I-35131 Padova, Italy. [10]University of Łódź, PL-90236 Lodz, Poland. [11]DESY Deutsches Elektronen-Synchrotron D-15738 Zeuthen, Germany. [12]Università di Siena, and INFN Pisa, I-53100 Siena, Italy. [13]Universitat de Barcelona Institut de Ciencias del Cosmos–Institut d'Estudis Especials de Catalunya (IEEC), E-08028 Barcelona, Spain. [14]Yerevan Physics Institute, AM-375036 Yerevan, Armenia. [15]Instituto de Astrofisica de Canarias, E-38200, La Laguna, Tenerife, Spain. [16]Departamento de Astrofisica, Universidad, E-38206 La Laguna, Tenerife, Spain. [17]Università di Udine, and INFN Trieste, I-33100 Udine, Italy. [18]Institut de Cienciès de l'Espai [IEEC-Consejo Superior de Investigaciones Cientificas (CSIC)], E-08193 Bellaterra, Spain. [19]Inst. de Astrofisica de Andalucia (CSIC), E-18080 Granada, Spain. [20]University of California, Davis, CA 95616–8677, USA. [21]Tuorla Observatory, Turku University, FI-21500 Piikkiö, Finland. [22]Institute for Nuclear Research and Nuclear Energy, BG-1784 Sofia, Bulgaria. [23]Humboldt-Universität zu Berlin, D-12489 Berlin, Germany. [24]INAF/Osservatorio Astronomico and INFN, I-34143 Trieste, Italy. [25]Institució Catalana de Recerca i Estudis Avancats, E-08010 Barcelona, Spain. [26]Università di Pisa, and INFN Pisa, I-56126 Pisa, Italy.

*To whom correspondence should be addressed. E-mail: rkbock@gmail.com
†Present address: Santa Cruz Institute for Particle Physics, University of California, Santa Cruz, CA 95064, USA.
‡Deceased.

Supporting Online Material

www.sciencemag.org/cgi/content/full/320/5884/1752/DC1
SOM Text
Figs. S1 to S3
References

27 February 2008; accepted 27 May 2008
10.1126/science.1157087

The Role of Interstitial Sites in the Ti*3d* Defect State in the Band Gap of Titania

Stefan Wendt,[1] Phillip T. Sprunger,[1,2] Estephania Lira,[1] Georg K. H. Madsen,[1] Zheshen Li,[1] Jonas Ø. Hansen,[1] Jesper Matthiesen,[1] Asger Blekinge-Rasmussen,[1] Erik Lægsgaard,[1] Bjørk Hammer,[1]* Flemming Besenbacher[1]*

Titanium dioxide (TiO_2) has a number of uses in catalysis, photochemistry, and sensing that are linked to the reducibility of the oxide. Usually, bridging oxygen (O_{br}) vacancies are assumed to cause the Ti*3d* defect state in the band gap of rutile TiO_2(110). From high-resolution scanning tunneling microscopy and photoelectron spectroscopy measurements, we propose that Ti interstitials in the near-surface region may be largely responsible for the defect state in the band gap. We argue that these donor-specific sites play a key role in and may dictate the ensuing surface chemistry, such as providing the electronic charge required for O_2 adsorption and dissociation. Specifically, we identified a second O_2 dissociation channel that occurs within the Ti troughs in addition to the O_2 dissociation channel in O_{br} vacancies. Comprehensive density functional theory calculations support these experimental observations.

Titanium dioxide (TiO_2), or titania, is used in a number of technological areas, including heterogeneous catalysis, photocatalysis, solar cells, gas sensors, waste remediation, and biocompatible materials. In its stoichiometric form, titania is an inert wide–band gap insulator; however, its applications are enabled by excess electrons originating from the defect state that is located within the band gap of reduced titania (TiO_{2-x}). Understanding the origin of the defect state is important for improving or expanding the scope of titania-based systems for specific applications. For example, the enhanced catalytic activity of titania-supported gold nanoparticles is coupled to local properties at the interface between gold and reduced titania (*1*–*4*).

Conventionally, the Ti*3d* derived state in the band gap (*5*–*7*) at ~0.85 eV below the Fermi level (E_F) has been fully ascribed to bridging oxygen (O_{br}) vacancies, because, in an ionic picture, the two excess electrons per O_{br} vacancy may be transferred to neighboring Ti atoms (*5*, *6*, *8*–*11*). This hypothesis was proposed more than three decades ago based on ultraviolet photoelectron spectroscopy (UPS) and low-energy electron-diffraction measurements on the TiO_2(110)–(1 × 1) surface (*8*), and has been generally accepted for years (*5*, *6*, *9*, *11*). In the UPS studies, this proposed O-vacancy model has largely been based on experimental observations that the defect state can be eliminated by O_2 exposure (*8*, *12*, *13*). Further possible support for the O-vacancy model came from scanning tunneling microscopy (STM) (*14*–*17*) and atomic force microscopy (*18*) studies, where O_{br} vacancies have been clearly identified on TiO_2(110). Although most first-principles density functional theory (DFT) calculations have not reproduced the experimentally observed state in the band gap (*11*), numerous theoretical papers still favor the O-vacancy model (*6*, *11*).

Nevertheless, the importance of Ti interstitials in rutile TiO_2(110) crystals has been noted. For example, the reoxidation of sputtered TiO_2(110) surfaces via vacuum annealing has been explained by Ti interstitial diffusion into the bulk (*19*–*21*). Similarly, when a reduced TiO_2(110) crystal is exposed to O_2 at elevated temperatures, diffusion of Ti interstitials to the surface has been reported (*2*, *22*–*24*). Therefore, in addition to O vacancies, Ti interstitials must also be considered as defect sites that may influence and even dictate the surface chemistry of titania.

By means of high-resolution STM and photoelectron spectroscopy (PES) measurements in conjunction with DFT calculations, we have systematically explored the origin of the Ti*3d* defect state in the band gap. We found that the gap state remains almost unchanged on surfaces where the O_{br} vacancies (or bridging OH groups) have been removed. To explain this finding, we propose that the gap state mainly stems from surplus Ti atoms in the near-surface region, most likely on interstitial sites. In addition to an O_2 dissociation channel in O_{br} vacancies, we discovered a non–vacancy-related O_2 dissociation channel that occurs within the Ti troughs.

The TiO_2(110)–(1 × 1) surface consists of alternating rows of fivefold-coordinated Ti (5f-Ti) atoms (the Ti troughs) and protruding, twofold-coordinated O_{br} atoms. As bulk Ti atoms in stoichiometric rutile, the Ti atoms underneath the O_{br} atoms are sixfold-coordinated. Ion-sputtering and vacuum-annealing the TiO_2(110) crystal results in a reduced n-type semiconductor, with a bulk conductivity that allows the use of STM and other electron spectroscopy techniques. Consistent with previous findings (*6*), the STM images (Fig. 1) of the TiO_2(110) surface are dominated by electronic effects; that is, the bright rows correspond to the Ti troughs, whereas geometrically protruding O_{br} atoms appear as the dark troughs in the STM images (*6*).

A high-resolution STM image recorded on a clean reduced TiO_2(110) surface [*r*-TiO_2(110)]

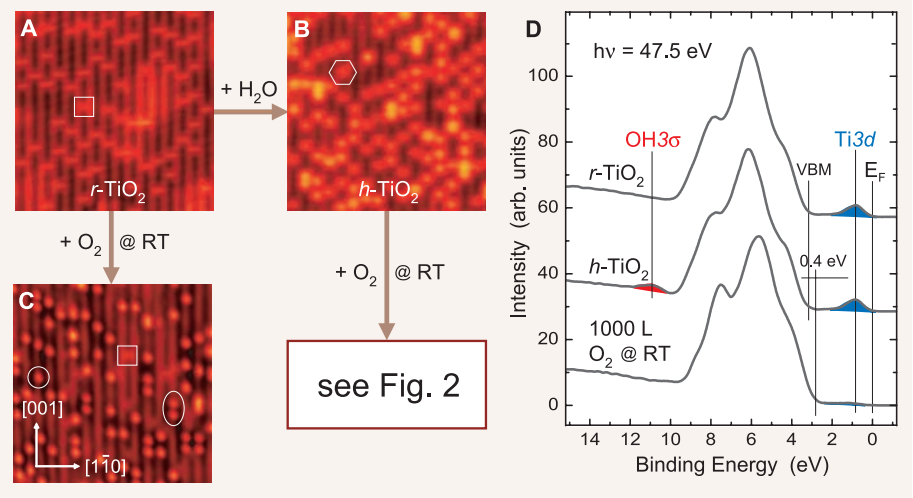

Fig. 1. STM images (105 by 105 Å) of *r*-TiO_2(110) (**A**), *h*-TiO_2(110) (**B**), and a RT O_2-saturated TiO_2(110) surface (**C**) acquired using a sample in a reduction state corresponding to an O_{br}-vacancy density of 11.4 ± 0.3% MLs. Symbols indicate O_{br} vacancies (square), capping H atoms (hexagon) in the O_{br} rows, and O_{ot} adatoms (circle), as well as pairs of next-nearest O_{ot} adatoms (ellipse) in the Ti troughs. STM images were collected with a tunneling current (I_t) ≤ 0.1 nA and a tunneling voltage (V_t) = 1.2 V. Directions throughout the paper are identical to those indicated in (C). Corresponding PES valence-band spectra are shown in (**D**). PES spectra and STM images were recorded at sample temperatures between 100 and 130 K. The position of the valence-band maximum is indicated by VBM and the Ti*3d* defect state is observed within the ~3.1-eV-wide band gap.

[1]Interdisciplinary Nanoscience Center (iNANO), Department of Physics and Astronomy, and Institute for Storage Ring Facilities, University of Aarhus, DK-8000 Aarhus C, Denmark. [2]Department of Physics and Astronomy, Louisiana State University, Baton Rouge, LA 70808, USA.

*To whom correspondence should be addressed. E-mail: hammer@phys.au.dk (B.H.); fbe@inano.dk (F.B.)

(Fig. 1A) shows faint protrusions that appear between the bright Ti troughs and that correspond to O_{br} vacancies in the O_{br} rows (*14*–*17*). Starting from an *r*-TiO_2(110) surface, we studied the effect of hydration by letting water dissociate in the O_{br} vacancies (Fig. 1B). The brighter protrusions in the O_{br} rows appearing on the resulting hydrated TiO_2(110) surface [*h*-TiO_2(110)] originate from capping H atoms or, in an alternative notation, from OH_{br} groups (*14*–*17*). In the PES valence-band spectra corresponding to *r*- and *h*-TiO_2(110) (Fig. 1D), the only obvious difference is the OH3σ feature at a binding energy (BE) of ~10.8 eV that is evident in the valence band after hydration (*12*). The Ti*3d* defect state at ~0.85 eV below E_F is only minimally affected by hydration, in spite of the complete absence of O_{br} vacancies on *h*-TiO_2(110).

In an attempt to "heal" the O_{br} vacancies on *r*-TiO_2(110) without producing capping H atoms on the O_{br} rows, we studied the interaction of O_2 with clean *r*-TiO_2(110) at room temperature (RT). The number of O_{br} vacancies decreased after the O_2 exposure (Fig. 1C), and a number of bright spots appeared simultaneously on the Ti troughs, some of which are next-nearest neighbors. Based on previous O_2 interaction experiments (*3*, *14*, *25*), the spots in the Ti troughs are assigned to O adatoms that reside on top of 5f-Ti atoms (O_{ot}). However, O_2 exposure at RT does not lead to the healing of all the O_{br} vacancies, even in the case of saturation (*26*). In the valence-band spectrum corresponding to the O_2-exposed TiO_2(110) surface, one feature is the strongly suppressed defect state at ~0.85 eV (Fig. 1D). In addition, compared with the spectra for *r*- and *h*-TiO_2(110), the dominating features between BEs of ~3 and ~9.5 eV [primarily O*2p*-derived (*5*, *7*, *12*, *27*)] were found to be shifted by ~0.4 eV toward E_F.

Both of these adsorption experiments, hydration of *r*-TiO_2(110) as well as oxidation of *r*-TiO_2(110) at RT, raise questions about the origin of the Ti*3d* defect state. In the case of the *h*-TiO_2(110) surface, the assignment of the defect state is hampered because of capping H atoms, which also could lead to a state in the band gap (*10*). Because O_2 exposure at RT to *r*-TiO_2(110) leads to a surface with O_{ot} adatoms and residual O_{br} vacancies, and not to a TiO_2(110) surface that is characterized by perfect O_{br} rows as was previously assumed (*8*), this experiment also does not reveal the origin of the defect state. In order to assign the Ti*3d* defect state, TiO_2(110) surfaces need to be prepared that are characterized by perfect O_{br} rows without O_{br} vacancies and capping H atoms, and by Ti troughs without O_{ot} adatoms.

Motivated by the observation that the capping H atoms on the O_{br} rows can be reacted off via reaction with O_2 (*28*), we exposed *h*-TiO_2(110) surfaces to O_2 at RT (Fig. 2). As revealed by the STM images depicted in Fig. 2, A to D, it is possible to react off all capping H atoms from the O_{br} rows and create a TiO_2(110) surface with perfect O_{br} rows. However, for O_2 exposures greater than an optimum value, all of the capping H atoms were removed, but additionally, new surface species with an elongated shape appeared within the Ti troughs (Fig. 2, C and D).

We considered the PES results acquired with surface preparations identical to those in the STM experiments and focused on the OH3σ feature at ~10.8 eV and on the Ti*3d* defect state (Fig. 2E). The OH3σ feature was completely attenuated after an O_2 exposure of 4 Langmuirs (L 1L = 1.33 × 10^{-6} mbar·sec, whereas much higher exposures were required to minimize the Ti*3d* defect state (420 L). For clarity, the evolutions of the Ti*3d* defect state and the OH3σ feature are shown in Fig. 2F in greater detail, and the development of the OH3σ feature for O_2 exposures of ≤4 L is shown in fig. S1 (*26*). One observation from Fig. 2F is that for 4-L O_2 exposure, where the TiO_2(110) surface is characterized by perfect O_{br} rows and essentially without capping H atoms, the Ti*3d* defect state was only slightly attenuated. In complete contradiction to the conventionally accepted O-vacancy model, the PES valence spectra in Fig. 2 reveal that the Ti*3d* defect state

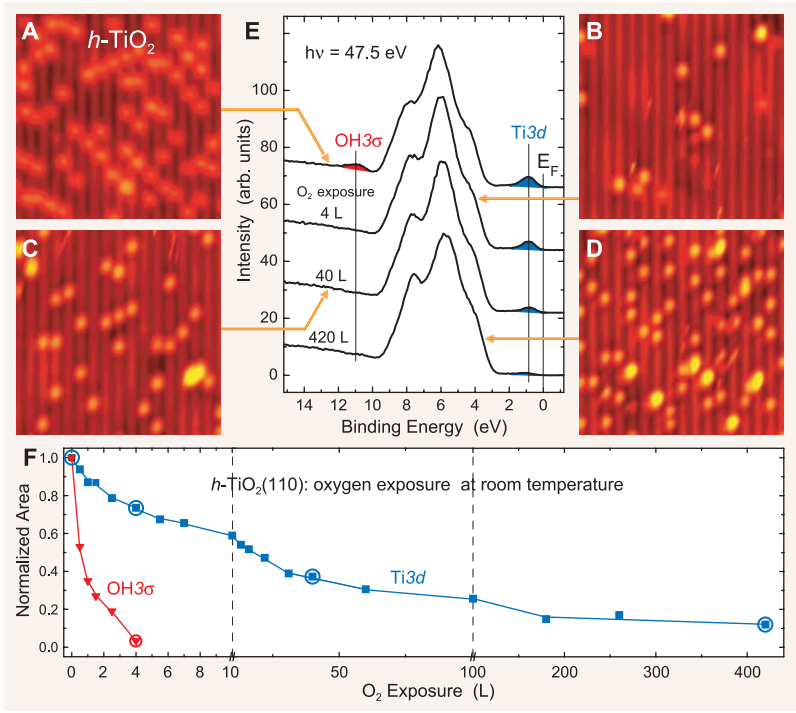

Fig. 2. (**A** to **D**) STM images (105 by 105 Å) of an *h*-TiO_2(110) surface that was exposed to increasing amounts of O_2 at RT. For these experiments we used a TiO_2(110) crystal with an O_{br}-vacancy density of 5.5 ± 0.2% MLs. (**E**) Selected PES valence-band spectra recorded on an *h*-TiO_2(110) surface that was exposed to O_2 at RT. Arrows indicate the representative STM images. For the PES experiments, a TiO_2(110) crystal was used with an O_{br}-vacancy density of 11.4 ± 0.3% MLs. (**F**) Normalized integrated intensities of the OH3σ (red) and Ti*3d* (blue) features for O_2 exposures up to 420 L from PES spectra; circles indicate intensity values that were obtained from the spectra shown in (E).

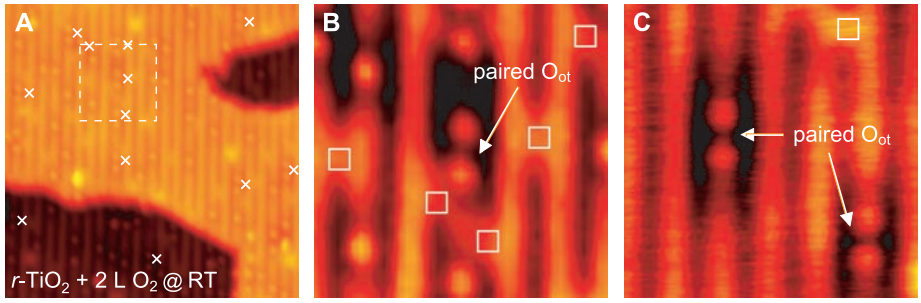

Fig. 3. STM results illustrating the reaction of O_2 with *r*-TiO_2(110) at RT. (**A**) STM image (155 by 155 Å) acquired after 2-L O_2 exposure. White crosses indicate pairs of next-nearest O_{ot} adatoms. (**B**) Zoom-in STM image (38 by 38 Å) of the area indicated by the dashed white square in (A). White squares indicate O_{br} vacancies. (**C**) Zoom-in STM image (38 by 38 Å) acquired after 200-L O_2 exposure at RT. Before the O_2 exposure, this *r*-TiO_2(110) crystal was characterized by an O_{br}-vacancy density of only ~1.7% MLs. STM images were acquired at temperatures between 110 and 130 K.

is caused by neither O_{br} vacancies nor capping H atoms on the O_{br} rows. Rather, we will show in the following that the Ti*3d* defect state can be directly correlated with the existence of near-surface Ti interstitial defect sites. Within this model, electronegative adsorbates, such as those shown in Fig. 2, C and D, are stabilized on TiO_2(110) surfaces with perfect O_{br} rows through charge transfer from Ti interstitials to the adsorbates.

Given the possibility of electron donation arising from Ti interstitial defects, we studied the interaction of O_2 with the clean *r*-TiO_2(110) surface at RT in further detail (Fig. 3). Specifically, we identified a non–vacancy-related O_2 dissociation channel occurring within the Ti troughs. That such a second O_2 dissociation channel exists, in addition to the known dissociation channel associated with O_{br} vacancies (*3*, *14*, *16*, *29*, *30*), is evident from the high number of paired O_{ot} adatoms observed on a partially oxidized *r*-TiO_2(110) surface (Fig. 3, A and B). After O_2 exposure, the densities of O_{br} vacancies {3.9% monolayers [MLs; 1 ML is the density of the (1 × 1) units, 5.2×10^{14} cm^{-2}]} and O_{ot} adatoms (6.0% MLs) together exceed the density of O_{br} vacancies before the exposure (7.9% MLs) by roughly the density of O_{ot} adatoms found in pairs (1.7% MLs). In the pairs, two O_{ot} adatoms are adsorbed on next-nearest Ti-5f atoms. Such O_{ot} pairs were also observed after oxidation of an *r*-TiO_2(110) surface with a very low density of O_{br} vacancies (Fig. 3C), where an unlikely but, in principle, possible O_{ot} pair formation through two separate O_2 dissociation reactions in O_{br} vacancies on adjacent O_{br} rows can be ruled out with certainty. O_{ot} pairs are also evident in the STM images reported by Henderson *et al.* (*25*).

To study the non–vacancy-related O_2 dissociation channel more in depth, we also exposed *r*-TiO_2(110) surfaces to O_2 at low temperatures (120 K) and subsequently annealed the crystals to temperatures of 393 K and 448 K, respectively (Fig. 4, A to E). After exposing the surface of a TiO_2(110) crystal with an O_{br} vacancy density of 4.5% MLs to 5 L of O_2 at 120 K, all the O_{br} vacancies disappeared and O_{ot} adatoms appeared in the Ti troughs (Fig. 4A). No O_{ot} pairs were evident in the STM images, indicating that the non–vacancy-related O_2 dissociation channel does not operate at this low temperature. This conclusion is consistent with the 1:1 correlation between the density of O_{br} vacancies before O_2 exposure and the density of O_{ot} adatoms after the exposure. However, after annealing this O_2-exposed TiO_2(110) surface to 393 K (Fig. 4B), the density of O_{ot} adatoms increased by a factor of ~2. This result shows that the non–vacancy-related O_2 dissociation channel is energetically more activated than the one associated with the O_{br} vacancies.

In addition, a number of small islands appeared on the terraces, one of which is indicated in Fig. 4B by a circle. These newly formed islands are positioned in between two Ti troughs and show up in the STM images with a height of ~2.2 Å. Subsequent annealing to an even higher temperature (448 K) led to an increase in the density of the islands, and, in this case, larger islands with a height of ~3.2 Å were observed, in addition to the small islands (Fig. 4C). A height of ~3.2 Å closely resembles the step height on TiO_2(110) crystals; that is, the height of one TiO_2 trilayer, which is ~3.25 Å. When applying identical experimental procedures for a more reduced TiO_2(110) crystal (with an O_{br} vacancy density of ~10.8% MLs and ~9.4% MLs O_{ot} adatoms density after saturation with 20 L O_2 at 120 K), the density of O_{ot} adatoms was slightly smaller after annealing to 393 K than before the anneal (Fig. 4, D and E), but, compared with the situation on the low-reduced TiO_2(110) crystal (Fig. 4B), the number of small islands after annealing to 393 K was higher.

In Fig. 4F, we present PES results for a similar annealing experiment. The Ti*3d* defect state reappeared after annealing to temperatures higher than 400 K. In Fig. 4F, the oxidation before the annealing at 400 K was carried out at RT, but we found results when the oxidation was performed at 120 K that were similar to those of the STM experiments depicted in Figs. 4, A to E. Concomitant with the recovery of the Ti*3d* defect state, the valence-band maximum (VBM) shifts back to the original value of the clean *r*-TiO_2(110) surface.

Based on the STM results (Fig. 4, A to E) and the PES data (Fig. 4F and figs. S2 and S3) (*26*), we propose the following model. Because exclusively Ti and O features are evident in the PES core-level spectra (fig. S2), the islands appearing on previously flat terraces must be newly formed TiO_x structures, with x ~ 2. This finding implies that Ti atoms have diffused from the near-surface region to the topmost surface layer, where reactions with O_{ot} adatoms and possibly also

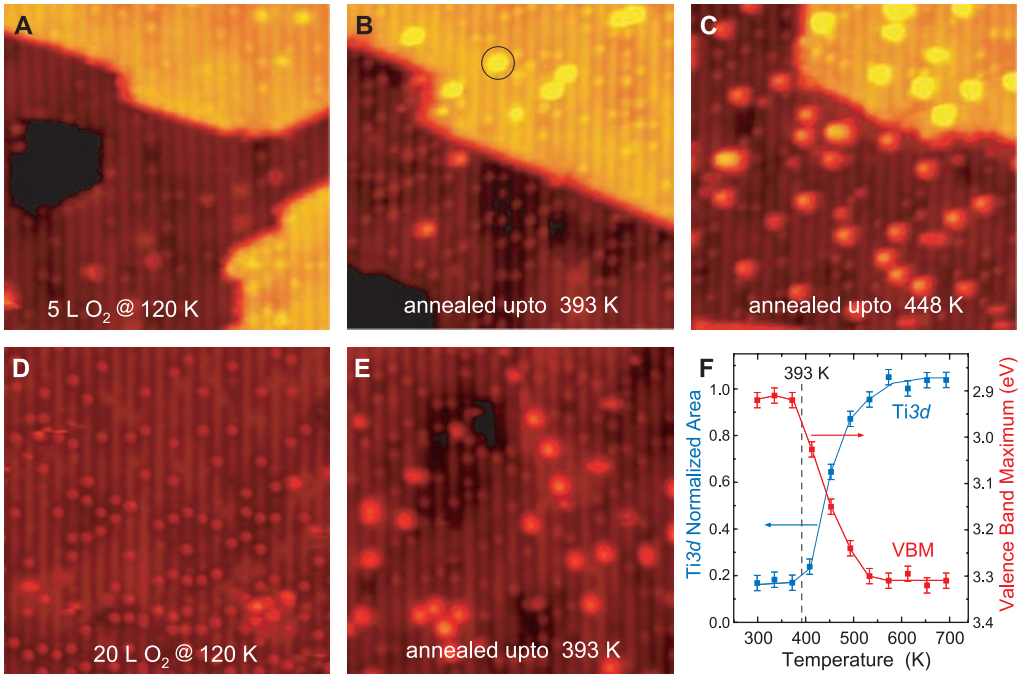

Fig. 4. (**A** to **C**) STM images (150 by 150 Å) of a TiO_2(110) crystal characterized by an O_{br}-vacancy density of ~4.5% MLs, (A) exposed to 5-L O_2 at 120 K, (B) subsequently annealed up to 393 K, and (C) further annealed up to 448 K. The circle in (B) indicates one of the newly formed TiO_x islands on the terraces with an STM height of ~2.2 Å. (**D** and **E**) STM images (150 by 150 Å) of a TiO_2(110) crystal characterized by an O_{br}-vacancy density of ~10.8% MLs, (D) exposed to 20-L O_2 at 120 K leading to an O_{ot} adatoms density of ~9.3% MLs and ~1.8% MLs residual O_{br} vacancies, and (E) after subsequent annealing up to 393 K where TiO_x islands have been formed. All STM images were acquired at temperatures between 110 and 130 K. Corresponding PES core-level scans are plotted in fig. S2 (*26*). Exclusively Ti- and O-related features were found in the PES spectra both after O_2 exposure at 120 K as well as after annealing to temperatures of ≥400 K. (**F**) Normalized integrated intensities of the Ti*3d* features (left axis, blue) and position of the VBM (right axis, red) as a function of the maximum annealing temperature. The VBM values are given in BE. The underlying valence-band spectra (fig. S3) were of an *r*-TiO_2(110) crystal that was reduced comparably to those crystals that were used to collect the data shown in Fig. 1 and Fig. 4, D and E. The crystal was oxidized at RT by exposing it to 1000 L of O_2.

with O_2 molecules occurred. The fact that the Ti*3d* defect state reappears after annealing to temperatures higher than 400 K can be explained by the migration of Ti interstitials from deeper layers to interstitial sites in the layers nearer the surface that had been depleted in the course of TiO_x island formation. Assuming a 1:2 correlation between Ti and O in the islands, we estimated a lower limit of Ti interstitials in the near-surface region, corresponding to 5 to 6% MLs for the TiO_2(110) crystals used in the experiments summarized in Fig. 4.

The STM and PES results shown in Fig. 4 are consistent with the temperature-programmed static secondary ion mass spectrometry data reported by Henderson (*19*), in which the onset of Ti interstitial diffusion occurred at ~400 K. Furthermore, similarities exist to previous STM results by Onishi *et al.* (*22*) and by Li *et al.* (*23*), in which O_2-induced growth of new structures on originally flat TiO_2(110) terraces were also obtained. However, because the experimental procedures applied in these previous studies were different from the ones in the present work, the structures obtained by Onishi *et al.* (*22*) and by Li *et al.* (*23*) are different from the ones obtained here.

The above-presented results addressing the O_2 interaction with *r*-TiO_2(110) reveal that Ti charge donors exist in the near-surface region of vacuum-annealed TiO_2 crystals, and that these donor sites strongly influence the O_2 interaction with *r*-TiO_2(110), even at temperatures as low as 120 K. Because the gap state remains largely unaffected by the removal of all surface defects (O_{br} and OH_{br}), we propose that the appearance of the gap state on clean reduced TiO_2(110) crystals, as is typically observed after vacuum annealing, is mainly associated with the Ti interstitials. Quenching of the gap state and so-called band-bending effects (Figs. 1D and 4F) can be ascribed to the withdrawal of electronic charge from the donor sites in the near-surface region through the accumulation of electronegative adsorbates, such as O_2 and O_{ot} adatoms on the surface.

To further explore this new interpretation, we performed first-principles DFT calculations using the DACAPO software package (https://wiki.fysik.dtu.dk/dacapo), using ultrasoft pseudopotentials and the revised Perdew-Burke-Ernzerhof exchange-correlation functional (*26*). We assumed a Ti interstitial (Fig. 5, blue) initially between the second and third trilayers of a five-TiO_2 trilayer slab with a *c*(4 × 2) surface-unit cell (Fig. 5B). On the surface of such a slab, an adsorbed O_2 molecule binds with ~1.6 eV, which is comparable to the ~1.9- and 0.8-to-2.0-eV bond strengths calculated for O_2 on *r*-TiO_2(110) (*14*) and *h*-TiO_2(110) (*31*), respectively. The DFT potential-energy diagram (Fig. 5A) shows that an energetically favorable pathway exists for a Ti interstitial to diffuse to the surface and to react with the adsorbed O_2 molecule to form a TiO_2 island on the terrace. The Ti interstitial diffusion proceeds via an exchange mechanism (*21*), in which a Ti atom on a regular lattice site (light blue) is released to an interstitial site toward the surface (Fig. 5C), and subsequently the lattice site is occupied by the original Ti interstitial atom (dark blue) from a deeper layer (Fig. 5D). Dissociation of the O_2 molecule (Fig. 5, E and F) gains ~4 eV in energy.

Relative to the initial configuration (Fig. 5B), the overall barrier for the formation of the TiO_x islands on the terraces is ~0.75 eV. However, with respect to the potential energy of the metastable intermediate configuration of the Ti interstitial between the first and second TiO_2 trilayer (Fig. 5C), the barrier becomes ~1.2 eV. The absolute value of this energy barrier is in good agreement with the experimental findings that the TiO_x islands appear on the flat TiO_2(110) terraces after annealing to temperatures well above RT (Fig. 4). If we tentatively assume that the Ti diffusion can be described as a first-order process, our rough estimate of the diffusion barrier from the Redhead formula is 1.2 eV.

If we start with a configuration wherein the O_2 molecule in Fig. 5 is replaced by an O_{ot} adatom, our DFT calculations still indicate favorable energetics for the diffusion of the Ti interstitial toward the surface. The two adsorbates, O_2 and O_{ot} adatoms, are quite similar electronically. According to a Bader charge analysis of our slab systems (*26*), a molecularly adsorbed O_2 species withdraws ~0.9 electron (*e*) from the TiO_2(110) substrate, whereas an O_{ot} adatom withdraws ~0.8 *e*. If these electronegative adsorbates are removed from the TiO_2(110) surface layer, the most favorable position of the Ti interstitial is the octahedral site (*32*) between the second and third TiO_2 trilayer. For a six-TiO_2 trilayer slab, our calculations show that the potential energy is higher by ~0.40 and ~0.23 eV, respectively, when locating the Ti interstitial one-TiO_2 trilayer higher or lower in the [110] direction.

To elucidate the mechanism of the second O_2 dissociation channel identified experimentally in Fig. 3 and Fig. 4, A and B, we performed additional calculations (figs. S4 and S5) (*26*). In agreement with previous reports (*14*, *33*, *34*), we found that O_2 molecules neither adsorb nor dissociate on stoichiometric TiO_2(110) unless the slab is reduced. Introduction of an O_{br} vacancy is sufficient to enable the adsorption of molecular O_2 (fig. S4B) (*26*) but not to dissociate O_2 in the Ti trough (fig. S4C) (*26*). Instead, when reducing the slab by adding a near-surface Ti interstitial, both the molecular (fig. S4D) and the dissociative adsorption (fig. S4E) of O_2 become feasible. If a Ti interstitial and an O_{br} vacancy occur simultaneously, the energy gain is even greater in both these adsorption modes (fig. S4, F and G). The experimental observation in Fig. 3 and Fig. 4, A and B, that dissociation of O_2 in the Ti troughs leads to next-nearest neighbors of O_{ot} adatoms is supported by the calculated preference for this configuration (fig. S5D) as com-

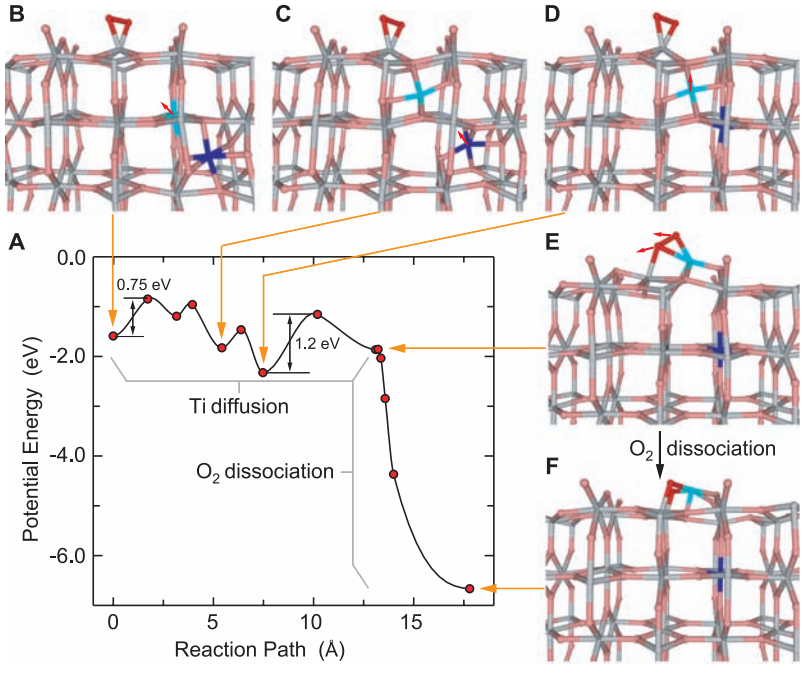

Fig. 5. (**A**) Potential-energy profile for the reaction of an adsorbed O_2 molecule and a Ti interstitial on TiO_2(110). The energy zero corresponds to O_2 in the gas phase and the Ti interstitial at the octahedral position between the second and third TiO_2 trilayer. (**B**) Adsorbed O_2 molecule (red). (**C**) Ti interstitial (dark blue) moved to tetrahedral position and lattice Ti (light blue) to tetrahedral position between the first and the second TiO_2 trilayer. (**D**) Original Ti interstitial (dark blue) now at lattice position. (**E**) Exchanged Ti interstitial (light blue) appearing at the surface. (**F**) Adsorbed O_2 dissociated and a surface TiO_2 island formed at the terrace. Orange arrows indicate positions on the potential-energy profile that correspond to the configurations shown in (B) to (F).

pared with a pair of nearest-neighbor O_{ot} adatoms (fig. S5C).

The role of the Ti interstitials in the O_2 adsorption and dissociation reactions is to provide the electronic charge for the adsorbates. According to the above Bader charge analysis, more electronic charge is required for dissociative adsorption ($2O_{ot}$) than for molecular adsorption ($1O_2$). Hence, dissociative adsorption is more sensitive to the amount of charge available on the surface than molecular adsorption, a fact clearly borne out by the DFT calculations in figs. S4 and S5. For instance, coadsorption of O_{ot} in fig. S5, B to D, decreases the stability of molecularly adsorbed O_2 by ~0.4 eV (fig. S5, B versus E) but that of dissociatively adsorbed oxygen by ~1.5 eV (fig. S5, C and D versus F and G). The coadsorbed O_{ot} adatom partially oxidizes the surface and thereby lowers the ease with which electronic charge is available for further surface reactions.

Within the scheme used for the calculations, the O_2 dissociation energy barrier is increased from ~0.3 to ~0.8 eV (fig. S5A) upon introduction of the O_{ot} adatom. This result explains why the coverage of O_{ot} adatoms remains low even under conditions in which the second O_2 dissociation channel operates (Fig. 3C); that is, the reaction is self-limiting. Similarly, some O_{br} vacancies remain unfilled even in the case of O_2 saturation (Figs. 1C and 4D); that is, the electronic charge required for the resulting O_{ot} adatoms depletes the source from the limited number of Ti interstitials. This charge-competition model also could explain why an O_2 desorption feature observed in the temperature-programmed desorption experiments by Henderson *et al*. (*30*) is evident only after exposing the *r*-TiO_2(110) surface at low temperature (below ~180 K). If impinging O_2 molecules can overcome the dissociation barrier, as observed in the experiments performed at RT (Fig. 3), the dissociation products deplete the electron donors in the bulk, and the accumulation of molecular O_2 is prohibited.

For a slab characterized by a Ti interstitial between the second and third TiO_2 trilayer and a pristine surface, our calculations reveal the existence of a gap state. This state lies ~2 eV above the VBM, in good agreement with the state observed in the PES experiments (Figs. 1D and 2E) as well as with DFT calculations addressing Ti interstitials in the bulk (*32*). A thorough analysis (fig. S6, A and B) of the spatially resolved electronic density of states shows that the gap state is spatially located in the region between the second and third TiO_2 trilayer, which strongly suggests that its origin is from the Ti interstitial. Further reduction of the surface layer by introduction of an O_{br} vacancy or a capping H atom (OH_{br} group) does not affect the gap state (fig. S6, C and D).

Conversely, adsorption of electronegative species such as O_2 or O_{ot} adatoms causes quenching of the gap state (fig. S6, E and F); in the case of adsorbed O_2, a new O_2-related state appears in the gap, in agreement with electron energy loss results by Henderson *et al*. (*30*). Most previous DFT papers addressing the gap state did not reveal a state in the gap for stoichiometric TiO_2 slabs with O_{br} vacancies or OH_{br} groups (*11*). Our calculations agree with these previous results (fig. S7, A to C) and further show no sign of a gap state when we introduce a hypothetical O vacancy in the bulk (fig. S7, D and E). These results challenge the conclusions derived by Di Valentin *et al*. (*10*) that a hybrid DFT setup is required to identify the gap state and that the gap state is related to O_{br} vacancies.

We propose that the surface redox chemistry on reduced titania is to a large extent associated with Ti interstitials in the near-surface region, because these defect sites provide the electronic charge, enabling important reactions. This conclusion is consistent with numerous experimental studies addressing the Ti*3d* defect state, including the pioneering work by Henrich *et al*. (*5*, *8*), electron paramagnetic resonance spectroscopy (*35*–*37*), bulk photonic (*38*) and transport (*39*) studies, recent photoelectron diffraction studies (*40*), and thin-film growth studies (*41*).

Moreover, several experimental results that were puzzling within an O vacancy model can now be revisited and explained more readily. For example, the simultaneous UPS and metastable impact electron spectroscopy (MIES) measurements of *r*-TiO_2(110) by Krischok *et al*. show no intensity between 0.5 to 1.0 eV below E_F in the MIES spectrum, whereas the Ti*3d* defect state is clearly observed in the UPS spectrum (*13*). Because of enhanced surface sensitivity with MIES as compared with UPS, the intensity of the Ti*3d* defect state is strongly suppressed in MIES (*13*). As a second example, it can be rationalized why the Ti*3d* defect state occurs for reduced bulk TiO_2 single crystals, but not for titania thin films grown on metal substrates. Particularly in the case of ultrathin titania films (*4*, *42*), there are no interstitial sites available and, hence, a defect state typical of reduced TiO_2 single crystals does not occur (*4*, *42*). Instead, the *d* electrons of the metal substrate can be considered a huge "bulk defect state" and thus fulfill the same function that the Ti interstitials do in reduced bulk TiO_2 crystals. Finally, at interfaces between two isolating oxide materials, the Ti interstitials may be the cornerstone to explain phenomena such as superconductivity, as has been reported for $LaAlO_3/SrTiO_3$ (*43*).

References and Notes

1. M. Haruta, T. Kobayashi, H. Sano, N. Yamada, *Chem. Lett.* **2**, 405 (1987).
2. M. Valden, X. Lai, D. W. Goodman, *Science* **281**, 1647 (1998).
3. D. Matthey *et al*., *Science* **315**, 1692 (2007).
4. M. Chen, Y. Cai, Z. Yan, D. W. Goodman, *J. Am. Chem. Soc.* **128**, 6341 (2006).
5. V. E. Henrich, P. Cox, *The Surface Science of Metal Oxides* (Cambridge Univ. Press, Cambridge, 1996).
6. U. Diebold, *Surf. Sci. Rep.* **48**, 53 (2003).
7. A. G. Thomas *et al*., *Phys. Rev. B* **75**, 035105 (2007).
8. V. E. Henrich, G. Dresselhaus, H. J. Zeiger, *Phys. Rev. Lett.* **36**, 1335 (1976).
9. T. L. Thompson, J. T. Yates, *Chem. Rev.* **106**, 4428 (2006).
10. C. Di Valentin, G. Pacchioni, A. Selloni, *Phys. Rev. Lett.* **97**, 166803 (2006).
11. M. V. Ganduglia-Pirovano, A. Hofmann, J. Sauer, *Surf. Sci. Rep.* **62**, 219 (2007).
12. R. L. Kurtz, R. Stockbauer, T. E. Madey, E. Roman, J. L. Desegovia, *Surf. Sci.* **218**, 178 (1989).
13. S. Krischok, J. Gűnster, D. W. Goodman, O. Höfft, V. Kempter, *Surf. Interface Anal.* **37**, 77 (2005).
14. S. Wendt *et al*., *Surf. Sci.* **598**, 226 (2005).
15. S. Wendt *et al*., *Phys. Rev. Lett.* **96**, 066107 (2006).
16. O. Bikondoa *et al*., *Nat. Mater.* **5**, 189 (2006).
17. Z. Zhang, O. Bondarchuk, B. D. Kay, J. M. White, Z. Dohnálek, *J. Phys. Chem. B* **110**, 21840 (2006).
18. J. V. Lauritsen *et al*., *Nanotechnology* **17**, 3436 (2006).
19. M. A. Henderson, *Surf. Sci.* **419**, 174 (1999).
20. K. T. Park, M. Pan, V. Meunier, E. W. Plummer, *Phys. Rev. B* **75**, 245415 (2007).
21. H. Iddir, S. Ogut, P. Zapol, N. D. Browning, *Phys. Rev. B* **75**, 073203 (2007).
22. H. Onishi, Y. Iwasawa, *Phys. Rev. Lett.* **76**, 791 (1996).
23. M. Li *et al*., *Surf. Sci.* **437**, 173 (1999).
24. R. A. Bennett, P. Stone, N. J. Price, M. Bowker, *Phys. Rev. Lett.* **82**, 3831 (1999).
25. M. A. Henderson, J. M. White, H. Uetsuka, H. Onishi, *J. Am. Chem. Soc.* **125**, 14974 (2003).
26. Materials and methods are available as supporting material on *Science* Online.
27. J. C. Woicik *et al*., *Phys. Rev. Lett.* **89**, 077401 (2002).
28. M. A. Henderson, W. S. Epling, C. H. F. Peden, C. L. Perkins, *J. Phys. Chem. B* **107**, 534 (2003).
29. W. S. Epling, C. H. F. Peden, M. A. Henderson, U. Diebold, *Surf. Sci.* **412-413**, 333 (1998).
30. M. A. Henderson, W. S. Epling, C. L. Perkins, C. H. F. Peden, U. Diebold, *J. Phys. Chem. B* **103**, 5328 (1999).
31. L. M. Liu, B. McAllister, H. Q. Ye, P. Hu, *J. Am. Chem. Soc.* **128**, 4017 (2006).
32. E. Cho *et al*., *Phys. Rev. B* **73**, 193202 (2006).
33. M. D. Rasmussen, L. M. Molina, B. Hammer, *J. Chem. Phys.* **120**, 988 (2004).
34. Z. Dohnálek, J. Kim, O. Bondarchuk, J. M. White, B. D. Kay, *J. Phys. Chem. B* **110**, 6229 (2006).
35. M. Li *et al*., *J. Phys. Chem. B* **104**, 4944 (2000).
36. A. L. Attwood, D. M. Murphy, J. L. Edwards, T. A. Egerton, R. W. Harrison, *Res. Chem. Intermediat.* **29**, 449 (2003).
37. M. Aono, R. R. Hasiguti, *Phys. Rev. B* **48**, 12406 (1993).
38. A. K. Ghosh, F. G. Wakim, R. R. Addiss, *Phys. Rev.* **184**, 979 (1969).
39. E. Yagi, R. R. Hasiguti, M. Aono, *Phys. Rev. B* **54**, 7945 (1996).
40. P. Krűger *et al*., *Phys. Rev. Lett.* **100**, 055501 (2008).
41. S. A. Chambers *et al*., *Chem. Phys.* **339**, 27 (2007).
42. P. Finetti *et al*., *J. Phys. Chem. C* **111**, 869 (2007).
43. N. Reyren *et al*., *Science* **317**, 1196 (2007).

44. We acknowledge financial support from the Danish Ministry of Science, Technology, and Innovation through iNANO, the Danish Research Councils, and the Danish Center for Scientific Computing. P.T.S. acknowledges support through NSF grants DMR-0504654 and CHE-0615606.

Supporting Online Material

www.sciencemag.org/cgi/content/full/1159846/DC1
Materials and Methods
Figs. S1 to S7
References

22 February 2008; accepted 28 May 2008
Published online 5 June 2008;
10.1126/science.1159846
Include this information when citing this paper.

Tryptophan-Accelerated Electron Flow Through Proteins

Crystal Shih,[1] Anna Katrine Museth,[1] Malin Abrahamsson,[1] Ana Maria Blanco-Rodriguez,[2] Angel J. Di Bilio,[1] Jawahar Sudhamsu,[4] Brian R. Crane,[4]* Kate L. Ronayne,[3] Mike Towrie,[3] Antonín Vlček Jr.,[2]* John H. Richards,[1]* Jay R. Winkler,[1]* Harry B. Gray[1]*

Energy flow in biological structures often requires submillisecond charge transport over long molecular distances. Kinetics modeling suggests that charge-transfer rates can be greatly enhanced by multistep electron tunneling in which redox-active amino acid side chains act as intermediate donors or acceptors. We report transient optical and infrared spectroscopic experiments that quantify the extent to which an intervening tryptophan residue can facilitate electron transfer between distant metal redox centers in a mutant *Pseudomonas aeruginosa* azurin. Cu^{I} oxidation by a photoexcited Re^{I}-diimine at position 124 on a histidine(124)-glycine(123)-tryptophan(122)-methionine(121) β strand occurs in a few nanoseconds, fully two orders of magnitude faster than documented for single-step electron tunneling at a 19 angstrom donor-acceptor distance.

Extensive experimental and theoretical investigations of iron and copper proteins have explored the factors controlling long-range electron transfer (ET) through folded polypeptide structures (*1*–*10*). In work on Ru-modified derivatives of *Pseudomonas aeruginosa* azurin, a relatively small blue copper protein (128 residues; β-barrel fold), we found that coupling-limited (activationless) Cu^{I} to Ru^{III} ET rates decrease exponentially with distance over a wide range (16 to 26 Å), which demonstrates that these reactions occur by single-step electron tunneling (decay constant, 1.1 $Å^{-1}$) (*2*, *11*–*13*). Electron transport over greater distances (>25 Å) likely involves multistep tunneling, often called hopping (*10*, *14*–*20*), in which redox-active amino acid side chains act as intermediate donors or acceptors rather than tunneling bridges (*2*, *3*, *21*). Calculations of hole hopping based on decay constants between 1.0 and 1.2 $Å^{-1}$, and reorganization energies in the 0.7 to 0.8 eV range, indicate that electrons could be transported 30 Å or more in hundreds of nanoseconds if an intervening redox center (Int) with a reduction potential [$E(Int^{+/0})$] well above that of the donor [$E(D^{+/0})$] but not more than 200 mV above that of the acceptor [$E(A^{0/-})$] is placed between D and A (*2*, *3*).

We have expressed three mutant *P. aeruginosa* azurins to test the proposition that an intervening tryptophan or tyrosine can facilitate electron transfer between distant metal redox centers (*22*). In these azurins, a histidine (H) ligand is at position 124 on the β strand extending from methionine-121 and either tryptophan (W), tyrosine (Y), or phenylalanine (F) is at position 122 (*23*, *24*). The construction was completed by attaching $Re^{I}(CO)_3$(4,7-dimethyl-1,10-phenanthroline) [$Re^{I}(CO)_3$(dmp)] to H^{124}. $Re^{I}(CO)_3(dmp)(H^{124})$ is a powerful oxidant in its triplet metal-to-ligand charge-transfer (^{3}MLCT) excited state: $E°[*Re^{II}(CO)_3(dmp^{\bullet-})(H^{124})/Re^{I}(CO)_3(dmp^{\bullet-})(H^{124})]$ = 1.4 V versus the normal hydrogen electrode (*25*). The x-ray crystal structure of the Re-labeled W^{122} variant $[Re^{I}(CO)_3(dmp)(H^{124})|(W^{122})|AzCu^{II}]$ (Fig. 1) shows that dmp and the W^{122} indole group are near van der Waals contact (~4 Å), and the Cu-Re distance is 19.4 Å.

Luminescence from electronically excited $Re^{I}(CO)_3(dmp)(H^{124})|(W^{122})|AzCu^{I}$ is substantially quenched relative to the F^{122} analog. Time-resolved luminescence data for the W^{122} protein reveal a biphasic excited-state decay pattern [τ_1 = 350(50) ps, τ_2 = 25(5) ns] (Fig. 2); this pattern contrasts with the single-exponential decay (τ = 1.3 μs) of the $Re^{I}(CO)_3(dmp)|(F^{122})|AzCu^{I}$ ^{3}MLCT state. Transient absorption measurements reveal rapid (<50 ns) formation of Cu^{II} after pulsed laser excitation (λ_{obs} = 632.8 nm; λ_{ex} = 355 nm, 8 ns pulsewidth) of $Re^{I}(CO)_3(dmp)(H^{124})|(W^{122})|AzCu^{I}$ (Fig. 2); data at 500 nm are consistent with concomitant formation of $Re^{I}(CO)_3(dmp^{\bullet-})(H^{124})$; charge recombination to regenerate $Re^{I}(CO)_3(dmp)(H^{124})|(W^{122})|AzCu^{I}$ proceeds with a time constant of ~3 μs. No evidence (λ_{obs} = 632.8, 500 nm) for $AzCu^{II}$ formation was found after excitation of $Re^{I}(CO)_3(dmp)(H^{124})|(F^{122})|AzCu^{I}$ or $Re^{I}(CO)_3(dmp)(H^{124})|(Y^{122})|AzCu^{I}$.

Owing to the sensitivity of C≡O stretching frequencies to the electron density distribution in a metallocarbonyl unit, time-resolved infrared absorption (TRIR) provides structural and kinetics information on both the electronic ground and MLCT-excited states of $Re^{I}(CO)_3(dmp)(H^{124})$, as well as on $Re^{I}(CO)_3(dmp^{\bullet-})(H^{124})$ (Fig. 2). TRIR spectra measured in the region of C≡O stretching frequencies show bleaches at 1920 and 2030 cm^{-1}, corresponding to the depleted ground-state population; absorptions at ~1960, 2012, and ~2040 cm^{-1}, characteristic of the ^{3}MLCT excited state (*26*); and most important, distinct peaks at 1888 and 2004 cm^{-1}, which are spectroscopic signatures of $Re^{I}(CO)_3(dmp^{\bullet-})(H^{124})$ (*27*). Both the MLCT and bleach features are fully developed within the instrument response time (<1 ps); the MLCT bands evolve with three time constants [35(15) ps, 350(50) ps, 25(5) ns, measured at frequencies in the range 1950 to 1960 cm^{-1}], and the bleach recovers with ~25 ns and ~3 μs kinetics. A small population (~20%) of $Re^{I}(CO)_3(dmp^{\bullet-})(H^{124})$ is present promptly (~1 ps) after excitation; this population continues to grow in three apparent kinetics phases with time constants of 35(15) ps, 350(50) ps, and 25(5) ns, followed by 3 μs decay.

TRIR spectra indicate that W^{122} is required for rapid formation of $Re^{I}(CO)_3(dmp^{\bullet-})(H^{124})$: The reduced complex also appears after excitation of $Re^{I}(CO)_3(dmp)(H^{124})|(W^{122})|AzCu^{II}$ and $Re^{I}(CO)_3(dmp)(H^{124})|(W^{122})|AzZn^{II}$, but not after excitation of $Re^{I}(CO)_3(dmp)(H^{124})|(Y^{122})|AzZn^{II}$. Nanosecond visible transient absorption experiments confirm that no Cu^{II} is formed upon excitation of $Re^{I}(CO)_3(dmp)(H^{124})|(F^{122})|AzCu^{I}$ or $Re^{I}(CO)_3(dmp)(H^{124})|(Y^{122})|AzCu^{I}$ at 355 nm.

The transient absorption, luminescence, and infrared spectra can be interpreted in terms of the

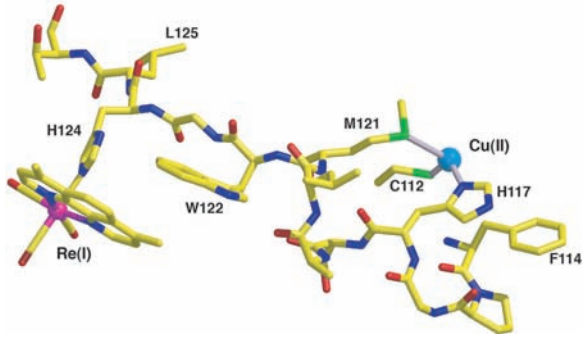

Fig. 1. Model of the Cu-W-Re electron-tunneling architecture from the 1.5 Å resolution x-ray crystal structure of $Re^{I}(CO)_3(dmp)(H^{124})|(W^{122})|AzCu^{II}$ (Az is azurin). The aromatic rings of dmp and W^{122} slightly overlap, with one dmp methyl group projecting over the indole ring and the plane of the respective π-systems making a 20.9° angle. The average separation of atoms on the overlapped six-membered rings is 3.82 Å, whereas 4.1 Å separates the edge of the W^{122} indole and the H^{124} imidazole. Distances between redox centers: Cu to W^{122} aromatic centroid, 11.1 Å; W^{122} aromatic centroid to Re, 8.9 Å; Cu to Re, 19.4 Å.

[1]Beckman Institute, California Institute of Technology, Pasadena, CA 91125, USA. [2]School of Biological and Chemical Sciences, Queen Mary, University of London, Mile End Road, London E1 4NS, UK. [3]Central Laser Facility, STFC Rutherford Appleton Laboratory, Chilton, Didcot, Oxfordshire OX11 0QX, UK. [4]Department of Chemistry and Chemical Biology, Cornell University, Ithaca, NY 14853, USA.

*To whom correspondence should be addressed. E-mail: bc69@cornell.edu (B.R.C.); a.vlcek@qmul.ac.uk (A.V); jhr@caltech.edu (J.H.R.); winklerj@caltech.edu (J.R.W.); hbgray@caltech.edu (H.B.G.)

kinetics model outlined in Fig. 3. Optical excitation of $Re^{I}(CO)_3(dmp)(H^{124})$ creates a ^{1}MLCT-excited state, which undergoes ~150 fs intersystem crossing (*28*) to a vibrationally excited ^{3}MLCT ($*^3$MLCT) state. Subpicosecond generation of $Re^{I}(CO)_3(dmp^{\bullet-})(H^{124})$ is attributable to ET from W^{122} to singlet-excited (^{1}MLCT) $Re^{I}(CO)_3(dmp)(H^{124})$. In previous work, we found that equilibration of the $*^3$MLCT state in $Re^{I}(CO)_3(phen)(H^{X})|AzCu^{II}$ (X = 83, 109), involving both vibrational and surrounding-medium relaxation, proceeds on the 10- to 100-ps time scale (*26*). Hence, the ~35-ps formation of $Re^{I}(CO)_3(dmp^{\bullet-})(H^{124})$ in $Re^{I}(CO)_3(dmp)(H^{124})|(W^{122})|AzCu^{I}$ likely involves parallel relaxation and reduction of the $*^3$MLCT state. The source of reducing equivalents in these fast ET reactions is the indole side chain of W^{122}; no evidence for $Re^{I}(CO)_3(dmp^{\bullet-})(H^{124})$ formation was observed with proteins containing F^{122} or Y^{122} residues.

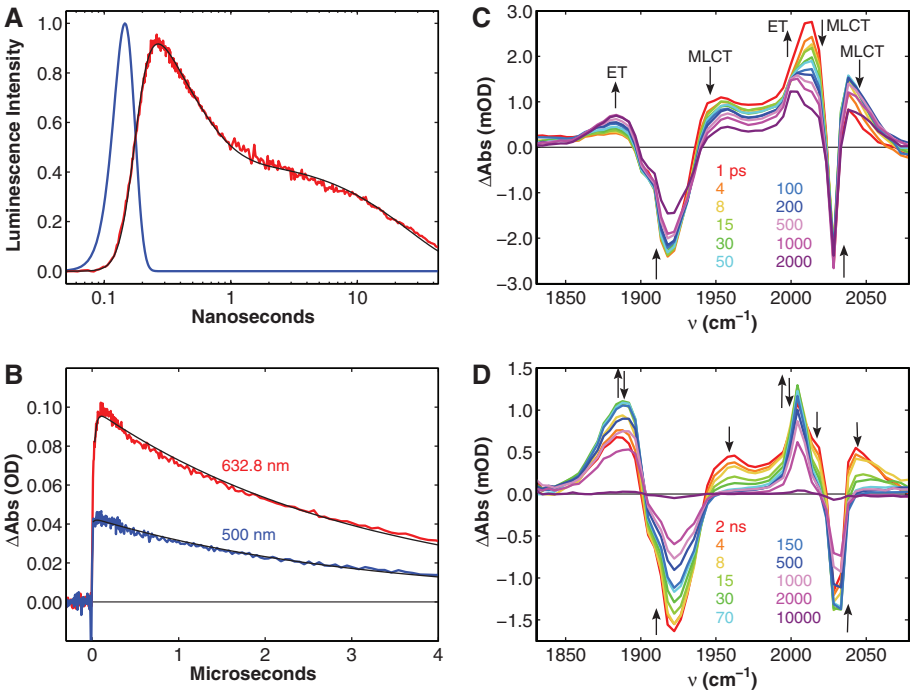

Fig. 2. Transient kinetics of $Re^{I}(CO)_3(dmp)(H^{124})|(W^{122})|AzCu^{I}$. (**A**) Time-resolved luminescence (red: λ_{obs} > 450 nm; λ_{ex} = 355 nm, 10 ps pulsewidth; pH 7.2), instrument response function (blue), and fit to a three-exponential kinetics model [black: τ_1 = 35 ps (growth); τ_2 = 363 ps (decay); τ_3 = 25 ns (decay)]. (**B**) Visible transient absorption [λ_{obs} = 632.8 (red), 500 nm (blue); λ_{ex} = 355 nm, 1.5 mJ, 8 ns pulsewidth; pH 7.2]. Black lines are fits to a biexponential kinetics model [τ_1 = 25 ns (growth); τ_2 = 3.1 μs (decay)]. (**C**) TRIR spectra measured (λ_{ex} = 400 nm, ~150 fs pulsewidth; D_2O, pD = 7.1, phosphate buffer) at selected time delays after femtosecond laser excitation. (**D**) TRIR spectra measured (λ_{ex} = 355 nm, ~0.7 ns pulsewidth; D_2O, pD = 7.1, phosphate buffer) at selected time delays after laser excitation.

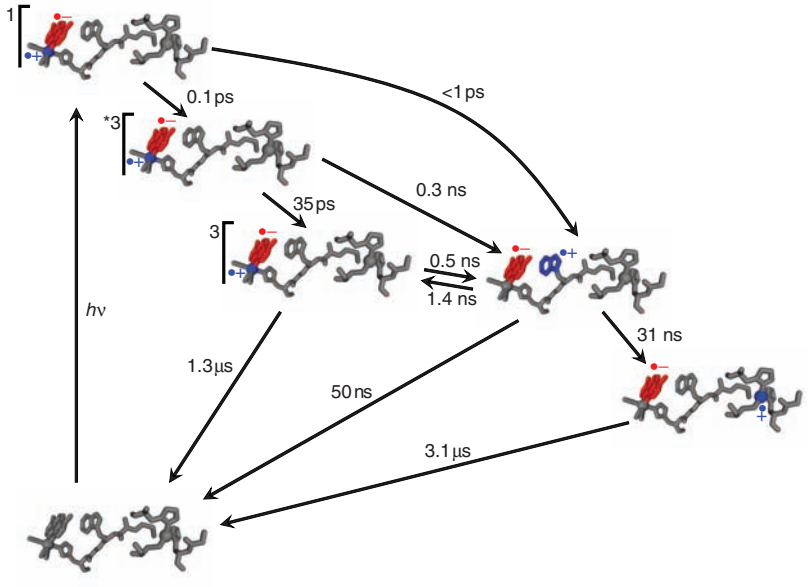

Fig. 3. Kinetics model of photoinduced electron transfer in $Re^{I}(CO)_3(dmp)(H^{124})|(W^{122})|AzCu^{I}$. Light absorption produces electron (red) and hole (blue) separation in the MLCT-excited Re^{I} complex. Migration of the hole to Cu^{I} via $(W^{122})^{\bullet+}$ is complete in less than 50 ns. Charge recombination proceeds on the microsecond time scale. Elementary rate constants were extracted from fits to time-resolved luminescence, visible absorption, and infrared spectroscopic data (*22*).

The 350(50)-ps kinetics phase is attributed to equilibration between the ^{3}MLCT state and $Re^{I}(CO)_3(dmp^{\bullet-})(H^{124})|(W^{122})^{\bullet+}|AzCu^{I}$, and the 25(5)-ns process to reduction of $(W^{122})^{\bullet+}$ by $AzCu^{I}$ to generate $Re^{I}(CO)_3(dmp^{\bullet-})(H^{124})|(W^{122})|AzCu^{II}$. Ground-state repopulation proceeds in 3 μs by long-range ET from $Re^{I}(CO)_3(dmp^{\bullet-})(H^{124})$ to $AzCu^{II}$. To extract rate constants corresponding to elementary reaction steps, we developed a numerical procedure to fit all of the time-resolved data to the rate laws defined by Fig. 3 (*22*). The transient spectra calculated using this model and the resulting elementary rate constants (Fig. 3) are in excellent agreement with the experimental data (Fig. 2).

The key finding is that Cu^{I} oxidation in $Re^{I}(CO)_3(dmp)(H^{124})|(W^{122})|AzCu^{I}$ is more than two orders of magnitude faster than expected for electron tunneling over 19 Å. Our analysis of the reaction kinetics reveals that the reduction potential of $*Re^{II}(CO)_3(dmp^{\bullet-})(H^{124})$ is just 28 mV greater than that of $(W^{122})^{\bullet+/0}$, but this is sufficient for very rapid (~ns) ET between adjacent dmp and W^{122} aromatic rings (Fig. 1). Replacement of W^{122} by Y or F inhibits this initial ET event, presumably because the $(Y^{122})^{\bullet+/0}$ and $(F^{122})^{\bullet+/0}$ reduction potentials are more than 200 mV above $E°[*Re^{II}(CO)_3(dmp^{\bullet-})(H^{124})/Re^{I}(CO)_3(dmp^{\bullet-})(H^{124})]$ (*29*). Concerted oxidation and deprotonation of Y^{122} by $*Re^{II}(CO)_3(dmp^{\bullet-})(H^{124})$ could be thermodynamically favorable, but likely would be accompanied by a significant activation barrier. Tryptophan radical cation is a relatively weak acid [pK_a = 4.5(2)] (*30*, *31*); its deprotonation, which is energetically favorable at pH 7, likely would proceed on a microsecond time scale (*17*). Hence, $(W^{122})^{\bullet+}$ can rapidly oxidize Cu^{I} in the azurin active site because it remains protonated in the hopping intermediate.

We have employed semiclassical ET theory (*22*) to generate a hopping map of driving-force effects on two-step (Cu^{I}→Int→*ML) and single-step (Cu^{I}→*ML) tunneling rates for a molecular framework analogous to $Re^{I}(CO)_3(dmp)(H^{124})|(W^{122})|AzCu^{I}$ (Fig. 4). The specific rate of each elementary ET reaction depends on three parameters: driving force, reorga-

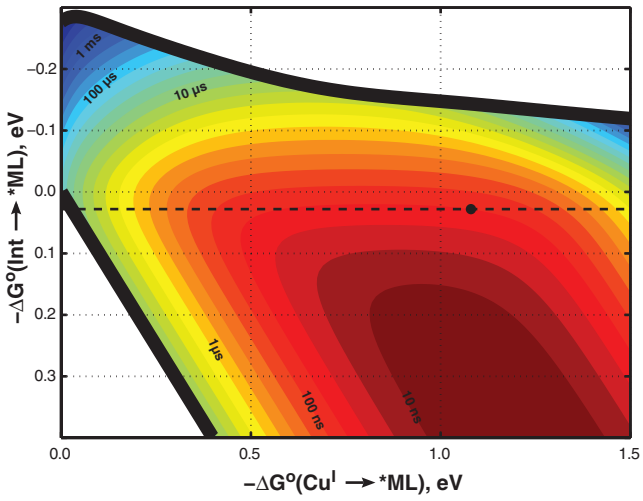

Fig. 4. Two-step hopping map for electron tunneling through Re^{I}-modified azurin. Colored contours reflect electron-transport time scales as functions of the driving force for the first tunneling step (ordinate, Int→*ML) and the overall electron-transfer process (abscissa, Cu^{I} →*ML). The heavy black lines enclose the region in which two-step hopping is faster than single-step tunneling. The dashed black line indicates the driving force for $*Re^{II}(CO)_3(dmp^{\bullet-})(H^{124})|(W^{122})|AzCu^{I}$ → $Re^{I}(CO)_3(dmp^{\bullet-})(H^{124})|(W^{122})^{\bullet+}|AzCu^{I}$ ET; the black dot corresponds to $*Re^{II}(CO)_3(dmp^{\bullet-})(H^{124})|(W^{122})|AzCu^{I}$ → $Re^{I}(CO)_3(dmp^{\bullet-})(H^{124})|(W^{122})^{\bullet+}|AzCu^{I}$ → $Re^{I}(CO)_3(dmp^{\bullet-})(H^{124})|(W^{122})|AzCu^{II}$ hopping.

nization energy, and electronic coupling (the overall advantage of two-step over single-step tunneling depends on seven independent parameters). The horizontal contours in the central part of the hopping map indicate that the overall charge-separation rate is more sensitive to the free-energy change for the first of the two tunneling steps. Indeed, the rate advantage of the multistep process is lost if the first tunneling step is too endergonic [$\Delta G°$(Int→*ML) > 200 meV] (*2*, *3*). Our modeling predicts a 54-ns time constant for Cu^{I} oxidation, in good agreement with the experimental value of 31 ns (*32*). We calculate that two-step hopping is more than 300 times as fast as single-step Cu^{I} to $*Re^{II}(CO)_3(dmp^{\bullet-})(H^{124})$ tunneling.

Biological redox machines often require multistep electron-tunneling architectures that can move charges rapidly over long distances with only a small loss of free energy. A hole originating on the Y^{122} radical in *Escherichia coli* ribonucleotide reductase is transferred some 35 Å to the active site, retaining sufficient oxidizing power to generate the C^{439} radical that initiates conversion of nucleotides to deoxynucleotides (*14*–*16*, *20*), and the photochemically generated hole in the P680 pigment [$E°(P680^{+\bullet/0}) \sim 1.3$ V] of the photosynthetic oxygen evolving center is transferred by Y_Z to the Mn-cluster active site where H_2O is oxidized to O_2 ($E° = 1.23$ V) (*18*, *33*). Our modeling demonstrates that the $Re^{I}(CO)_3(dmp)(H^{124})|(W^{122})|AzCu^{I}$ architecture could provide a suitable framework for an artificial solar energy storage device. The weak dependence of rates on $-\Delta G°(Cu^{I}\rightarrow *ML)$ (Fig. 4) confirms that more than 2 eV can be stored in a photochemical charge-separation process without a substantial sacrifice in rate. We anticipate no change in charge-separation rate constant if, through site-directed mutagenesis, the reduction potential of the blue copper active site in $Re^{II}(CO)_3(dmp^{\bullet-})(H^{124})|(W^{122})|AzCu^{I}$ were raised by 0.6 V. If the potential of the copper site were high enough to oxidize water, charge separation would proceed with a 1.4-µs time constant, an improvement by a factor of more than 600 over a direct $Cu^{I}\rightarrow Re^{II}$ single-step process.

References and Notes

1. H. B. Gray, J. R. Winkler, *Annu. Rev. Biochem.* **65**, 537 (1996).
2. H. B. Gray, J. R. Winkler, *Q. Rev. Biophys.* **36**, 341 (2003).
3. H. B. Gray, J. R. Winkler, *Proc. Natl. Acad. Sci. U.S.A.* **102**, 3534 (2005).
4. J. R. Winkler, A. Di Bilio, N. A. Farrow, J. H. Richards, H. B. Gray, *Pure Appl. Chem.* **71**, 1753 (1999).
5. S. S. Skourtis, I. Balabin, T. Kawatsu, D. N. Beratan, *Proc. Natl. Acad. Sci. U.S.A.* **102**, 3552 (2005).
6. A. A. Stuchebrukhov, *J. Chem. Phys.* **105**, 10819 (1996).
7. J. J. Regan *et al.*, *Chem. Biol.* **2**, 489 (1995).
8. C. Kobayashi, K. Baldridge, J. N. Onuchic, *J. Chem. Phys.* **119**, 3550 (2003).
9. T. R. Prytkova, I. V. Kurnikov, D. N. Beratan, *Science* **315**, 622 (2007).
10. C. C. Page, C. C. Moser, X. Chen, P. L. Dutton, *Nature* **402**, 47 (1999).
11. B. R. Crane, A. J. Di Bilio, J. R. Winkler, H. B. Gray, *J. Am. Chem. Soc.* **123**, 11623 (2001).
12. R. Langen *et al.*, *Science* **268**, 1733 (1995).
13. L. K. Skov, T. Pascher, J. R. Winkler, H. B. Gray, *J. Am. Chem. Soc.* **120**, 1102 (1998).
14. B. M. Sjöberg, *Struct. Bonding* **88**, 139 (1997).
15. J. Stubbe, D. G. Nocera, C. S. Yee, M. C. Y. Chang, *Chem. Rev.* **103**, 2167 (2003).
16. M. C. Y. Chang, C. S. Yee, D. G. Nocera, J. Stubbe, *J. Am. Chem. Soc.* **126**, 16702 (2004).
17. C. Aubert, M. H. Vos, P. Mathis, A. P. M. Eker, K. Brettel, *Nature* **405**, 586 (2000).
18. C. Tommos, G. T. Babcock, *Biochim. Biophys. Acta-Bioenerg.* **1458**, 199 (2000).
19. P. A. Frey, *Chem. Rev.* **90**, 1343 (1990).
20. J. Stubbe, W. A. van der Donk, *Chem. Rev.* **98**, 705 (1998).
21. Y. A. Berlin, G. R. Hutchison, P. Rempala, M. A. Ratner, J. Michl, *J. Phys. Chem. A* **107**, 3970 (2003).
22. Materials and methods are available as supporting material on *Science* Online.
23. All other tyrosines and the tryptophan in wild-type azurin were replaced with phenylalanine, and the surface histidine at position 83 was replaced with glutamine ($W^{48}F$, $H^{83}Q$, $Y^{72}F$, $Y^{108}F$, $L^{122}W/Y/F$, $T^{124}H$).
24. Single-letter abbreviations for the amino acid residues are as follows: A, Ala; C, Cys; D, Asp; E, Glu; F, Phe; G, Gly; H, His; I, Ile; K, Lys; L, Leu; M, Met; N, Asn; P, Pro; Q, Gln; R, Arg; S, Ser; T, Thr; V, Val; W, Trp; and Y, Tyr.
25. W. B. Connick, A. J. Di Bilio, M. G. Hill, J. R. Winkler, H. B. Gray, *Inorg. Chim. Acta* **240**, 169 (1995).
26. A. M. Blanco-Rodriguez *et al.*, *J. Am. Chem. Soc.* **128**, 4365 (2006).
27. A. Gabrielsson *et al.*, *J. Am. Chem. Soc.* **128**, 4253 (2006).
28. A. Cannizzo *et al.*, *J. Am. Chem. Soc.* **130**, in press (2008).
29. Although endergonic initial steps can still produce an advantage over single-step tunneling, transport time constants increase by roughly one order of magnitude for each 100 meV increase in $-\Delta G°$ (Int→*ML). Hence, tunneling through less stable intermediates, although possible, offers neither a kinetic nor an energetic advantage over a reaction involving exergonic tunneling steps.
30. A. Harriman, *J. Phys. Chem.* **91**, 6102 (1987).
31. S. Solar, N. Getoff, P. S. Surdhar, D. A. Armstrong, A. Singh, *J. Phys. Chem.* **95**, 3639 (1991).
32. On the basis of a large body of experimental data, we assume a reorganization energy of 0.8 eV for all ET steps (*2*, *3*). Earlier work has established that the rates of individual tunneling reactions in azurin depend exponentially on the donor-acceptor separation distance, with a decay constant of 1.1 $Å^{-1}$ (*12*); rates also depend on driving force [estimated from electrochemical measurements and from the observed $*Re^{II}(CO)_3(dmp^{\bullet-})(H^{124})|(W^{122})|AzCu^{I}$: $Re^{I}(CO)_3(dmp^{\bullet-})(H^{124})|(W^{122})^{\bullet+}|AzCu^{I}$ equilibrium constant].
33. K. N. Ferreira, T. M. Iverson, K. Maghlaoui, J. Barber, S. Iwata, *Science* **303**, 1831 (2004).

34. We thank C. Grădinaru, B. Leigh, and J. Miller for assistance in the early stages of this work. Supported by NIH (DK19038 to H.B.G.); NSF (CHE-0749997 to B.R.C., and CHE-0533150 to H.B.G. and J.R.W.); the Foundation BLANCEFLOR Boncompagni-Ludovisi, née Bildt; STINT, the Swedish Foundation for International Cooperation in Research and Higher Education (MLAA); the Engineering and Physical Sciences Research Council; Queen Mary, University of London; and the Science and Technology Facilities Council (CMSD43). The coordinates of the $Re^{I}(CO)_3(dmp)(H^{124})|(W^{122})|AzCu^{II}$ crystal structure have been deposited in the Protein Data Bank (accession number 2I7O).

Supporting Online Material

www.sciencemag.org/cgi/content/full/320/5884/1760/DC1
Materials and Methods
Figs. S1 to S3
Table S1
References

24 March 2008; accepted 21 May 2008
10.1126/science.1158241

A Phylogenomic Study of Birds Reveals Their Evolutionary History

Shannon J. Hackett,[1]* Rebecca T. Kimball,[2]*† Sushma Reddy,[1]* Rauri C. K. Bowie,[1,3,4] Edward L. Braun,[2] Michael J. Braun,[5,6] Jena L. Chojnowski,[2] W. Andrew Cox,[2] Kin-Lan Han,[2,5,6] John Harshman,[1,7] Christopher J. Huddleston,[5] Ben D. Marks,[8] Kathleen J. Miglia,[9] William S. Moore,[9] Frederick H. Sheldon,[8] David W. Steadman,[10] Christopher C. Witt,[8,11] Tamaki Yuri[2,5]

Deep avian evolutionary relationships have been difficult to resolve as a result of a putative explosive radiation. Our study examined ~32 kilobases of aligned nuclear DNA sequences from 19 independent loci for 169 species, representing all major extant groups, and recovered a robust phylogeny from a genome-wide signal supported by multiple analytical methods. We documented well-supported, previously unrecognized interordinal relationships (such as a sister relationship between passerines and parrots) and corroborated previously contentious groupings (such as flamingos and grebes). Our conclusions challenge current classifications and alter our understanding of trait evolution; for example, some diurnal birds evolved from nocturnal ancestors. Our results provide a valuable resource for phylogenetic and comparative studies in birds.

Although well studied, the evolutionary relationships among major avian groups are contentious (*1*–*6*). Recovering deep evolutionary relationships in birds is difficult, probably reflecting a rapid divergence early in their evolutionary history (*1*–*3*, *7*, *8*) that has resulted in many distinctive, morphologically cohesive groups (e.g., owls, parrots, and doves) with few, if any, extant intermediary forms linking them to other well-defined groups. This extreme radiation also makes it difficult to place fossil taxa, which further contributes to the difficulty in precisely timing avian divergences (*3*, *9*).

Only two nodes at the base of the avian tree are consistently supported by both molecular and morphological phylogenetic studies (*2*–*5*, *10*–*14*). The first divides the Paleognathae (ratites and tinamous) and Neognathae (all other birds), and the second splits the neognaths between the Galloanserae (chickens, ducks, and allies) and Neoaves (other neognaths). Although the Neoaves represents the majority of avian diversity (95% of extant species) and is the focus of most comparative studies, little consensus exists regarding relationships within this clade (*1*–*5*, *8*). The absence of intermediate forms linking well-defined groups, combined with the difficulty of resolving relationships, led to hypotheses that the base of Neoaves represents an unresolved evolutionary radiation (polytomy) (*7*, *8*). Previous efforts to reconstruct these phylogenetic relationships have been limited by taxon sampling, the number of loci, and/or slowly evolving loci with limited power to resolve short internodes [e.g., (*3*, *4*, *10*, *12*, *14*)]. Moreover, conflicting results have been obtained with morphology (*13*, *15*), DNA-DNA hybridization (*6*), whole mitochondrial genomes (*16*–*18*), and different nuclear exon, ribosomal RNA, and intron sequences (*1*, *3*, *4*, *10*, *12*, *14*).

Phylogenomics is useful for resolving difficult phylogenies and for verifying or overturning relationships created on the basis of single genes (*19*–*21*). We collected a large DNA sequence data set to address avian phylogenetic relationships from 171 species representing all but three nonpasserine families, all major passerine clades, and two crocodilian outgroups (*22*). Our alignment of 32 kb represents 19 nuclear loci located on 15 different chromosomes in the chicken genome (*22*), with introns (74%), coding exons (23%), and untranslated regions (UTRs) (3%). Data quality and sequence alignments were assessed before analyses (*22*). We analyzed the data using different optimality criteria and distinct tree-search algorithms (*22*).

Our sampling of many loci allowed us to assess whether relationships were supported by a signal across the genome or were driven by a single locus. We (i) analyzed individual loci, (ii) conducted "gene-jackknifing" (excluding one locus at a time, then analyzing the remaining data) to determine whether conclusions were driven by a single locus, (iii) conducted a partitioned–maximum likelihood (ML) analysis (where each locus had a distinctive set of parameters), and (iv) coded the data as R (purine) or Y (pyrimidine) to avoid conclusions driven by base-compositional biases [e.g., (*16*)].

Analyses of individual loci showed that no single gene was able to recover all nodes identified with the concatenated data (Fig. 1). The low power of individual loci was the most pronounced in short and slowly evolving genes, which generally did not resolve any interordinal relationships (Fig. 1).

Consistent with previous studies, we recovered genome-wide support for basal divergences between Paleognathae and Neognathae and between Galloanserae and Neoaves (Fig. 2) with robust support. The topology at the base of Neoaves, with extremely short internodes, indicated a rapid radiation (Fig. 3) that likely explains conflicts among previous studies. However, we consistently found several, well-supported, deep divisions within Neoaves (highlighted in different colors in Figs. 2 to 4).

Our study (i) revealed robust higher-level groupings within Neoaves, (ii) suggested several previously unrecognized interordinal relationships, (iii) supported previously proposed clades, (iv) reinforced established relationships not consistently recovered in previous studies, and (v) found well-supported groupings at the tips of major clades. The results discussed below focus on groups that are found with multiple analytical methods and partitions and that exhibit strong support (ML bootstrap support ≥ 70%) (*23*).

The largest clade in Neoaves was a well-supported land bird clade (green, node F, Fig. 2) (*3*) that contained the Passeriformes (perching birds, representing more than half of all avian species), which is allied with several morphologically diverse orders. These included Piciformes (woodpeckers and allies), Falconiformes (hawks and falcons), Strigiformes (owls), Coraciiformes (kingfishers, hornbills, rollers, and allies), Psittaciformes (parrots), Coliiformes (mousebirds), and Trogoniformes (trogons). One of the most unexpected findings was the sister relationship between Passeriformes and Psittaciformes (node A, Fig. 2), with Falconidae (falcons) sister to this clade. This relationship varied slightly among analyses and gene-jackknifing (Fig. 1), yet the close relationship between passerines with parrots and/or falcons appeared consistently.

Sister to the land birds is the Charadriiformes (shorebirds, gulls, and alcids; yellow, node G, Fig. 2). This grouping seems to be driven primarily by the β-*fibrinogen* gene (*FGB*), because it was present in analyses of only this gene and disappeared when the gene was removed through jackknifing (Fig. 1). Regardless of the exact placement of the Charadriiformes in our analyses, we consistently support that this order is not basal within Neoaves (*24*) and thus refute the hypothesis that transitional shorebirds gave rise to all modern birds (*7*). Our phylogeny revealed a highly supported water bird clade (blue, node H, Fig. 2) (*3*, *14*), including members of the Pelecaniformes (totipalmate birds), Ciconiiformes (storks and allies), Procellariiformes (tube-nosed birds), Sphenisciformes (penguins), and Gaviiformes (loons). Basal to the water birds were two clades of terrestrial and arboreal taxa

[1]Zoology Department, Field Museum of Natural History, 1400 South Lake Shore Drive, Chicago, IL 60605, USA. [2]Department of Zoology, University of Florida, Gainesville, FL 32611, USA. [3]Museum of Vertebrate Zoology and Department of Integrative Biology, University of California, Berkeley, CA 94720, USA. [4]Department of Science and Technology–National Research Foundation Centre of Excellence at the Percy FitzPatrick Institute, Department of Botany and Zoology, Stellenbosch University, Matieland 7602, South Africa. [5]Department of Vertebrate Zoology, Smithsonian Institution, 4210 Silver Hill Road, Suitland, MD 20746, USA. [6]Behavior, Ecology, Evolution, and Systematics Program, University of Maryland, College Park, MD 20742, USA. [7]Pepperwood Way, San Jose, CA 95124, USA. [8]Museum of Natural Science, 119 Foster Hall, Louisiana State University, Baton Rouge, LA 70803, USA. [9]Department of Biological Sciences, Wayne State University, 5047 Gullen Mall, Detroit, MI 48202, USA. [10]Florida Museum of Natural History, University of Florida, Gainesville, FL 32611, USA. [11]Department of Biology and Museum of Southwestern Biology, University of New Mexico, Albuquerque, NM 87131, USA.

*These authors contributed equally to this work.
†To whom correspondence should be addressed. E-mail: rkimball@ufl.edu

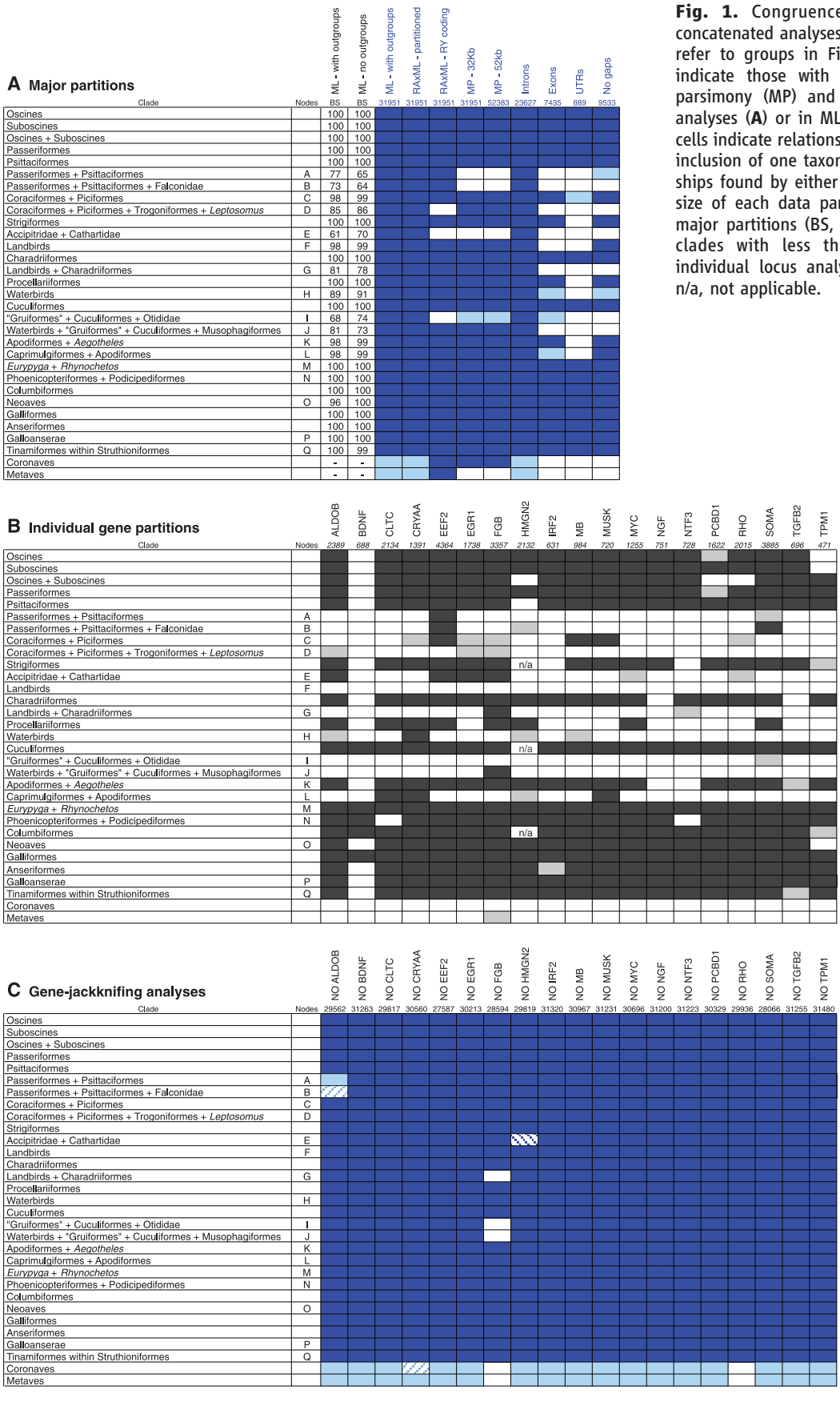

Fig. 1. Congruence of clades as determined from concatenated analyses and multiple data partitions. Nodes refer to groups in Fig. 2. Dark blue or dark gray cells indicate those with relationships present in maximum parsimony (MP) and ML [GARLI (*31*) and RAxML (*32*)] analyses (**A**) or in ML (**B** and **C**); light blue or light gray cells indicate relationships present with the exception of or inclusion of one taxon; and striped cells indicate relationships found by either GARLI or RAxML, but not both. The size of each data partition is listed below its name. (A) major partitions (BS, bootstrap support; dashes represent clades with less than 50% bootstrap support); (B) individual locus analyses; (C) gene-jackknifing analyses. n/a, not applicable.

(node J, Fig. 2): Musophagiformes (turacos) and a clade (gray, node I, Fig. 2) including core Gruiformes (rails, cranes, and allies), Cuculiformes (cuckoos), and Otididae (bustards, which are typically considered as belonging to Gruiformes). These latter relationships were also largely dependent on the presence of *FGB* (Fig. 1) and require further study to determine their validity.

One of our most important findings was that several well-accepted orders were not monophyletic. Our analyses provided strong support that (i) Tinamiformes (tinamous) are found

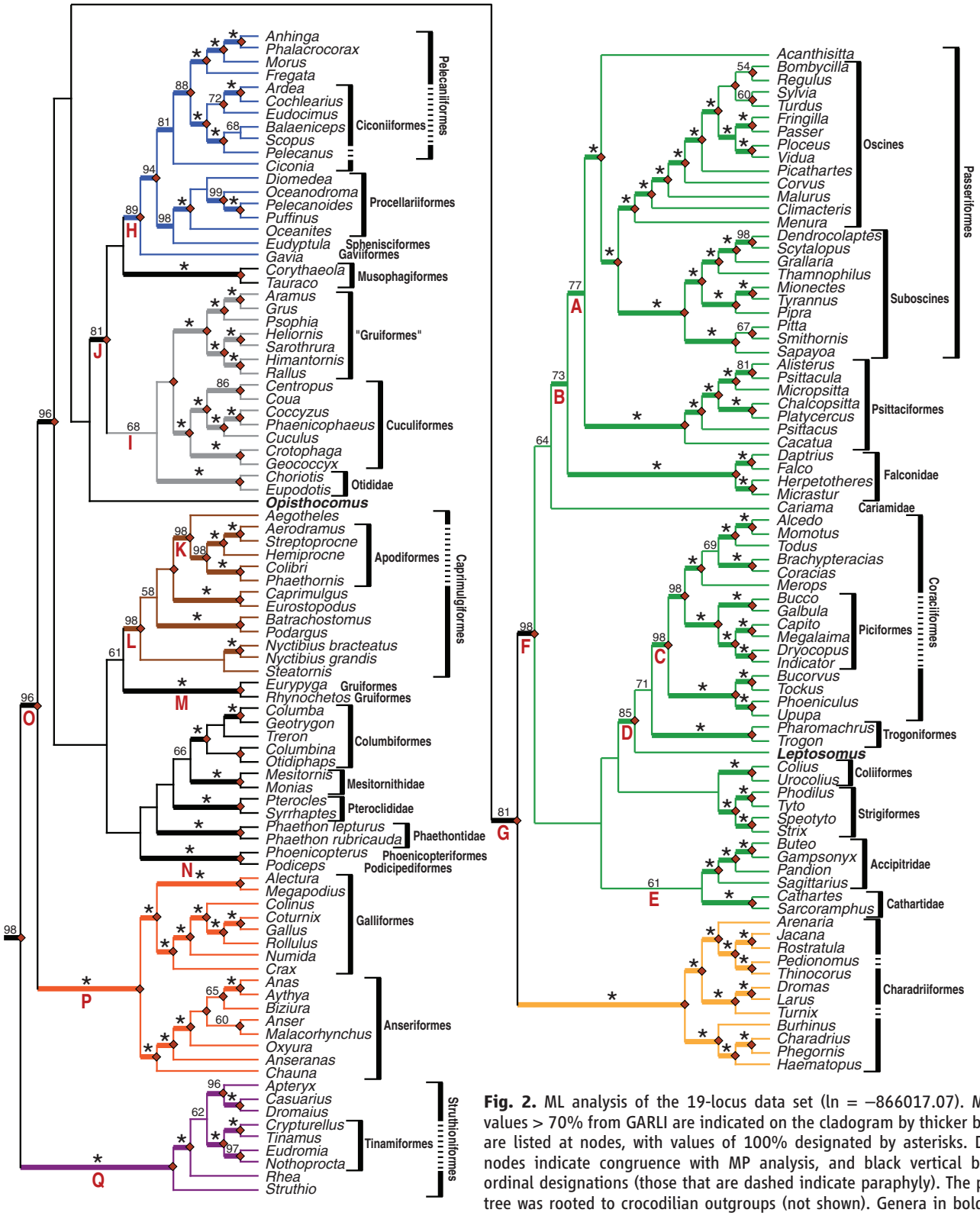

Fig. 2. ML analysis of the 19-locus data set (ln = −866017.07). ML bootstrap values > 70% from GARLI are indicated on the cladogram by thicker branches and are listed at nodes, with values of 100% designated by asterisks. Diamonds at nodes indicate congruence with MP analysis, and black vertical bars refer to ordinal designations (those that are dashed indicate paraphyly). The phylogenetic tree was rooted to crocodilian outgroups (not shown). Genera in bold are icertae sedis. Branch colors represent major clades supported in this study: land birds (green), charadriiforms (yellow), water birds (blue), core gruiforms and cuckoos (gray), apodiforms and caprimulgiforms (brown), galloanserae (orange), and paleognaths (purple). Large capital letters indicate groups discussed in the text and Fig. 1.

within Struthioniformes (ostriches and allies; purple, node Q, Fig. 2), (ii) Apodiformes (hummingbirds and swifts) are found within Caprimulgiformes (nightjars and their allies; brown, node L, Fig. 2), and (iii) Piciformes are found within Coraciiformes (node C, Fig. 2). Typical Pelecaniformes and Ciconiiformes [sensu (*13*, *25*)] were intermixed in a clade (Fig. 2) that excludes one traditional pelecaniform family: the Phaethontidae (tropicbirds). The Gruiformes represented at least four distinct clades in our tree (Fig. 4), depending on the circumscriptions of this order [reviewed in (*6*)]. Finally, Falconidae and Accipitridae (hawks and osprey) formed distinct clades in all analyses, rather than a monophyletic Falconiformes (Fig. 2) (*18*).

Several disparate taxa were robustly placed in our analyses. Cariamidae (seriemas) has traditionally been classified as a gruiform, although convergence with Falconiformes was noted (*6*). We found strong support for placing Cariamidae within land birds near other raptorial groups. *Leptosomus* (cuckoo roller) is generally placed within Coraciiformes, though a relationship with Falconiformes has also been suggested (*6*). Our data set placed *Leptosomus* sister to a clade including Piciformes, Coraciiformes, and Trogoniformes (node D, Fig. 2).

Our results suggest resolution of some controversial groupings. For example, Cathartidae (New World vultures)—traditionally placed within Falconiformes—were previously allied with Ciconiidae (storks) (*6*). However, our phylogeny demonstrated no affinity with storks [see also (*3*, *18*, *26*)] and instead strongly supported placement of Cathartidae within the land birds (usually with Accipitridae). We support that *Turnix* (buttonquail) belongs within the Charadriiformes (*3*, *4*, *27*) and that Podicipediformes (grebes) and Phoenicopteriformes (flamingos; node N, Fig. 2) (*14*) are sister taxa. Finally, we recovered a sister relationship between *Rhynochetos* (kagu) and *Eurypyga* (sunbittern) (node M, Fig. 2) (*28*): two monospecific and geographically disparate families that grouped outside of the core Gruiiformes.

The previously proposed division of Neoaves into Coronaves and Metaves is driven by two loci (*4*) in our analyses (Fig. 1) and may not represent the species tree. Many taxa assigned to Metaves are composed of small numbers of closely related extant species, including Mesitornithidae (mesites), Phaethontidae, Pteroclididae (sandgrouse), and Columbiformes (pigeons and doves). The difficulty in placing them may be driven by long, unbreakable branches leading to the tips (Fig. 3). The enigmatic *Opisthocomus* (hoatzin) still cannot be confidently placed, but some putative sister relationships can be rejected (*29*).

Modern birds occupy a wide diversity of niches and exhibit a variety of behaviors. The broad structure of our phylogeny suggested diversification along general ecological divisions, such as water birds, shorebirds, and land birds. However, adaptations to these environments clearly arose multiple times (*4*), because many aquatic birds were not part of the water bird clade (e.g., tropicbirds, flamingos, and grebes) and terrestrial birds were found outside of the land bird clade (e.g., turacos, doves, sandgrouse, and cuckoos). Our phylogeny also indicated several distinctive niches, such as nocturnal (owls, nightjars, and allies), raptorial (falcons, hawks, eagles, New World vultures, seriema, and owls), or pelagic (tubenosed birds, frigatebirds, and tropicbirds) lifestyles, have evolved multiple times. Furthermore, our results reinterpret the evolution of various adaptations (e.g., the diurnal Apodiformes evolved from nocturnal/crepuscular Caprimulgiformes, and flighted Tinamiformes arose within the flightless Struthioniformes) and biogeographic patterns (e.g., the New Caledonian kagu and Neotropical sunbittern are sister taxa).

Given the number of nonmonophyletic groups in our study, we compared our results with major classifications [supporting online material (SOM) text]. Unexpectedly, roughly the same percentage (35%) of orders defined by different classifications (*13*, *25*, *30*) was not monophyletic relative to the results of our study (Fig. 4). Some orders, such as Gruiformes and the broadly encompassing Ciconiiformes [sensu (*30*)], were particularly problematic. Other traditional orders were not monophyletic because of the exclusion or inclusion of one or a few taxa (e.g., placing *Turnix* within Charadriiformes contradicts all three classifications). Only six orders were defined consistently across taxonomies and monophyletic in our study (Fig. 4). Given our results, conclusions from comparative studies that depended upon these classifications may need to be re-evaluated in light of this understanding of avian evolution.

Deciphering the roots of the avian tree of life has been a lingering problem in evolutionary biology. The inclusion of multiple loci with diverse rates of evolution, particularly the large proportion of rapidly evolving introns, yielded a well-supported phylogenetic tree at multiple taxonomic depths. Although some higher-level avian relationships remain unresolved, simulations suggest that additional sequence data from rapidly evolving loci may resolve these remaining questions (*1*). It is also evident that future classifications will

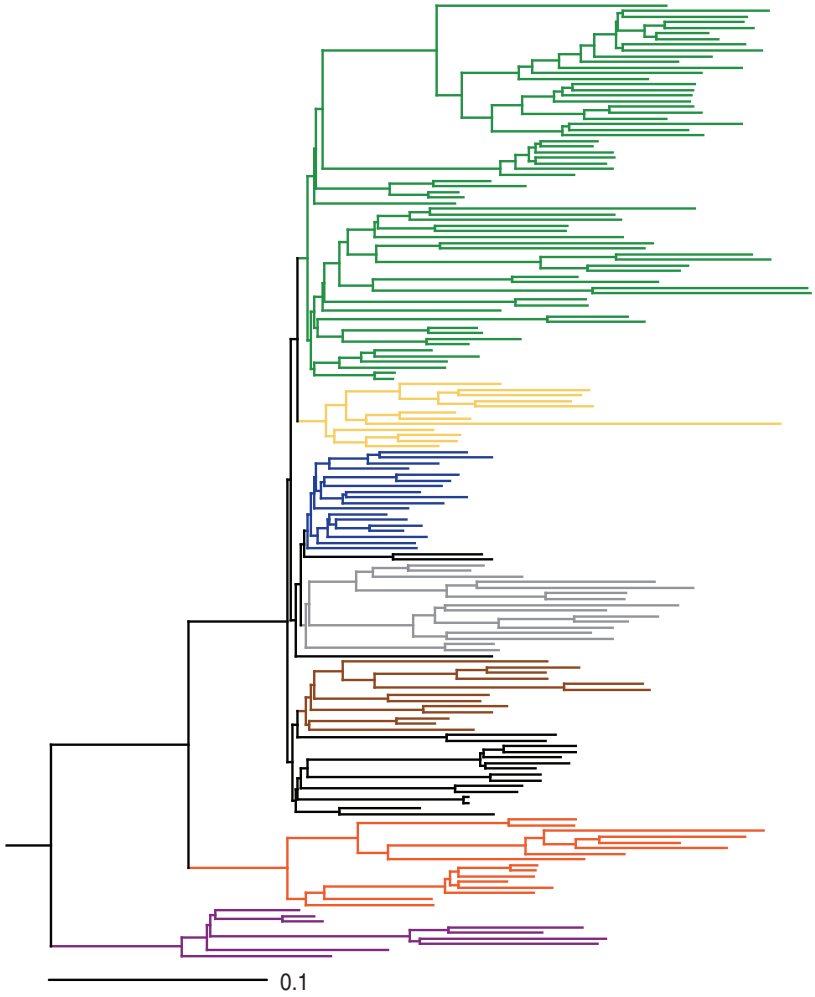

Fig. 3. ML phylogram demonstrating the short internodes at the base of Neoaves and highlighting certain extreme examples of rate variation across avian lineages. Colors are as in Fig. 2. Scale bar indicates substitutions per site. Figure S1 shows the phylogram with taxon names.

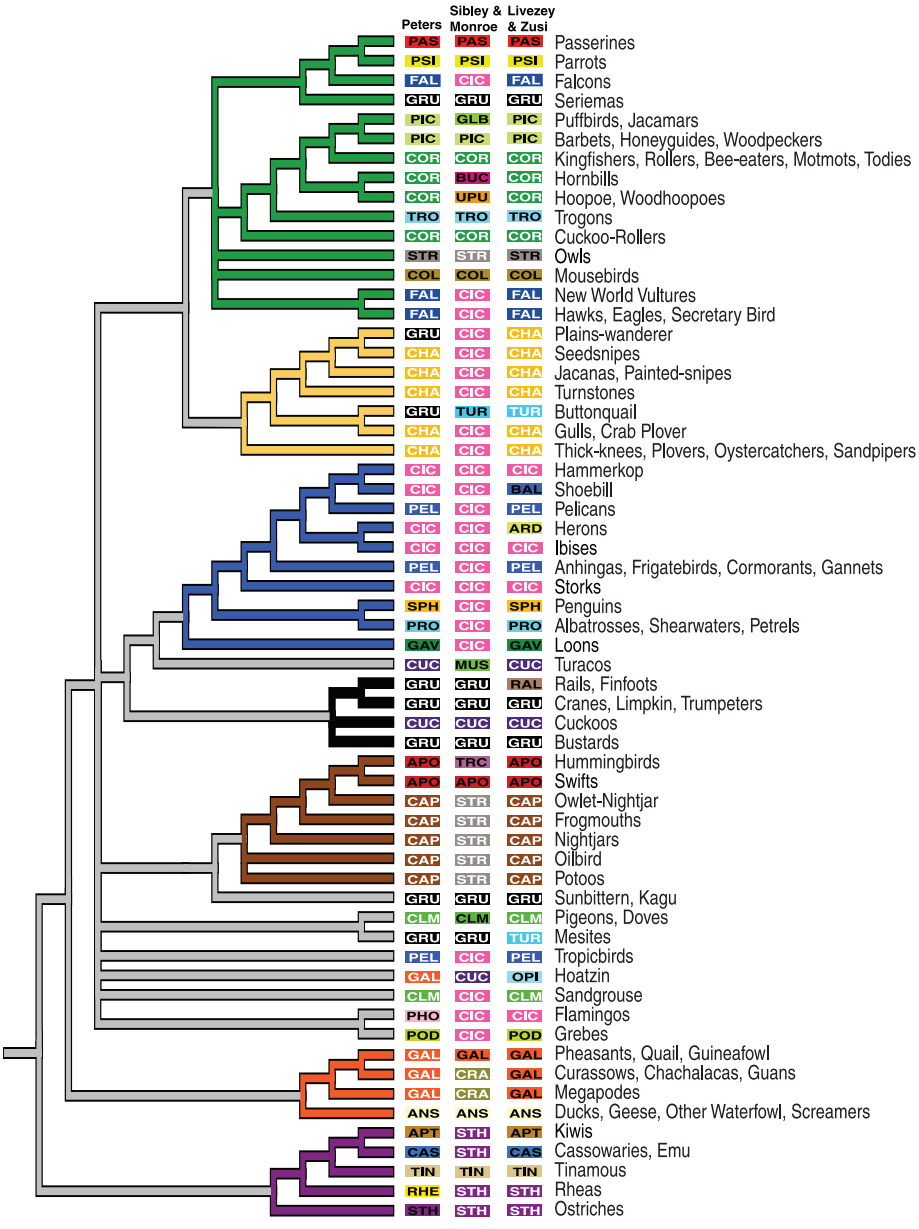

Fig. 4. Our phylogeny differs from and agrees with previous classifications. We merged well-supported (>70% bootstrap values) monophyletic clades at the tips with the same ordinal designation across all three classifications (e.g., 24 species called Passerines). Only higher relationships supported by bootstrap values >50% are shown. Colors are as in Fig. 2. Color bars to the right of the tree show membership in three different classifications: Peters' (*25*) (left), Sibley and Monroe's (*30*) (middle), and Livezey and Zusi's (*13*) (right). Black text within the bars indicates monophyletic orders in our phylogeny, whereas white text within the bars indicates nonmonophyletic orders. Ordinal name codes: ANS (Anseriformes), APO (Apodiformes), APT (Apterygiformes), ARD (Ardeiformes), BAL (Balaenicipitiformes), BUC (Bucerotiformes), CAP (Caprimulgiformes), CAS (Casuariiformes), CHA (Charadriiformes), CIC (Ciconiiformes), CLM (Columbiformes), COL (Coliiformes), COR (Coraciiformes), CRA (Craciformes), CUC (Cuculiformes), FAL (Falconiformes), GAL (Galliformes), GAV (Gaviiformes), GLB (Galbuliformes), GRU (Gruiformes), MUS (Musophagiformes), OPI (Opisthocomiformes), PAS (Passeriformes), PEL (Pelecaniformes), PIC (Piciformes), POD (Podicipediformes), PRO (Procellariiformes), PSI (Psittaciformes), RAL (Ralliformes), RHE (Rheiformes), SPH (Sphenisciformes), STH (Struthioniformes), STR (Strigiformes), TIN (Tinamiformes), TRC (Trochiliformes), TRO (Trogoniformes), TUR (Turniciformes), and UPU (Upupiformes).

change dramatically, based on our phylogenetic study, and that our results will stimulate comparative studies to address the growing number of questions regarding the evolution of birds.

References and Notes

1. J. L. Chojnowski, R. T. Kimball, E. L. Braun, *Gene* **410**, 89 (2008).
2. J. Cracraft *et al.*, in *Assembling the Tree of Life*, J. Cracraft, M. J. Donoghue, Eds. (Oxford Univ. Press, New York, 2004), pp. 468–489.
3. P. G. P. Ericson *et al.*, *Biol. Lett.* **2**, 543 (2006).
4. M. G. Fain, P. Houde, *Evolution Int. J. Org. Evolution* **58**, 2558 (2004).
5. J. Harshman, in *Reproductive Biology and Phylogeny of Birds*, B. G. M. Jamieson, Ed. (Science Publishers, Enfield, NH, 2007), pp. 1–35.
6. C. G. Sibley, J. E. Ahlquist, *Phylogeny and Classification of Birds: A Study in Molecular Evolution* (Yale Univ. Press, New Haven, CT, 1990).
7. A. Feduccia, *Science* **267**, 637 (1995).
8. S. Poe, A. L. Chubb, *Evolution Int. J. Org. Evolution* **58**, 404 (2004).
9. J. W. Brown, J. S. Rest, J. Garcia-Moreno, M. D. Sorenson, D. P. Mindell, *BMC Biol.* **6**, 6 (2008).
10. A. L. Chubb, *Mol. Phylogenet. Evol.* **30**, 140 (2004).
11. J. Cracraft, J. Clarke, in *New Perspectives on the Origin and Early Evolution of Birds: Proceedings of the International Symposium in Honor of John H. Ostrom*, J. Gauthier, L. F. Gall, Eds. (Yale Univ. Press, New Haven, CT, 2001), pp. 143–156.
12. J. G. Groth, G. F. Barrowclough, *Mol. Phylogenet. Evol.* **12**, 115 (1999).
13. B. C. Livezey, R. L. Zusi, *Zool. J. Linn. Soc.* **149**, 1 (2007).
14. M. van Tuinen, D. B. Butvill, J. A. W. Kirsch, S. B. Hedges, *Proc. R. Soc. London Ser. B* **268**, 1345 (2001).
15. G. Mayr, J. Clarke, *Cladistics* **19**, 527 (2003).
16. E. L. Braun, R. T. Kimball, *Syst. Biol.* **51**, 614 (2002).
17. D. P. Mindell *et al.*, *Syst. Biol.* **48**, 138 (1999).
18. K. E. Slack, F. Delsuc, P. A. Mclenachan, U. Arnason, D. Penny, *Mol. Phylogenet. Evol.* **42**, 1 (2007).
19. F. Delsuc, H. Brinkmann, H. Philippe, *Nat. Rev. Genet.* **6**, 361 (2005).
20. E. Jiménez-Guri, H. Philippe, B. Okamura, P. W. H. Holland, *Science* **317**, 116 (2007).
21. W. J. Murphy, P. A. Pevzner, S. J. O'Brien, *Trends Genet.* **20**, 631 (2004).
22. Materials and methods are available as supporting material on *Science* Online.
23. D. M. Hillis, J. J. Bull, *Syst. Biol.* **42**, 182 (1993).
24. T. Paton, O. Haddrath, A. J. Baker, *Proc. R. Soc. London Ser. B* **269**, 839 (2002).
25. J. L. Peters *et al.*, *Check-list of Birds of the World*, J. L. Peters *et al.*, Eds. (Museum of Comparative Anatomy, Cambridge, MA, 1931 to 1979), vols. I to XV.
26. C. S. Griffiths, *Auk* **111**, 787 (1994).
27. T. A. Paton, A. J. Baker, J. G. Groth, G. F. Barrowclough, *Mol. Phylogenet. Evol.* **29**, 268 (2003).
28. J. Cracraft, *Geobios Memoire Spec.* **6**, 25 (1982).
29. M. D. Sorenson, E. Oneal, J. García-Moreno, D. P. Mindell, *Mol. Biol. Evol.* **20**, 1484 (2003).
30. C. G. Sibley, B. L. Monroe Jr., *Distribution and Taxonomy of Birds of the World* (Yale Univ. Press, New Haven, CT, 1990).
31. D. J. Zwickl, thesis, University of Texas at Austin (2006).
32. A. Stamatakis, *Bioinformatics* **22**, 2688 (2006).

33. This work is a contribution of the Early Bird project, supported by NSF's Assembling the Tree of Life program (DEB-0228675, DEB-0228682, DEB-0228688, and DEB-0228617). We thank the American Museum of Natural History, Australian National Wildlife Collection, Burke Museum of Natural History and Culture (University of Washington), Field Museum of Natural History, University of Kansas Natural History Museum and Biodiversity Center, L. Densmore private collection, Louisiana State University Museum of Natural Science, Marjorie Barrick Museum (University of Nevada, Las Vegas), Museum of Southwestern Biology (University of New Mexico), Museum of Vertebrate Zoology (University of California, Berkeley), Museum Victoria, National Museum of Natural History, San Francisco Zoological Garden, and Zoological Museum University of Copenhagen, as well as many different collectors for tissue samples (table S1). We appreciate support from D. Zwickl and R. Ree for analysis; the DePaul Bioinformatics Group, part of the Illinois Bio-grid at DePaul University, for access to their supercomputing facilities; and J. Bates, D. Levey, P. Makovicky, T. Schulenberg, and P. Soltis for comments. Z. Bear, N. Block, B. Burkley, M. Burns, Z. Burns, S. Coplowitz, R. Flynn, K. Hammons, V. Heimer-Torres, E. Sackett-Hermann,

A. Hudson, S. Hunter-Smith, S. Kearney, L. Kimball, K. Rozofsky, J. Smith, and P. Tester provided assistance in the lab. Sequence accession numbers in GenBank are EU737149 to EU740386, EF521416 to EF521576, and EU302706 to EU302748.

Supporting Online Material
www.sciencemag.org/cgi/content/full/320/5884/1763/DC1
Materials and Methods
SOM Text
Figs. S1 to S3
Tables S1 to S3
References

12 March 2008; accepted 29 May 2008
10.1126/science.1157704

A Significant Upward Shift in Plant Species Optimum Elevation During the 20th Century

J. Lenoir,[1]* J. C. Gégout,[1] P. A. Marquet,[2,3,4] P. de Ruffray,[5] H. Brisse[6]

Spatial fingerprints of climate change on biotic communities are usually associated with changes in the distribution of species at their latitudinal or altitudinal extremes. By comparing the altitudinal distribution of 171 forest plant species between 1905 and 1985 and 1986 and 2005 along the entire elevation range (0 to 2600 meters above sea level) in west Europe, we show that climate warming has resulted in a significant upward shift in species optimum elevation averaging 29 meters per decade. The shift is larger for species restricted to mountain habitats and for grassy species, which are characterized by faster population turnover. Our study shows that climate change affects the spatial core of the distributional range of plant species, in addition to their distributional margins, as previously reported.

Recent warming has induced biological and ecological responses from animals and plants throughout the world (*1*–*3*). Consistent responses to global warming or "fingerprints" are apparent in the phenology and distribution of species (*1*–*5*). For plants, invertebrates, and vertebrates, climate change has strongly influenced distribution and abundance at range margins both in latitude (polar margins) (*5*–*8*) and in elevation (upper margins) (*5*, *9*–*11*), and even in depth for marine fishes (*8*). Shifts at the upper edge of altitudinal range agree with the hypothesis of an upward trend to escape rising temperatures (*12*–*14*). Changes in range limits, however, are just one, albeit important, expression of the likely consequences of climate change. More subtle changes within the ranges of species are also likely and, although poorly explored as yet, might have important ecological and evolutionary consequences. Assuming niche conservatism over evolutionary time (*15*), we tested for large-scale (across temperate and Mediterranean mountain forests in west Europe), long-term (over the 20th century), and multispecies (through an assemblage of 171 species) climate-related responses in forest plant altitudinal distributions. We analyzed species responses by measuring shifts in the altitudinal position of species' maximum probability of presence within their distribution, instead of focusing on distributional extremes. Additionally, we tested for the effect of ecological and life history traits on the magnitude of the response to climate warming (*16*). In particular, we tested whether species restricted to mountain areas (*10*–*12*, *17*, *18*) and/or fast generation times (*19*) are particularly sensitive to temperature changes.

We studied species in forest communities found between lowland to the upper subalpine vegetation belt (0 to 2600 m above sea level) over six mountain ranges in west Europe (the Western Alps, the Northern Pyrenees, the Massif Central, the Western Jura, the Vosges, and the Corsican range). Climatic change in France has been characterized by increases in average temperature of far greater magnitude than increases in the world mean annual temperature, of about 0.6°C over the 20th century (*20*), reaching up to 0.9°C (*21*) and even close to 1°C in the alpine region since the early 1980s (*22*). From two large-scale floristic inventories (about 28,000 surveys) (*23*), we extracted two well-balanced subsamples, including 3991 surveys each, carried out across the studied mountain ranges (see fig. S1 for surveys location). The first subsample included surveys carried out before the mid-1980s (1905–1985), and the other one, after 1985 (1986–2005) (see fig. S2 for altitudinal distribution of surveys). We chose this temporal threshold because the analysis of yearly mean surface temperature anomalies between 1965 and 2005 shows that in 1986 the studied mountain ranges experienced a temperature regime shift (Fig. 1A), staying above the average baseline conditions. In contrast, analysis of annual precipitation anomalies between 1965

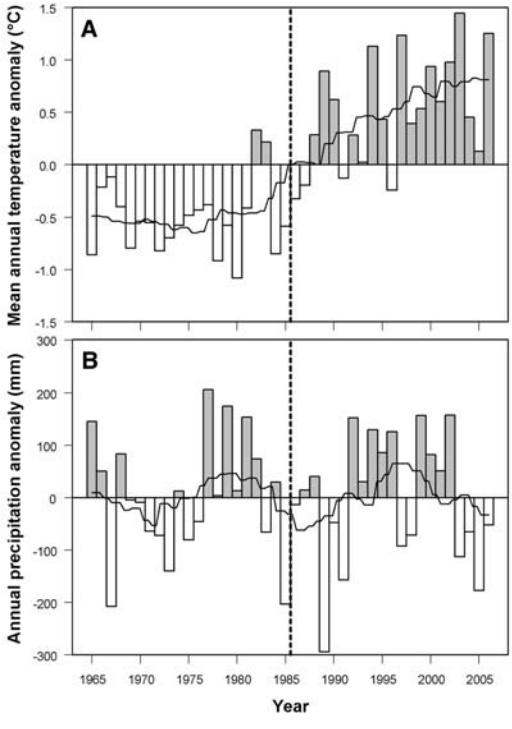

Fig. 1. Climatic trends from 1965 to 2006. (**A**) Yearly mean surface temperature anomalies (using overall mean temperature as baseline) and (**B**) annual precipitation anomalies (using overall mean annual precipitation as baseline) averaged for 73 elevation sites in the French mountains ranging in altitude from 10 to 2010 m above sea level. Solid gray bars refer to positive anomalies, whereas open bars refer to negative ones. The solid curve is the smoothed average with use of a 10-year filter. The vertical dotted lines mark the split between the two studied periods. Data have been gathered from the French National Climatic Network (Météo-France).

[1]AgroParisTech, UMR 1092, Laboratoire d'Etude des Ressources Forêt-Bois (LERFoB), 14 rue Girardet, F-54000 Nancy, France. [2]Center for Advanced Studies in Ecology and Biodiversity (CASEB), Departamento de Ecologia, Pontificia Universidad Católica de Chile, Alameda 340 C.P. 6513677, Santiago, Chile. [3]Institute of Ecology and Biodiversity (IEB), Casilla 653, Santiago, Chile. [4]Santa Fe Institute, 1399 Hyde Park Road, Santa Fe, NM 87501, USA. [5]CNRS, Institut de Biologie Moléculaire des Plantes (IBMP), Université Louis Pasteur, 12 Rue du Général Zimmer, F-67084 Strasbourg Cedex, France. [6]CNRS, UMR 6116, Institut Méditerranéen d'Ecologie et de Paléoécologie (IMEP), Faculté des Sciences de Saint Jérôme, case 461, F-34397 Marseille Cedex 20, France.

*To whom correspondence should be addressed. E-mail: jonathan.lenoir@agroparistech.fr

and 2005 does not show any trend or precipitation regime shift (Fig. 1B). The subsampling method (*23*) was carried out in order to avoid a potential bias attributable to an uneven sampling effort between periods. In particular, we controlled for artificial warming (fig. S1) (*23*), which could be generated by the sampling of recent plots located in warmer conditions (i.e., southern latitude) regardless of climate warming. Our study was restricted to forest communities where long-term changes outweigh short-term tendencies because the forest canopy acts as a buffer zone, smoothing extreme interannual variation in temperature, in comparison with open areas that are far more influenced by both interannual climatic variation and agricultural practices. Changes in species distribution under the forest canopy can therefore be considered as fingerprints of regional trends rather than reflecting idiosyncratic trends in time or space.

Because we were more interested in the unexplored phenomenon of within-range shifts in plant species, we investigated changes in species optimum elevation over the study period instead of changes at the upper and lower boundaries of their distributions, which are more sensitive to sampling effort (*24*). By using simple logistic regression, we computed the altitude of maximum probability of presence, also called optimum elevation, within each period for 171 species (table S2) that were best described by unimodal bell-shaped models (*23*) and had more than 50 occurrences (*25*). In total, the studied species account for almost 62% of occurrences in our data set. The change in the altitudinal distribution of species was measured as the difference in their optimum elevation between 1905–1985 and 1986–2005.

The optimum elevation of forest plant species shifted mostly upward during the end of the 20th century (Fig. 2). The general upward trend between 1971 (mean year of surveys occurring from 1905 to 1985) and 1993 (mean year of surveys occurring from 1986 to 2005) is statistically highly significant [mean difference in optimum elevation 64.8 m, 95% confidence interval (95% CI) for mean = 40.8, 88.8; $n = 171$; Student's paired-sample t test, $t = 5.33$; df = 170; $P < 10^{-4}$], amounting to an average of 29.4 m per decade. As a test of the robustness of the observed trend, we confirmed that the potential existence of an artifact in optimum elevation estimations because of the use of unimodal symmetric curves (*26*) did not account for the observed pattern of positive shifts in altitudinal distributions. Indeed, such potential artifacts should affect optimum elevation estimations regardless of the period, and thus no trend should be expected. Interestingly, the size of the species altitudinal range around the optimum elevation (*27*) did not show a significant change between periods. The observed change in optimum elevation and lack of it in amplitude or range suggest that both the upper and the lower distributional margins may have shifted upward, implying the displacement of the whole altitudinal range.

Most species in the 1986–2005 period had higher optimum elevations than those in the 1905–1985 period (Fig. 2). More than two-thirds (118/171) of the species shifted their optima upward, whereas only one-third (53/171) shifted their optima downward. Change in optimum elevation of any individual species or taxon may have a number of possible explanations, but confounding factors decline with increasing numbers of species studied (*1*). This overall upward trend for an assemblage of 171 forest plant species in western European mountains is consistent with results focusing on the highest alpine and nival vegetation belts (*10*–*12*, *28*). We provide strong evidence that forest plant species, as many vertebrates and invertebrates species (*8*, *24*, *29*–*31*), have already followed the pace of climate change by shifting their distributions to higher altitudes and that these changes affect the core of their ranges or those areas where habitat suitability or maximum probability of presence is the highest. Thus, climate warming does not only affect species at their range boundaries, but its consequences ripple through the whole range of species.

In general, our results show that species displayed different rates of movement, behaving in a seemingly idiosyncratic way in response to climate change (Fig. 2 inset). However, species that share the same ecological properties may show similar consistent patterns of changes (*32*). We tested the hypothesis that species geographically restricted to mountains and/or with a shorter life cycle show more pronounced changes in distribution than those not restricted to mountain habitats and/or long-lived (*23*). Figure 3A illustrates a larger shift in the optimum elevation for the mountainous (area of occupancy restricted to mountain ranges) *Orthilia secunda* than for the ubiquitous (area of occupancy that encompassed both mountain ranges and lowland areas) *Paris quadrifolia*, whereas Fig. 3B illustrates a larger shift for the small grassy (associated with a fast breeding rate) *Galium rotundifolium* than for the large woody (associated with a slow breeding rate) *Sorbus aria* (see also tables S1 and S2). Overall, species that shifted the most are mountainous species as compared with ubiquitous species (Fig. 4) [one-way analysis of variance (ANOVA), $F = 10.73$, $n = 171$, df = 1, $P < 10^{-4}$]. Similarly, most shifting species tend to have life forms (herbs, ferns, and mosses) involving faster life history traits (shorter life cycle, faster maturation, and smaller sizes at maturity) than do species showing a reduced shift (trees and shrubs) (Fig. 4) (one-way ANOVA, $F = 5.73$, $n = 171$, df = 1, $P = 0.02$). Larger distributional shifts for faster life cycle species are consistent with results already observed in vertebrate taxa (*8*). Similarly, larger shifts for

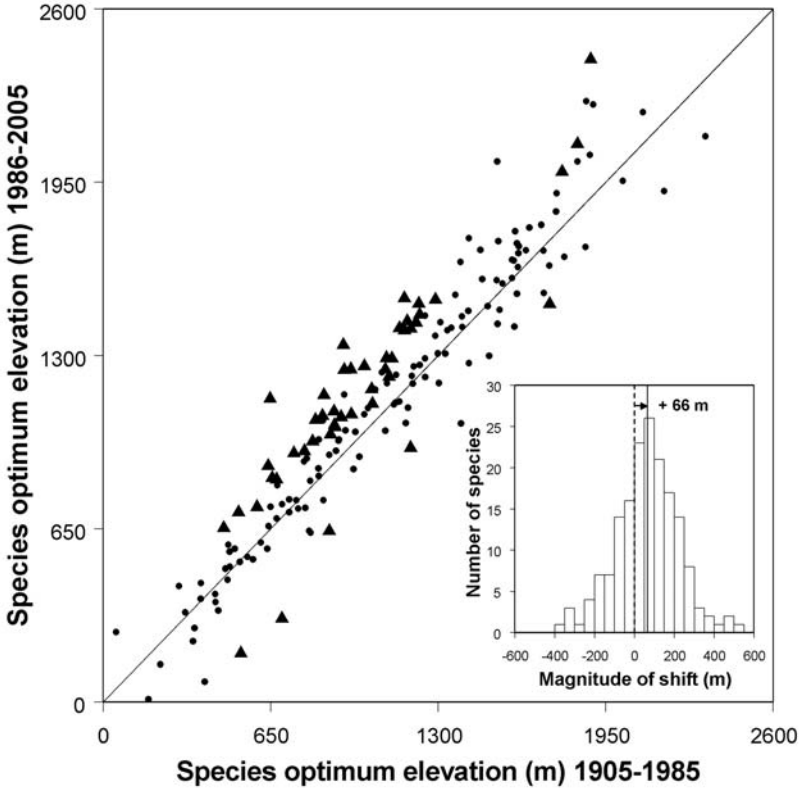

Fig. 2. Scatter diagram of forest plant species ($n = 171$) optimum elevation (i.e., altitude value at maximum probability of presence) for the periods 1905–1985 and 1986–2005. Each point represents one species: Species showing nonoverlapping 95% CIs around the optimum elevation between periods are displayed as solid triangles (▲) ($n = 46$), whereas species with overlapping 95% CIs are displayed as solid circles (●) ($n = 125$) (see tables S1 and S2 for details) (*23*). (**Inset**) The distribution of the species differences in optimum elevation between periods. The vertical dotted line marks zero shift, and the vertical solid line marks the median shift. The arrow describes the direction of the shift.

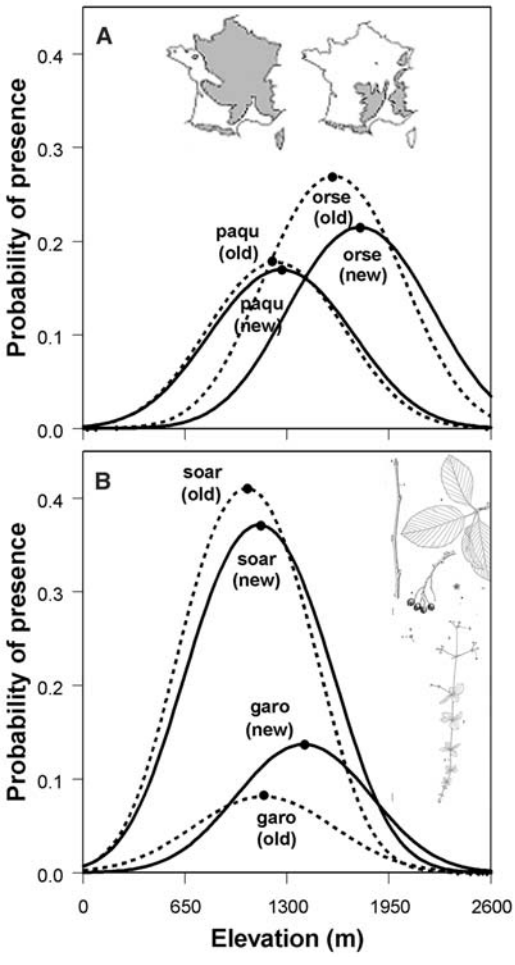

Fig. 3. Examples of western European plant distributions that have shifted upward. Elevational response curves derived with logistic regression models during 1905–1985 (dotted lines) and during 1986–2005 (solid lines) for two species according to geographic distribution pattern (**A**), ubiquitous *P. quadrifolia* (paqu) and mountainous *O. secunda* (orse), and also for two species according to life form (**B**), grassy *G. rotundifolium* (garo) and woody *S. aria* (soar). The solid circles (•) indicate the position of the optimum elevation. Maps and drawing pictures (D. Mansion) are from the Flore Forestière Française Sources (Institut pour le Développement Forestier).

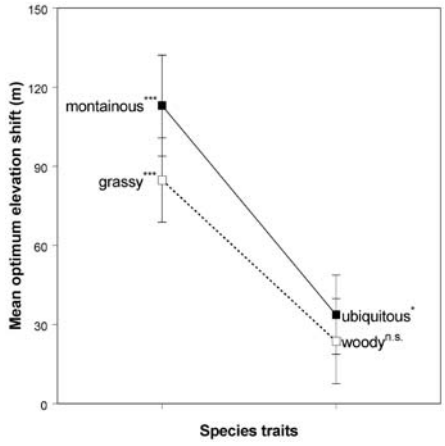

Fig. 4. Magnitude of optimum elevation shifts for plant species in relation to their ecological and life history traits (*23*). Shifts in mean optimum elevation according to geographic distribution pattern (solid line and symbols) correspond to ubiquitous (n = 104), and mountainous species (n = 67). Shifts in mean optimum elevation according to life form (dotted line and open symbols) correspond to woody (n = 56) and grassy species (n = 115). Means are shown with standard errors. Significance of the magnitude of mean shift from the null hypothesis of zero shift is displayed for each trait (n.s. indicates nonsignificant, *$P < 0.05$, **$P < 0.01$, ***$P < 0.001$; Student's paired sample t test).

mountainous species are in agreement with the suggestion that plant species would be more sensitive to climate change at high-altitude locations (*10*, *11*, *17*). There is no significant interaction between geographic distribution pattern and life form (two-way ANOVA, $F = 0.24$, $n = 171$, df = 1, $P = 0.63$), which rules out the possibility that forest plant species restricted to mountains show larger changes because most of them exhibit a grassy life form.

Recent meta-analyses have conclusively showed the response of species to climate change (*1*, *3*, *5*). However, little is known regarding how climate change interplay with other regional- to global-scale drivers of changes in affecting species distributions such as variation in precipitation regime, nitrogen (N) deposition, land-use changes, invasive species, and CO_2 increases. Decadal-scale variation in precipitation has remained the same before and after the slicing of our studied period (Fig. 1B); thus, it cannot directly affect the distributional changes we observed. Atmospheric N deposition are important at high elevations, with rates ranging from 6 to 30 kg ha^{-1} $year^{-1}$ in western European mountains (*33*). However, we found a slightly lesser but not significant N demand (*23*) for upward-shifting species as compared with those shifting downward (mean N demands for upward and downward species were 4.38 and 4.97, respectively; Student's two-sample t test, $t = 1.72$; $n = 127$; df = 125; $P = 0.09$); hence, N deposition did not explain the general upward shift. The effect of land-use changes can also be ruled out because we paid particular attention to restricting our analysis to mature forests (*23*), where land-use changes are of reduced magnitude. Lastly, neither invasive species introduction nor changing concentration of atmospheric CO_2 seem to be important in determining the observed regional pattern of positive shifts in altitudinal distributions; if present, no significant trend in altitudinal shift would be expected because these drivers are nondirectional regarding species responses and would affect as many increases as decreases.

The average magnitude of change in forest plant species optimum elevation across the entire altitudinal gradient [29.4 ± 10.9 m per decade (*23*)] closely matches the figure observed for the shift of alpine plants above the tree line [27.8 ± 14.6 m per decade (*12*)] and even improves the precision. Further, if we assume a temperature lapse rate of 0.6°C, our results imply a 0.39°C increase in 22 years, which is coherent with the observed warming trend, supporting the hypothesis that climate warming is the main driving force for the observed patterns. The wide variability in the magnitude of optimum elevation shifts among species within assemblages may likely result in the disruption of biotic interactions and the ecological networks wherein these species are embedded. Further studies aimed at disentangling the magnitude and consequences of these changes, and their impact on species persistence and ecosystem functioning, are urgently needed.

References and Notes

1. C. Parmesan, G. Yohe, *Nature* **421**, 37 (2003).
2. G. R. Walther *et al.*, *Nature* **416**, 389 (2002).
3. T. L. Root *et al.*, *Nature* **421**, 57 (2003).
4. L. Hughes, *Trends Ecol. Evol.* **15**, 56 (2000).
5. R. Hickling, D. B. Roy, J. K. Hill, R. Fox, C. D. Thomas, *Glob. Change Biol.* **12**, 450 (2006).
6. M. Sturm, C. Racine, K. Tape, *Nature* **411**, 546 (2001).
7. F. S. Chapin III *et al.*, *Ambio* **33**, 361 (2004).
8. A. L. Perry, P. J. Low, J. R. Ellis, J. D. Reynolds, *Science* **308**, 1912 (2005); published online 12 May 2005 (10.1126/science.1111322).
9. P. Tryjanowski, T. H. Sparks, P. Profus, *Divers. Distrib.* **11**, 219 (2005).
10. F. Keller, F. Kienast, M. Beniston, *Reg. Environ. Change* **1**, 70 (2000).
11. G. Grabherr, M. Gottfried, H. Pauli, *Nature* **369**, 448 (1994).
12. G. R. Walther, S. Beibner, C. A. Burga, *J. Veg. Sci.* **16**, 541 (2005).
13. J. Penuelas, M. Boada, *Glob. Change Biol.* **9**, 131 (2003).
14. L. Kullman, *J. Ecol.* **90**, 68 (2002).
15. A. T. Peterson, J. Soberon, V. Sanchez-Cordero, *Science* **285**, 1265 (1999).
16. S. Lavergne, J. Molina, M. Debussche, *Glob. Change Biol.* **12**, 1466 (2006).
17. H. Pauli, M. Gottfried, K. Reiter, C. Klettner, G. Grabherr, *Glob. Change Biol.* **13**, 147 (2007).
18. W. Thuiller, S. Lavorel, M. B. Araujo, M. T. Sykes, I. C. Prentice, *Proc. Natl. Acad. Sci. U.S.A.* **102**, 8245 (2005).

19. M. Cardillo *et al.*, *Science* **309**, 1239 (2005).
20. P. D. Jones, T. J. Osborn, K. R. Briffa, *Science* **292**, 662 (2001).
21. J. M. Moisselin, M. Schneider, C. Canellas, O. Mestre, *Meteorologie* **38**, 45 (2002).
22. M. Beniston, H. F. Diaz, R. S. Bradley, *Clim. Change* **36**, 233 (1997).
23. Materials and methods are available as supporting material on *Science* Online.
24. L. P. Shoo, S. E. Williams, J. M. Hero, *Austral Ecol.* **31**, 22 (2006).
25. C. Coudun, J.-C. Gégout, *Ecol. Modell.* **199**, 164 (2006).
26. The impact of the symmetry assumption in Gaussian logistic regressions (GLR) on our results was tested by using a more flexible curve-fitting tool, namely generalized additive models (GAM), which allows for asymmetry in hump-shaped curves (*23*). We also found a statistically highly significant shift of 27 m per decade (mean difference in optimum elevation 59.4 m, 95% CI = 16.5, 102.4; n = 171; Student's paired-sample t test, t = 2.73; df = 170; $P < 10^{-2}$).
27. The ecological amplitude is a proxy for the size of the species altitudinal range around the optimum elevation (*23*). We found no significant differences between 1905–1985 and 1986–2005 (mean difference in ecological amplitude 2.3 m, 95% CI = −11.9, 16.6; n = 171; Student's paired-sample t test, t = 0.32; df = 170; P = 0.75).
28. P. Lesica, B. McCune, *J. Veg. Sci.* **15**, 679 (2004).
29. R. J. Wilson *et al.*, *Ecol. Lett.* **8**, 1138 (2005).
30. M. Konvicka, M. Maradova, J. Benes, Z. Fric, P. Kepka, *Glob. Ecol. Biogeogr.* **12**, 403 (2003).
31. J. K. Hill *et al.*, *Proc. R. Soc. London Ser. B* **269**, 2163 (2002).
32. W. Thuiller, S. Lavorel, M. B. Araujo, *Glob. Ecol. Biogeogr.* **14**, 347 (2005).
33. E. Dambrine *et al.*, in *Forest Decline and Atmospheric Deposition Effects in the French Mountains*, G. Landmann, M. Bonneau, Eds. (Springer Verlag, Berlin, 1994), pp. 177–200.
34. We thank the thousand of recorders who contributed to the building of EcoPlant and Sophy databases; J.-D. Bontemps, J.-C. Pierrat, and C. Coudun for their much-appreciated statistical advice; J.-L. Dupouey for stimulating discussion; and three anonymous reviewers for helpful comments on previous versions of this manuscript that strongly improved the quality of our analyses. EcoPlant is a phytoecological database financed by the French Environment and Energy Management Agency (ADEME) and the Office National des Forêts (ONF). Part of this work was conducted while P.A.M. was a Sabbatical Fellow at the National Center for Ecological Analysis and Synthesis, a center funded by NSF (grant DEB-0072909), the University of California, and the Santa Barbara campus. P.A.M. acknowledges support from a Guggenheim Fellowship and grants FONDAP-FONDECYT 1501-0001 and ICM P05-02 PFB-23 CONICYT. J.C.G. acknowledges support from FONDECYT 11060313 and FONDECYT Cooperacion Internacional 7070147. J.L. was found by a Ph.D. grant from the French National Institute for Agricultural Research (INRA).

Supporting Online Material

www.sciencemag.org/cgi/content/full/320/5884/1768/DC1
Materials and Methods
Figs. S1 and S2
Tables S1 and S2
References

21 February 2008; accepted 22 May 2008
10.1126/science.1156831

Polarization of the *C. elegans* Embryo by RhoGAP-Mediated Exclusion of PAR-6 from Cell Contacts

Dorian C. Anderson, Jason S. Gill,* Ryan M. Cinalli,* Jeremy Nance†

Early embryos of some metazoans polarize radially to facilitate critical patterning events such as gastrulation and asymmetric cell division; however, little is known about how radial polarity is established. Early embryos of *Caenorhabditis elegans* polarize radially when cell contacts restrict the polarity protein PAR-6 to contact-free cell surfaces, where PAR-6 regulates gastrulation movements. We have identified a Rho guanosine triphosphatase activating protein (RhoGAP), PAC-1, which mediates *C. elegans* radial polarity and gastrulation by excluding PAR-6 from contacted cell surfaces. We show that PAC-1 is recruited to cell contacts, and we suggest that PAC-1 controls radial polarity by restricting active CDC-42 to contact-free surfaces, where CDC-42 binds and recruits PAR-6. Thus, PAC-1 provides a dynamic molecular link between cell contacts and PAR proteins that polarizes embryos radially.

Early embryos can polarize radially when cell contacts differentiate the contacted (inner) and contact-free (outer) surfaces of each cell. Radial polarity, called compaction in mammals, provides a foundation for executing critical patterning events such as cell fate specification and gastrulation (*1*, *2*). For example, radial polarity in *Caenorhabditis elegans* allows gastrulating cells to enrich myosin at their outer surfaces; myosin constricts these surfaces to help drive gastrulating cells into the embryo (*2*, *3*). The *C. elegans* embryo polarizes radially when cell contacts restrict the polarity proteins PAR-6 [PSD-95/DLG/ZO-1 (PDZ) and semi-Cdc42/Rac-interactive-binding (semi-CRIB) domain protein], PAR-3 (PDZ domain protein), and PKC-3 (atypical protein kinase C) to the outer surfaces of early embryonic somatic cells (EES cells) (*2*, *4*–*6*). This "inner-outer" PAR asymmetry begins at the four-cell stage and persists through early embryogenesis (*6*). The molecular link between cell contacts and the inner-outer PAR asymmetries they induce to polarize embryos is not known.

To learn how radial polarity is established, we screened for mutations preventing the inner-outer asymmetry of green fluorescent protein (GFP)–tagged PAR-6 (PAR-6-GFP). Two mutations (*xn1* and *xn6*) in a gene we named *pac-1* (PAR-6-at-contacts) caused PAR-6-GFP to associate with both inner and outer surfaces of EES cells (Fig. 1, A and B). *pac-1* mutations are maternal-effect, and hereafter we refer to embryos produced by *pac-1(xn6)* mutant mothers as *pac-1* embryos.

We immunostained *pac-1* embryos to examine the localization of endogenous PAR proteins. PAR-6, PAR-3, and PKC-3 are restricted to outer surfaces of wild-type EES cells, but each protein showed a symmetric cortical localization in *pac-1* EES cells (Fig. 1, C to H, and table S2). PAR proteins within the zygote and germline precursor cell of wild-type early embryos develop anterior-posterior (A/P) asymmetries that are not patterned strictly by cell contacts. These PAR asymmetries appeared normal in *pac-1* embryos (fig. S1). *pac-1* mutations also did not disrupt PAR-6 asymmetry in epithelial cells, which are born at later stages and localize PAR-6 apically (*7*). Thus, *pac-1* is essential for contact-mediated PAR asymmetries that develop during radial polarization but appears dispensable for other types of PAR asymmetries.

Depleting PAR-6 or PAR-3 specifically from EES cells causes slowed gastrulation (*2*). In wild-type embryos, gastrulation begins when the two endodermal precursor cells (EPCs) ingress into the interior. We filmed *pac-1* embryos to determine whether loss of inner-outer PAR asymmetry also disrupts gastrulation. EPCs ingressed significantly more slowly in *pac-1* embryos (*8*) and were often present on the surface at a time that they would be internalized in wild type (Fig. 2, A and B, movies S1 and S2). Similar to embryos lacking PAR-3 or PAR-6 in EES cells (*2*), the slowed cell ingressions in *pac-1* embryos did not prevent EPC descendants from ultimately internalizing, and embryos were viable.

PAR-3 is required for nonmuscle myosin to concentrate at and constrict the EPC outer surfaces (*2*, *3*). To determine whether the gastrulation defects we detected might be explained by altered myosin localization or activity, we immunostained embryos for activated myosin regulatory light chain (p-rMLC) (*9*). In wild type, p-rMLC concentrated at outer surfaces of ingressing EPCs, similar to published reports (Fig. 2C) (*9*). By contrast, levels of p-rMLC at outer surfaces of *pac-1* EPCs were reduced significantly (Fig. 2D and fig. S2). These data suggest that PAC-1 regulates gastrulation by restricting PAR-3 to the outer cortex, where PAR-3 is needed to concentrate active myosin.

We cloned the *pac-1* gene (*8*), which encodes a protein containing a pleckstrin homology (PH) and a RhoGAP domain (Fig. 3A and fig. S3A). RhoGAP domains inhibit Rho guanosine triphosphatase (GTPase) signaling by converting active guanosine triphosphate–bound Rho proteins to inactive guanosine diphosphate–bound forms (*10*).

Kimmel Center for Biology and Medicine of the Skirball Institute, New York University School of Medicine, 540 First Avenue, New York, NY 10016, USA.

*These authors contributed equally to this work.
†To whom correspondence should be addressed. E-mail: nance@saturn.med.nyu.edu

xn6 contains a nonsense mutation predicted to truncate PAC-1 before the RhoGAP domain and causes a phenotype indistinguishable from *pac-1 (RNAi)* (fig. S3, D to F), which suggests that *xn6* eliminates *pac-1* function. *xn1* alters an invariant splice donor base. BLAST (Basic Local Alignment Search Tool) searches identified two related human proteins, ARHGAP10 and ARHGAP23, as PAC-1 homologs (fig. S3B). In cultured cells, ARHGAP10 can regulate Golgi morphology, endocytosis, and α-catenin localization at epithelial junctions. ARHGAP10 is thought to function by inhibiting the Rho GTPase Cdc42 (*11*–*13*).

To learn where PAC-1 localizes within EES cells, we expressed a GFP-PAC-1 fusion protein in early embryos. GFP-PAC-1 rescued PAR-6 localization in *pac-1* embryos (Fig. 3B and table S2) and localized to inner but not outer surfaces of EES cells (Fig. 3C). GFP-PAC-1 localized identically in *par-6* mutant embryos (22 of 23 embryos) (Fig. 3D), indicating that PAC-1 functions upstream of PAR-6 to polarize EES cells. We combined cultured embryos to create new contacts; GFP-PAC-1 localized to endogenous and induced contacts (7 of 7 embryos) (Fig. 3E), indicating that cell contacts recruit PAC-1 to inner surfaces.

To define when PAC-1 is needed for inner-outer PAR asymmetry, we first removed PAC-1 specifically from EES cells and asked whether PAR-6 asymmetry was lost. To remove PAC-1, we fused it to the PIE-1 ZF1 domain, which targets proteins for degradation in EES cells but not in the germline precursor cell (*2*, *14*). Because EES cells arise sequentially from asymmetric divisions of the germline precursor cell, ZF1-fusion proteins degrade in a reproducible mosaic pattern. GFP-ZF1-PAC-1 was functional (fig. S4, A and B) and showed the same localization as GFP-PAC-1 before degrading from EES cells after the four-cell stage (Fig. 3F). In *pac-1(ZF1)* embryos (*pac-1* embryos expressing GFP-ZF1-PAC-1), PAR-6 localized symmetrically in cells lacking GFP-ZF1-PAC-1 (69 of 69 embryos) (Fig. 3G). We next asked whether introducing PAC-1 into EES cells of *pac-1* embryos could induce PAR-6 asymmetry. We expressed GFP-PAC-1 using the *med-1* promoter, which is active zygotically after the four-cell stage in a subset of EES cells (*15*). Cells expressing GFP-PAC-1 showed normal inner-outer PAR-6 asymmetry (21 of 22 embryos), whereas PAR-6 remained symmetric in cells not expressing GFP-PAC-1 (19 of 22 embryos) (Fig. 3, H and I). Together, these experiments suggest that PAC-1 functions continuously within EES cells to exclude PAR-6 from the inner cortex.

It was shown previously that the PAC-1 RhoGAP domain inhibits the Rho GTPases RHO-1/RHOA, CED-10/RAC, and CDC-42 in vitro (*16*). To determine whether the RhoGAP domain is required for inner-outer PAR asymmetry, we mutated a conserved catalytic arginine (R984) essential for the activity of other RhoGAPs, including ARHGAP10 (fig. S3C) (*11*, *12*). GFP-PAC-1(R984A) was expressed comparably to GFP-PAC-1, localized to inner surfaces of EES cells (Fig. 4A), but could not rescue PAR-6 localization in *pac-1* embryos (Fig. 4B and table S2). Thus, PAC-1 likely excludes PAR-6 from the inner cortex by inhibiting Rho GTPases.

An attractive candidate target for PAC-1 is CDC-42, which regulates PAR-6 localization in the zygote (*17*–*21*). A functional hemagglutinin (HA)–tagged CDC-42 (fig. S4, C and D) was uniformly cortical in wild-type and *pac-1* EES cells (fig. S5), strongly suggesting that PAC-1 and CDC-42 overlap at inner surfaces. In *cdc-42(RNAi)* embryos, GFP-PAR-6 localized to the cytoplasm of EES cells (16 of 16 embryos) instead of the outer cortex as in wild type (fig. S6, A and B). We removed CDC-42 specifically from EES cells by fusing HA-CDC-42 to the ZF1 domain and expressing HA-ZF1-CDC-42 in *cdc-42* embryos [hereafter *cdc-42(ZF1)* embryos]. PAR-6 remained in the cytoplasm of cells where HA-ZF1-CDC-42 was degraded (31 of 31 embryos) (Fig. 4, C and D). By contrast, GFP-PAC-1 localized normally in *cdc-42(ZF1)* embryos (49 of 49 embryos) (fig. S6, C and D). Thus, CDC-42 is required within EES cells to asymmetrically position PAR-6, but not PAC-1, at the cortex.

The opposite distribution of PAR-6 in *pac-1* and *cdc-42(ZF1)* embryos suggests that PAC-1 controls PAR-6 localization by inhibiting CDC-

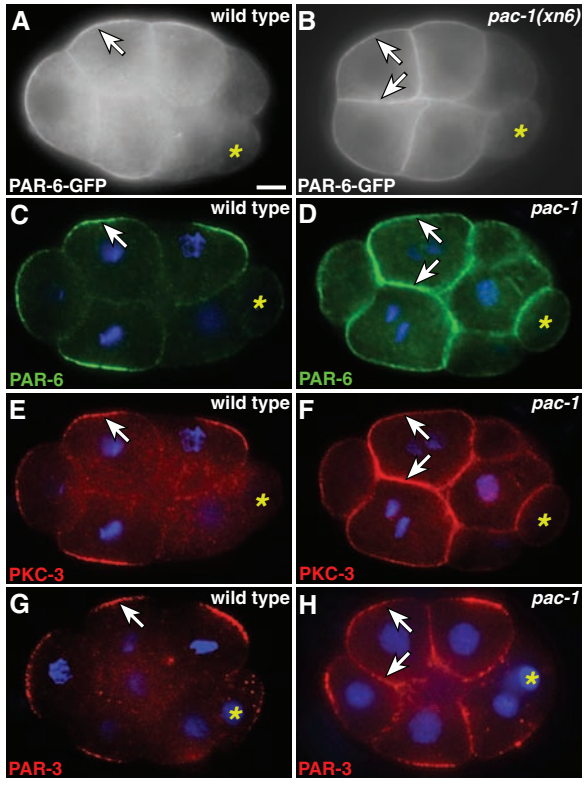

Fig. 1. Inner-outer PAR asymmetry. In all figures, anterior is left, nuclei are blue, and asterisk indicates germline precursor cell. Genotypes (italicized) and proteins shown (capitalized) are indicated. Scale bar in first panel applies to all panels unless indicated. (**A** and **B**) Live eight-cell embryos. (**C** to **H**) Immunostained eight-cell embryos. Arrows indicate PAR proteins. Scale bar, 5μm.

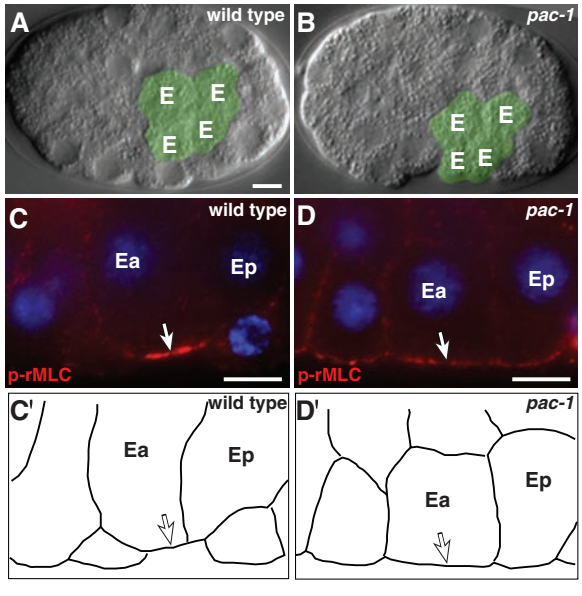

Fig. 2. Gastrulation and myosin localization. (**A** and **B**) Live 44-cell embryos. EPC descendants ("E," colored green) have ingressed in wild type (A) but not in the *pac-1* embryo (B). (**C** and **D**) Mid-26-cell embryos. EPCs (Ea and Ep) are indicated. Arrows, p-rMLC. (**C′** and **D′**) Cell outlines. Scale bar, 5μm.

42. PAR-6 showed the same cytoplasmic localization in *pac-1(RNAi) cdc-42(ZF1)* embryos as in *cdc-42(ZF1)* embryos (39 of 39 embryos) (fig. S6, E and F), consistent with CDC-42 functioning downstream of PAC-1. We asked whether expressing constitutively active (CA) CDC-42 (*17*), which should not be inactivated by PAC-1, caused PAR-6 to bind both inner and outer surfaces of EES cells. In cells expressing HA-CDC-42(CA) from a heat shock promoter (30 of 30 embryos), but not in control heat-shocked embryos (1 of 35 embryos) (fig. S7A) or embryos expressing HA-CED-10/RAC(CA) or HA-RHO-1(CA) (fig. S7, C to F), PAR-6 showed a uniform cortical localization indistinguishable from that in *pac-1* embryos (Fig. 4, E and F) (*8*). Altogether, these data suggest that PAC-1 controls inner-outer PAR-6 asymmetry by inactivating CDC-42 at the inner surfaces of EES cells, although it is possible that other Rho GTPases also participate in radial polarization.

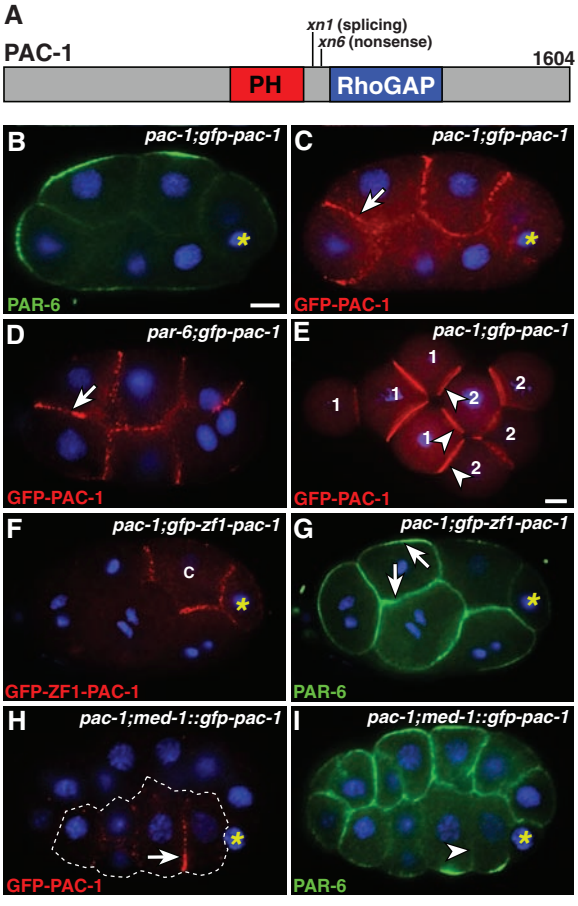

Fig. 3. PAC-1 localization and time of function. (**A**) Predicted PAC-1 protein showing domains and mutations. (**B** and **C**) Coimmunostained seven-cell embryo; arrow, GFP-PAC-1. (**D**) Eight-cell embryo; arrow, GFP-PAC-1. (**E**) Double embryo with ectopic contacts (arrowheads); cells from each embryo are numbered differently. GFP-PAC-1 is present at endogenous and ectopic contacts. (**F** and **G**) Coimmunostained eight-cell embryo. GFP-ZF1-PAC-1 has degraded from somatic cells except "C" cell (labeled). PAR-6 (arrows) localizes symmetrically in cells lacking GFP-ZF1-PAC-1. (**H** and **I**) Coimmunostained 26-cell embryo; cells expressing GFP-PAC-1 (arrow) are outlined (H). PAR-6 is absent from inner surfaces (arrowhead) of cells expressing GFP-PAC-1 (I). Scale bar, 5μm.

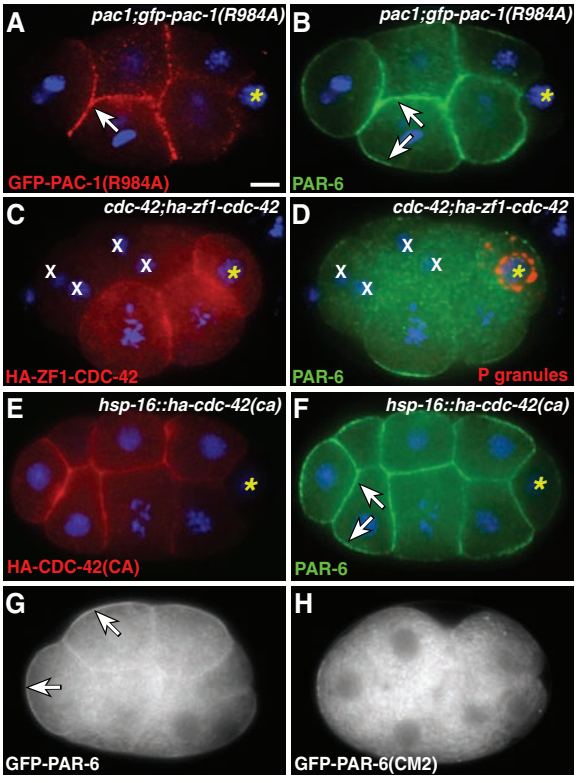

Fig. 4. PAR-6 localization by the PAC-1 RhoGAP domain and CDC-42. (**A** and **B**) Coimmunostained eight-cell embryo. GFP-PAC-1(R984A) localizes to inner surfaces [arrow in (A)], but PAR-6 localizes symmetrically [arrows in (B)]. (**C** and **D**) Coimmunostained eight-cell embryo; restriction of P granules to germline precursor cell indicates normal A/P polarity. HA-ZF1-CDC-42 has mostly degraded from cells marked "x," and PAR-6 is cytoplasmic in these cells. (**E** and **F**) Coimmunostained 12-cell embryo expressing HA-CDC-42(CA). PAR-6 localizes to inner and outer surfaces (arrows). (**G** and **H**) Live eight-cell embryos. GFP-PAR-6 is enriched at the outer cortex (arrows); GFP-PAR-6(CM2) localizes to the cytoplasm. Scale bar, 5μm.

Active CDC-42 can bind the PAR-6 semi-CRIB domain, and this interaction is required for GFP-PAR-6 to associate stably with the zygote cortex (*17*). Therefore, we considered the possibility that active CDC-42 at the outer cortex of EES cells recruits PAR-6 directly. PAR-6 containing mutations in the semi-CRIB domain, PAR-6(CM2), cannot bind CDC-42 but still interacts with PAR-3 and PKC-3 (*17*). When expressed at equivalent levels in EES cells (*8*), GFP-PAR-6 and GFP-PAR-6(CM2) showed different localizations: Both fusion proteins were present within the cytoplasm, but only GFP-PAR-6 was enriched significantly at the outer cortex (Fig. 4, G and H, and fig. S8). HA-CDC-42(CA) forced GFP-PAR-6 (34 of 34 embryos), but not GFP-PAR-6(CM2) (0 of 26 embryos), to localize symmetrically at the cortex (fig. S7, B, G, and H). These results support the hypothesis that active CDC-42 positions PAR-6 at the outer cortex through interactions with the PAR-6 semi-CRIB domain.

Our findings provide a model for how cell contacts polarize embryos radially. We propose that PAC-1, recruited to inner surfaces by cell contacts, locally inactivates CDC-42 and therefore restricts active CDC-42 to outer surfaces. Active CDC-42 would interact with the PAR-6 semi-CRIB domain, allowing PAR-6 to associate stably with the outer cortex and thereby creating an inner-outer asymmetry in PAR-6 localization. Thus, PAC-1 provides a continuous molecular link between cell contacts and cell polarity, allowing embryos to control polarity dynamically as cell divisions and movements remodel patterns of contact. This control may be especially important for rapid cytoskeletal changes during gastrulation, when *pac-1* regulates myosin localization in gastrulating cells. In the *C. elegans* zygote, the RhoGAP CYK-4 provides an analogous link between transient sperm polarity cues and cytoskeletal reorganization that induces A/P PAR asymmetry (*22*).

It will be interesting to learn whether PAC-1 homologs mediate radial polarity in other animal embryos. Radial polarization/compaction of early mammalian embryos shares many molecular similarities with *C. elegans* radial polarization (*1*). During mouse compaction, cell contacts restrict PAR-6, PAR-3, and aPKC/PKC-3 to outer surfaces (*23*, *24*); these asymmetries are thought to help parcel cells into separate inner (embryonic) and

outer (extra-embryonic) lineages (*23*). Rho GTPases are required for compaction (*25*), but how Rho activity is controlled has not been established.

References and Notes

1. M. H. Johnson, J. M. McConnell, *Semin. Cell Dev. Biol.* **15**, 583 (2004).
2. J. Nance, E. M. Munro, J. R. Priess, *Development* **130**, 5339 (2003).
3. J.-Y. Lee, B. Goldstein, *Development* **130**, 307 (2003).
4. B. Etemad-Moghadam, S. Guo, K. J. Kemphues, *Cell* **83**, 743 (1995).
5. T. J. Hung, K. J. Kemphues, *Development* **126**, 127 (1999).
6. J. Nance, J. R. Priess, *Development* **129**, 387 (2002).
7. R. Totong, A. Achilleos, J. Nance, *Development* **134**, 1259 (2007).
8. Materials and methods are available as supporting material on *Science* Online.
9. J. Y. Lee *et al.*, *Curr. Biol.* **16**, 1986 (2006).
10. S. Etienne-Manneville, A. Hall, *Nature* **420**, 629 (2002).
11. T. Dubois *et al.*, *Nat. Cell Biol.* **7**, 353 (2005).
12. S. Sousa *et al.*, *Nat. Cell Biol.* **7**, 954 (2005).
13. S. Kumari, S. Mayor, *Nat. Cell Biol.* **10**, 30 (2008).
14. K. J. Reese, M. A. Dunn, J. A. Waddle, G. Seydoux, *Mol. Cell* **6**, 445 (2000).
15. M. F. Maduro, M. D. Meneghini, B. Bowerman, G. Broitman-Maduro, J. H. Rothman, *Mol. Cell* **7**, 475 (2001).
16. W. Chen, J. Blanc, L. Lim, *J. Biol. Chem.* **269**, 820 (1994).
17. D. Aceto, M. Beers, K. J. Kemphues, *Dev. Biol.* **299**, 386 (2006).
18. M. Gotta, M. C. Abraham, J. Ahringer, *Curr. Biol.* **11**, 482 (2001).
19. A. J. Kay, C. P. Hunter, *Curr. Biol.* **11**, 474 (2001).
20. F. Motegi, A. Sugimoto, *Nat. Cell Biol.* **8**, 978 (2006).
21. S. Schonegg, A. A. Hyman, *Development* **133**, 3507 (2006).
22. N. Jenkins, J. R. Saam, S. E. Mango, *Science* **313**, 1298 (2006).
23. B. Plusa *et al.*, *J. Cell Sci.* **118**, 505 (2005).
24. S. Vinot *et al.*, *Dev. Biol.* **282**, 307 (2005).
25. L. Clayton, A. Hall, M. H. Johnson, *Dev. Biol.* **205**, 322 (1999).

26. We thank A. Hyman, K. Kemphues, and G. Seydoux for reagents. Some antibodies and strains were obtained from the Developmental Studies Hybridoma Bank and the *Caenorhabditis* Genetics Center. We thank G. Fishell, M. Rosenberg, and Nance laboratory members for comments. Funding was provided by NIH [T32HD07520 (D.C.A.) and R01GM078341 (J.N.)] and the Edward Mallinckrodt, Jr. Foundation (J.N.). *pac-1* GenBank accession: EU752496.

Supporting Online Material

www.sciencemag.org/cgi/content/full/320/5884/1771/DC1
Materials and Methods
Figs. S1 to S8
Tables S1 and S2
Movies S1 and S2
References

4 February 2008; accepted 29 May 2008
10.1126/science.1156063

FGF-Dependent Mechanosensory Organ Patterning in Zebrafish

Alex Nechiporuk*† and David W. Raible†

During development, organ primordia reorganize to form repeated functional units. In zebrafish (*Danio rerio*), mechanosensory organs called neuromasts are deposited at regular intervals by the migrating posterior lateral line (pLL) primordium. The pLL primordium is organized into polarized rosettes representing proto-neuromasts, each with a central *atoh1a*-positive focus of mechanosensory precursors. We show that rosettes form cyclically from a progenitor pool at the leading zone of the primordium as neuromasts are deposited from the trailing region. *fgf3/10* signals localized to the leading zone are required for rosette formation, *atoh1a* expression, and primordium migration. We propose that the fibroblast growth factor (FGF) source controls primordium organization, which, in turn, regulates the periodicity of neuromast deposition. This previously unrecognized mechanism may be applicable to understanding segmentation and morphogenesis in other organ systems.

Primordia segmentation into reiterated structures occurs in the development of such diverse structures as photoreceptor ommatidia in the *Drosophila* compound eye and segregation of vertebrate paraxial mesoderm into somites. We describe the organization and regulation of segmentation in the zebrafish lateral line, where mechanosensory organs—called neuromasts—form in discrete clusters along the trunk. This pattern is produced by repeated segmentation of the pLL primordium, which migrates along the trunk, depositing 20 to 30 cells at regular (five-to-seven somite) intervals (*1*). Although the lateral line is an emerging system for the study of collective migration, mechanosensory hair cell development, and hair cell regeneration, the regulation of its initial development and cyclic segmentation is unknown.

The migrating pLL primordium is organized into rosettes, each corresponding to a proto-neuromast (*1*). Cells within each rosette have distinct polarity, with apical ends centrally constricted and nuclei basally localized. We analyzed the relationships between rosette addition, primordium migration, and neuromast deposition by time-lapse imaging. The pLL primordium is first recognized as a group of cells caudal to the otic vesicle with a single anteriorly positioned rosette (Fig. 1A). Over the next few hours, additional rosettes are sequentially added to the posterior, toward the future primordium leading edge (Fig. 1, A to D, and movie S1). Migration begins once two to three rosettes have formed, and the onset of neuromast deposition correlates with formation of the fourth rosette in the leading zone. During deposition, the trailing proto-neuromast gradually slows down before coming to a complete stop (movie S2). Over the course of migration, the primordium exhibits a cyclical behavior with a new rosette generated near the leading (posterior) zone soon after a proto-neuromast separates from the trailing (anterior) edge, alternating from three to four proto-neuromast rosettes (Fig. 1, E and F, and movie S2). This cyclical behavior produces five to six primary neuromasts

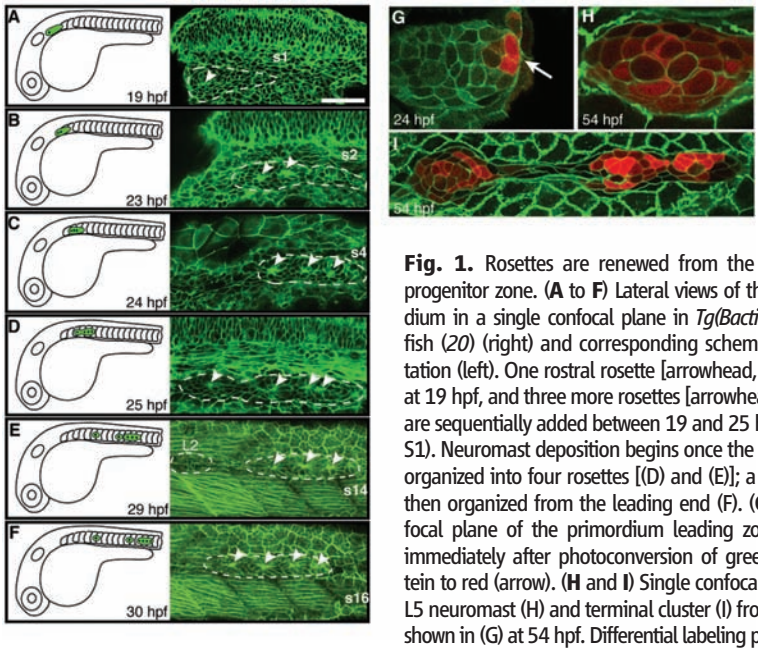

Fig. 1. Rosettes are renewed from the leading-edge progenitor zone. (**A** to **F**) Lateral views of the pLL primordium in a single confocal plane in *Tg(Bactin:HRAS-EGFP)* fish (*20*) (right) and corresponding schematic representation (left). One rostral rosette [arrowhead, (A)] is formed at 19 hpf, and three more rosettes [arrowheads, (B) to (D)] are sequentially added between 19 and 25 hpf (see movie S1). Neuromast deposition begins once the primordium is organized into four rosettes [(D) and (E)]; a new rosette is then organized from the leading end (F). (**G**) Single confocal plane of the primordium leading zone at 24 hpf immediately after photoconversion of green Kaede protein to red (arrow). (**H** and **I**) Single confocal planes of the L5 neuromast (H) and terminal cluster (I) from the embryo shown in (G) at 54 hpf. Differential labeling possibly reflects different proliferation rates and/or differential origin. s, somite; L1 to L5, trunk neuromasts. Scale bar in (A), 50 μm.

University of Washington, School of Medicine, Department of Biological Structure, Seattle, WA 98195–7420, USA.

*Present address: Oregon Health and Science University School of Medicine, Department of Cell and Developmental Biology, Portland, OR 97239, USA.

†To whom correspondence should be addressed. E-mail: nechipor@ohsu.edu (A.N.); draible@u.washington.edu (D.W.R.)

[named L1 to L6, following the convention in (*2*)] deposited along the trunk and a terminal cluster of two to three neuromasts at the end of the tail.

We reasoned that if leading-edge cells act as a progenitor zone, then they should contribute to new neuromasts once already-formed proto-neuromasts are deposited. Following cell fates by photoconversion of Kaede protein (*3*, *4*) confirmed this hypothesis (Fig. 1G). In a majority of embryos (77%, $n = 17$), the labeling of leading cells, after two to three rosettes had formed, resulted in labeled cells only in L3 to L6 neuromasts and the terminal cluster (Fig. 1, H and I, and table S1). In every case, almost all cells within neuromasts were labeled (Fig. 1H), indicating that a small number of cells act as a progenitor zone.

FGFs regulate cellular morphogenesis in many systems (*5*, *6*). Using the FGF receptor (Fgfr) inhibitor SU5402 (*7*) or an inducible dominant-negative Fgfr1 transgenic strain *hsp70:dn-fgfr1* (*8*), we found that FGF signaling is necessary for rosette formation, neuromast deposition, and proper primordium migration (fig. S1, A to H). Application of increasing concentrations of SU5402 caused corresponding reductions in neuromast numbers, confirming specificity of the drug-induced phenotype (fig. S1, I and J). Application of SU5402 beginning at 13 hours postfertilization (hpf), before lateral line placodes were induced (*9*), did not affect formation of the first, most rostral rosette but blocked formation of more caudal rosettes (fig. S2, A and B, and movie S3). This defect in rosette formation did not alter initial migration onset. These results suggest that FGF signals are not needed for initial primordium formation or polarization, a process whose regulation remains unknown.

Later FGF inhibition during primordium migration altered its organization and movement (fig. S1, D to G, and movie S4). Migration was not affected immediately after inhibitor application, and a single neuromast was deposited. However, subsequent rosette renewal was blocked, and after migrating a distance of 8 to 10 somites, the primordium became disorganized and stopped moving. Alterations in migration were probably caused by changes in expression of the chemokine receptors *cxcr4b* and *cxcr7b* (fig. S3), which are required for proper migration (*10*–*12*). FGF-inhibitor effects were reversible; after inhibitor removal, the primordium reorganized into three to four rosettes and then resumed migration (movie S5).

Expression of FGF signaling components is consistent with a role in primordium organization. *fgfr1* was strongly expressed in the primordium trailing region, with lower expression in the leading zone (Fig. 2A). *pea3*, a downstream target of FGF signaling (*13*, *14*), was expressed in the trailing zone (Fig. 2B). Of 22 FGF ligands screened, only *fgf3* (*15*) and *fgf10* (*16*) were expressed in the pLL primordium, broadly in the leading zone and restricted to a focus of one to two cells in trailing rosettes (Fig. 2, C and E). As the primordium organizes into rosettes, both *fgf3*

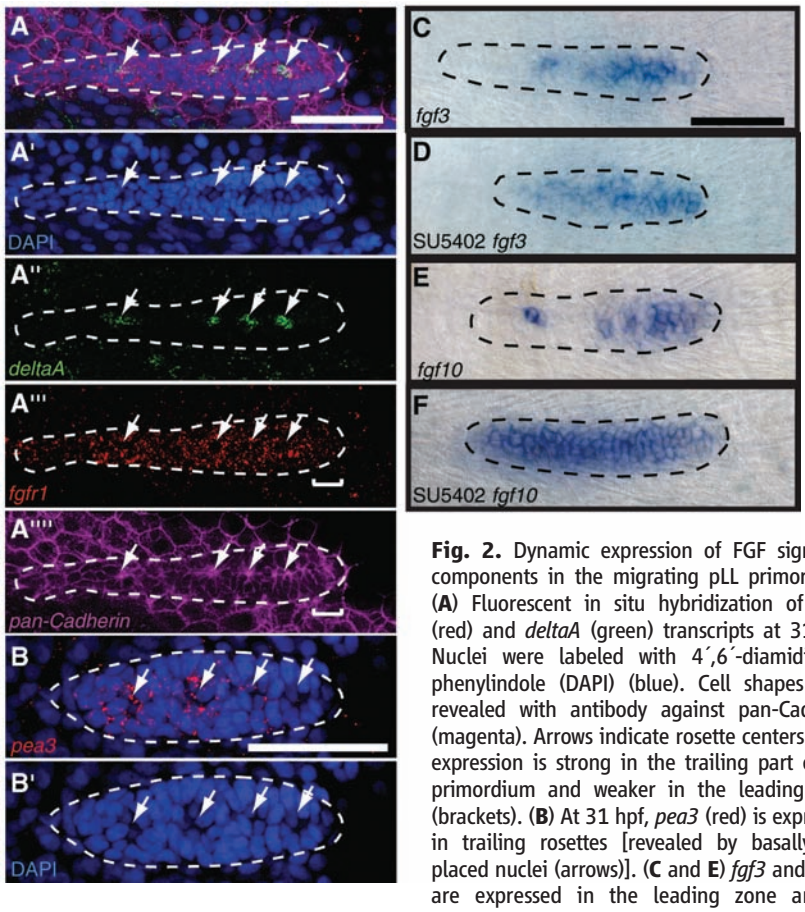

Fig. 2. Dynamic expression of FGF signaling components in the migrating pLL primordium. (**A**) Fluorescent in situ hybridization of *fgfr1* (red) and *deltaA* (green) transcripts at 31 hpf. Nuclei were labeled with 4′,6′-diamidino-2-phenylindole (DAPI) (blue). Cell shapes were revealed with antibody against pan-Cadherin (magenta). Arrows indicate rosette centers. *fgfr1* expression is strong in the trailing part of the primordium and weaker in the leading zone (brackets). (**B**) At 31 hpf, *pea3* (red) is expressed in trailing rosettes [revealed by basally displaced nuclei (arrows)]. (**C** and **E**) *fgf3* and *fgf10* are expressed in the leading zone and in distinct foci in the trailing zone. *fgf3* is expressed at relatively low levels as compared with *fgf10*. (**D** and **F**) Expanded *fgf3* and *fgf10* expression after treatment with SU5402 between 27 to 31 hpf. Primordia are outlined by dotted lines. Scale bars in (A) to (C), 50 μm.

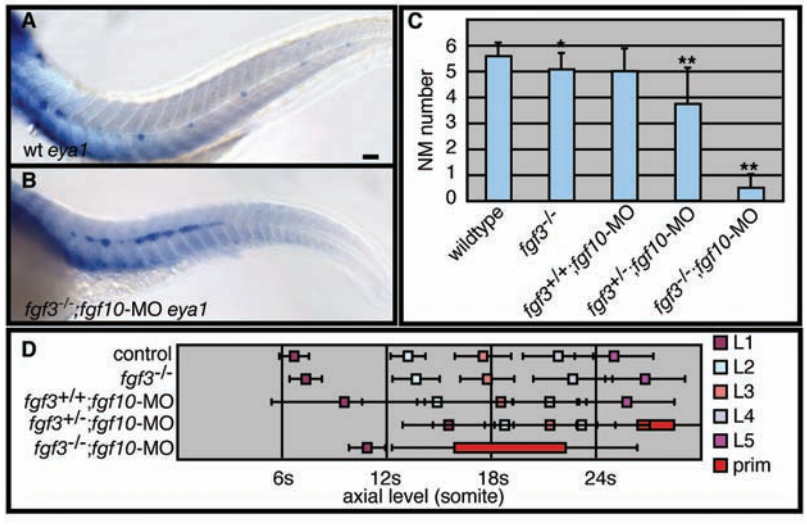

Fig. 3. Fgf3 and Fgf10 are necessary for primordium organization and neuromast deposition. (**A** and **B**) Zygotes derived from $fgf3^{+/-}$ parents were injected with *fgf10*-MO, collected at 48 hpf, analyzed for *eya1* expression, and genotyped. (A) In wild-type ($fgf3^{+/+}$ or $fgf3^{+/-}$) embryos, the pLL primordium migrated through the trunk and deposited five to six neuromasts. (B) $fgf3^{-/-}$ embryos injected with *fgf10*-MO displayed only one or no neuromasts and showed complete disorganization of the primordium. (**C** and **D**) Neuromast (NM) numbers decrease and neuromast positions shifted caudally, as FGF signaling is reduced. Data are shown as means ± SD. (*$P < 0.05$; **$P << 0.001$, Mann-Whitney U test). Scale bar in (A), 50 μm. prim, primordium.

and *fgf10* exhibit dynamic expression (fig. S4). *fgf* transcripts were first detected at the trailing and middle regions (19 to 23 hpf), then confined to the leading zone (24 hpf), and resolved to a single focus in the trailing edge by 25 hpf. When FGF signaling was blocked, *fgf3* and *fgf10* transcripts were detected throughout the primordium (Fig. 2, D and F), suggesting negative-feedback regulation.

Functional importance was demonstrated by injecting *fgf10* morpholino oligonucleotides (*fgf10*-MO) (fig. S5) into zygotes derived from $fgf3^{+/-}$ crosses. Whereas reduction of Fgf3 or Fgf10 alone resulted in mild alterations, combined reduction significantly reduced neuromast number and inhibited primordium migration (Fig. 3, A to D). Intermediate phenotypes seen with *fgf10*-MO injection into zygotes with one functional *fgf3* allele (Fig. 3, C and D) were analogous to those found at intermediate concentrations of SU5402 inhibitor, suggesting that neuromast position and number are sensitive to overall levels of FGF signal. In Fgf3/10-deficient embryos, the most rostral rosette formed normally, but subsequent rosette formation was blocked (fig. S2C and movie S6). The combined Fgf3/10-deficient phenotype, although similar to that observed when all FGF signaling was blocked with an SU5402 inhibitor, is not as severe (compare fig. S1G and Fig. 3D), and thus we cannot exclude the involvement of another FGF ligand in these processes.

Correct patterning of hair cell and support cell precursors, already established within the migrating primordium (*2*, *17*, *18*), also requires Fgf3 and Fgf10 function. The Atonal homolog *atoh1a* and Notch ligand *deltaA* are specifically expressed in sensory hair cell precursors, whereas *notch3* is expressed in undifferentiated and support cells (*18*). Expression of all three genes was absent in $fgf3^{-/-}$;*fgf10*-MO embryos, whereas $fgf3^{+/-}$;*fgf10*-MO embryos exhibited intermediate phenotypes (fig. S6, A to I). Brief (3-hour) treatment with SU5402 almost completely abolished precursor gene expression (fig. S6, J to L).

Taken together, our results demonstrate that Fgf3 and Fgf10 are critical for both proto-neuromast organization and for proper specification of precursors within the migrating primordium. These processes might be separately regulated by FGF signaling or may be interdependent. To distinguish among these possibilities, we transplanted cells derived from homozygous *hsp70:dn-fgfr1* embryos into the prospective pLL placode domain of wild-type embryos. When intracellular FGF signaling was blocked after heat shock, transgenic cells failed to differentiate into hair cells but were capable of incorporating into all neuromasts (fig. S7, A to C). These results indicate that hair cell precursors may directly require FGF signals to differentiate, whereas support cells do not. Alternatively, FGF signals may be necessary for general differentiation of progenitor cells into hair and support cells, a possibility that could be resolved as specific support cell markers become available. To test whether proto-neuromast organization might depend on differentiation of hair cell precursors, we examined embryos injected with *atoh1a*-MO (*19*). Rosette formation, as well as neuromast number and placement, were not affected by loss of *atoh1a* function (fig. S8, A to I), and expression of *fgf10* and *pea3* was not

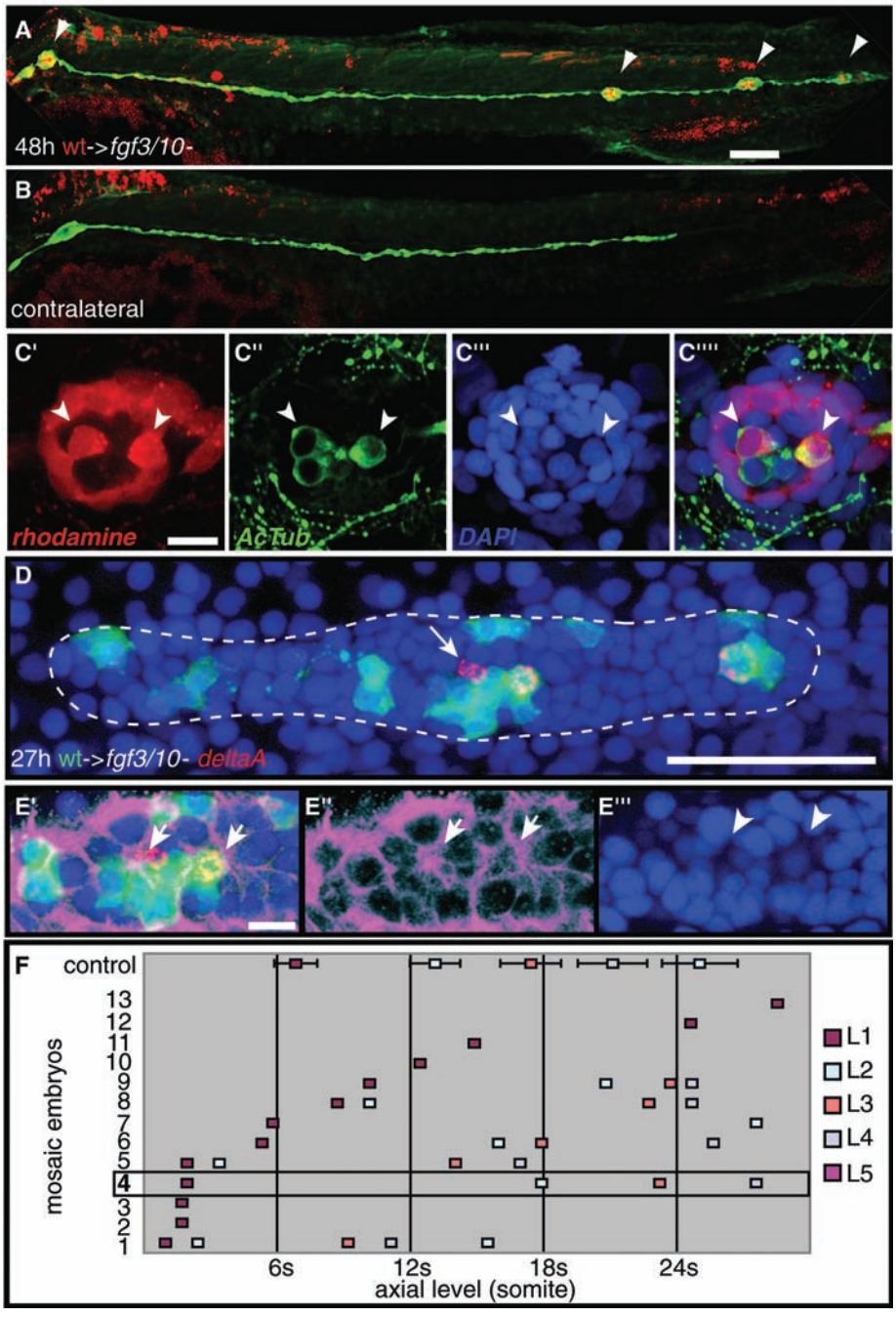

Fig. 4. FGF signaling is necessary for rosette formation and proper segmental deposition. (**A**) Primordium migration and neuromast deposition (arrowheads) are partially rescued after transplantation of wild-type cells (rhodamine dextran, red) into embryos injected with *fgf3*- and *fgf10*-MO. Donor and host carry *Et(krt4:EGFP)sqet20* transgene (green) (*21*) to mark the lateral line. (**B**) Contralateral control side. (**C**) Wild-type cells (red) restore hair cell differentiation [acetylated tubulin (AcTub), green] at 48 hpf in $fgf3^{-/-}$ embryos injected with *fgf10*-MO; nuclei are DAPI-stained (blue). Hair cells are derived from both wild-type donor (arrowheads) and $fgf3^{-/-}$;*fgf10*-MO host. (**D** and **E**) Wild-type cells (fluorescein dextran, green) are sufficient to rescue *deltaA* expression [red, (D)] and rosette organization [(E), arrows]. (D) Arrow indicates *deltaA*-positive cell derived from $fgf3^{-/-}$;*fgf10*-MO host, seen in four of seven embryos. (E) Same embryo as in (D). Wild-type cells restore apical constriction (arrows; pan-Cadherin antibody, magenta) and basally displaced nuclei (arrowheads) (Fig. 2A). (**F**) Distribution of neuromasts in 13 *fgf3/10*-MO embryos that received wild-type transplants [embryo 4 is shown in (A)] is randomized. Scale bars, 50 μm [in (A) and (D)] and 10 μm [in (C) and (E)]. Error bars in (F) indicate SDs.

significantly altered (fig. S8, J to M). Our results suggest that FGF signaling acts independently to organize rosettes and then to specify differentiation of one or more cell types within each rosette.

Finally, we asked whether reintroduction of wild-type cells could restore neuromast production in Fgf3/10-deficient embryos. Transplantation of wild-type cells rescued migration defects and restored some neuromast deposition, with all rescued neuromasts containing some wild-type cells (Fig. 4, A and B). Hair cell differentiation was partially restored, with hair cells derived from donor or host in any combination (Fig. 4C). Rosette formation and *deltaA* expression within the primordium were also partially restored in the presence of wild-type cells ($n = 7$; Fig. 4, D and E). In four cases, we observed a single host-derived *deltaA*-positive cell that was always immediately adjacent to wild-type transplants (Fig. 4D, arrow), indicating that FGFs function as short-range signals within individual rosettes. Wild-type cells partially restored rosette formation with apical constriction and basally displaced nuclei (Fig. 4E). However, because randomization of wild-type cells (the only FGF source) in mosaic embryos caused irregular rosette formation, neuromast position and spacing were also randomized (Fig. 4F).

We suggest that ultimate placement of neuromasts along the trunk (pLL segmentation) is a direct result of primordium organization into proto-neuromasts (fig. S9). Our data indicate that primordium organization and neuromast position depend on both the overall levels and the location of FGF signaling. Lower levels of FGF signaling, caused either by exposure to intermediate doses of FGF inhibitor or by injection of *fgf10*-MO into *fgf3* heterozygotes, presumably delayed generation of new rosettes from the leading progenitor zone, which translated into altered neuromast position and number. Randomization of the FGF source in mosaic primordia resulted in sporadic rosette formation and subsequent random neuromast placement. We presume that rosette progenitors are still generated in the absence of FGF signaling, because relatively high proliferation levels still persist in the SU5402-treated embryos and *fgf3/10* morphants (fig. S10). In support of this idea, primordium cells reorganize into rosettes after SU5402 removal (movie S5). Our study demonstrates that FGF signaling coordinates multiple processes during pLL primordium segmentation, including organization into polarized rosettes, formation of hair cell precursors, and regulation of migration. Control of primordium patterning and migration by the same FGF signaling pathway represents an elegant way to couple these two processes and would ensure that migration continues only as rosettes are renewed. Understanding how FGF signals are translated into polarity and patterning signals during pLL development may shed light on segmentation and morphogenesis in other organ systems.

References and Notes

1. A. Ghysen, C. Dambly-Chaudiere, *Genes Dev.* **21**, 2118 (2007).
2. N. Gompel *et al*., *Mech. Dev.* **105**, 69 (2001).
3. R. Ando, H. Hama, M. Yamamoto-Hino, H. Mizuno, A. Miyawaki, *Proc. Natl. Acad. Sci. U.S.A.* **99**, 12651 (2002).
4. H. Mizuno *et al*., *Mol. Cell* **12**, 1051 (2003).
5. P. Huang, M. J. Stern, *Cytokine Growth Factor Rev.* **16**, 151 (2005).
6. D. M. Ornitz, *Bioessays* **22**, 108 (2000).
7. M. Mohammadi *et al*., *Science* **276**, 955 (1997).
8. Y. Lee, S. Grill, A. Sanchez, M. Murphy-Ryan, K. D. Poss, *Development* **132**, 5173 (2005).
9. P. Andermann, J. Ungos, D. W. Raible, *Dev. Biol.* **251**, 45 (2002).
10. C. Dambly-Chaudiere, N. Cubedo, A. Ghysen, *BMC Dev. Biol.* **7**, 23 (2007).
11. P. Haas, D. Gilmour, *Dev. Cell* **10**, 673 (2006).
12. G. Valentin, P. Haas, D. Gilmour, *Curr. Biol.* **17**, 1026 (2007).
13. F. Raible, M. Brand, *Mech. Dev.* **107**, 105 (2001).
14. H. Roehl, C. Nusslein-Volhard, *Curr. Biol.* **11**, 503 (2001).
15. P. Kiefer, U. Strahle, C. Dickson, *Gene* **168**, 211 (1996).
16. H. Grandel, B. W. Draper, S. Schulte-Merker, *Development* **127**, 4169 (2000).
17. P. P. Hernandez, F. A. Olivari, A. F. Sarrazin, P. C. Sandoval, M. L. Allende, *Dev. Neurobiol.* **67**, 637 (2007).
18. M. Itoh, A. B. Chitnis, *Mech. Dev.* **102**, 263 (2001).
19. B. B. Millimaki, E. M. Sweet, M. S. Dhason, B. B. Riley, *Development* **134**, 295 (2007).
20. M. S. Cooper *et al*., *Dev. Dyn.* **232**, 359 (2005).
21. B. G. Choo *et al*., *BMC Dev. Biol.* **6**, 5 (2006).

22. We thank D. Kimelman, T. Piotrowski, T. Nechiporuk, and T. Reh for critical comments; K. Poss, A. Carmany-Rampey, J. Topczewski, M. Hammerschmidt, and W. Herzog for reagents; and D. White for excellent fish care. This work was supported by NSF (D.W.R.).

Supporting Online Material

www.sciencemag.org/cgi/content/full/320/5884/1774/DC1
Materials and Methods
Figs. S1 to S10
Table S1
References
Movies S1 to S6

15 February 2008; accepted 29 May 2008
10.1126/science.1156547

β-Arrestin–Mediated Localization of Smoothened to the Primary Cilium

Jeffrey J. Kovacs,[1,2] Erin J. Whalen,[1] Renshui Liu,[1] Kunhong Xiao,[3] Jihee Kim,[1] Minyong Chen,[1] Jiangbo Wang,[1] Wei Chen,[1] Robert J. Lefkowitz[1,2,3,4]*

β-Arrestins have important roles in the regulation of seven-transmembrane receptors (7TMRs). Smoothened (Smo) is a 7TMR that mediates effects of Hedgehog on developmental processes and whose dysregulation may cause tumorigenesis. β-Arrestins are required for endocytosis of Smo and signaling to Gli transcription factors. In mammalian cells, Smo-dependent signaling requires translocation to primary cilia. We demonstrated that β-arrestins mediate the activity-dependent interaction of Smo and the kinesin motor protein Kif3A. This multimeric complex localized to primary cilia and was disrupted in cells transfected with β-arrestin small interfering RNA. β-Arrestin 1 or β-arrestin 2 depletion prevented the localization of Smo to primary cilia and the Smo-dependent activation of Gli. These results suggest roles for β-arrestins in mediating the intracellular transport of a 7TMR to its obligate subcellular location for signaling.

β-Arrestins (βarrs) are mediators of seven-transmembrane receptor (7TMR) desensitization and internalization (*1*, *2*), and also function as scaffolding proteins that mediate distinct receptor-activated signaling events (*3*). The roles of the 7TMR Smoothened (Smo), a component of the Hedgehog (Hh) signaling pathway, have been well defined in multiple organisms (*4*), yet regulatory mechanisms of Smo signaling are only now being elucidated. Smo activity is repressed by the 12-membrane–spanning receptor Patched (Ptc). Hh binding to Ptc relieves repression of Smo, allowing Smo to act as a positive mediator of Hh signaling by activating the Gli family of transcription factors. Hh signaling regulates patterning and cell fate, thus the loss of Hh pathway activity causes birth defects in several organisms (*5*), whereas inappropriate activation of the pathway leads to tumorigenic phenotypes (*6*). βarrs are important for Smo-mediated signaling and Sonic Hedgehog (Shh) responsiveness in mammalian and zebrafish model systems (*7*–*9*). Activation of Smo causes increased association between β-arrestin 2 (βarr2) and Smo in a heterotrimeric guanine nucleotide–binding protein–coupled

[1]Department of Medicine, Duke University Medical Center, Durham, NC 27710, USA. [2]Department of Immunology, Duke University Medical Center, Durham, NC 27710, USA. [3]Department of Biochemistry, Duke University Medical Center, Durham, NC 27710, USA. [4]Howard Hughes Medical Institute, Duke University Medical Center, Durham, NC 27710, USA.

*To whom correspondence should be addressed. E-mail: lefko001@receptor-biol.duke.edu

receptor kinase 2 (Grk2)–dependent manner (*7*). Furthermore, morpholino-mediated silencing of βarr2 recapitulates Shh-signaling defects and causes a lack of Gli responsiveness in zebrafish (*9*). Smo requires translocation to the primary cilium to function properly (*10*–*12*) and to activate Gli (*5*, *13*). We therefore tested whether β-arrestin 1 (βarr1) and βarr2 might function in mediating activity-dependent translocation of Smo to the primary cilium.

We checked for localization of βarrs to the primary cilium. Primary cilia were visualized by confocal microscopy in mouse NIH-3T3 cells (Fig. 1A) (*14*). βarrs were localized and concentrated in the primary cilium when stained alone, or stained together with acetylated tubulin, a common marker for primary cilia (Fig. 1A) or in cells also stained for pericentrin (Fig. 1B), which marks the basal bodies of the primary cilia. We also found that βarrs had no effect on ciliogenesis (fig. S1). The βarrs join a list of Smo-related signaling molecules that localize to the primary cilium (*15*, *16*).

The translocation of Smo to primary cilia is mediated by members of the intraflagellar transport (IFT) complex (*17*). One IFT family member that has been implicated in Shh-mediated signaling, Kif3A, is a subunit of the kinesin-2 motor complex (*15*), an anterograde molecular motor that transports protein complexes to and within cilia and flagella (*18*). Kif3A is essential for Shh-mediated signaling in mammalian systems (*5*), and we identified Kif3A as a binding partner of βarr1 in a proteomics screen (*19*). To test whether βarrs, Smo, and Kif3A might work in concert, we examined cells for localization of these proteins together at the primary cilia. Both βarr1 and βarr2 localized to the primary cilia along with an overexpressed green fluorescent protein (GFP)–Smo fusion protein in NIH-3T3 cells (Fig. 1C). The Smo in these cells was constitutively active, because endogenous amounts of the Smo suppressor Ptc are insufficient for inactivation of overexpressed Smo (*7*). Thus, as expected, GFP-Smo was localized to the cilia without Shh stimulation, as were βarr1, βarr2, and Kif3A (Fig. 1C).

To assess the interaction of endogenous βarrs, Smo, and Kif3A, we examined NIH-3T3 cells left untreated or treated with Shh. Stimulation of cells with Shh increased the amount of endogenous Smo and Kif3A that coimmunoprecipitated with βarrs (Fig. 2A). Treatment of cells with cyclopamine prevented this Shh-induced association (Fig. 2A). Thus, activation of Smo in response to Shh-mediated inhibition of Ptc activity causes the formation of a complex between endogenous Smo, βarrs, and Kif3A.

We next examined the nature of this complex with constituitively active Smo in the overexpression system used to localize Smo, βarrs, and Kif3A to the primary cilium. Increasing the amount of Smo overexpression led to an increased association between endogenous Kif3A and endogenous βarr1 and βarr2 (Fig. 2B). This increased binding supports the idea that βarrs act as facilitators of Smo binding to Kif3A, thus regulating subsequent Smo translocation to the primary cilia. If this is correct, small interfering RNA (siRNA)–mediated depletion of the βarrs should affect the binding of Smo to Kif3A (fig. S2). In cells treated with control nonsilencing siRNA oligonucleotide, endogenous Kif3A coimmunoprecipitated with GFP-Smo. However, this interaction was lost upon depletion of βarr1 or βarr2 (Fig. 2C). Inhibition of constitutively active GFP-Smo by treatment of cells with cyclopamine also abolished the interaction between endogenous Kif3A and overexpressed Smo (Fig. 2C). Our previous results suggest that cyclopamine treatment inhibits the association of overexpressed βarr2 with Smo (*7*), and here endogenous βarr1 and βarr2 dissociated from the receptor after cyclopamine treatment (fig. S3). Furthermore, we examined the amount of FLAG-Smo present in endogenous Kif3A immunoprecipitates under various conditions. In cells treated with a control siRNA oligonucleotide, stably overexpressed FLAG-Smo coimmunoprecipitated with endogenous Kif3A. However, after depletion of βarr1 or βarr2, the interaction between motor and receptor was reduced (Fig. 2D). Similarly, the interaction between Smo and endogenous Kif3A was also abolished by cyclopamine treatment in this context. These results clearly show that active Smo and Kif3A form a complex in a βarr1- and βarr2-dependent manner.

We investigated whether the βarr-mediated association of Smo and Kif3A affects the localization of Smo to primary cilia. NIH-3T3 cells overexpressing a FLAG-Smo fusion protein were immunostained with antibody to FLAG and examined by confocal microscopy. Fields

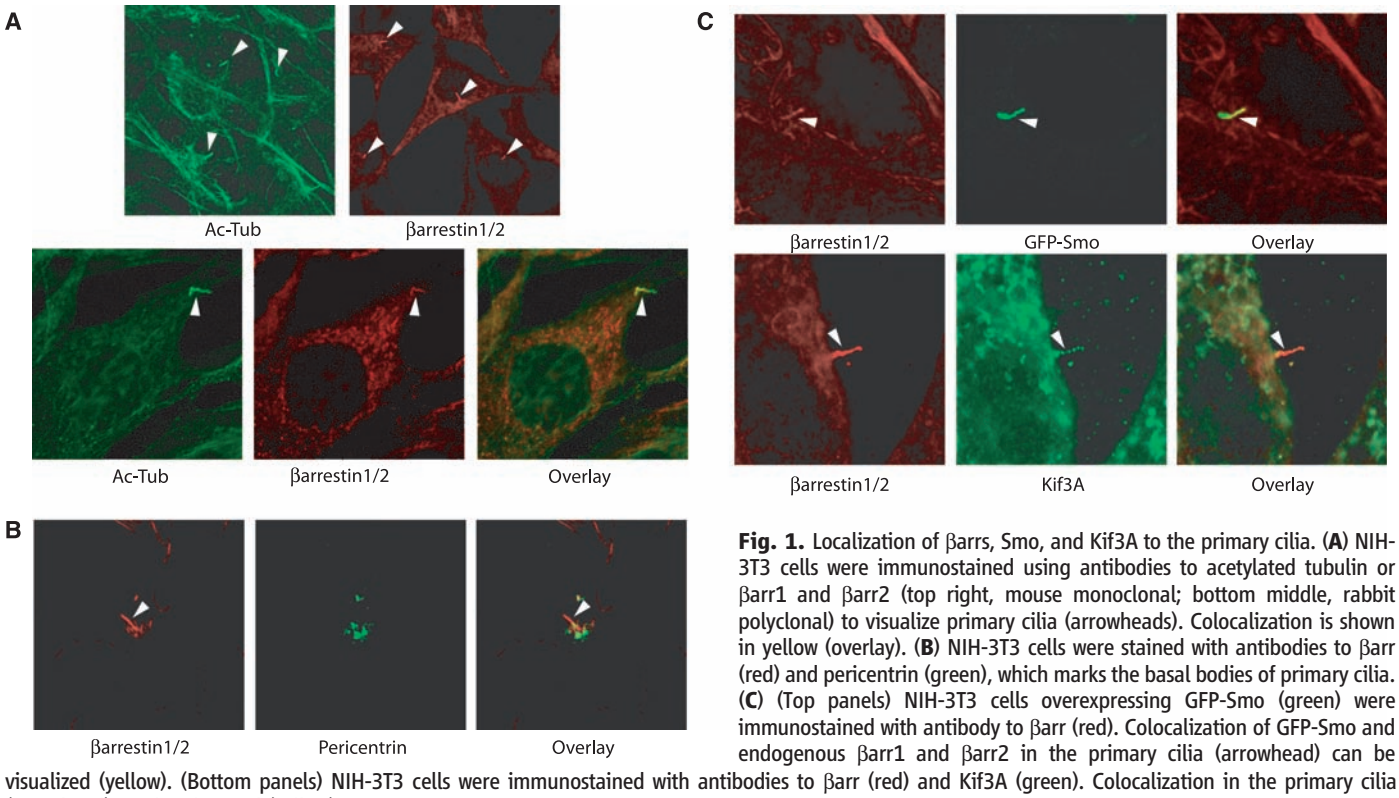

Fig. 1. Localization of βarrs, Smo, and Kif3A to the primary cilia. (**A**) NIH-3T3 cells were immunostained using antibodies to acetylated tubulin or βarr1 and βarr2 (top right, mouse monoclonal; bottom middle, rabbit polyclonal) to visualize primary cilia (arrowheads). Colocalization is shown in yellow (overlay). (**B**) NIH-3T3 cells were stained with antibodies to βarr (red) and pericentrin (green), which marks the basal bodies of primary cilia. (**C**) (Top panels) NIH-3T3 cells overexpressing GFP-Smo (green) were immunostained with antibody to βarr (red). Colocalization of GFP-Smo and endogenous βarr1 and βarr2 in the primary cilia (arrowhead) can be visualized (yellow). (Bottom panels) NIH-3T3 cells were immunostained with antibodies to βarr (red) and Kif3A (green). Colocalization in the primary cilia (arrowhead) can be observed (yellow).

were scored for the percentage of Smo-containing cilia per total number of cells (Fig. 3A). A significant decrease in the percentage of Smo-containing cilia was seen after depletion of either βarr1 or βarr2 (Fig. 3B). We also observed a significant decrease in Smo-containing primary cilia in cells treated with Kif3A siRNA (Fig. 3B). To ensure that knockdown of βarr1, βarr 2, or Kif3A did not alter cilia formation in this assay, we assessed the total percentage of cilia that contained Smo by staining FLAG-Smo and acetylated tubulin. We then counted the total number of cilia that were marked with acetylated tubulin, and counted the number of those cilia that also contained FLAG-Smo (Fig. 3C). A significant decrease in the percentage of cilia containing Smo was seen after depletion of βarr1 by four different βarr1 siRNA oligonucleotides, after depletion of βarr2 by three different βarr2 siRNA oligonucleotides, and after depletion of Kif3A by three different Kif3A siRNA olgonucleotides (Fig. 3D). Visualization of cilia with antibody to acetylated tubulin demonstrates that functional cilia were formed in these cells, and that Smo was not properly localized after siRNA treatment (Fig. 3C). The use of numerous specific siRNA oligonucleotides also confirms that these are on-target effects. Furthermore, the loss of Smo localization to the primary cilia could be rescued by the overexpression of constructs containing silent mutations that overcame the depletion of endogenous βarr1 and βarr 2 (Fig. 4, A and B). Using these rescue constructs, we counted the number of transfected cells in which overexpressed Smo could be detected in cilia (Fig. 4A). Cells transfected with either of the rescue constructs showed percentages of Smo-containing cilia similar to those in control cells (Fig. 3C). Thus, βarr1, βarr2, and Kif3A appear to be required for localization of Smo to the primary cilia.

Next we examined whether the altered localization of Smo to primary cilia is correlated with a change in Gli activity. We monitored Shh-mediated gene induction in NIH-3T3 cells that endogenously expressed Ptc, Smo, βarr1 and βarr2, and Kif3A. After βarr1, βarr2, or Kif3A were depleted, cells were treated with Shh for 18 hours and Gli-reporter activity was assayed. Silencing βarr1 or βarr2 through the use of multiple oligonucleotides caused a complete loss of Shh-mediated Gli reporter activation (Fig. 5A).

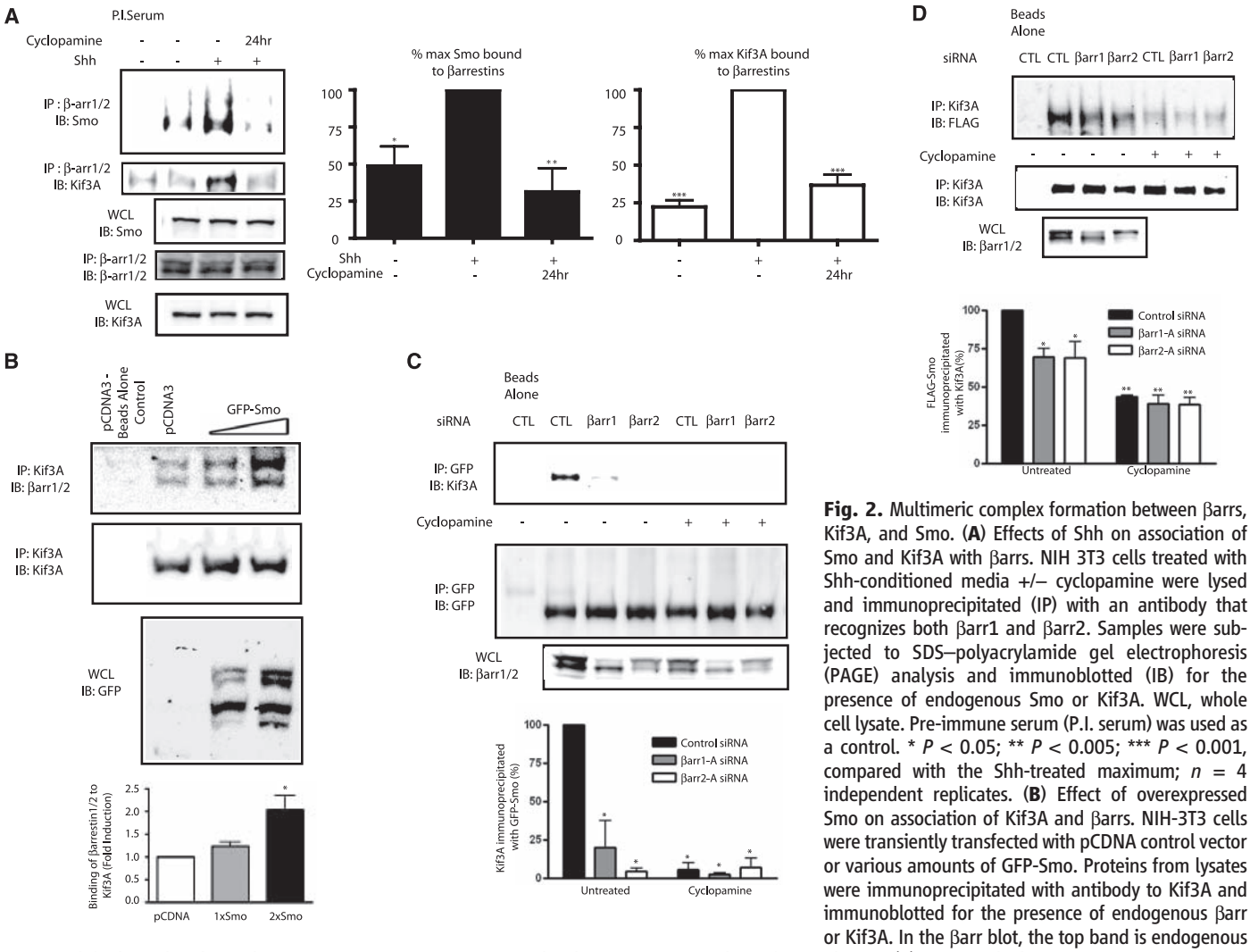

Fig. 2. Multimeric complex formation between βarrs, Kif3A, and Smo. (**A**) Effects of Shh on association of Smo and Kif3A with βarrs. NIH 3T3 cells treated with Shh-conditioned media +/– cyclopamine were lysed and immunoprecipitated (IP) with an antibody that recognizes both βarr1 and βarr2. Samples were subjected to SDS–polyacrylamide gel electrophoresis (PAGE) analysis and immunoblotted (IB) for the presence of endogenous Smo or Kif3A. WCL, whole cell lysate. Pre-immune serum (P.I. serum) was used as a control. * $P < 0.05$; ** $P < 0.005$; *** $P < 0.001$, compared with the Shh-treated maximum; $n = 4$ independent replicates. (**B**) Effect of overexpressed Smo on association of Kif3A and βarrs. NIH-3T3 cells were transiently transfected with pCDNA control vector or various amounts of GFP-Smo. Proteins from lysates were immunoprecipitated with antibody to Kif3A and immunoblotted for the presence of endogenous βarr or Kif3A. In the βarr blot, the top band is endogenous βarr1 and the lower band is endogenous βarr2. * $P < 0.05$ compared with pCDNA; $n = 3$ independent replicates. (**C**) Effect of depletion of βarrs on association of Kif3A with GFP-Smo. NIH-3T3 cells stably overexpressing GFP-Smo were transfected with control (CTL), βarr1, or βarr2 siRNA oligonucleotides. Samples were mock treated [dimethyl sulfoxide (DMSO)] or treated with 6 μM cyclopamine for 1 hour. Proteins from lysates were immunoprecipitated with antibody to GFP followed by immunoblotting for endogenous Kif3A and GFP-Smo. * $P < 0.001$ compared with the control siRNA untreated sample, $n = 4$ independent replicates. (**D**) Effect of depletion of βarrs on the association of FLAG-Smo with Kif3A. NIH-3T3 cells stably overexpressing FLAG-Smo were transfected with CTL, βarr1, or βarr2 siRNA oligonucleotides. Samples were mock treated (DMSO) or treated with 6 μM cyclopamine for 1 hour. Cells were lysed and proteins were immunoprecipitated with antibody to Kif3A and immunoblotted for FLAG-Smo and endogenous Kif3A. * $P < 0.05$; ** $P < 0.001$ when compared with the control siRNA; $n = 3$ independent replicates. All P values were analyzed by one-way analysis of variance (ANOVA) with Bonferoni correction. Data are shown as means ± SEM.

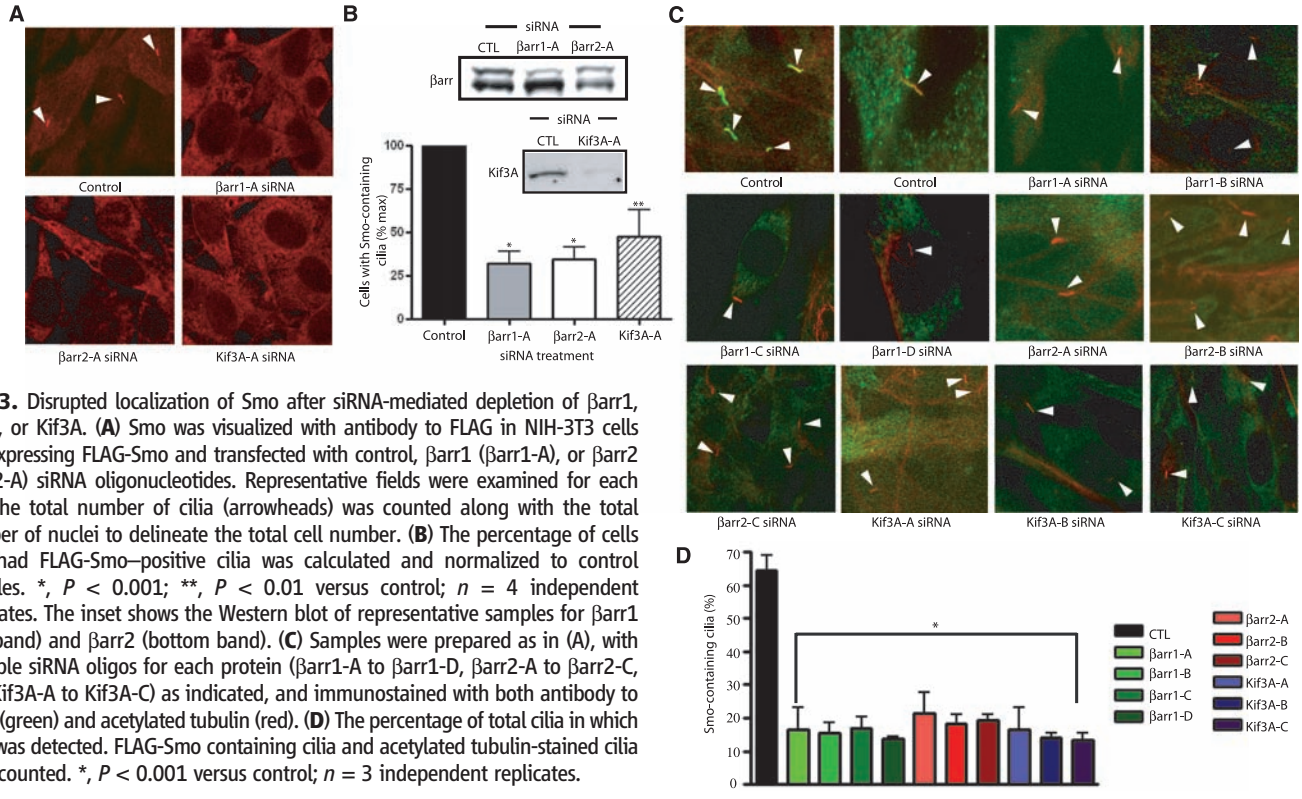

Fig. 3. Disrupted localization of Smo after siRNA-mediated depletion of βarr1, βarr2, or Kif3A. (**A**) Smo was visualized with antibody to FLAG in NIH-3T3 cells overexpressing FLAG-Smo and transfected with control, βarr1 (βarr1-A), or βarr2 (βarr2-A) siRNA oligonucleotides. Representative fields were examined for each and the total number of cilia (arrowheads) was counted along with the total number of nuclei to delineate the total cell number. (**B**) The percentage of cells that had FLAG-Smo–positive cilia was calculated and normalized to control samples. *, $P < 0.001$; **, $P < 0.01$ versus control; $n = 4$ independent replicates. The inset shows the Western blot of representative samples for βarr1 (top band) and βarr2 (bottom band). (**C**) Samples were prepared as in (A), with multiple siRNA oligos for each protein (βarr1-A to βarr1-D, βarr2-A to βarr2-C, and Kif3A-A to Kif3A-C) as indicated, and immunostained with both antibody to FLAG (green) and acetylated tubulin (red). (**D**) The percentage of total cilia in which Smo was detected. FLAG-Smo containing cilia and acetylated tubulin-stained cilia were counted. *, $P < 0.001$ versus control; $n = 3$ independent replicates.

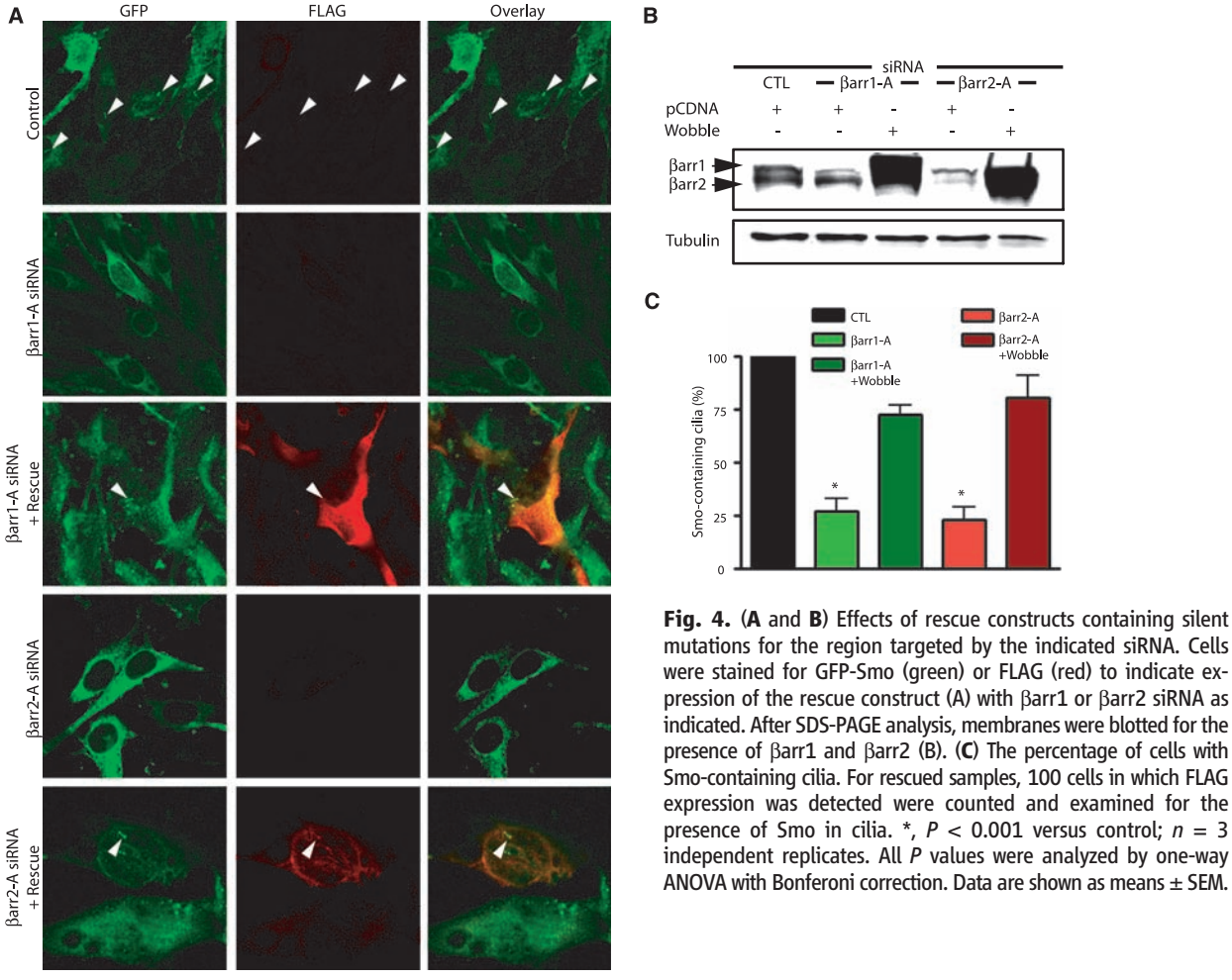

Fig. 4. (**A** and **B**) Effects of rescue constructs containing silent mutations for the region targeted by the indicated siRNA. Cells were stained for GFP-Smo (green) or FLAG (red) to indicate expression of the rescue construct (A) with βarr1 or βarr2 siRNA as indicated. After SDS-PAGE analysis, membranes were blotted for the presence of βarr1 and βarr2 (B). (**C**) The percentage of cells with Smo-containing cilia. For rescued samples, 100 cells in which FLAG expression was detected were counted and examined for the presence of Smo in cilia. *, $P < 0.001$ versus control; $n = 3$ independent replicates. All P values were analyzed by one-way ANOVA with Bonferoni correction. Data are shown as means ± SEM.

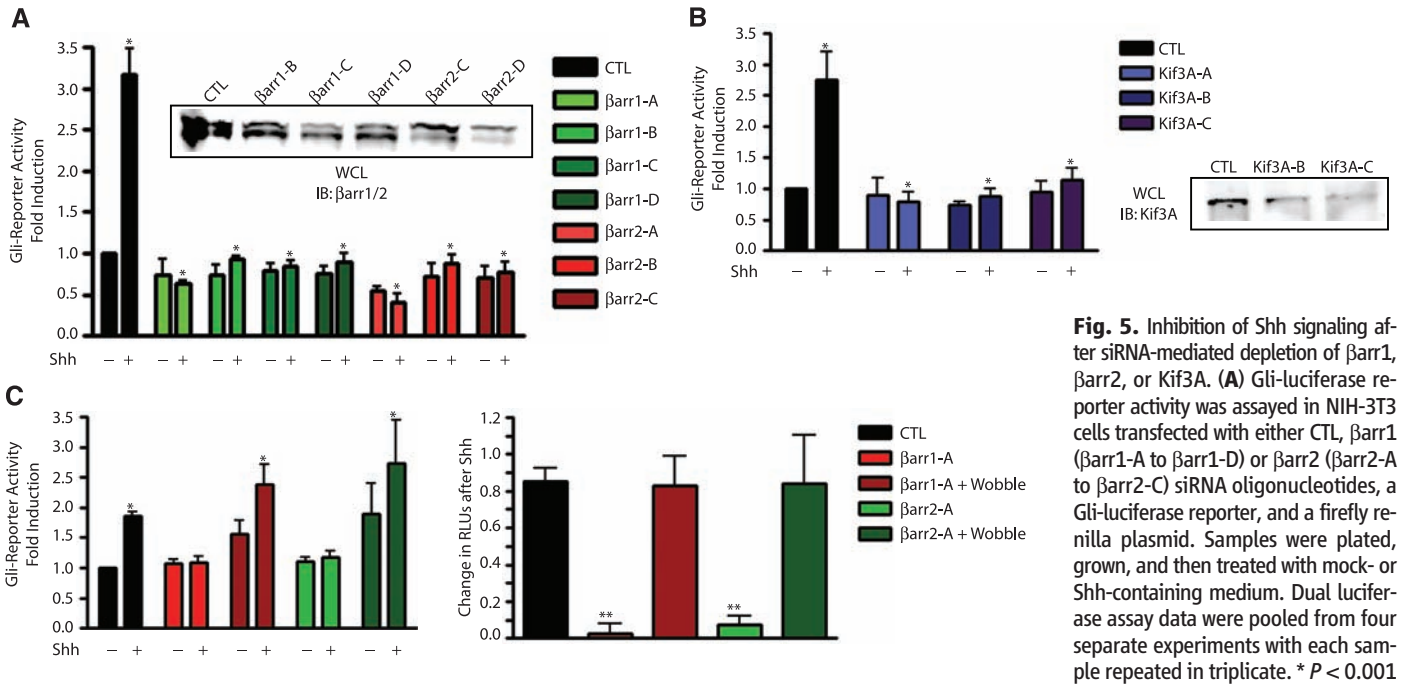

Fig. 5. Inhibition of Shh signaling after siRNA-mediated depletion of βarr1, βarr2, or Kif3A. (**A**) Gli-luciferase reporter activity was assayed in NIH-3T3 cells transfected with either CTL, βarr1 (βarr1-A to βarr1-D) or βarr2 (βarr2-A to βarr2-C) siRNA oligonucleotides, a Gli-luciferase reporter, and a firefly renilla plasmid. Samples were plated, grown, and then treated with mock- or Shh-containing medium. Dual luciferase assay data were pooled from four separate experiments with each sample repeated in triplicate. * $P < 0.001$ versus control or Shh-treated samples; $n = 5$ independent replicates. Inset shows the Western blot for the βarr knockdown. (**B**) Effect of depletion of Kif3A in NIH-3T3 cells transfected with either CTL or Kif3A (Kif3A-A to Kif3A-C) siRNA oligonucleotides, a Gli-luciferase reporter, and a firefly renilla plasmid. Lysates were examined as above. * $P < 0.001$ versus control Shh-treated samples; $n = 3$ independent replicates. Inset shows the Western blot for the Kif3A knockdown. (**C**) Rescue of siRNA-treated NIH-3T3 cells transfected with either CTL; βarr1 (βarr1-A) or βarr2 (βarr2-A) siRNA oligonucleotides, alone or with the corresponding rescue construct; a Gli-luciferase reporter; and a firefly renilla plasmid as an internal control. Samples were plated, grown, and then treated with mock- or Shh-containing media. For the left panel, data were plotted as in (A) and (B). * $P < 0.05$ versus control untreated samples as analyzed by one-way ANOVA with Bonferoni correction; $n = 4$ independent replicates. For the right panel, values in each individual experiment were analyzed for the change in relative luciferase units (RLUs) after Shh treatment as a relative measure of induction over basal for the indicated condition. ** $P < 0.001$ versus control or Shh-treated samples; $n = 4$ independent replicates. All P values were analyzed by one-way ANOVA with Bonferoni correction. Data are shown as means ± SEM.

Several siRNA oligos to Kif3A showed a similar effect (Fig. 5B). Gli-reporter activity could be rescued in this system by overexpression of βarr mutants not subject to siRNA-mediated silencing (Fig. 5C). The rescue constructs increased basal activity in the Gli-reporter system (Fig. 5C), but the total change in Gli activity in response to Shh in such cells was similar to that observed in the control samples (Fig. 5C). Thus, βarrs appear to be required for efficient downstream signaling through Gli in these cells, probably because of their effects on localization of Smo to the primary cilium.

Our findings indicate that, together, βarrs and Kif3A may mediate the transport of Smo to the primary cilium, where it must reside to activate Gli transcription factors. Although Kif3A functions downstream of Ptc in response to Shh stimulation, it may both positively and negatively regulate Smo activity (*20*, *21*). Kif3A also mediates the transport of another ciliary protein, von Hippel–Lindau (*22*), and is responsible for transporting visual arrestin between the inner and outer segments of the mammalian photoreceptor, which is a specialized and modified primary cilium (*23*). Furthermore, in addition to Smo, several other 7TMRs localize to the primary cilium, including the 5-HT(6) serotonin receptor (*24*), the somatostatin receptor sst3 (*25*), and the angiotensin II receptor (*26*). Consequently, it seems plausible that βarrs may regulate localization of 7TMRs and other signaling proteins to the primary cilia, and function at the primary cilia to regulate signaling networks.

References and Notes

1. R. J. Lefkowitz, E. J. Whalen, *Curr. Opin. Cell Biol.* **16**, 162 (2004).
2. S. K. Shenoy, R. J. Lefkowitz, *J. Biol. Chem.* **278**, 14498 (2003).
3. R. J. Lefkowitz, K. Rajagopal, E. J. Whalen, *Mol. Cell* **24**, 643 (2006).
4. Y. Wang, A. P. McMahon, B. L. Allen, *Curr. Opin. Cell Biol.* **19**, 159 (2007).
5. D. Huangfu, K. V. Anderson, *Development* **133**, 3 (2006).
6. M. Evangelista, H. Tian, F. J. de Sauvage, *Clin. Cancer Res.* **12**, 5924 (2006).
7. W. Chen *et al.*, *Science* **306**, 2257 (2004).
8. A. R. Meloni *et al.*, *Mol. Cell. Biol.* **26**, 7550 (2006).
9. A. M. Wilbanks *et al.*, *Science* **306**, 2264 (2004).
10. K. C. Corbit *et al.*, *Nature* **437**, 1018 (2005).
11. D. Huangfu, K. V. Anderson, *Proc. Natl. Acad. Sci. U.S.A.* **102**, 11325 (2005).
12. P. Satir, S. T. Christensen, *Annu. Rev. Physiol.* **69**, 377 (2007).
13. C. J. Haycraft *et al.*, *PLoS Genet.* **1**, e53 (2005).
14. Materials and methods are available as supporting material on *Science* Online.
15. D. Huangfu *et al.*, *Nature* **426**, 83 (2003).
16. R. Rohatgi, L. Milenkovic, M. P. Scott, *Science* **317**, 372 (2007).
17. S. R. May *et al.*, *Dev. Biol.* **287**, 378 (2005).
18. N. Hirokawa, *Traffic* **1**, 29 (2000).
19. K. Xiao *et al.*, *Proc. Natl. Acad. Sci. U.S.A.* **104**, 12011 (2007).
20. E. Kolpakova-Hart, M. Jinnin, B. Hou, N. Fukai, B. R. Olsen, *Dev. Biol.* **309**, 273 (2007).
21. E. Koyama *et al.*, *Development* **134**, 2159 (2007).
22. D. A. Mans *et al.*, *Exp. Cell Res.* **314**, 1229 (2008).
23. J. R. Marszalek *et al.*, *Cell* **102**, 175 (2000).
24. I. Brailov *et al.*, *Brain Res.* **872**, 271 (2000).
25. M. Handel *et al.*, *Neuroscience* **89**, 909 (1999).
26. P. G. Woost *et al.*, *In Vitro Cell. Dev. Biol. Anim.* **42**, 189 (2006).

27. We thank S. Dewire, J. Violin, S. Ahn, and E. Reiter for critical commentary; J. Reiter for scientific discussions; C. Hubbert and A. Guardiola for technical assistance; D. Addison, E. Hall, and D. Sawyer for administrative assistance; and P. Beachy for GFP-Smo plasmid. This work was supported in part by NIH grants HL16037 and HL70631. Additional funding was provided by NIH grant 5RO1 CA113656-02. J.J.K. is supported by NIH grant 5T32 AI007217-25. W.C. is a V Foundation Scholar. R.J.L. is an investigator with the Howard Hughes Medical Institute.

Supporting Online Material

www.sciencemag.org/cgi/content/full/1157983/DC1
Materials and Methods
Figs. S1 to S3
References

18 March 2008; accepted 7 May 2008
Published online 22 May 2008;
10.1126/science.1157983
Include this information when citing this paper.

Both Catalytic Steps of Nuclear Pre-mRNA Splicing Are Reversible

Chi-Kang Tseng[1,2] and Soo-Chen Cheng[1,2]*

Nuclear pre–messenger RNA (pre-mRNA) splicing is an essential processing step for the production of mature mRNAs from most eukaryotic genes. Splicing is catalyzed by a large ribonucleoprotein complex, the spliceosome, which is composed of five small nuclear RNAs and more than 100 protein factors. Despite the complexity of the spliceosome, the chemistry of the splicing reaction is simple, consisting of two consecutive transesterification reactions. The presence of introns in spliceosomal RNAs of certain fungi has suggested that splicing may be reversible; however, this has never been demonstrated experimentally. By using affinity-purified spliceosomes, we have shown that both catalytic steps of splicing can be efficiently reversed under appropriate conditions. These results provide considerable insight into the catalytic flexibility of the spliceosome.

To examine the potential reversibility of splicing, we used a dominant-negative mutant of Prp22, a DExD/H-box RNA helicase. Prp22 is required for the second catalytic step and the release of mature message (fig. S1) (*1*, *2*). The prp22$_{S635A}$ mutant retains its adenosine triphosphatase activity and its ability to promote the catalysis of the second transesterification step but is defective in releasing mRNA from the spliceosome; it remains associated with the spliceosome after completion of splicing (*3*). We purified the V5-tagged version of the mutant protein and added to in vitro splicing assays. As expected, the spliceosome purified with antibody to V5 contained primarily spliced products (lariat intron and mature mRNA) with a small amount of splicing intermediates (Fig. 1A, lane 2). The availability of these essentially homogeneous postcatalytic spliceosomes allowed us to explore the possibility that the splicing reactions could be reversed.

After trying different incubation conditions, we observed, in the absence of monovalent ions, what appeared to be efficient reversal of the second step (the R2 reaction), that is, a dramatic reduction in spliced products accompanied by a corresponding increase in splicing intermediates (lanes 3 to 6). To confirm that this was indeed the case, we performed a number of analyses. Primer extension probing the 5′ end of the intron and branch point indicated that the accumulated splicing intermediates did in fact result from the faithful reversal at the second transesterification reaction. Moreover, sequence analysis of cloned reverse transcription polymerase chain reaction products confirmed the restoration of the authentic 3′ splice junction (table S1). The reverse reaction was precise, with no errors detected in the 28 clones analyzed (table S1), and was independent of pH over the range of 6.8 to 8.8 (Fig. 1A, lanes 3 to 6). These results unambiguously indicated that reversal of splicing occurred in the absence of monovalent ions. The reverse reaction was strongly inhibited by an addition of 150 mM KCl (lanes 7 to 10).

Kinetic analysis revealed that the R2 reaction was remarkably efficient (Fig. 1B, lanes 9 to 15). We then tested whether R2 was itself "reversible." We incubated the purified spliceosome in the absence of KCl for 1 hour and then added KCl. Strikingly, the splicing intermediates were rapidly converted to spliced products (the F2 reaction) (lanes 16 to 18). These results indicate that the purified spliceosomes were in a dynamic state, with the forward reaction strongly favored in the presence of KCl, whereas the reverse reaction was strongly favored in the absence of KCl.

[1]Institute of Microbiology and Immunology, National Yang-Ming University, Shih-Pai, Taipei, Taiwan, Republic of China. [2]Institute of Molecular Biology, Academia Sinica, Nankang, Taipei, Taiwan, Republic of China.

*To whom correspondence should be addressed. E-mail: mbscc@ccvax.sinica.edu.tw

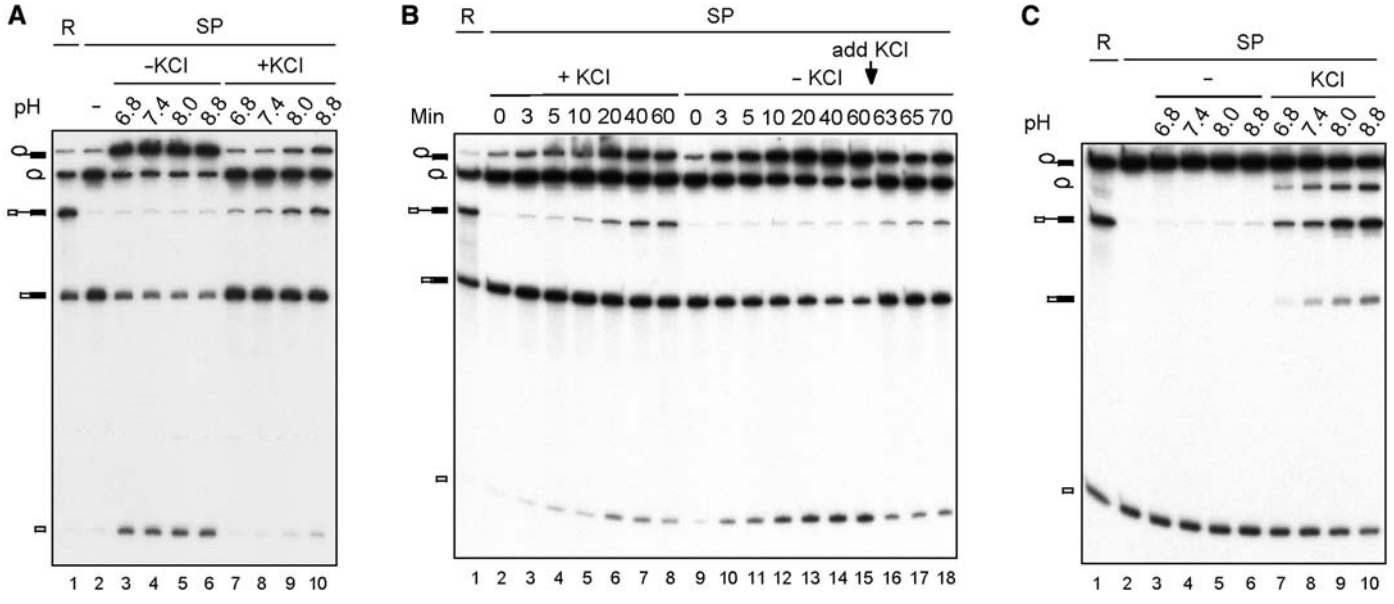

Fig. 1. Reverse splicing of both catalytic steps. (**A** and **B**) Splicing was carried out in the presence of recombinant V5-tagged prp22$_{S635A}$ protein (lane 1). The spliceosome precipitated by antibody to V5 (lane 2) was then incubated at 25°C under various conditions. (A) 10 mM Tris-HCl at pH 6.8, 7.4, 8.0, or 8.8, 4 mM $MgCl_2$ without (lanes 3 to 6) or with (lanes 7 to 10) 150 mM KCl for 1 hour. (B) 10 mM Tris-HCl, pH 8.8, 4 mM $MgCl_2$, 150 mM KCl for 3, 5, 10, 20, 40, or 60 min (lanes 3 to 8), or without KCl for 3, 5, 10, 20, 40, or 60 min (lanes 10 to 15), then the addition of 150 mM KCl for an additional 3, 5, and 10 min (lanes 16 to 18). (**C**) Splicing was carried out with ACAC pre-mRNA, using extracts with V5-tagged Prp22 (lane 1). The spliceosome precipitated by antibody to V5 (lane 2) was then incubated at 25°C in 10 mM Tris-HCl at pH 6.8, 7.4, 8.0, or 8.8, 4 mM $MgCl_2$ without (lanes 3 to 6) or with (lanes 7 to 10) 150 mM KCl for 1 hour. R, reaction; SP, spliceosome.

In these analyses, we noticed that when the purified spliceosomes were incubated in the presence of KCl, a small amount of intact pre-mRNA was also generated, indicating reversal of the first step (the R1 reaction). Since KCl also promoted F2, we speculated that R1 might be in competition with F2, and the efficiency of R1 would increase if F2 were blocked. We then prepared spliceosomes arrested after the first transesterification reaction using pre-mRNA with 3′ splice site mutations (ACAC) that prevent exon ligation (*4*). Spliceosomes formed on the mutant substrate still bind V5-tagged Prp22 but could not produce spliced products (fig. S1), and the affinity-purified spliceosome contained largely splicing intermediates (Fig. 1C, lane 2). Indeed, we found that reversal of the step one reaction was also highly efficient, but in this case required KCl (lanes 7 to 10). The R1 reaction was remarkably precise, with no error detected at the 5′ splice site in 33 clones analyzed (table S1) (*5*). Under these conditions, we also observed the completion of the second transesterification reaction to a certain degree (lanes 7 to 10), yet with a high error rate (tables S1 and S2) (*5*), consistent with a previous report (*6*). The F2 reaction appeared to be less precise than the reverse reaction because errors were also detected with the wild-type substrate. In this analysis, spliceosomes containing spliced products were incubated in the absence of KCl to drive R2 followed by the addition of KCl to drive F2, and the yielded mRNA was analyzed. Three out of 43 clones analyzed had products of aberrant ligation (tables S1 and S2) (*5*).

We then examined the divalent cation requirements for the reverse reactions. We found that 4 mM Ca^{2+} and Mn^{2+}, but not Zn^{2+}, supported R1 in the presence of KCl (Fig. 2A, lanes 8 to 10), but at a lower efficiency than Mg^{2+} (lane 7). Mn^{2+} efficiently promoted F2 but with relaxed specificity, particularly in the absence of KCl (tables S1 and S2, lane 5). In contrast, the R2 reaction had a strict requirement for Mg^{2+} at a concentration of 4 mM (Fig. 2B, lanes 4 to 7 and 9 to 12). The difference in divalent cation requirements for the two reactions is intriguing, but we currently do not understand the mechanistic reasons for this phenomenon.

In the presence of Mn^{2+}, we also observed production of the 5′ exon (E1) and the 3′ exon (E2) (Fig. 2B, lane 11), presumably from cleavage of mRNA at the splice junction, a reaction analogous to spliced exon reopening (SER), known to be catalyzed by Group II intron (*7*). Precise cleavage at the splice junction was confirmed by primer extension analysis of gel-purified E2 fragment (Fig. 2C). Nevertheless, we cannot exclude the possibility that cleavage occurred on the lariat intron-exon 2 following the R2 reaction. Titration of Mn^{2+} for SER revealed a requirement for Mn^{2+} at a concentration of ≥4 mM (Fig. 2D, lanes 7 to 9) and high pH (Fig. 2E, lanes 9 and 10). Lower Mn^{2+} concentrations or pH promoted R2 instead (Fig. 2D, lanes 4 to 6; Fig. 2E, lanes 7 and 8). These results suggest that spliceosomal introns also catalyze SER.

We have shown that both catalytic steps of pre-mRNA splicing are reversible under appropriate conditions. The reverse reactions were extremely precise, with no errors detected in either catalytic step. This is in contrast to the forward reactions, in which aberrant exon ligation was detectable even with the wild-type substrate. The biological importance of higher fidelity in the reverse reaction remains to be explored.

Reversible splicing has been inferred by the presence of introns in spliceosomal small nuclear RNAs (snRNAs) of certain fungi (*8*) and the fact that identical transesterification reactions are readily reversible in the context of Group II introns (*9*, *10*). Nevertheless, the reversibility in the context of a fully assembled spliceosome is highly efficient. In this regard, the assembly of the spliceosome is a complex and intricately orchestrated process (*11*, *12*), and each chemical step requires the prior action of specific DExD/H-box RNA helicases to prepare the spliceosome for catalysis (*13*, *14*). Our results indicate that these rearrangements are not required for the reverse reaction, at least for the Prp16-dependent step, given that Prp16 is not retained on the purified spliceosome (fig. S2).

Furthermore, our results indicate that the catalytic center of the spliceosome is highly stable but chemically adaptable. Relatively subtle changes in ionic environment can drive the reaction either forward or in reverse direction, or toward SER, which suggests that large conformational rearrangements are not required between these catalytic steps. These observations are consistent with the two-stage model of spliceosome activity proposed by Query and Konarska. Their model suggests that conformations that favor the first step inhibit the second step and vice versa (*15*). It will be of considerable interest to probe the snRNA topology in the presence and absence of monovalent ions to obtain insight into the active site of the spliceosome.

We have also shown that the spliceosome could catalyze SER, which has previously been demonstrated in Group II introns, and suggested to represent hydrolytic reversal of the second step (*7*). In this regard, SER is a nonproductive pathway of the reverse reaction. Our results have not only shown that the spliceosome is able to catalyze hydrolytic reaction but also indicated that SER is conserved between these two types of

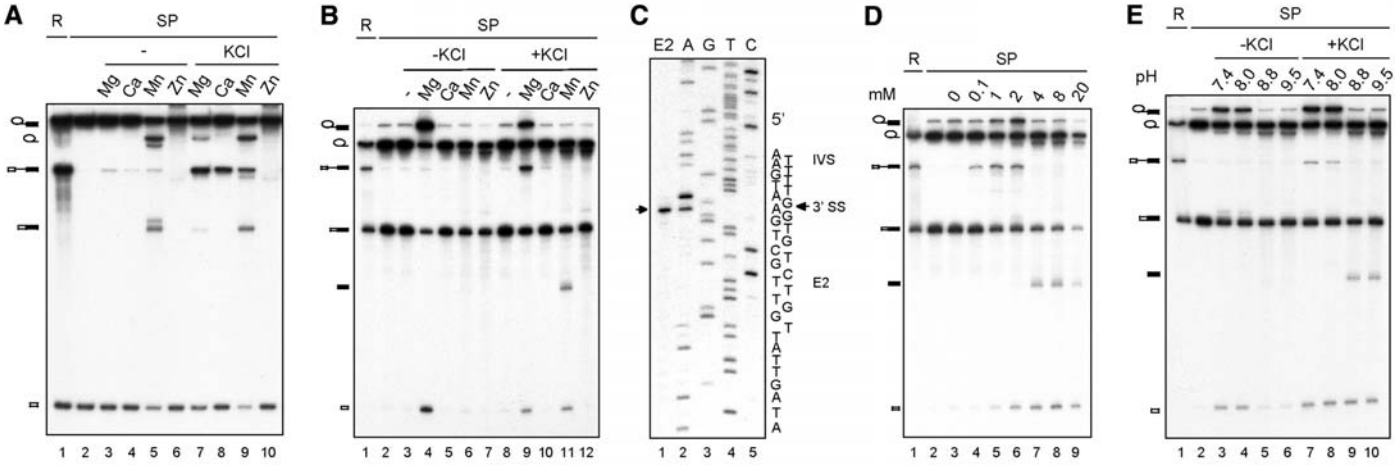

Fig. 2. Divalent cation requirements and the SER reaction. (**A**) Splicing was carried out with ACAC pre-mRNA using extracts with V5-tagged Prp22 (lane 1). The spliceosome precipitated by antibody to V5 (lane 2) was then incubated at 25°C in 10 mM Tris-HCl, pH 8.8, 4 mM $MgCl_2$, $CaCl_2$, $MnCl_2$, or $ZnCl_2$, without (lanes 3 to 6) or with (lanes 7 to 10) 150 mM KCl for 1 hour. (**B** to **E**) Splicing was carried out in the presence of $prp22_{S635A}$-V5 (lane 1). The spliceosome precipitated by antibody to V5 (lane 2) was then incubated under various conditions. (B) 10 mM Tris-HCl, pH 8.8, 0 or 4 mM $MgCl_2$, $CaCl_2$, $MnCl_2$, or $ZnCl_2$, without (lanes 3 to 7) or with (lanes 8 to 12) 150 mM KCl for 1 hour. (C) Primer extension analysis of the putative E2 fragment to map the cleavage site. (D) 10 mM Tris-HCl, pH 8.8, 150 mM KCl with 0, 0.1 mM, 1 mM, 2 mM, 4 mM, 8 mM, or 20 mM $MnCl_2$ (lanes 3 to 9) for 1 hour. (E) 10 mM Tris-HCl at pH 7.4, 8.0, 8.8, or 9.5, 8 mM $MnCl_2$ without (lanes 3 to 6) or with (lanes 7 to 10) 150 mM KCl for 1 hour. R, reaction; SP, spliceosome.

introns, although the importance of such a nonproductive pathway in the splicing reaction is unknown.

References and Notes

1. M. Company, J. Arenas, J. Abelson, *Nature* **349**, 487 (1991).
2. B. Schwer, C. H. Gross, *EMBO J.* **17**, 2086 (1998).
3. B. Schwer, T. Meszaros, *EMBO J.* **19**, 6582 (2000).
4. U. Vijayraghavan *et al.*, *EMBO J.* **5**, 1683 (1986).
5. Materials and methods are available as supporting material on *Science* Online.
6. R. M. Mayas, H. Maita, J. P. Staley, *Nat. Struct. Mol. Biol.* **13**, 482 (2006).
7. K. A. Jarrell, C. L. Peebles, R. C. Dietrich, S. L. Romiti, P. S. Perlman, *J. Biol. Chem.* **263**, 3432 (1988).
8. T. Tani, Y. Ohshima, *Nature* **337**, 87 (1989).
9. S. Augustin, M. W. Müller, R. J. Schweyen, *Nature* **343**, 383 (1990).
10. M. Mörl, C. Schmelzer, *Cell* **60**, 629 (1990).
11. D. A. Brow, *Annu. Rev. Genet.* **36**, 333 (2002).
12. C. L. Will, R. Lührmann, in *The RNA World,* R. F. Gesteland, T. R. Cech, J. F. Atkins, Eds. (Cold Spring Harbor Laboratory, New York, 2006), pp. 369–400.
13. S.-H. Kim, R.-J. Lin, *Mol. Cell. Biol.* **16**, 6810 (1996).
14. B. Schwer, C. Guthrie, *EMBO J.* **11**, 5033 (1992).
15. C. C. Query, M. M. Konarska, *Mol. Cell* **14**, 343 (2004).

16. We are grateful to T. Nilsen for critical comments and help on the manuscript. We also thank M. M. Konarska and C. Query for reading the manuscript and H. Wilson for English editing. This work was supported by a grant from Academia Sinica and National Science Council (Taiwan) grant NSC95-2321-B-001-014.

Supporting Online Material

www.sciencemag.org/cgi/content/full/320/5884/1782/DC1
Materials and Methods
Figs. S1 and S2
Tables S1 and S2
References

11 April 2008; accepted 22 May 2008
10.1126/science.1158993

Virus Attenuation by Genome-Scale Changes in Codon Pair Bias

J. Robert Coleman,[1] Dimitris Papamichail,[2]* Steven Skiena,[2] Bruce Futcher,[1] Eckard Wimmer,[1]† Steffen Mueller[1]

As a result of the redundancy of the genetic code, adjacent pairs of amino acids can be encoded by as many as 36 different pairs of synonymous codons. A species-specific "codon pair bias" provides that some synonymous codon pairs are used more or less frequently than statistically predicted. We synthesized de novo large DNA molecules using hundreds of over- or underrepresented synonymous codon pairs to encode the poliovirus capsid protein. Underrepresented codon pairs caused decreased rates of protein translation, and polioviruses containing such amino acid–independent changes were attenuated in mice. Polioviruses thus customized were used to immunize mice and provided protective immunity after challenge. This "death by a thousand cuts" strategy could be generally applicable to attenuating many kinds of viruses.

The redundancy of the genetic code means that a typical 300–amino acid protein can be encoded in about 10^{151} ways, raising the question of to what extent the actual encoding is optimal. Actual encodings are biased to use some synonymous codons more frequently than others (the "codon bias"). For instance, in humans, the Ala codon GCC is used four times as frequently as the synonymous codon GCG. Similarly, but independently, some synonymous codon pairs are used more or less frequently than expected (the "codon pair bias") (*1*). For instance, on the basis of codon frequencies, the amino acid pair Ala-Glu is expected to be encoded by GCCGAA and GCAGAG about equally often. In fact, the codon pair GCCGAA is strongly underrepresented, even though it contains the most frequent Ala codon, such that it is used only one-seventh as often as GCAGAG (*2*) (table S1). Although it is not clear why some codon pairs are under- or overrepresented, it is possible that codon pair usage affects translation (*3*).

[1]Department of Molecular Genetics and Microbiology, Stony Brook University, Stony Brook, NY 11794, USA. [2]Department of Computer Science, Stony Brook University, Stony Brook, NY 11794, USA.

*Present address: Department of Computer Science, University of Miami, Coral Gables, FL 33124, USA.

†To whom correspondence should be addressed. E-mail: ewimmer@ms.cc.sunysb.edu

We previously reported the generation of poliovirus de novo in the absence of natural template (*4*), using reverse genetics and the ability to synthesize large DNAs. We and others recently synthesized novel polioviruses encoding precisely the same amino acid sequences as wild-type poliovirus, but using rare codons (*5*, *6*); these viruses were attenuated. Here, we used poliovirus as a model system to explore the consequences of genome-scale manipulation of codon pair bias (Fig. 1A). We call the process of designing such viruses "synthetic attenuated virus engineering" or SAVE.

We developed a computer algorithm that can recode a given amino acid sequence, but using different codon pairs, while controlling other features of the sequence such as the codon bias and the folding free energy of the RNA (*2*) (figs. S1 and S2). This algorithm was used to design two new polioviruses, PV-Min and PV-Max (Fig. 1), with a P1 region (encoding the viral capsid, 2643 nucleotides) containing under- or overrepresented codon pairs. The P1 region is suitable for such experiments because it can be deleted or substituted without affecting genome replication (*7*). Virus PV-Min was recoded to use codon pairs that are underrepresented relative to the human genome, and it contains 631 synonymous mutations. Virus PV-Max was recoded to use overrepresented codon pairs, and it contains 566 synonymous mutations. PV-Min has a codon pair bias score (CPB score) much lower than that of normal human genes (Fig. 1B). Both PV-Min and PV-Max encode precisely the same amino acid sequences as the wild type, but they use different pairwise arrangements of synonymous codons [Fig. 1B; for calculation of CPB scores, see (*2*)]. These P1 fragments were synthesized, sequenced, and incorporated into a full-length cDNA construct of poliovirus (Fig. 1C) (*2*, *8*).

In vitro transcribed RNAs of PV-Max, PV-Min, and wild-type virus were transfected into HeLa R19 cells to assess virus production (*5*, *8*). PV-Max produced 90% cytopathic effect within 24 hours after RNA transfection, similar to the transfection of wild-type RNA (*8*). The PV-Max virus generated plaques identical in size to the wild type (Fig. 1F). In contrast, the PV-Min RNA produced no visible cytopathic effect after 96 hours, and no viable virus could be isolated even after four blind passages of the supernatant from transfected cells.

We subcloned portions of the PV-Min P1 region into an otherwise wild-type virus to reduce the number of underrepresented codon pairs (Fig. 1C). These subclones yielded viruses with varying degrees of attenuation (Fig. 1, C, D, and F). Viruses containing P1 fragments X and Y were each slightly attenuated; however, when added together they yielded virus PV-MinXY, which was substantially attenuated (Fig. 1C). Virus PV-MinZ was about as attenuated as PV-MinXY. Construct PV-YZ did not yield viable virus (Fig. 1, C and D). We conclude that the inviability of PV-Min was due to the sum of defects in the various subportions.

One-step growth kinetics were examined. Like the wild-type virus, the chimeric viruses had an eclipse phase followed by exponential growth. However, as measured by plaque-forming units (PFUs), the final titer of PV-Min constructs was decreased by up to a factor of 1000 with respect to wild-type viruses (Fig. 1D). This low plaque titer could have resulted from lower production of virions (i.e., cells infected with PV-Min constructs produced fewer virus particles), or from lower specific infectivity of those virions (i.e., the particles that were produced were less efficient in establishing a plaque), or both. We examined both possibilities (*2*). When the number of viral particles produced per infected cell

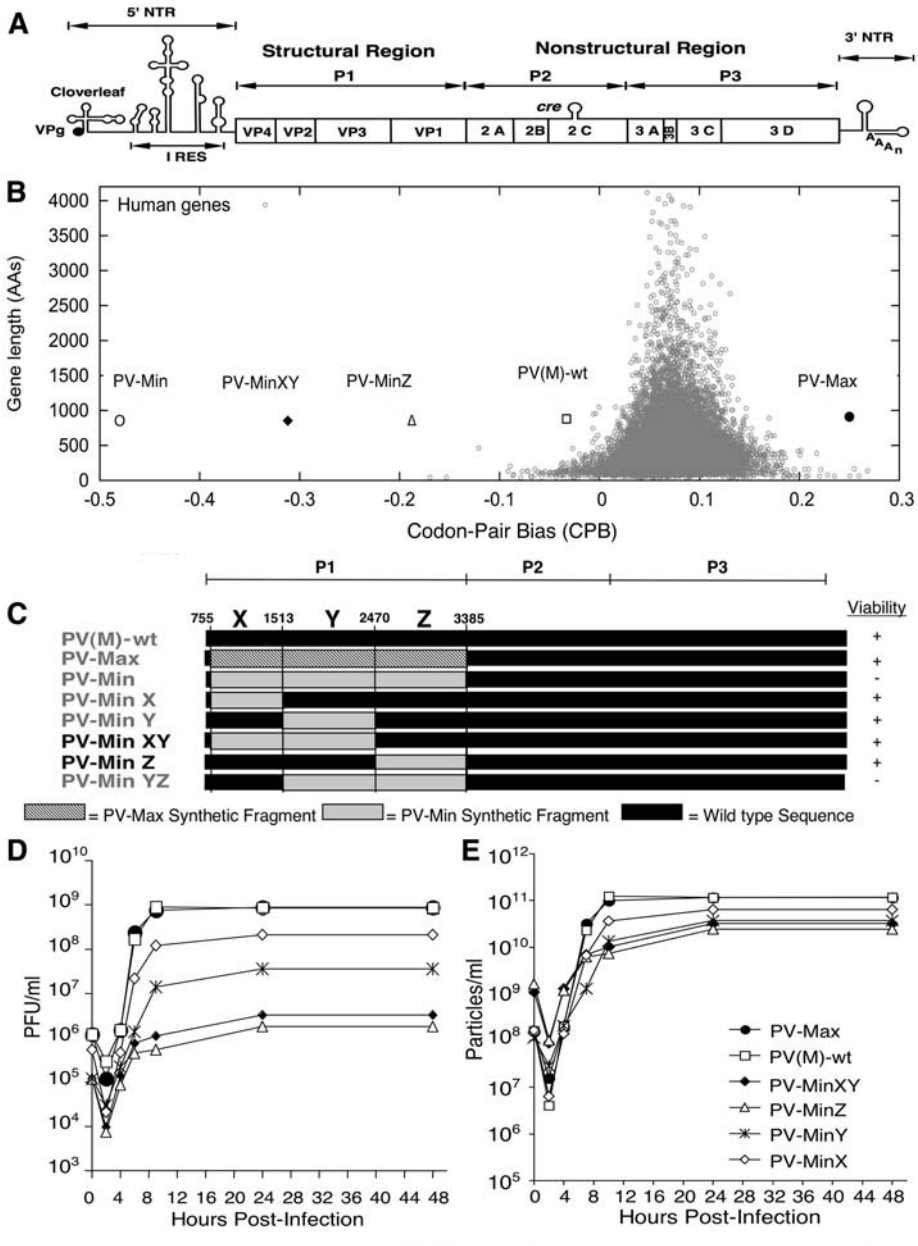

Fig. 1. (**A**) The poliovirus genome. Shown is the viral RNA with its covalently linked 5′ viral protein VPg, the 5′ nontranslated region [consisting of cloverleaf and internal ribosomal entry site (IRES)]; the long open reading frame (open box) encoding the polyprotein that is cleaved into P1 (capsid precursor), P2, and P3 (precursors to nonstructural proteins); and the 3′ nontranslated region terminated with poly(A) (*7*). The polypeptide precursors P1, P2, and P3 are processed into functional proteins by virus-encoded proteinases (*7*). *Cre* is a stem-loop structure functioning as a cis-acting replication element. (**B**) Calculated codon pair bias (CPB) score for all 14,795 annotated human genes. Each dot represents the calculated CPB score of a gene plotted against its amino acid length. Underrepresented codon pairs yield negative scores. Various poliovirus constructs are represented by symbols; PV(M)-wt is the wild-type poliovirus (CPB = −0.02). (**C**) The structures of the various chimeric, partly synthetic poliovirus constructs, and their viability on cultured cells. Nucleotide positions are shown. (**D**) A one-step growth curve with respect to PFUs. An MOI of 2 was used to infect a monolayer of HeLa R19 cells. Symbols: open squares, PV(M)-wt; solid circles, PV-Max; open diamonds, PV-Min755-1513; asterisks, PV-Min1513-2470; solid diamonds, PV-MinXY; open triangles, PV-MinZ. (**E**) As (D), but with results graphed with respect to viral particles instead of PFUs. (**F**) Plaque phenotypes of viruses after 72 hours of incubation, stained with crystal violet (plate diameter, 35 mm).

was measured, we found that cells infected with PV-MinXY or PV-MinZ produced fewer viral particles than did the wild type, but the effect was only about a factor of 10 or slightly less (Fig. 1E and Table 1). When the number of particles per PFU was measured, we found a more striking effect: PV-MinXY and PV-MinZ each required about 100 times as many viral particles as the wild type to generate a plaque (Table 1). For wild-type virus, the number of virions applied per plaque generated was about 137, whereas for PV-MinZ, the number of virions applied per plaque generated was 13,500; hence, the main defect was reduced specific infectivity of the virions. The total attenuation from both effects together was a factor of ~1000.

The heat stability of PV-MinXY and PV-MinZ was identical to that of the wild type. This observation suggests that their low specific infectivity is not a result of gross defects in the capsid (*2*) (fig. S3).

To measure the possible effect of codon pair bias on translation, we used a dicistronic reporter encoding both R-Luc and F-Luc (*2*, *5*) (Fig. 2A). Because the F-Luc reporter is translated as a fusion protein with the proteins of the P1 region, the translatability of the P1 region directly affects the amount of F-Luc protein produced. Thus, the ratio of F-Luc luminescence to R-Luc luminescence is a measure of the translatability of the various P1 encodings.

The variously encoded P1 regions were tested (Fig. 2). PV-MinXY, PV-MinZ, and PV-Min produced much less F-Luc per unit of R-Luc than did the wild-type P1 region, which strongly suggests that the underrepresented codon pairs reduced translation (Fig. 2B). The reduced translation is probably sufficient to explain the attenuated phenotype, because smaller reductions in translation caused by other methods have been observed to attenuate poliovirus; apparently, poliovirus has a fairly high threshold requirement for translation (*5*, *9*). In contrast, PV-Max P1 produced more F-Luc per unit of R-Luc than did the wild type, consistent with enhanced translation (Fig. 2B).

PV-MinXY and PV-MinZ each contain hundreds of mutations (407 and 224, respectively). If the attenuation of these viruses were due to hundreds of small defects, it should be difficult for these viruses to revert to wild-type virulence. Alternatively, if most mutations are neutral, with a small minority contributing to attenuation, then reversion should occur. To distinguish these possibilities, we serially passaged viruses PV-MinXY and PV-MinZ in HeLa R19 cells 17 and 19 times, respectively, at a multiplicity of infection (MOI) of 0.5. The titer was monitored for phenotypic reversion, and the passaged virus was sequenced. After 17 or 19 passages of PV-MinXY or PV-MinZ, respectively, no phenotypic change was detected (i.e., same titer, induction of cytopathic effect) and no nucleotide changes were seen in the synthetic region, supporting the idea that there are many small defects.

We next tested whether the synthetic viruses were also attenuated in animals. Viruses were administered to CD155 transgenic (tg) mice (which express the poliovirus receptor) via intracerebral injection (*10*), allowing direct exposure to the central nervous system, the ultimate target of poliovirus pathogenesis (*11*). PV-MinXY and PV-MinZ viruses were attenuated by a factor of 1000 (as measured by particles) or a factor of 10 (as measured by PFUs) (Table 1) (*2*). PV-Max virulence was identical to that of the wild type.

Because PV-MinZ and PV-MinXY encode exactly the same proteins as wild-type virus, they might provoke a protective immune response. Alternatively, the relatively poor translation of the mutant mRNAs might prevent such a response. To distinguish these possibilities, we administered PV-MinZ and PV-MinXY to groups of eight CD155 tg mice at a dose of 10^8 particles once a week for 3 weeks via intraperitoneal injection. Ten days after the final injection, the protective antibodies of the seven surviving mice in each group were measured via microneutralization assay, and a robust immune response was detected (fig. S3). Subsequent challenge of the immunized mice with an otherwise lethal dose of wild-type poliovirus via intramuscular injection did not lead to death or signs of paralysis or paresia; in contrast, all mock-immunized mice died.

Technology for the synthesis of large DNAs and for the redesign of living systems (*5*, *6*, *12*) allows the reengineering of viruses for specific purposes such as vaccines. We have used these approaches to generate polioviruses that use a large proportion of under- or overrepresented codon pairs. Although it has been known for many years that codon pair usage is biased (*1*), this phenomenon has previously been studied primarily by informatics (*13*, *14*). We now find that underrepresented codon pairs cause poor translation and attenuation in poliovirus. One theory for the existence of codon pair bias is that certain tRNAs interact poorly on the ribosome (*3*), and so the codon pairs causing the juxtaposition of such tRNAs are underrepresented; our translation data are consistent with this theory.

We note that attenuation is not caused by random changes in synonymous codons if those changes do not systematically reduce codon bias or codon pair bias. Previously we created the virus PV-SD, with 937 mutations in synonymous codons in the P1 region (*5*). In PV-SD, neither codon bias nor codon pair bias was changed, and that virus was not attenuated (*2*, *5*) (table S2). Here, we created virus PV-Max, which similarly contained 566 mutations in synonymous codons, and it was also not attenuated (Fig. 2). It is noteworthy that even though PV-Max contains overrepresented codons, it is not more virulent than the wild type (Table 1), possibly because evolution has already effectively optimized encoding.

The correlation between the degree of codon pair deoptimization and the degree of viral attenuation, as well as the lack of viral reversion upon passaging, are consistent with the idea that many of the 631 mutations in PV-Min cause small, additive defects. Thus, these attenuated viruses should be stable genetically, because an increase in virulence might require dozens or hundreds of reversions. This genetic stability is important; for example, the oral poliovirus vaccine (OPV) has 51 mutations, but only 5 have been shown to contribute to attenuation (*15*). Thus, OPV can (rarely) revert to neurovirulence in vaccine recipients, causing vaccine-associated paralytic poliomyelitis. Even more seriously, the vaccine strains may evolve into highly virulent circulating vaccine–derived polioviruses by mutation and recombination with related Coxsackie A viruses (*15*, *16*). Such viruses have caused small epidemics of poliomyelitis (*15*, *17*).

Finally, these results suggest that synthetic attenuated virus engineering (SAVE) could play a role in creating new vaccines for various types of viruses. By deoptimizing codon pair bias, one could systematically attenuate a virus to variable but controllable and predictable extents. This approach has four key features: (i) It produces a virus encoding precisely the same amino acid sequences as the wild-type virus, and therefore eliciting the same immune response. (ii) It is a systematic method apparently applicable to many viruses, and possibly not requiring detailed, virus-specific research. (iii) The attenuation is not subject to reversion, simply because of the sheer number of mutations. (iv) It can be combined with other attenuating changes (such as amino acid changes from adaptation of the virus to low temperatures or alternative species) or with other synthetic biology approaches to attenuation (*18*, *19*), thus taking advantage of additional modes of attenuation while providing the unique advantage of limited reversion. This "death by a thousand cuts" strategy is in contrast to existing methods of attenuation, which typically depend on a small number of mutations, and which can revert. Even for an inactivated rather than live virus approach, these features would allow a vaccine to be made from a safer starting material than the corresponding wild-type virus.

Table 1. Poliovirus specific infectivity and attenuation. PLD_{50} is the amount of virus that caused paralysis in 50% of infected mice.

Virus	Absorbance at 260 nm	Purified particles/ml*	Purified PFUs/ml	Relative specific infectivity†	PLD_{50} (particles)‡	PLD_{50} (PFUs)‡
PV(M)-wt	0.956	8.97×10^{12}	6.0×10^{10}	1.00	$10^{4.0}$	$10^{1.9}$
PV-Max	0.842	7.91×10^{12}	6.0×10^{10}	1.04	$10^{4.0}$	$10^{1.9}$
PV-MinXY	0.944	8.87×10^{12}	9.6×10^{8}	0.015	$10^{7.1}$	$10^{3.2}$
PV-MinZ	0.731	6.87×10^{12}	5.1×10^{8}	0.010	$10^{7.3}$	$10^{3.2}$

*Calculated by the formula 9.4×10^{12} particles/ml = 1 OD_{260} (*5*). †Calculated by dividing the PFU/ml of purified virus on HeLa R19 cells by particles/ml, and then normalizing to the wild-type value. In absolute terms, wild-type specific infectivity was 1/137. ‡Calculated after intracerebral injection of virus into CD155 tg mice at varying doses.

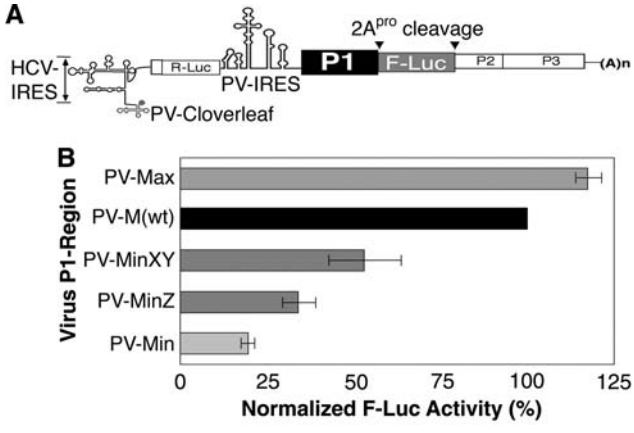

Fig. 2. Effect of altered codon pair bias on translation. (**A**) Structure of a dicistronic reporter (*5*). The first cistron uses the hepatitis C virus (HCV) IRES to initiate translation of *Renilla* luciferase (R-Luc). This first cistron provides an internal control to normalize the amount of input RNA. The second cistron uses the poliovirus IRES to initiate translation of Firefly luciferase (F-Luc). The region labeled P1 was replaced by the recoded, synthetic P1 regions of the indicated viruses. (**B**) Each dicistronic RNA was transfected, in the presence of 2 mM guanidine hydrochloride [to block replication of the transfected genome (*7*)], into HeLa R19 cells, and after 6 hours the R-Luc and F-Luc were measured. The F-Luc/R-Luc values are expressed relative to the wild type, which was set to 100%. The graph displays the average (±SD) of three independent experiments.

References and Notes

1. G. A. Gutman, G. W. Hatfield, *Proc. Natl. Acad. Sci. U.S.A.* **86**, 3699 (1989).
2. See supporting material on *Science* Online.
3. J. Buchan, *Nucleic Acids Res.* **34**, 1015 (2006).
4. J. Cello, A. Paul, E. Wimmer, *Science* **297**, 1016 (2002); published online 11 July 2002 (10.1126/science.1072266).
5. S. Mueller, D. Papamichail, J. R. Coleman, S. Skiena, E. Wimmer, *J. Virol.* **80**, 9687 (2006).
6. C. C. Burns *et al.*, *J. Virol.* **80**, 3259 (2006).
7. E. Wimmer, C. U. Hellen, X. Cao, *Annu. Rev. Genet.* **27**, 353 (1993).
8. S. van der Werf, J. Bradley, E. Wimmer, F. W. Studier, J. J. Dunn, *Proc. Natl. Acad. Sci. U.S.A.* **83**, 2330 (1986).

9. W. D. Zhao, E. Wimmer, *J. Virol.* **75**, 3719 (2001).
10. S. Koike, in *Cellular Receptors for Animal Viruses*, E. Wimmer, Ed. (Cold Spring Harbor Laboratory Press, Cold Spring Harbor, NY, 1994), pp. 463–480.
11. K. Landsteiner, E. Popper, *Z. Immun. Forsch. Orig.* **2**, 377 (1909).
12. L. Chan, S. Kosuri, D. Endy, *Mol. Syst. Biol.* **1**, 10.1038/msb4100025 (2005).
13. A. Fedorov, S. Saxonov, W. Gilbert, *Nucleic Acids Res.* **30**, 1192 (2002).
14. G. Moura *et al.*, *PLoS ONE* **2**, e847 (2007).
15. O. Kew, R. Sutter, E. De Gourville, W. Dowdle, M. Pallansch, *Annu. Rev. Microbiol.* **59**, 587 (2005).
16. P. Jiang *et al.*, *Proc. Natl. Acad. Sci. U.S.A.* **104**, 9457 (2007).
17. O. Kew *et al.*, *Science* **296**, 356 (2002); published online 14 March 2002 (10.1126/science.1068284).
18. E. B. Flanagan, J. M. Zamparo, L. A. Ball, L. L. Rodriguez, G. W. Wertz, *J. Virol.* **75**, 6107 (2001).
19. H. Toyoda, J. Yin, S. Mueller, E. Wimmer, J. Cello, *Cancer Res.* **67**, 2857 (2007).
20. We thank H. Toyoda for lending his expertise to the mouse experiments, W. McCaig for performing serial passages of viral variants, and J. Cello and W. Karzai for comments on the manuscript. All authors declare that they have a patent pending relating to certain aspects of this work. Supported by NIH grants AI075219 and AI15122 (E.W.) and NSF grant EIA-0325123 (S.S.).

Supporting Online Material

www.sciencemag.org/cgi/content/full/320/5884/1784/DC1
Materials and Methods
Figs. S1 to S4
Tables S1 and S2
References

28 January 2008; accepted 27 May 2008
10.1126/science.1155761

Paleo-Eskimo mtDNA Genome Reveals Matrilineal Discontinuity in Greenland

M. Thomas P. Gilbert,[1] Toomas Kivisild,[2] Bjarne Grønnow,[3] Pernille K. Andersen,[4] Ene Metspalu,[5] Maere Reidla,[5] Erika Tamm,[5] Erik Axelsson,[1] Anders Götherström,[6] Paula F. Campos,[1] Morten Rasmussen,[1] Mait Metspalu,[5] Thomas F. G. Higham,[7] Jean-Luc Schwenninger,[7] Roger Nathan,[7] Cees-Jan De Hoog,[8] Anders Koch,[9] Lone Nukaaraq Møller,[10]* Claus Andreasen,[11] Morten Meldgaard,[12] Richard Villems,[5] Christian Bendixen,[4] Eske Willerslev[1]†

The Paleo-Eskimo Saqqaq and Independence I cultures, documented from archaeological remains in Northern Canada and Greenland, represent the earliest human expansion into the New World's northern extremes. However, their origin and genetic relationship to later cultures are unknown. We sequenced a mitochondrial genome from a Paleo-Eskimo human by using 3400- to 4500-year-old frozen hair excavated from an early Greenlandic Saqqaq settlement. The sample is distinct from modern Native Americans and Neo-Eskimos, falling within haplogroup D2a1, a group previously observed among modern Aleuts and Siberian Sireniki Yuit. This result suggests that the earliest migrants into the New World's northern extremes derived from populations in the Bering Sea area and were not directly related to Native Americans or the later Neo-Eskimos that replaced them.

Studies into the peopling of the New World have demonstrated that a number of cultures have inhabited the geographic region encompassed by Greenland and the northern extremes of the American continent. Archaeological evidence has provided several insights into the Paleo-Eskimo cultures that ultimately migrated into Greenland, including that they comprised at least two temporally distinct extinct, and one extant, groups. Known collectively as the Paleo-Eskimos, the two waves of the extinct cultures are represented by the Independence I–Saqqaq and Pre-Dorset culture, which spanned about 3900 to 2500 ^{14}C years before present (yr B.P.), and the Independence II–Dorset cultures of circa (ca.) 2500 to 700 ^{14}C yr B.P. (*1*). Subsequently the region was peopled by the Neo-Eskimo Thule culture, a group genetically distinct from modern Native Americans and whose present-day descendants include the modern Alaskan Yupik and Inupiat and the Canadian and Greenlandic Inuit [Fig. 1; see (*2*) for subdistinction of cultures]. The genetic source of the Paleo-Eskimo cultures and their relationship to each other and to the Neo-Eskimos have not been determined. Competing theories have attributed the origin of the Paleo-Eskimos to an offshoot of the populations that gave rise to the Native American populations of North America, alternatively from the same Beringian source as the Neo-Eskimos, or even from a source population that was distinct from both the Native Americans and the Neo-Eskimos (*1*).

The majority of modern and ancient Neo-Eskimo populations have been classified with mitochondrial DNA (mtDNA) sequences of the hypervariable I (HVS1) region. Belonging mainly to haplogroups (Hgs) A2a and A2b (*3*–*7*) with a low representation (≈5%) of Hg D3 (*3*), these groups exhibit relatively low sequence variation. This supports archaeological evidence suggesting that the Thule culture originated in Alaska about 1000 years ago and spread rapidly over the next 200 years across northern Canada and Greenland (*8*).

Ancient DNA (aDNA) studies can be used to uncover genetic signatures that have been lost through population extinctions, as long as there is suitably well-preserved material for analysis. However, Paleo-Eskimo human material is scarce, despite the relative youth of the cultures and the cold preservation conditions offered by the Arctic. Thus, aDNA studies of this region have been limited to three Canadian skeletons belonging to the Dorset culture and between 800 and 1800 years old (*9*, *10*).

Archaeological excavations between 1983 and 1987 at Qeqertasussuk, Disko Bay, in western Greenland (*11*, *12*) (Fig. 1) yielded human remains from the first Paleo-Eskimo expansion into the far north of the New World. Stone tools, coupled with ^{14}C-dated twigs found among the artifacts, show that the site occupants belong both culturally and temporally to the early Saqqaq culture, 3900 to 3100 ^{14}C yr B.P. Beside four poorly preserved human long bones (*13*), the site yielded a large clump of permafrost-preserved hair that was morphologically identified as human (*2*) (fig. S1). Because hair shaft are often a suitable source of well-preserved, contaminant-free aDNA (*14*, *15*), we investigated how the Saqqaq hair clump offered insights into Paleo-Eskimo genetics.

To investigate the long-term DNA survival at the site, we first obtained 16*S* mtDNA from bowhead whale baleen (*Balaena mysticetus*) recovered from within the hair sample itself (*2*) (table S1). We then reproducibly polymerase chain reaction (PCR)–amplified, cloned, and sequenced mtDNA HVS1 sequences from the human hair and found that they appeared to derive from a single clade, Hg D2. Subsequent typing of an Hg D diagnostic C→A single-nucleotide polymorphism (SNP) at nucleotide position (n.p.) 5178 confirmed this classification (*2*) (tables S1 to S3).

[1]Center for Ancient Genetics, Department of Biology, Universitetsparken 15, DK-2100 Copenhagen, Denmark. [2]Leverhulme Centre for Human Evolutionary Studies, University of Cambridge, Cambridge CB2 1QH, UK. [3]SILA (The Greenland Research Centre at the National Museum of Denmark), Frederikisholms Kanal 12, DK1220 Copenhagen, Denmark. [4]Department of Genetics and Biotechnology, Faculty of Agricultural Sciences, University of Aarhus, Post Office Box 50, DK-8830 Tjele, Denmark. [5]Department of Evolutionary Biology, University of Tartu and Estonian Biocentre, Riia 23B, Tartu, 51010 Estonia. [6]Department of Evolutionary Biology, Uppsala University, Norbyvagten 18D, 74236 Uppsala, Sweden. [7]Research Laboratory for Archaeology and the History of Art, University of Oxford, Dyson Perrins Building, South Parks Road, Oxford OX1 3QY, UK. [8]Department of Earth Sciences, University of Oxford, Parks Road, Oxford OX1 3PR, UK. [9]Department of Epidemiology Research, Statens Serum Institut, Artillerivej 5, DK-2300 Copenhagen S, Denmark. [10]Danish Centre for Experimental Parasitology, Department of Veterinary Pathobiology, Faculty of Life Sciences, University of Copenhagen, Bülowsvej 17, DK-1870 Frederiksberg C, Denmark. [11]Greenland National Museum and Archives, 3900 Nuuk, Greenland. [12]Natural History Museum of Denmark, Geologisk Museum, Øster Voldgade 5-7, DK-1350 Copenhagen, Denmark.

*Present address: Ilaqutariinnermut Pitsaaliuinermullu Aqutsisoqarfik/Family and Prevention Agency, PAARISA, Box 1160, 3900 Nuuk, Greenland.

†To whom correspondence should be addressed. E-mail: ewillerslev@bi.ku.dk

The absence of the D2 haplotype in modern European populations and Greenlandic Inuit populations (the excavation team was composed of local Inuit and Danish archaeologists) suggests that the result was not explainable by contamination at the excavation site (fig. S2). We thus sequenced the complete ancient human mtDNA genome.

Large amounts of contaminant-free mtDNA have been recovered from mammoth hair shafts by using the FLX sequencing-by-synthesis platform (Roche, Basel, Switzerland) (*15*). A preliminary trial on 0.1 g of modern human hair shafts confirmed the cross-applicability of the method and yielded DNA sequences that were 2.18% mtDNA (*2*). We applied this method to an extract of 0.1 g of the Saqqaq hair sample (*2*), resulting in ≈0.2% mtDNA (table S4). Variation in mtDNA sequence frequency among extracts (within single species) is consistent with the mammoth data of a previous study (*15*) in which mtDNA yields varied between 0.3 to 2.09%. This variability might be due to intra-individual differences in hair keratinocyte formation, variation in hair types, or even the age or health of the individual.

Our assembly of the near-complete mtDNA genome had about 10.7× coverage, and all Hg-diagnostic SNPs sequenced confirmed the D2 assignment, further supporting a lack of contamination (*2*) (table S7). Although contamination of ancient human samples is a routine problem for studies that use bone or tooth as a substrate, this finding is unsurprising given previous reports on the ease with which keratinous materials can be decontaminated (*2*, *7*, *14*, *15*). In total, 176,520 base pairs (bp) of mtDNA were sequenced from the Saqqaq DNA library (*2*) (tables S4 and S5). There was a large variation around the mean contig length because several expected short fragments were not sequenced at all, and one fragment in the HVS1 region exhibited 93× coverage. To ensure the accuracy of the FLX approach, we resequenced 18 short regions that had <fourfold coverage by using conventional methods (*2*) (tables S1 and S7). These data were consistent with the FLX-generated sequence (*2*) (table S7).

The Saqqaq complete mtDNA genome differs from the revised Cambridge Reference Sequence [the mtDNA genome routinely used to compare mtDNA sequences (*16*)] at 40 SNPs and has a novel and likely heteroplasmic site at n. p. 11,234 (*2*) (table S7). The random sequencing process used by the FLX platform renders contamination with nuclear mitochondrial copies statistically unlikely (*15*). However, to rule out the possibility of laboratory contamination, four SNPs characteristic to Hg D2 were retyped from an independent extraction by using conventional PCR and pyrosequencing in a second laboratory (*2*) (table S6). These data were fully consistent with the FLX reads (*2*). Lastly, we note that we detected no significant level of contaminant or mosaic sequence variation at any of the phylogenetically important SNPs. The variation detected at a minority of the SNPs can be explained as DNA damage (*2*) (table S7).

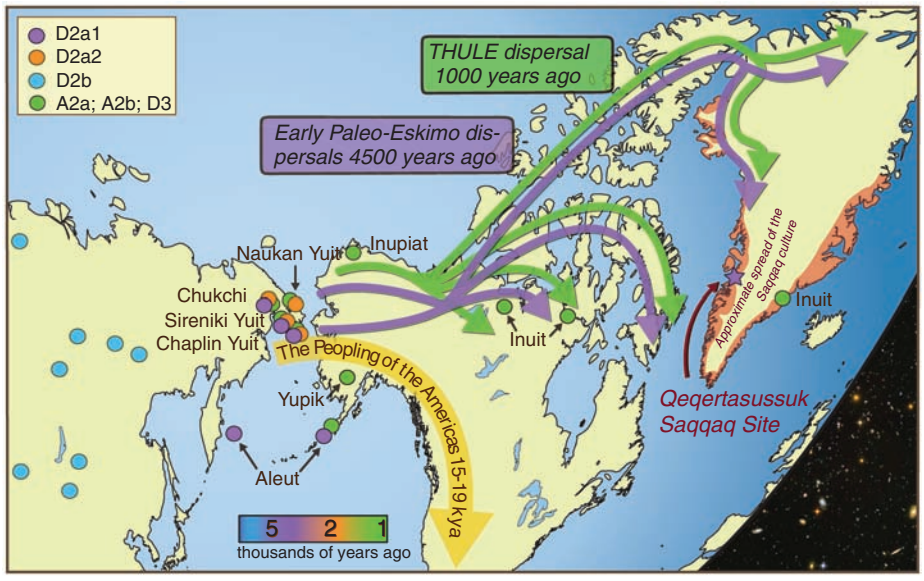

Fig. 1. Sequential waves of human dispersals into the northern extremes of the New World. For clarity, the dispersal that brought the Dorset culture is omitted. Shown are the approximate geographic distribution of contemporary Neo-Eskimo populations, location of the Qeqertasussuk archaeological Paleo-Eskimo (Saqqaq culture) site, and distribution of related extant mtDNA haplogroups. The timing of the initial peopling of the Americas, which did not reach the northern extremes, is shown as estimated by two recent studies (*17*, *18*). kya, thousands of years ago.

Over 300 complete mtDNA genome sequences are available that derive from Native American populations (*17*–*19*) and their close relatives in northeast Asia (*20*, *21*). These data sets do not, however, include any Neo-Eskimos. We therefore generated 14 complete mtDNA genomes from contemporary Greenlandic Inuit, yielding 4 Hg A2a and 10 Hg A2b mitotypes (*2*) (table S8 and fig. S2). The complete mtDNA genome data indicate that the Saqqaq sample is distinct from modern and ancient Neo-Eskimos (*3*–*7*). Diagnostic SNPs (at n.p. 3010, 3316, 7493, 8414, 8703, 9536, 9667, 11,215, 11,959, 14,668, 16,129, and 16,271) within the Saqqaq mtDNA genome refine the samples' placement within Hg D to Hg D2a1 (Fig. 2 and fig. S2). The sample is closely related to D2a1a, a common mtDNA haplogroup found among Aleuts, in particular those of the Commander islands (*20*), who are descendents of a forced colonization of the Medny and Bering islands in the mid-19th century (*22*). The sample is also closely related to a subset of the Siberian Sireniki Yuit (Eskimos) (Figs. 1 and 2 and fig. S2) (*23*). However, the Saqqaq sequence is unique and does not share specific mutations with these groups (n.p. 8910 for D2a1a and n.p.s 16,111 and 16,366 for D2a1b), but rather branches off of the root of D2a1 on the basis of two homoplasmic (n.p.s 14,226 and 16,092) and the putatively heteroplasmic (n.p. 11,234) private mutations (Fig. 2 and fig. S2).

On the basis of the contemporary Sireniki Yuit and Aleutian mtDNA data, the coalescence of the D2a1 clade was estimated to 2000 ± 3400 years ago (±SE) with use of the synonymous transition clock (*24*) or 7500 ± 4500 years when the clock is calibrated over all coding region sites (*25*). These broadly bracket the age of the sample and the Saqqaq presence in Greenland. The high variance around the molecular date of D2a1 derives from the fact that Aleutian and Sireniki samples come from populations with extremely small effective population sizes and reflects the coalescence of only two independent lineages. For comparison, the complete sequence-based founder age [following the approach of (*4*)] of the modern A2a1 and A2b1 variants in Greenland, where both clades separately yield older coalescent times (fig. S2) and are commonly shared among the Aleutian and Canadian Native Indians (*5*, *26*), is 970 (± 970) years. This is consistent with the hypothesis of a more recent origin and spread of the Neo-Eskimo Thule culture.

In contrast to the geographic spread of the related D2a2 sequences observed in Siberian Yuit, Aleutians, and Chukchi and the D2b sequences that are distributed across a wide territory stretching from Lower Yenissey to northeast China (*17*, *20*, *21*, *23*), the geographic distribution of modern D2a1 types is restricted to the Bering Strait region (Fig. 1). Furthermore, Hg D2 derives from an Asian-specific Hg D4e and not from any of the five Native American founding Hgs (A2, B2, C1, D1, and X) [for example, (*17*–*19*)]. Neither do the Neo-Eskimo Hgs A2a, A2b, and D3 (fig. S2) derive from this Beringian mtDNA type found by us also in the Paleo-Eskimo hair sample. This result suggests that the migrations that first lead human populations to colonize the far north of the New World (and subsequently Greenland) originated neither from the Native American populations that had been present in the

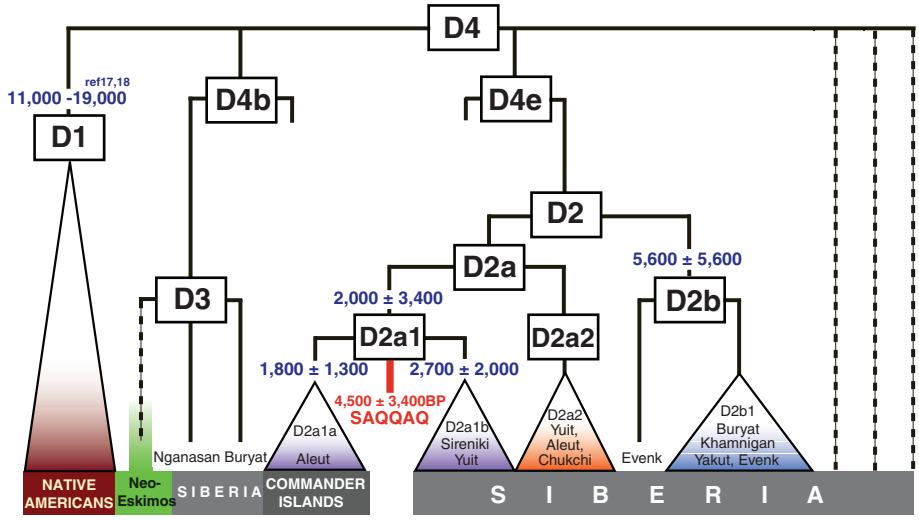

Fig. 2. Schematic tree of mtDNA haplogroup D4 variation in Siberia and the New World, showing the Saqqaq sequence in relation to modern populations. Solid branches of the tree are supported by mtDNA complete sequence evidence; dashed lines refer to lineages defined by partial sequences. Complete previously published genomes derive from studies (*17*, *20*, *21*, *23*). The ^{14}C-derived age bracket of the Saqqaq material is shown in red, and mtDNA coalescent time estimates (based on variation at synonymous sites) are shown in blue near their respective clades.

Americas from at least 14,350 calendar years ago (*27*, *28*) nor from the populations that gave rise to the later Neo-Eskimo expansion from Alaska around 1000 years ago.

Unfortunately, the genetic relationship between the matrilineal carriers of the Saqqaq and the intermediate Dorset culture is still unresolved because the Dorset remains that were previously studied have so far only been identified to Hg D in general (*9*, *10*). Whether the Dorset samples belong to Hg D3, as characteristic of some Neo-Eskimos, D2a1 such as the Saqqaq sample, or even to an alternative branch remains to be determined.

Our conclusions have their basis in the analysis of a single Saqqaq Palaeo-Eskimo mtDNA genomic sequence in a rich phylogeographic context of Native American, Beringian, and Siberian pools of mtDNA. In particular, they show that, in accordance with archaeological evidence, the Saqqaq are not descended from Native Americans and that there appears to be a matrilineal discontinuity between the Saqqaq and the Neo-Eskimos (*29*–*31*). We would be remiss, however, were we not careful to stress that only further efforts in analyzing ancient DNA may tell us whether the found discontinuity results from their different Siberian and Beringian origins or is caused by the loss of the "Saqqaq lineage" in gene pools of the Neo-Eskimos and/or Native Americans due to demographic events like random genetic drift.

References and Notes

1. D. E. Damas, in *Handbook of North American Indians, Vol. 5: Arctic*, D. Damas, Ed. (Smithsonian Institution, Washington, DC, 1984), pp. 72–79.
2. Materials and methods are available on *Science* Online.
3. G. F. Shields *et al.*, *Am. J. Hum. Genet.* **53**, 549 (1993).
4. J. Saillard *et al.*, *Am. J. Hum. Genet.* **67**, 718 (2000).
5. A. Helgason *et al.*, *Am. J. Phys. Anthropol.* **130**, 123 (2006).
6. M. H. Crawford, *Am. J. Hum. Biol.* **19**, 203 (2007).
7. M. T. P. Gilbert *et al.*, *Am. J. Phys. Anthropol.* **133**, 847 (2007).
8. R. McGhee, in *Identities and Cultural Contacts in the Arctic*, M. Appelt, J. Berglund, H. C. Gullov, Eds. (Danish Polar Center, Copenhagen, 2000), pp. 181–191.
9. M. G. Hayes, J. B. Coltrain, D. H. O'Rourke, in *Mummies in a New Millennium: Proceedings of the 4th World Congress on Mummy Studies*, N. Lynnerup, C. Andreasen, J. Berglund, Eds. (Danish Polar Center, Copenhagen, 2003), pp. 125–128.
10. M. G. Hayes, J. B. Coltrain, D. H. O'Rourke, in *Contributions to the Study of the Dorset Palaeo-Eskimos*, P. Sutherland, Ed. (Canadian Museum of Civilization, Mercury Series, Hull, Canada, 2005), pp. 11–32.
11. B. Grønnow, in *Threads of Arctic Prehistory: Papers in Honour of William E. Taylor Jr.*, D. Morrison, J. L. Pilon, Eds. (Canadian Museum of Civilization, Mercury Series, Hull, Canada, 1994), pp. 197–23.
12. M. Meldgaard, *Ancient Harp Seal Hunters of Disko Bay: Subsistence and Settlement at the Saqqaq Culture Site Qeqertasussuk (2400-1400 BC), West Greenland*, vol. 30 of *Meddelelser om Grønland: Man and Society* (Danish Polar Center, Copenhagen, 2004).
13. B. Koch, Frølich, N. Lynnerup, J. P. H. Hansen, in *The Paleo-Eskimo Cultures of Greenland: New Perspectives in Greenlandic Archaeology*, B. Grønnow, J. Pind, Eds. (Danish Polar Center, Copenhagen, 1996), pp. 3–38.
14. M. T. P. Gilbert *et al.*, *Curr. Biol.* **14**, R463 (2004).
15. M. T. P. Gilbert *et al.*, *Science* **317**, 1927 (2007).
16. R. M. Andrews *et al.*, *Nat. Genet.* **23**, 147 (1999).
17. E. Tamm *et al.*, *PLoS One* **2**, e829 (2007).
18. A. Achilli *et al.*, *PLoS One* **3**, e1764 (2008).
19. N. J. R. Fagundes *et al.*, *Am. J. Hum. Genet.* **82**, 583 (2008).
20. O. A. Derbeneva *et al.*, *Am. J. Hum. Genet.* **71**, 415 (2002).
21. M. Derenko *et al.*, *Am. J. Hum. Genet.* **81**, 1025 (2007).
22. M. Zlojutro *et al.*, *Am. J. Phys. Anthropol.* **129**, 446 (2006).
23. E. B. Starikovskaya *et al.*, *Ann. Hum. Genet.* **69**, 67 (2005).
24. T. Kivisild *et al.*, *Genetics* **172**, 373 (2006).
25. D. Mishmar *et al.*, *Proc. Natl. Acad. Sci. U.S.A.* **100**, 171 (2003).
26. R. Rubicz *et al.*, *Hum. Biol.* **75**, 809 (2003).
27. T. Goebel, M. R. Waters, D. H. O'Rourke, *Science* **319**, 1497 (2008).
28. M. T. P. Gilbert *et al.*, *Science* **320**, 786 (2008); published online 3 April 2008 (10.1126/science.1154116).
29. R. McGhee, *Ancient People of the Arctic* (Univ. of British Columbia Press, Vancouver, Canada, 1996).
30. M. Appelt, H. C. Gulløv, *Late Dorset in High Arctic Greenland: Final Report on the Gateway to Greenland Project* (Danish Polar Center, Copenhagen, 1999).
31. P. Schledermann, *Crossroads to Greenland: 3000 Years of Prehistory in the Eastern High Arctic* (Arctic Institute of North America, Calgary, Canada, 1990).

32. We thank the Danish Natural Science Research Council (M.T.P.G. and E.W.), the Danish National Research Foundation (M.R., E.A., and E.W.), Genetime, a Marie Curie training site (P.F.C. and E.W.), the Swedish Collegium of Advanced Studies (R.V.), and the Estonian Research Council (R.V., E.M., M.R., E.T., and M.M.) for financial support. Data are deposited as accessions EU725607 to EU725621 in GenBank.

Supporting Online Material

www.sciencemag.org/cgi/content/full/1159750/DC1
Materials and Methods
Figs. S1 to S2
Tables S1 to S9
References
Database S1

28 April 2008; accepted 20 May 2008
Published online 29 May 2008;
10.1126/science.1159750
Include this information when citing this paper.

New Products

FTIR Spectrometer

Exoscan is a small, compact Fourier transform infrared (FTIR) spectrometer designed to move spectroscopy out of the laboratory and into the field. The innovative analyzer can perform nondestructive on-site surface and bulk analysis applications. Weighing less than seven pounds, the Exoscan is easy to use and features analytical performance that rivals larger and more expensive traditional FTIR spectrometers. It is also capable of handling attenuated total reflectance applications. It can be powered by a rechargeable lithium ion battery or AC power and can sample from a wide variety of materials including solids, pastes, gels, and liquids.

A2 Technologies
For information 203-312-1106
www.a2technologies.com

Protein Characterization and Purification Columns

The Jupiter 3 μm C18 300 Å high-performance liquid chromatography columns are for protein characterization and purification. Jupiter 3 μm C18 columns fully resolve posttranslational modifications and are suitable for research on proteins such as cytochrome C, insulin, and β-lactoglobulin. All Jupiter 300 columns feature extended pH stability ensured by extensive testing and quality control documentation. Jupiter's bonding and silica technology provide scalability from analytical and preparative media to bulk material.
Phenomenex
For information 310-212-0555
www.phenomenex.com

High-Resolution Liquid Chromatography

The Series 275 HRes Liquid Chromatography (LC) System provides the opportunity to increase throughput and improve resolution using small particle–size column technology at ultrahigh pressure ranges. The system is designed to support quality control in the food and beverage, environmental, pharmaceutical, and materials testing markets. The system's new Brownlee HRes LC Column technology features newly developed small particles for high resolution and speed of separation. The system also includes the Series 275 Autosampler, which allows for automation and repeatability in the critical injection phase. A new Series 275 Binary Micro Pump supports the small particle/high resolution LC columns.
PerkinElmer
For information 781-663-6900
www.perkinelmer.com

Redesigned Nylon Filter

The Nylon Net Steriflip filter unit is a disposable, sterile filtration system used in the preparation of tissue culture media, buffers, microbiological media, and other aqueous solutions. The device features a new, streamlined design that provides easier cell manipulation and optimal performance in a variety of applications. This new nylon mesh version enables faster separation of large volumes of cellular material to improve recovery and lessen the time to collect isolated cells. Four mesh sizes allow for optimal performance in stem cell, cardiomyocyte, neurological, and skeletal tissue applications. The new Nylon Net Steriflip device is available in 20 μm, 40 μm, 60 μm, and 100 μm sizes. Steriflip devices are vacuum assisted, closed systems that ensure sample sterility.
Millipore
For information 800-548-7853
www.millipore.com

Automated Cell Culture

MACCS is an automated cell culture system that offers a cost-effective solution in a variety of applications, including the uniform supply of cells and proteins for drug discovery research efforts. The system offers a modular, expandable design with the ability to work with labware, including Roboflasks, T-flasks, shaker and spinner flasks, microtiter plates, and roller bottles. Online cell monitoring ensures consistent cell supply. Vaporized hydrogen peroxide sterilization and high efficiency particulate air filtration ensure a continuously sterile environment. A six-axis robotic arm provides high throughput, reliability, and sophisticated motion control for gentle processing of cell cultures.
MatriCal
For information 509-343-6225
www.matrical.com

Spectrophotometer

NanoVue is a sensitive ultraviolet/visible light spectrophotometer that accurately quantifies DNA, RNA, oligonucleotide, and protein samples in under five seconds. NanoVue's measurement speed is due to the system's proprietary "drop-and-measure" hydrophobic sample plate and user-friendly built-in software. NanoVue does not require a computer and users can select predefined methods or create their own directly from the system's display. The instrument's sensitivity enables measurements of sample volumes as low as 0.5 μl. The system eliminates the use of cuvettes or capillaries and is easy to clean, reducing the risk of contamination. Other features include up to 90 user-defined methods, an optional built-in printer or data output via USB, optional wireless connectivity, and a small footprint.
GE Healthcare
For information 262-501-0777
www.gehealthcare.com

Electronically submit your new product description or product literature information! Go to **www.sciencemag.org/products/newproducts.dtl** for more information.

Newly offered instrumentation, apparatus, and laboratory materials of interest to researchers in all disciplines in academic, industrial, and governmental organizations are featured in this space. Emphasis is given to purpose, chief characteristics, and availabilty of products and materials. Endorsement by *Science* or AAAS of any products or materials mentioned is not implied. Additional information may be obtained from the manufacturer or supplier.

POSITIONS OPEN

The U.S. Department of Energy, Office of Science, Office of Biological and Environmental Research (BER) is seeking a **DIRECTOR** for the Life and Medical Sciences Division. BER leads basic research supporting the energy and environmental missions of the Department of Energy. The Life and Medical Sciences Division supports research in genomics, proteomics, structural biology, plant biology, microbiology, radiation biology, radiochemistry, and development of advanced imaging instrumentation. The Division also supports the state-of-the-art Joint Genome Institute/Productions Genomics Facility for high throughput DNA sequencing and genomic analysis of environmental microbes and plants. The Director leads a group of 16 program managers and support staff with a budget of over $250 million. The Director is also responsible for the Genomes to Life: Bioenergy Research Centers which are playing a leadership role in scientific innovation for sustainable bioenergy. The Director is involved in strategic planning, multiyear program planning and implementation, and budgeting. The Director is a member of the Senior Executive Service, with a salary range of $114,468 to $158,500. For further information about this position and the instructions on how to apply and submit an application, please go to **website: http://jobsearch.usajobs.gov/getjob.asp?JobID=72095987&AVSDM=2008%2D05%2D23+06%3A52%3A04&Logo=0&lid=456&FedEmp=N&sort=rv&vw=b&brd=3876&ss=0&jbf565=1&FedPub=Y&caller=/ses.asp&SUBMIT1.x=48&SUBMIT1.y=18**. It is imperative that you follow the instructions as stated on the announcement SES-SC-HQ-022 (cg). To be considered for this position, you must apply online and submit a copy of your college transcripts to meet the positive education requirement. This announcement closes on July 22, 2008.

FACULTY POSITIONS at the UNIVERSITY of VIRGINIA

The Department of Pharmacology **(website: http://www.healthsystem.virginia.edu/internet/pharmacology/)** is seeking to fill two positions at the **ASSISTANT/ASSOCIATE/FULL PROFESSOR** level. Individuals conducting original research in the general area of obesity/diabetes including central control of appetite, lipid metabolism, et cetera are invited to apply. The successful applicant will be provided with a substantial startup package, including laboratory space within the Pharmacology Department and access to state-of-the-art core facilities. A doctoral degree in pharmacology, physiology, chemistry, biochemistry, medicine, or related discipline with at least two years of postdoctoral training and evidence of significant research productivity is required. To apply send curriculum vitae, a two-page research plan, and names and addresses of at least three references (including e-mail address and telephone number) to: **Pharmacology Search Committee, Department of Pharmacology, University of Virginia, P.O. Box 800735, Charlottesville, VA 22908-0735 (e-mail: pharmsearch@virginia.edu).** Review of applications will begin July 15, 2008; however, the positions will remain open until filled. *The University of Virginia is an Equal Opportunity/Affirmative Action Employer.*

FORMULATION CHEMIST needed with two years of experience to develop bioavailable efficacious and stable formulations. Prep stability protocols. Prep and review standard operating procedures. Install, validate (installation qualification/operational qualification), and maintain equipment under current good manufacturing practice. Use capsule filler, tablet press, hi-shear granulator, fluid bed dryer, tablet coater, disintegration, and friability tester. Send resumes to: **QS Pharma LLC, 3 Chelsea Parkway, Suite 305, Boothwyn, PA 19061.** Job location: Boothwyn, Pennsylvania.

POSITIONS OPEN

VCU

POSTDOCTORAL RESEARCH POSITION
Functional Analysis of a Novel Cancer-Specific Apoptosis-Inducing Cytokine

A Postdoctoral position is open for a talented scientist to be part of a project studying structure, function, and translational applications of an apoptosis-inducing cytokine mda-7/IL-24. A Ph.D. with strong background in molecular and cellular biology, virology, gene therapy, and immunology is required. Candidate with expertise in analyzing apoptosis, nude mouse xenograft studies, and transgenic animal models of cancer preferred. Applications with curriculum vitae and names of three references to: **Dr. Paul B. Fisher, Professor and Chair, Department of Human and Molecular Genetics, Director, VCU Institute of Molecular Medicine, Virginia Commonwealth University, School of Medicine, Richmond, VA; e-mails: pbfisher@vcu.edu** and **ldownes@vcu.edu.**

ASSISTANT or ASSOCIATE PROFESSOR in HUMAN GENETICS TENURE-TRACK POSITION

The University of Tennessee Health Science Center Clinical and Translational Science Institute and the Department of Preventive Medicine seek a full-time, tenure-track **ASSISTANT or ASSOCIATE PROFESSOR** in human genetics. Requirements for the position include an M.D. or Ph.D. degree with demonstrated research expertise in human genetics, genetics, molecular biology, or related discipline, and an established track record in human genetics research. Candidates with an active laboratory research program in the areas of human genomics, human genetic epidemiology, and systems biology of human disease are especially encouraged to apply. Additional information is available at **website: http://www.utmem.edu/CTSI/.** Interested applicants should submit a copy of curriculum vitae, a cover letter describing research interests and teaching experience, and names and addresses of three references to: **Julia Krushkal, Ph.D., Chair of the Human Geneticist Search Committee, Department of Preventive Medicine, The University of Tennessee Health Science Center, 66 North Pauline, Suite 633, Memphis, TN 38163. E-mail: jkrushka@utmem.edu.** *The University of Tennessee Health Science Center is an Equal Opportunity/Affirmative Action Employer.*

OPPORTUNITY in AQUATIC and MARINE ENVIROMENTAL MODELING
United States Army Engineer Research and Development Center

The Environmental Laboratory of the U.S. Army Engineer Research and Development Center, Vicksburg, Mississippi, is seeking an individual with expertise in modeling aquatic and marine environmental systems. Candidates should have a Ph.D. in environmental science, engineering, or related field and should be capable of applying multidimensional, mass-conservation based models that incorporate aspects of aquatic physics, chemistry, and biology. This position provides opportunity to work with established experts in the field and to collaborate with specialists in other fields to develop solutions to complex environmental issues of national and international importance. *U.S. citizenship is required.* This is a full-time, permanent DB04 position (GS12-GS14), and starting salary will depend on qualifications and experience. Candidates can send resume to **e-mail: pamela.k.corulla@usace.army.mil** or contact **Ms. Corulla** at **telephone: 601-634-3861.** *The U.S. Army Engineer Research and Development Center is an Equal Opportunity Employer.*

NIDDK | NATIONAL INSTITUTE OF DIABETES AND DIGESTIVE AND KIDNEY DISEASES

New Research Initiative – Fatty Liver Disease & Obesity - Tenure Track Position

The Liver Diseases Branch of the National Institute of Diabetes and Digestive and Kidney Diseases (NIDDK), National Institutes of Health (NIH) invites applications for one tenure track position from scientists interested in basic and/or clinical research involving non-alcoholic fatty liver disease and metabolic syndrome. Specific areas of research interest include pathogenesis and mechanism of metabolic derangement in non-alcoholic fatty liver disease and its pathophysiologic link to inflammation, insulin resistance, metabolic syndrome and obesity. Priority will be given to applicants at the Assistant Professor level in traditional universities or those finishing their post-doctoral/fellowship positions. The applicant must have a proven record of accomplishments and will be expected to propose and pursue an independent research program in one of these fields. The position offers unparalleled opportunities for interdisciplinary collaboration within NIDDK and throughout NIH.

The Liver Diseases Branch of NIDDK is located on the main intramural campus of the NIH in Bethesda, Maryland, a suburb of Washington, D.C.

Interested applicants should send a Curriculum Vitae and list of publications, copies of three major publications, a summary of research accomplishments, a plan for future research, and two letters of recommendation (preferred but not required) to **Ms. Michelle Whitley, Search Committee, Liver Diseases Branch, NIDDK, Building 10-9B16, NIH, Bethesda, MD, 20892-1800. Application deadline: September 15, 2008**.

National Institute of General Medical Sciences
National Institutes of Health
Department of Health and Human Services

The National Institute of General Medical Sciences (NIGMS) in Bethesda, Maryland is seeking applications from outstanding candidates with a strong background in clinical genetics/genomics for a Medical Officer position in the Division of Genetics and Developmental Biology. The Division, which primarily supports basic research and research training, has an interest in expanding its support for research on the genetics/genomics of complex human phenotypes.

The incumbent for this position will be responsible for developing and managing a portfolio of research grants that emphasizes the application of genetic and genomic data to understand the biological basis of normal human phenotypes and genetic disorders. Candidates must have clinical genetics experience and a broad background in genetics/genomics, as well as specialized experience in one or more of the following areas: DNA replication, mutagenesis, and repair, regulation of gene expression, physiology, computational/systems biology, or related areas.

Applicants must possess an M.D. or Doctor of Osteopathy degree, clinical genetics experience, independent research experience, and knowledge of the NIH peer review and grants process.

Salary is commensurate with qualifications, and includes a full package of benefits. A detailed vacancy announcement **(NIGMS-08-266255-DH)** with the mandatory qualifications and application procedures can be obtained via the NIGMS web page at **http://www.nigms.nih.gov/about/job_vacancies.html** and the USAJobs web page at **http://www.usajobs.opm.gov**. Questions on application procedures may be addressed to **Wendy Evans at (301) 594-2386**. Applications, and supporting documentation, must be received by close of business **07/01/2008**. The NIH is an equal opportunity employer.

The National Institutes of Health inspires public confidence in our science by maintaining high ethical principles. NIH employees are subject to Federal government-wide regulations and statutes as well as agency-specific regulations described at **http://ethics.od.nih.gov**. We encourage you to review this information.

National Cancer Institute

The Center for Cancer Research presents:

Chemical Insights into Biological Processes

August 15–16, 2008

Hood College, Frederick, MD

Organized by the Chemistry and Structural Biology Faculty

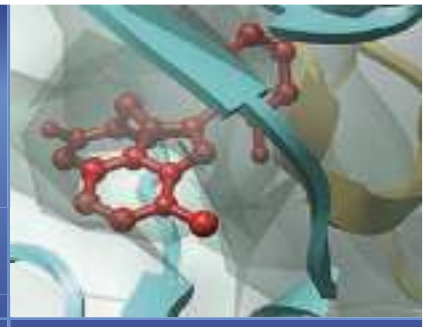

Invited Speakers Include:

Gregory L. Verdine, Ph.D.
Harvard University

Carolyn Bertozzi, Ph.D.
University of California, Berkeley

Benjamin F. Cravatt, III, Ph.D.
Skaggs Institute for Chemical Biology, Scripps Research Institute

Jon Clardy, Ph.D.
Harvard Medical School

Peter G. Schultz, Ph.D.
Scripps Research Institute

Angela Belcher, Ph.D.
Massachusetts Institute of Technology

James R. Heath, Ph.D.
California Institute of Technology

Laura L. Kiessling, Ph.D.
University of Wisconsin-Madison

Lawrence J. Marnett, Ph.D.
Vanderbilt Institute of Chemical Biology

Milan Mrksich, Ph.D.
University of Chicago

Alanna Schepartz, Ph.D.
Yale University

Mike E. Jung, Ph.D.
University of California, Los Angeles

Cynthia J. Burrows, Ph.D.
University of Utah

Moungi G. Bawendi, Ph.D.
Massachusetts Institute of Technology

Space is limited, so advance registration is required by August 1, 2008, at:

www.ncifcrf.gov/events/ccrcbs/2008

The deadline for poster abstract submissions is July 25, 2008.

NATIONAL INSTITUTES OF HEALTH · NATIONAL CANCER INSTITUTE

CENTER FOR CANCER RESEARCH

National Institute on Aging

Scientific Review Officer (Health Scientist Administrator)

The National Institute on Aging is seeking a Scientific Review Officer (Health Scientist Administrator) to organize meetings to conduct reviews of grant applications in areas of science of importance to aging, particularly in neuroscience and Alzheimer's disease research and/or behavioral science. Broad knowledge of principles, theories and practices related to the scientific fields of contemporary science is expected. Experience with peer review of health research grant applications is desirable. Candidates must possess doctorate level training or equivalent in one or more of the areas specified, independent research experience, and progressive responsibilities in research program administration.

The position is located in downtown Bethesda, MD, near the NIH campus, and is easily accessible by Metro. To apply and to review qualifications, evaluation criteria, application instructions, and salary and benefits information, please visit **http://jobsearch.usajobs.opm.gov/** and apply on-line to **Announcement Number: NIA-08-268007-CR-DE** (open to all U.S. citizens) and/or **NIA-08-268007-CR-MP** (open to current and former competitive service Federal employees). For additional information, call **Lauren Carroll Tedesco at (301) 594-2288**. Applications must be received by **July 18, 2008**.

The NIH Director's Wednesday Afternoon Lecture Series

Biomedical scientists around the world are invited to join us online to hear leading investigators present their latest results to the NIH Intramural Research community. Lectures may be viewed live at 3:00 p.m., EST (20:00 GMT) on Wednesdays, from September through June. Live webcasts can be viewed under "Today's Events" at: <http://videocast.nih.gov/>

The Director's Lecture Series has terminated for the summer and will resume on September 3, 2008.

All past lectures are archived and is available for viewing at <http://videocast.nih.gov/>, Past Events, Wednesday Afternoon Lectures.

Immunology Editor for *Science*

Science is seeking a full-time Associate Editor in the biological sciences to work in our Washington, DC, USA or Cambridge, UK office. We are looking for an exceptional life scientist with broad interests, a lively curiosity, and experience with cutting-edge research in immunology, with additional knowledge of at least one other area of biomedicine. Responsibilities include managing the review, selection, and editing of manuscripts, working with authors on revisions, soliciting reviews and special issues, and fostering contacts and communication with the scientific community. The ability to work constructively as a member of a team is necessary, but previous editorial experience is not a prerequisite. Candidates are expected to travel to scientific meetings.

For this position, we require a Ph.D. in immunology plus postdoctoral experience and multiple publications.

Science is published by the AAAS, the world's largest multidisciplinary scientific membership organization. Visit us at **www.aaas.org**.

For consideration send a cover letter and resume, along with your salary requirements, to:

AAAS
Human Resources Office, Suite 101
1200 New York Ave., NW
Washington, DC 20005
Or by email to: **jobs@aaas.org**
Or by fax to: **202-682-1630**

EOE. Nonsmoking work environment.

www.uni-frankfurt.de

GOETHE UNIVERSITÄT FRANKFURT AM MAIN

Goethe University Frankfurt, Department of Computer Science and Mathematics, invites applications for the following position:

Full Professorship (W3) for Bioinformatics

with an Emphasis on Simulation of Biological Systems

Applicants shall have a strong track record in development of methods in the application area systems biology/in silico methods. The successful candidate will be also member of the Department of Biological Sciences.
The designated salary for the position is based on „W" on the German university scale or equivalent. The Goethe University is committed to a pluralistic campus community through affirmative action and equal opportunity. For details see: www.unifrankfurt.de/aktuelles/ausschreibung/professuren/index.html.

Applications accompanied by the usual information (CV, degrees and certificates, list of publications, details on teaching and international experience, information on successful grant applications), should be sent within **four weeks** of publication of this announcement to: **Goethe University Frankfurt, Dean of the Department of Computer Science and Mathematics, E-Mail: dekan@fb12.uni-frankfurt.de.**

OPPORTUNITY FOR SCIENTISTS OF INDIAN ORIGIN

GOVERNMENT OF INDIA
MINISTRY OF SCIENCE & TECHNOLOGY, DEPARTMENT OF BIOTECHNOLOGY
"RAMALINGASWAMI FELLOWSHIP"

Applications are invited for **"Ramalingaswami Fellowship",** a re-entry scheme of the Department of Biotechnology, Ministry of Science & Technology, Govt. of India.

Objective
1. The scheme is aimed at bringing back scientists of Indian origin working out side the country in various fields of biotechnology, including agriculture, health sciences, bio-engineering, energy, environment, bioinformatics and all other related areas, and who are desirous of pursuing R&D in an Indian institution.

Eligibility
2. The applicant should possess a higher degree, such as Ph. D, MD or equivalent with an outstanding track record reflected in publications and other recognitions.
3. Only candidates of Indian origin working overseas are eligible to apply. Those who have already returned to India and are working in India are not eligible.

About the fellowship
4. Each awardee will receive the following: (a) consolidated fellowship amount of Rs. 50,000/ pm for the first three years and Rs. 60,000/pm for the next two years; and (b) contingency grant of Rs. 5.00 lakhs/ year for one or more of the following: purchase of consumables, minor equipment, international and/or domestic travel, engaging manpower and other contingent expenditure to be incurred in connection with his or her research project. However, the institute / university where the applicant proposes to work may consider giving additional benefits (such as house rent allowance /housing, medical expenses, leave travel allowance and other benefits) as applicable to regular faculty. This may be directly taken up by the applicants with the Indian institution that proposes to host them.

Duration
5. The duration of the fellowship will be for a period of five years.

Other
6. Each awardee is expected to submit an annual progress report highlighting major achievements during the preceeding year in which fellowship was awarded (1st April - 31st March) & will end the following March.
7. The Ramalingaswami Fellowship cannot be availed along with a regular salary. In case the awardee finds a job either before or during the tenure of the fellowship, either the fellowship or the salary can be availed at one and the same time. However, the contingency grant can be availed with the salary after obtaining due permission from DBT.
8. Application should be routed through the Indian Institution where the awardee wishes to avail the fellowship.
The application alongwith separate summary sheets (10 copies) duly forwarded by the competent authority may be sent to **Dr. Meenakshi Munshi, Joint Director, Department of Biotechnology, Block-2, 7th Floor, CGO Complex, Lodhi Road, New Delhi -110 003, Email :- meenakshi29.dbt@nic.in** latest by **31st July, 2008** as per prescribed format (available on DBT website: www.dbtindia.gov.in)

UNIVERSITY OF MINNESOTA

3M Harry Heltzer Multidisciplinary Chair in Science and Technology

The Graduate School and the Institute of Technology at the University of Minnesota-Twin Cities invites applications and nominations for the position of 3M Harry Heltzer Multidisciplinary Chair in Science and Technology. This is a tenured endowed position at the rank of associate or full professor (dependent upon qualifications/experience) in the area of physical and biological structures characterization utilizing microscopy and imaging. Candidates must have distinguished academic and research record in this area, with several years of successful research and teaching experience. A Ph.D. degree and dedication to teaching, graduate student advising, and regular and sustained interaction with industry are required. Candidates are sought whose research agenda will contribute to building cross-disciplinary and cross-college collaboration in one or more areas of strategic importance university-wide, including within the Institute of Technology and with other units at the University of Minnesota. This endowed chair is intended to foster industry-university research interaction and collaboration while advancing scientific and technological expertise in new frontiers of knowledge relevant to the Institute of Technology and 3M. Candidates with a background in any relevant areas of science or engineering are encouraged to apply. Department affiliation will depend on the candidate's area of expertise, with the possibility of a joint appointment with one or more units in the University.

Applications should be submitted online at: **https://employment.umn.edu**, under Req. **#154636**, and include a cover letter, curriculum vitae (including list of publications), research description/plan, statement of teaching interest, and contact information for three references. Review of applications will begin **June 1, 2008**, and continue until the position is filled. For further information, contact **Douglas Ernie** at **ernie@umn.edu**.

The University of Minnesota is an Equal Opportunity Employer.

Alberta
CANCER BOARD

ENDOWED CHAIR IN BREAST CANCER RESEARCH

The Alberta Cancer Research Institute is currently searching for a prominent breast cancer researcher to become "The Weekend to End Breast Cancer Research Chair".

This position provides the opportunities and infrastructure to collaborate with a diverse and vibrant research community to measurably impact the breast cancer burden. The successful applicant will promote breast cancer research across disciplines in the Alberta Cancer Board (**www.albertacancer.ca**) facilities, the University of Alberta (**www.ualberta.ca**) and University of Calgary (**www.ucalgary.ca**). The Alberta Cancer Research Institute's Weekend to End Breast Cancer Research Chair will give the recipient a unique opportunity to take a leadership role in enhancing the high quality clinical, basic and population health research in breast cancer in Alberta.

This successful applicant's program will build on existing strengths in Alberta breast cancer research, which include:

- A world-class provincial clinical research program spanning in-house studies, phase I through III intervention trials, and major involvement in breast cancer collaborative groups (NSABP, NCIC, SWOG, RTOG).
- An internationally recognized Provincial Cancer Registry and Population Health Research Unit providing statistical, administrative and research support.
- Multi-disciplinary teams of discovery researchers, translational researchers, epidemiologists and clinician scientists conducting metabolomic, proteomic, transcriptomic, stem cell, and molecular cancer epidemiology.
- World-class cell imaging, experimental animal and clinical radiological facilities.
- The Alberta Cancer Research Institute Biorepository.
- Unique provincial funding opportunities with the Alberta Cancer Research Institute and Alberta Cancer Foundation (**www.albertacancer.ca**), Alberta Heritage Foundation for Medical Research (**www.ahfmr.ab.ca**) and other agencies.

The location of the Chair's primary residence will either be in Calgary or Edmonton, Alberta, depending on the preference of the candidate and where the research interests of the candidate best fits. A relocation package is available for external candidates.

Applicants are asked to send their CV, a list of 3 references with contact information and a brief outline of their five-year research goals to the **Vice-President, Research, Alberta Cancer Board, Suite 1500, 10123 – 99 Street, Edmonton, Alberta, T5J 3H1**. The closing date for receipt of applications is **August 31, 2008**. Due to the collaborative nature of this initiative, an applicant's CV may be shared with other research and administrative leaders within the Alberta Cancer Research Institute. *EOE*

For full details and qualifications, please visit our website at
www.albertacancer.jobs

PENNSTATE
University Park

Immunologist, Professor or Associate Professor

Department of Veterinary & Biomedical Sciences in the College of Agricultural Sciences and The Huck Institutes of the Life Sciences at The Pennsylvania State University on the University Park campus is seeking an Immunologist at the level of Professor, although outstanding applicants at the Associate Professor level will be considered. Candidates will be expected to have developed and to maintain a vigorous national and internationally competitive externally funded research program in any area of Immunology. Applicants working in innate and adaptive immunity, or immune system-pathogen interactions, would complement current strengths at Penn State. The candidate will be expected to provide leadership in immunological research and actively participate in undergraduate and graduate teaching in the areas of immunology and infectious diseases. This position is part of a University-wide initiative to recruit at least a dozen new faculty positions in Immunology & Infectious Diseases. Successful candidates will have a unique opportunity to work in a dynamic interactive and collaborative environment with scientists with general interests in immunology and infectious disease in the Huck Institutes for the Life Sciences (http://www.huck.psu.edu/institutes-and-centers), in the Centers for Molecular Immunology & Infectious Disease, Infectious Disease Dynamics, Molecular Toxicology & Carcinogenesis, Gene Regulation, and the Institute for Genomics, Proteomics & Bioinformatics. Significant opportunities also exist for interactions with researchers in the physical and computing sciences, as well as with the Medical School at Hershey. Qualified applicants should possess a Ph.D., D.V.M/Ph.D, M.D./Ph.D. or equivalent degree. Significant start-up funds and a competitive salary will be available.

The Huck Institutes of the Life Sciences, College of Agricultural Sciences and The Department of Veterinary & Biomedical Sciences have taken a lead role in meeting new challenges in the basic sciences related to animal and human health by creating an environment that fosters excellence in research and teaching. The Department of Veterinary & Biomedical Sciences has a critical mass of faculty in the areas of immunology & infectious disease, toxicology, and animal health research. State-of-the-art core facilities exist for cell biology, genomics, proteomics and transgenic animal models that offer unique and diverse research experiences. (See http://www.vetsci.psu.edu for more information about the department.) Candidates should send a cover letter, curriculum vitae and contact information for at least three references by August 31, 2008 to receive full consideration, although applications will be accepted until the position is filled. Inquiries and applications (using .pdf files, please) should be sent to:

Avery August
Chair, Immunologist Search
Center for Molecular Immunology & Infectious Disease
Department of Veterinary & Biomedical Sciences
115 Henning Building
The Pennsylvania State University
University Park, PA 16802
Email: axa45@psu.edu

Penn State is committed to affirmative action, equal opportunity and the diversity of its workforce.

PENN STATE ***Making Life Better***

MONASH University

ARMI

Faculty Positions, Australian Regenerative Medicine Institute

About the Australian Regenerative Medicine Institute: Monash University, the Victorian State Government and the Australian Commonwealth Government are investing over $AUD150m in ARMI, a new research institute for regenerative medicine, focused on unraveling basic mechanisms of the regenerative process and developing clinical applications. The Institute will integrate research in three key platforms: structural biology (molecular level), cell biology (cell level) and regenerative biology (organism level). Working with multiple centres and disciplines at Monash University and the neighboring Australian Stem Cell Centre, the Institute will lay the groundwork for the development of future clinical applications, and will pursue rapid commercial transfer for its technologies.

ARMI is being established on the Monash University Clayton campus in Melbourne and is affiliated with the Faculty of Medicine, Nursing and Health Sciences. ARMI research groups will be located in new, state of the art laboratories with well-equipped common facilities creating a framework for a creative and highly interactive environment. The aim of this new initiative is to enhance the field of regenerative medicine by promoting the career opportunities for young scientists. As the headquarters of the EMBL Australia Partner Laboratory Network, ARMI will also include at least 6 junior groups operated according to the EMBL research model and philosophy.

About Monash University: Monash is a young, dynamic and internationally recognized university with an established reputation for providing excellence in biomedical research, training and education in campuses around the world. Its Melbourne-based campuses are affiliated with several excellent hospitals. The University is highly regarded for its innovative approach to teaching, research and learning and our graduates are sought after by employers from Australia and overseas. Monash is one prestigious Group of Eight universities which are Australia's leading research institutions.
The University is home to 100 research centres and is involved with 19 cooperative research centres. In addition, Monash has research links with more than 110 institutions throughout the world. Monash has built a strong international reputation in research especially in fields such as stem cell science, nanotechnology, reproductive biology, drug development and discovery. The Monash community includes more than 55,000 students from over 130 countries, over 6,000 full-time staff and an extensive network of more than 220,000 alumni. Monash has eight campuses, six in Australia, one in Malaysia and one in South Africa, as well a centre in Prato, Italy. Further details about Monash University can be found at **www.monash.edu.au**.

About the Positions: ARMI is now recruiting Faculty at the Associate Professor level or higher who wish to establish/relocate their research groups to new research facilities at Monash University. We seek dynamic, independent scientists with outstanding research track records, demonstrated experience in fields relevant to regeneration, and a desire to work in a multidisciplinary environment. We encourage applicants addressing fundamental questions in developmental and regenerative biology, utilising modern genetic and genomic approaches to apply. Successful candidates will bring a strong track record for attracting independent funding and are expected to initiate and maintain strong research programs synergising with the Monash research environment and to take active part in collaborative research. Positions are available from early 2009. The fixed appointments will normally be for five years with extension possible upon review.

Further details are available from:
Prof. Nadia Rosenthal, Director **nadia.rosenthal@armi.monash.edu.au**
Prof. Peter Currie, Deputy Director, **peter.currie@armi.monash.edu.au**
Silvio Tiziani, Chief Operating Officer, **silvio.tiziani@armi.monash.edu.au**
www.med.monash.edu.au/armi

To Apply: Applicants should submit an expression of interest to include a cover letter, curriculum vitae, a list of publications (indicating ten most significant publications), a concise description of research interests and statement of previous research achievements and teaching merits, a research plan (maximum 8 pages/ font 12), a financial plan, and a list of at least three reference persons, all in a .pdf binder. Your complete submission, referenced "ARMI Faculty" should be sent to **positions@armi.monash.edu.au** by August 31st 2008. **We look forward to receiving your application!**

USDA ARS Agricultural Research Service
www.ars.usda.gov

CENTER DIRECTOR
Salary Range $114,468 – 158,500 per annum

The U. S. Meat Animal Research Center (MARC) in Clay Center, Nebraska, operated by the USDA-ARS is the nation's premier federal research institution devoted solely to the management and improvement of the meat animal industry. We are seeking a highly qualified individual with an established record of scientific achievement and management experience to serve as Center Director. This is an excellent opportunity for the right person to provide leadership for an interdisciplinary scientific and support staff in addition to providing guidance and operational accountability for the Center's research programs. Current research being done at MARC is to develop new information and technology to increase the efficiency of livestock production for the benefit of consumers. The multidisciplinary and interdisciplinary research program includes research on genetics, breeding and molecular biology, food safety and meats science, animal health, nutrition, reproduction efficiency, life-cycle production systems, biological engineering and waste management. New knowledge evolving from these programs will contribute toward obtaining optimum resource use by the beef cattle, sheep, and swine industries, while limiting environmental impact. A degree in a field of science associated with animal biology or animal agriculture is required. Additionally, demonstrated knowledge of genetics and breeding, molecular biology, food safety, meat science, animal health, nutrition, reproduction, animal production systems, physiology, and biochemistry is required. A Ph.D. is highly desirable. Applicants must have excellent communication and interpersonal skills with a demonstrated ability to guide research programs and provide leadership while also maintaining a research program. This is a permanent, full-time position.

For application information and procedures, you may contact **Deborah Crump** at **(301) 504-1448** or via e-mail at **deborah.crump@ars.usda.gov**. For position information you may contact **Dr. W. H. Blackburn** at **(970) 492-7057** (or email at **Will.Blackburn@ars.usda.gov**). A full copy of the job announcement is available on ARS website **http://www.ars.usda.gov/careers/** Applications must be postmarked by **August 26, 2008**.

ARS is an Equal Opportunity Employer.

UNIVERSITY OF MINNESOTA

Institute for Translational Neuroscience
Translational Neuroscience Scholars Program
Multiple Faculty Positions in Neuroengineering

THE INSTITUTE FOR TRANSLATIONAL NEUROSCIENCE (ITN) at the University of Minnesota is seeking to fill up to five tenure-track or tenured positions to enhance its research strengths in neuroengineering. The Institute is interested in the study of mechanisms of neural systems using engineering methods, with these studies translating into potential clinical applications. Areas of specific interest include, but are not limited to, neural interfacing, neural prostheses, functional neural stimulation, and neural imaging.

SUCCESSFUL CANDIDATES will be affiliated with the newly established Center for Neuroengineering, and will have their tenure home in an academic department. Such candidates are expected to establish a vigorous, externally funded research program, have a genuine commitment to undergraduate and graduate education, and to collaborative program development.

REQUIREMENTS include an earned doctorate in an appropriate discipline at the time of the appointment and outstanding academic and research records. Rank and salary commensurate with qualifications and experience.

REVIEW OF APPLICATIONS starts immediately and will continue until positions are filled. Submit curriculum vitae, statement of research and teaching interests, and names of three references to **ITN Neuroengineering Faculty Search Committee at cne@umn.edu**. The applications should also be simultaneously registered with personal information on-line at **http://employment.umn.edu**. Tenure-track position applicants: use requisition **#153840**. Tenured position applicants: use requisition **#153815**.

The University of Minnesota is committed to diversifying its faculty and encourages applications from women and minorities. EOE.

RESEARCH ASSISTANT PROFESSOR

The Vascular Biology Center at the Medical College of Georgia is inviting applications from enthusiastic candidates, well trained in protein chemistry and molecular biology, for the position of Assistant Professor, non-tenure track. This is a unique opportunity for the right individual to devote 100% of his/her time in research, in a well-equipped laboratory, exploring the mechanisms of vascular actions of heat shock protein 90 inhibitors, as well as other topics of the candidate's interest related to vascular biology. Ample opportunities for collaboration exist and are encouraged. The successful candidate will have an earned Ph.D. degree, strong post-doctoral training, and will be encouraged to obtain his/her own extramural research funding and compete for available tenure-track positions.

E-mail applications, statement of research interest/career plans and three reference letters, by **July 26 2008** to: **Dr. John D. Catravas, jcatrava@mcg.edu**.

The Medical College of Georgia is an Equal Opportunity and Equal Access Institution; AA/EEO/Equal Access or AA/EEO/Equal Access/ADA Employer.

SOOCHOW UNIVERSITY

Faculty Positions at Orthopedic Research Institute First Affiliated Hospital, Suzhou, Jiangsu, China

The Orthopedic Department at the First Affiliated Hospital of Soochow University in Jiangsu Province is a leading center for orthopedic clinic and research, a national key subject. The University will create a new Orthopedic Research Institute and is seeking outstanding candidates for 5 faculty positions to work in the fields of **(1) molecular and cell biology of skeletal tissues, (2) biomaterials and bone tissue engineering, and (3) genetic studies on bone tumors**.

Candidates should have a Ph.D. and/or M.D. with extensive research experience, an outstanding record of publication in peer-reviewed journals, and demonstrated success in obtaining external funding. Appointments will be at the Associate Professor or Professor level depending on the seniority and experience of the successful candidate. Priority will be given to candidates who have the ability to develop independent research projects. Competitive salaries/benefits, generous start-up packages, and sufficient lab space will be provided.

Please send curriculum vitae, a statement of research interests and future plans, and a list of three references to: **Prof. Huilin Yang, The First Affiliated Hospital of Soochow University, 188 Shizi Street, Suzhou, China 215006, Tel: 86-512-6778-0101, Fax: 86-512-6778-0999, E-mail: suzhouspine@163.com**.

Shriners Hospitals for Children™

Postdoctoral Research Fellowships

Shriners Hospitals for Children is actively seeking outstanding postdoctoral researchers to join our team. Our research programs focus on inherited and acquired musculoskeletal diseases, burns, spinal cord injuries/neural repair, cleft lip and palate, and related topics. Additional information about our research programs can be found at: **http://www.shrinershq.org/Hospitals/_Hospitals_for_Children/Research/**.

Candidates with a Ph.D. or M.D. obtained during the last three years are eligible to apply. Candidates with more than three years of postdoctoral experience may be considered on a case-by-case basis. The fellowship program supports trainees for three years of research mentored by internationally renowned scientists at one of the eight Shriners Hospitals for Children Research Centers of Excellence. Salary, benefits, and resources are nationally competitive.

For further information and application instructions, please contact **Zakir H. Bengali, Ph.D.**, Vice President for Research, at **mlowery@shrinenet.org** or **813-281-8611.**

Closing date: **August 15, 2008**

"A One-of-a-Kind Pediatric Health Care System"

BOSTON UNIVERSITY

Associate Provost, Division of Graduate Medical Sciences Boston University Medical Campus

Boston University Medical Campus invites applications for the position of Associate Provost of the Division of Graduate Medical Sciences (DGMS), a flourishing unit that oversees PhD, MD/PhD and MA education, and other innovative educational programs.

The successful candidate will be:
- a leader in research and teaching
- committed to innovative, high quality graduate programs
- an outstanding administrator with financial skills
- collegial and collaborative, constructive and accessible
- concerned for achievement and quality of student experience

Review of applications will begin immediately and will continue until the position is filled. For additional information, visit: **http://www.bumc.bu.edu/gms**. To apply, submit a full CV and a statement of educational philosophy online at: **www.bumc.bu.edu/medapp/DGMSAssociateProvost** or by email to: **goldring@bu.edu**.

Boston University School of Medicine is an Equal Opportunity/Affirmative Action Employer.

MSSM MOUNT SINAI SCHOOL OF MEDICINE

Structural Biology or Biophysics

The Department of Structural and Chemical Biology at Mount Sinai School of Medicine invites applications for a tenure-track or tenured faculty position at the rank of Assistant, Associate or Full Professor in the areas of X-ray crystallography of membrane proteins or experimental single-molecule biophysics. We seek outstanding candidates with demonstrated excellence in the study of the role of proteins in human biology and disease.

The Mount Sinai School of Medicine offers a highly collaborative culture and provides excellent shared facilities for advanced structural biology and biophysical approaches. The successful candidate is expected to establish dynamic, independently funded research program and participate in graduate training at the interface between chemistry, biophysics and biology. Candidates must hold a PhD or MD/PhD degree and have a strong record of research accomplishments.

We offer a salary commensurate with experience and a competitive benefits package. Please submit a curriculum vitae, a brief statement of research interests and future plan, copies of 2-3 publications and three letters of reference (sent independently) to: **Faculty Search Committee, Mount Sinai School of Medicine, 1425 Madison Avenue, Box 1677, New York, NY 10029**, e-mail: **CSCB.search@mssm.edu**.

EOE

PEW Latin American FELLOWS PROGRAM in the BIOMEDICAL S·C·I·E·N·C·E·S

The Pew Latin American Fellows Program in the Biomedical Sciences provides support for young scientists from Latin America for post-doctoral training in the United States.

The nineteenth class of Fellows will be selected in 2009. An award of $60,000 will be provided as a salary stipend for the fellow during the period of training (two years) and will be administered by the sponsoring U.S. institution. The sponsoring institution is required to supplement the salary stipend with at least $5,000 a year and to provide full medical benefits for the fellow. Following the two-year fellowship, the Program will issue an additional $35,000 award to the sponsoring institution to purchase equipment and supplies for the fellow to establish a laboratory in his or her home country.

Applicants must have held a Ph.D. and/or M.D. degree, or equivalent, for no more than five years as of July 1, 2009. Applicants who received their degree from schools outside of Latin America, will not be accepted. Applicants may not have had previous post-doctoral training outside of Latin America, nor may they have begun a post-doctoral position in the U.S. prior to July 1, 2008. Applicants are not required to have a commitment of a position and laboratory space after the fellowship. However, applicants must submit a written statement of intent to return to Latin America. Fellows must accept a position and have confirmed laboratory space in Latin America by the end of the fellowship period in order to obtain the $35,000 portion of the award.

Fellows will be selected on the basis of their promise as outstanding investigators, as well as the scientific merit of their research proposal, their record of training and how well their interests coincide with the laboratory of their sponsor in the U.S. If potential applicants need assistance with the identification of an appropriate sponsoring laboratory in the U.S., they may contact the Program Office before August 1, 2008. The program will accept applications from Mexico, Central and South America. Applications may be obtained from the Regional Committee contact listed here for each country or from our website at: **www.pewlatinfellows.com**

The application deadline is October 1, 2008. Winners will be notified in April 2009 and the fellowship should begin no later than August 2009.

APPLICATION DEADLINE IS OCTOBER 1, 2008.

ARGENTINA
Maria Fernanda Ceriani, Ph.D., Chair
Fundación Instituto Leloir
Phone: (54) (11) 5238-7500 Ext. 3109
Fax: (54) (11) 5238-7501
E-mail: fceriani@leloir.org.ar

BRAZIL
Sandro Jose de Souza, Ph.D., Chair
Ludwig Institute for Cancer Research
Phone: (55) (11) 3388-3211
Fax: (55) (11) 3207-7001
E-mail: sandro@ludwig.org.br

CHILE
María Estela Andrés, Ph.D., Chair
Catholic University of Chile
Phone: (562) 354-2559
Fax: (562) 354-2660
E-mail: mandres@bio.puc.cl

MEXICO
Enrique Alejandro Reynaud Garza, Ph.D., Chair
Instituto de Biotecnología, UNAM
Phone: (52) (777) 329-0831
Fax: (52) (777) 317-2388
E-mail: enrique@ibt.unam.mx

All Other Countries
Silvia Montano de Jiménez, MPA
The Pew Latin American Fellows Program
3333 California Street, Suite 410
San Francisco, CA 94118
Phone: (415) 476-5116
Fax: (415) 502-4992
E-mail: montano@thecenter.ucsf.edu
Website: http://www.pewlatinfellows.com/

ETH

Eidgenössische Technische Hochschule Zürich
Swiss Federal Institute of Technology Zurich

Professor in Experimental Systems Biology or Synthetic Biology
Assistant Professor (Tenure Track) in Experimental Systems Biology or Synthetic Biology

ETH Zurich invites applications for two positions in Systems Biology or Synthetic Biology at the Department of Biosystems Science and Engineering in Basel (www.dbsse.ethz.ch). Research areas of interest include, but are not limited to, quantitative analyses of cell signaling pathways to predict the intracellular physiological and structural consequences, analyses of gene networks involved in distinct cellular functions and communication between cells, design and application of novel theory-based synthetic approaches to perturb biological systems in order to uncover basic network principles or to produce new cellular functions or components.

D-BSSE of ETH Zurich is located in Basel, the heart of the BioValley providing excellent opportunities for collaboration within this strong life science research community at the academic, clinical, and pharmaceutical industry level. SystemsX.ch (www.systemsx.ch), the Swiss initiative in systems biology, offers a dynamic and interactive research environment.

The educational goal of D-BSSE is interdisciplinary science and engineering. He or she will contribute to the ongoing study programs of the department including the curriculum in biotechnology, as well as be involved in establishing new master programs in systems and synthetic biology. Teaching responsibilities include courses in quantitative cell biology, analytical systems biology, and principles of synthetic biology. He or she will be expected to teach undergraduate level courses (German or English) and graduate level courses (English).

The positions can be filled either at full professor, associate or assistant professor level, depending on the age, scientific experience, and record of the applicant. Assistant professorships have been established to promote the careers of younger scientists. Their initial appointment is for four years with the possibility of renewal for an additional two-year period and promotion to a permanent position.

Please submit your application together with curriculum vitae, a list of publications, and a statement on future teaching and research activities **to the President of ETH Zurich, Prof. Dr. Ralph Eichler, Raemistrasse 101, 8092 Zurich, Switzerland, no later than August 31, 2008.** With a view toward increasing the number of female professors, ETH Zurich specifically encourages female candidates to apply.

POSITIONS OPEN

WAYNE STATE UNIVERSITY SCHOOL OF MEDICINE

TENURE-TRACK FACULTY POSITION

The Departments of Anatomy/Cell Biology and of Ophthalmology (Kresge Eye Institute), Wayne State University, invite applications for candidates with M.D. and/or Ph.D. degrees for a joint appointment, tenure-track position (rank of **ASSISTANT PROFESSOR** or higher). Current external funding and interest including, but not limited to, macular degeneration, inherited retinal diseases, uveitis, or glaucoma are preferred. Successful candidates will participate in teaching, contribute to the growth of a strong vision science research group, and have access to train talented Ph.D. students.

Information on the Departments can be found at **websites: http://www.med.wayne.edu/kresgeeye** and **http://www.med.wayne.edu/anatomy/.**

Positions include competitive recruitment package, salary, and comprehensive benefits. Interested applicants should respond to posting #035170 and apply online at **website: http://jobs.wayne.edu.**

Wayne State University is an Equal Opportunity Employer.

EVOLUTION/POPULATION BIOLOGY/ECOLOGY

The Biology Department of Franklin and Marshall College invites applications for two **VISITING ASSISTANT PROFESSOR** positions, beginning January 2009. The first position is for spring semester 2009, and academic year 2009-2010; the second is for spring semester 2009, only. Teaching responsibilities in spring semesters will include lectures and laboratories in an evolution-centered, introductory course that includes Mendelian genetics and ecology. The first position will also involve teaching an upper-level lecture/laboratory course in evolution, behavioral ecology, or population biology in fall 2009. Candidates should have a Ph.D. and demonstrated strength in teaching and research. Franklin and Marshall College has a tradition of excellence in science and student research. A new life sciences building opened in August 2007.

Please send a letter of application, a statement that includes plans for actively engaging undergraduates through teaching, curriculum vitae, and undergraduate and graduate transcripts to: **Prof. D. Ardia, Department of Biology, Franklin and Marshall College, Lancaster, PA 17604-3003.** Applicants should also have three reference letters sent directly to **Prof. Ardia.** Review of applications begins August 8, 2008. Electronic submissions cannot be accepted. **Telephone: 717-291-3949; fax: 717-358-4548; e-mail: dardia@fandm.edu; website: http://www.fandm.edu/biology.xml.**

Franklin and Marshall College is a highly selective liberal arts college with a demonstrated commitment to cultural pluralism. Equal Opportunity Employer.

POSTDOCTORAL POSITIONS. Several Postdoctoral positions are immediately available to study the role of lipoxygenases/eicosanoids in angiogenesis and vascular wall remodeling. Experience with animal models of angiogenesis and/or molecular cloning is highly desirable. Based on experience competitive salaries are offered. Interested and highly motivated candidates with Ph.D., M.D., or M.D./Ph.D. degree should send curriculum vitae and three letters of references to: **Gadiparthi N. Rao, Ph.D., Department of Physiology, University of Tennessee Health Science Center, 894 Union Avenue, Memphis, TN 38163. E-mail: grao@physio1.utmem.edu.** *The University of Tennessee is an Equal Employment Opportunity/Affirmative Action Title VI/Title IX/Section 504/ADA/ADEA institution in the provision of its education and employment programs and services.*

POSITIONS OPEN

TENURE-TRACK PROFESSOR GRADUATE PROGRAM DIRECTOR POSITION # F3004
Virginia Commonwealth University

The Department of Physiology and Biophysics is seeking a Graduate Program Director for its doctoral, Master's, and certificate programs. The candidate should be senior faculty of international stature with an active and continuously federally funded research program throughout his/her career. The candidate should possess extensive experience in leading a graduate program in disciplines such as physiology, biophysics, or neuroscience. Candidates should have an extensive training record. Demonstrated leadership in minority training programs would be preferred. In addition to the departmental duties, candidates will be expected to also contribute significantly to the Graduate Program within the School of Medicine that serves all the Basic Science Departments. Experience with umbrella programs emphasizing interdisciplinary training is required. Extensive experience in graduate admissions, academic advisement, training grant preparation, and management is expected. Experience with undergraduate teaching and mentorship is also desirable. Applicants should have M.D., Ph.D., or equivalent degree, and will be expected to contribute to the Department's research and teaching missions and develop vigorous collaborations at Virginia Commonwealth University (VCU). Applications deadline date: August 1, 2008. Submit curriculum vitae, names of three references with e-mail addresses, and research plans to **Dr. Clive Baumgarten** at **e-mail: baumgart@vcu.** *VCU is an Equal Opportunity/Affirmative Action Employer. Women, minorities, and persons with disabilities are encouraged to apply.*

Two **POSTDOCTORAL POSITIONS** are available at the Institute of Environmental Genomics (IEG) and Department of Botany and Microbiology, University of Oklahoma (OU) for individuals with background in molecular biology, genetics, biochemistry, and microbiology. Position One will mainly work on functional and comparative genomics of *clostridium, thermoanaerobacter, shewanella*, and *desulfovibrio* species related to bioremediation, and/or bioenergy using integrated genomics technologies and conventional approaches to understand gene functions, regulations, evolution, and networks. Position Two will focus on microbial ecology and community genomics including developing and using functional gene arrays (GeoChip) and metagenomics approaches (e.g. 454 sequencing) to analyze microbial communities related to bioenergy, bioremediation, global changes and agricultural practice. All postdoctoral candidates must have Ph.D. with demonstrated experience in molecular biology, genetics, microbial physiology, microbial ecology, or environmental engineering. Additional experience is desired but not required in bioinformatics, or genomic technology. All individuals will work cooperatively with scientists at different institutions. Interested candidates should send their curriculum vitae, descriptions of research accomplishments and interests, and the names and telephone numbers of at least three references to **Dr. Jizhong Zhou (e-mail: jzhou@ou.edu).** Further information can be found on the IEG **website: http://ieg.ou.edu/.** *The University of Oklahoma is an Affirmative Action/Equal Opportunity Employer and encourages diversity in the workplace.*

STAFF ASSOCIATE
Columbia University, Institute for Cancer Genetics

Position available immediately to study the mechanisms responsible for the maintenance of genomic stability. Candidate must have demonstrated knowledge and experience with cloning techniques; DNA and RNA isolation, purification and electrophoresis; real time polymerase chain reaction; DNA sequencing; cell culture and virus maintenance and infection; and recombinant protein expression and purification. Ability to work independently and collaboratively, laboratory organizational skills are required. Publications required. E-mail curriculum vitae to **Dr. Jean Gautier** at **e-mail: jg130@columbia.edu.**

Columbia University is an Equal Opportunity/Affirmative Action Employer.

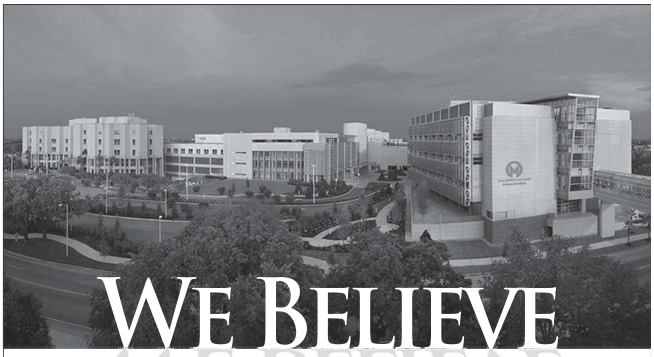

THE CURE WILL BE FOUND RIGHT HERE

Research Faculty Position
Molecular Oncology

Consistently ranked in U.S. News & World Report "Best Cancer Hospitals" for the past nine years, Moffitt Cancer Center and Research Institute is a free-standing, not-for-profit cancer center. Moffitt opened on the campus of Tampa's University of South Florida in October, 1986 and became Florida's only NCI designated Comprehensive Cancer Center in 2001. There is vast opportunity within our framework for information technology, scientific research, clinical treatment and quality of life studies, as we see over 15,000 new cancer patients each year. Our environment is one of multi-modality, patient-centered care requiring highly collaborative clinical research programs.

The Cancer Center is comprised of a large ambulatory care facility, 162 inpatient beds, including a dedicated transplant unit, 12 state-of-the art operating suites, a 22 bed intensive care unit, a high volume screening program, and a basic science research facility. The Moffitt Research Institute is comprised of approximately 140 Principal Investigators, 58 laboratories, and 306,000 square feet of research space. Our University of South Florida affiliation allows for a wide range of residency and fellowship programs, and Faculty of the Moffitt Cancer Center are eligible for academic appointments in their College of Medicine, commensurate with qualifications and experience.

Application Requirements

The successful candidates must possess a Ph.D. or M.D. degree and a demonstrated potential for extramural funding. Individuals with a research interest in proteomics are especially encouraged to apply, but any areas of gene regulation, signal transduction, cancer genetics, and functional genomics will be considered. Applicants must have a proven track record of independent research and demonstrated sustained extramural funding. In addition, the Associate Member rank requires at least five years experience with continuing and productive service as an Assistant Member. The Senior Member rank requires documentation of national recognition, leadership ability and at least five years experience with continuing and productive service as an Associate Member.

Please reference position no. MRI08. Interested candidates should send curriculum vitae and a brief statement of major academic interests in one single pdf document to The Molecular Oncology Search Committee at donna.blaha@moffitt.org.

For more information about this and other opportunities, and to apply online, visit our website moffittcareers.org.

MOFFITT CANCER CENTER

Moffitt Cancer Center provides a tobacco-free work environment, is an equal opportunity, affirmative action employer, and a drug free workplace.

Imperial College London

Division of Cell & Molecular Biology
Department of Life Sciences
Faculty of Natural Sciences

Lecturer/Senior Lecturer in Immunology

Lecturer - Salary: £40,050 - £44,730 p.a.
Senior Lecturer - Salary: £49,400 p.a.

Imperial College is ranked the fifth best university in the world (Times Higher QS World University Rankings 2007).

We are seeking two new permanent members of academic staff to be based at the South Kensington Campus of Imperial College London. Applicants should have a strong record of academic achievement and be able to direct an exciting independent research programme in an area of immunology that synergises with our current research activities, such as the immunology of infectious disease, innate immunity or molecular immunology. Molecular and Cellular Imaging is a new strategic focus across Imperial and we are especially interested in applicants wishing to establish a research programme in imaging immunology in the whole organism.

The successful applicants will use newly refurbished laboratories with access to state of the art facilities and cutting-edge novel fluorescence imaging technologies, including multi-photon imaging. In addition to the other members of the Department of Life Sciences, there will also be opportunities to establish links with the large community of medical and physical scientists interested in Immunology at Imperial.

Informal enquiries can be made to Prof Dan Davis, d.davis@imperial.ac.uk or Prof Maggie Dallman, m.dallman@imperial.ac.uk

Further details and an application form can be obtained from the College employment website: http://www3.imperial.ac.uk/employment/academic

Applications and requests for further information should be made to Pat Evans, Department of Life Sciences, Sir Alexander Fleming Building, Imperial College London, London, SW7 2AZ, email: pat.evans@imperial.ac.uk Applications should include a completed application form, a curriculum vitae, a brief statement of research interests, and names and contact details of three referees. Please quote reference: **NS2008085DP**

Closing date: 18 July 2008.

Valuing diversity and committed to equal opportunities

Imperial College London is a Silver Swan Award Holder

POSITIONS OPEN

POSTDOCTORAL RESEARCH ASSOCIATE: PAIN RESEARCH. Position available for M.D. or Ph.D. with experience in pain research to join multidisciplinary research group at the Center for Neuroscience and Regeneration Research of Yale University. Superb opportunity to interact with a highly collaborative team of pathobiologists, cell and molecular biologists, electrophysiologists, pharmacologists, et cetera. Prior experience and publications in whole-animal pain models are essential. Send letter of interest, curriculum vitae, and three letters of recommendation to: **Stephen G. Waxman, M.D., Ph.D., Department of Neurology, LCI 708, P.O. Box 208018, New Haven, CT 06520-8018; e-mail: stephen.waxman@yale.edu.** *Qualified women and members of underrepresented minority groups are encouraged to apply. Affirmative Action and Equal Opportunity Employer.*

POSTDOCTORAL RESEARCH ASSOCIATE

Background: Sustainability is a key economic and environmental issue in bioenergy feedstock production. Strategies that minimize anthropogenic energy inputs by promoting biological N fixation are needed to achieve the goal of sustainable production of bioenergy feedstocks. **Dr. Angela Kent** will be investigating the contribution of nitrogen-fixing bacterial endophytes to bioenergy crops. The proposed research aims to identify and characterize diazotrophs that colonize potential bioenergy crops, to determine the magnitude of their contribution to plant N requirements, and to examine the ecological factors that influence the colonization and activity of nitrogen-fixing endophytes. Using this knowledge, we aim to design strategies to promote colonization and activity of N2-fixing endophytes.

Responsibilities: (1.) Survey the endophyte populations in potential bioenergy crops using culture-based and culture-independent approaches. (2.) Examine ecological factors that influence the colonization and activity of diazotrophs in potential bioenergy crops. (3.) Conduct metagenomic analyses on *Miscanthus endophyte* populations. (4.) Design and execute 15N experiments to measure the magnitude of nitrogen fixation in bioenergy crops in greenhouse and field experiments (5.) Analyze and report research findings at scientific meetings and in the scientific literature. (6.) Supervise undergraduate researchers and collaborate with graduate research assistants.

Qualifications: Successful candidates will have a Ph.D. in microbiology, microbial ecology, or closely related field. Demonstrated research abilities in microbial ecology, plant-microbe interactions, and nucleic acid-based methods are necessary, as is an aptitude for conducting independent research and publishing research findings. Experience with microscopy and bioinformatics is highly desirable.

Please send resume and cover letter to:

Dr. Angela Kent
University of Illinois
Department of Natural Resources and Environmental Sciences
1102 W. Gregory Drive
Urbana, IL 61801

POSTDOCTORAL POSITION in insect molecular biology/biochemistry with **Gary Blomquist,** biochemistry and molecular biology at (UNR), Reno, Nevada, to study regulation and production of pine bark beetle monoterpene pheromone biosynthesis and P450 enzymes. We seek a candidate with a Ph.D. in a molecular life science field and a solid background in molecular biology and/or protein chemistry. Experience with enzymology, molecular modeling, and/or gas chromatography/mass spectrometry an asset but not required. Salary commensurate with experience. To apply follow the link to the University of Nevada, Reno **website: http://www.unrsearch.com/applicants/Central?quickFind=53262.** *UNR is an Equal Opportunity Affirmative Action Employer.*

POSITIONS OPEN

Two **POSTDOCTORAL/RESEARCH ASSOCIATE POSITIONS** available at the University of Michigan for **ENZYMOLOGISTS** to study the mechanism of action of cytochrome P450 with its redox partners, cytochrome b5, and cytochrome P450 reductase. A Ph.D. in chemistry or biochemistry required. The laboratory is investigating how the redox partners modulate the catalytic mechanism, structure, and function of cytochrome P450. One position involves generating and characterizing the function of mutant proteins. The second will consist of biophysical characterization of heme and flavoproteins (electron paramagnetic resonance, mass spectrometry, pre-steady state kinetics under anaerobic conditions). Experience with heme and/or flavoproteins desirable. E-mail resume and names of three references to **L. Waskell** at **e-mail: waskell@umich.edu.**

MEDICAL RESEARCHER

Highly intelligent individual with exceptional communication skills sought to help research and coordinate family medical and healthcare issues. Act as liaison with leading medical researchers and consultants in academia and industry, with responsibility for technical, financial, and administrative functions. Considerable weight given to evidence of unusual academic or other intellectual distinction. Scientific background a plus, but not required. Excellent compensation with significant upside potential.

Resume to **e-mail: fmc4@spsfind.com.**

ENVIRONMENTAL SCIENTIST

Conduct environment inspections and soil and groundwater sampling. Compile and analyze derived data. Support operation of remediation system. Write risk assessments, prepare reports, and manage database. Required: B.S. in environmental engineering or environmental science, or foreign equivalent. Forty hours/week. Job/interview site: Irvine, California. Fax curriculum vitae to: **GeoTrans, Incorporated. Human Resources, fax: 240-804-8008.**

POSITIONS OPEN

POSTDOCTORAL RESEARCH ASSOCIATE: SPINAL CORD INJURY (SCI). Position available for M.D. or Ph.D. with experience in SCI research to join multidisciplinary research group at the Center for Neuroscience and Regeneration Research of Yale University. Superb opportunity to interact with a highly collaborative team of pathobiologists, cell and molecular biologists, electrophysiologists, pharmacologists, et cetera. Prior experience and publications in mammalian in vivo SCI are essential. Send letter of interest, curriculum vitae, and three letters of recommendation to: **Stephen G. Waxman, M.D., Ph.D., Department of Neurology, LCI 708, P.O. Box 208018, New Haven, CT 06520-8018; e-mail: stephen.waxman@yale.edu.** *Qualified women and members of underrepresented minority groups are encouraged to apply. Affirmative Action and Equal Opportunity Employer.*

MARKETPLACE